

**NASA/TP-20220014814**



# **Astrodynamics Convention and Modeling Reference for Lunar, Cislunar, and Libration Point Orbits**

Version 1.1, 12/1/2022

*David Folta, Natasha Bosanac, Ian Elliott, Laurie Mann, Rebecca Mesarch  
and Jose Rosales*

---

**December 2022**

## NASA STI Program ... in Profile

Since its founding, NASA has been dedicated to the advancement of aeronautics and space science. The NASA scientific and technical information (STI) program plays a key part in helping NASA maintain this important role.

The NASA STI program operates under the auspices of the Agency Chief Information Officer. It collects, organizes, provides for archiving, and disseminates NASA's STI. The NASA STI program provides access to the NTRS Registered and its public interface, the NASA Technical Reports Server, thus providing one of the largest collections of aeronautical and space science STI in the world. Results are published in both non-NASA channels and by NASA in the NASA STI Report Series, which includes the following report types:

- **TECHNICAL PUBLICATION.** Reports of completed research or a major significant phase of research that present the results of NASA Programs and include extensive data or theoretical analysis. Includes compilations of significant scientific and technical data and information deemed to be of continuing reference value. NASA counterpart of peer-reviewed formal professional papers but has less stringent limitations on manuscript length and extent of graphic presentations.
- **TECHNICAL MEMORANDUM.** Scientific and technical findings that are preliminary or of specialized interest, e.g., quick release reports, working papers, and bibliographies that contain minimal annotation. Does not contain extensive analysis.
- **CONTRACTOR REPORT.** Scientific and technical findings by NASA-sponsored contractors and grantees.

- **CONFERENCE PUBLICATION.** Collected papers from scientific and technical conferences, symposia, seminars, or other meetings sponsored or co-sponsored by NASA.

- **SPECIAL PUBLICATION.** Scientific, technical, or historical information from NASA programs, projects, and missions, often concerned with subjects having substantial public interest.

- **TECHNICAL TRANSLATION.** English-language translations of foreign scientific and technical material pertinent to NASA's mission.

Specialized services also include organizing and publishing research results, distributing specialized research announcements and feeds, providing information desk and personal search support, and enabling data exchange services.

For more information about the NASA STI program, see the following:

- Access the NASA STI program home page at <http://www.sti.nasa.gov>
- E-mail your question to [help@sti.nasa.gov](mailto:help@sti.nasa.gov)
- Phone the NASA STI Information Desk at 757-864-9658
- Write to:  
NASA STI Information Desk  
Mail Stop 148  
NASA Langley Research Center  
Hampton, VA 23681-2199

**NASA/TP-20220014814**



# **Astrodynamics Convention and Modeling Reference for Lunar, Cislunar, and Libration Point Orbits**

Version 1.1, 12/1/2022

*David Folta*  
*Goddard Space Flight Center, Greenbelt, Maryland*

*Natasha Bosanac*  
*University of Colorado, Boulder, Colorado*

*Ian Elliott*  
*University of Colorado, Boulder, Colorado*

*Laurie Mann, Rebecca Mesarch and Jose Rosales*  
*Goddard Space Flight Center, Greenbelt, Maryland*

National Aeronautics and  
Space Administration

Goddard Space Flight Center  
Greenbelt, Maryland 20771

---

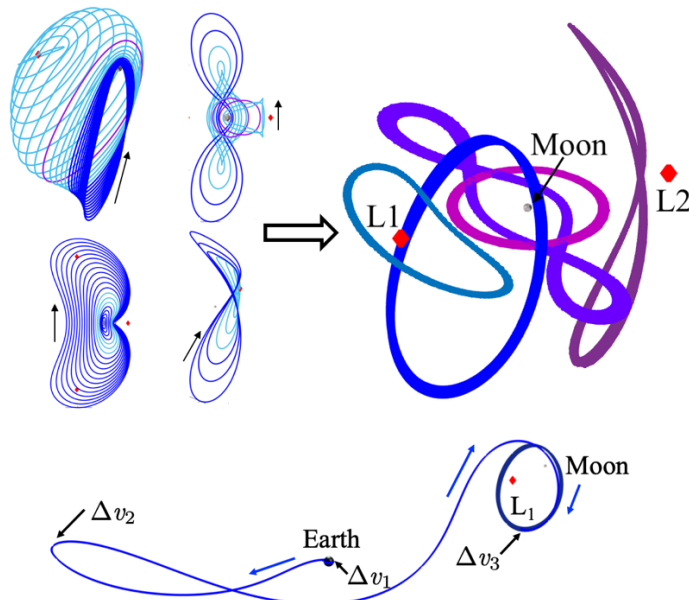
**December 2022**

Trade names and trademarks are used in this report for identification only. Their usage does not constitute an official endorsement, either expressed or implied, by the National Aeronautics and Space Administration.

*Level of Review: This material has been technically reviewed by technical management.*



# Astrodynamics Convention and Modeling Reference for Lunar, Cislunar, and Libration Point Orbits



Version 1.1, 12/1/22

*David Folta  
NASA Goddard Space Flight Center, Greenbelt, Maryland*

*Natasha Bosanac  
University of Colorado, Boulder, Colorado*

*Ian Elliott  
University of Colorado, Boulder, Colorado*

*Laurie Mann,  
Rebecca Mesarch,  
Jose Rosales  
NASA Goddard Space Flight Center, Greenbelt, Maryland*

## Executive Summary

The purpose and direction of this document is to provide U.S. government agencies, specifically National Aeronautics and Space Administration (NASA) and Department of Defense (DoD) space related centers, with a foundational summary of astrodynamics concepts for trajectory design, navigation, and operations in the cislunar, lunar, and libration point regions. This document is provided in response to an Interagency Agreement (IAA) between NASA and the National Geospatial-Intelligence Agency (NGA).

With applications to these regions of the Earth-Moon system, this document summarizes: the definitions of standard and unique coordinate systems for Positioning, Navigation, Timing and targeting (PNT), transformations between those coordinate frames, definitions of common time systems, a description of numerical integration, description of a widely-used and approximate dynamical model of a three-body system for preliminary analysis and nomenclature definition, description of higher-fidelity models of cislunar space, and the application of these concepts to sample scenarios with a focus on common steps in trajectory and maneuver design for a spacecraft in cislunar space. This information is critical to mission design and navigation far above the geosynchronous orbit region, where lunar perturbations are required to be modeled accurately and consistently but render trajectory design and analysis a complex procedure. Software tools such as the Goddard Space Flight Center (GSFC) open source General Mission Analysis Tool (GMAT) is used as a reference, along with a wide variety of resources constructed by NASA and other government agencies, academia, and industry, for mathematical specifications and practical considerations.

This document has been prepared by and under the auspices of NASA. The GSFC Mission Engineering and Systems Analysis (MESA) Division (Code 590) and the Navigation and Mission Design Branch (Code 595) are part of NASA. Their engineers and scientists have expertise in lunar, cislunar, and libration point region trajectory guidance and navigation and timing. NASA GSFC has supported many successful lunar and cislunar missions over the past several decades. These missions include the Lunar Reconnaissance Orbiter (LRO), the two Acceleration, Reconnection, Turbulence and Electrodynamics of the Moon’s Interaction with the Sun (ARTEMIS) spacecraft, Transiting Exoplanet Survey Satellite (TESS), Lunar Prospector, Lunar Crater Observation and Sensing Satellite (LCROSS), Clementine, and several Sun-Earth libration point missions such as WIND and Deep Space Climate Observatory (DSCOVR), dating back four decades. NASA GSFC also supports the upcoming Gateway lunar mission, the Artemis Lunar Program and Human Landing Systems, and leads both the Lunar IceCube low thrust mission and concept design for the Lunar Communication Relay and Navigation System (LCRNS).

## Contributions

This document was developed and drafted as part of the support task that the National Aeronautics and Space Administration's (NASA's) NASA Goddard Space Flight Center (GSFC) Navigation and Mission Design Branch (NMB) carried out for the National Geospatial Intelligence Agency (NGA). The effort was completed by GSFC, under an Interagency Agreement (IAA).

Reference herein to any commercial software product, process, or services by trade name, trademark, manufacturer, or otherwise, does not constitute or imply its endorsement by the United States Government or the NASA GSFC.

**The authors for this document are:**

- David Folta (NASA Goddard Space Flight Center)
- Natasha Bosanac (University of Colorado Boulder)
- Ian Elliott (University of Colorado Boulder)
- Laurie Mann (NASA Goddard Space Flight Center)
- Jose Rosales (NASA Goddard Space Flight Center)
- Rebecca Mesarch (NASA Goddard Space Flight Center)

**We are grateful for the contribution, reviews, feedback and information received from the following people:**

- Yousaf Butt (Department of Defense)
- Cheryl Gramling, (NASA Goddard Space Flight Center)
- Steve Hughes (NASA Goddard Space Flight Center)
- Darrel Conway (Thinking Systems Inc)
- Alan Segerman and the Mathematics and Orbit Dynamics group within the U.S. Naval Research Laboratory
- Wayne Yu (NASA Goddard Space Flight Center)
- Noble Hatten (NASA Goddard Space Flight Center)
- Alinda Mashiku (NASA Goddard Space Flight Center)
- Erwan Mazarico (NASA Goddard Space Flight Center)
- Carolina Restrepo (NASA Goddard Space Flight Center)
- Noah Petro (NASA Goddard Space Flight Center)
- NASA Goddard Space Flight Center Navigation and Mission Design Branch, Code 595

**Funding:** The work performed to prepare this document was supported by an IAA between NASA and NGA. The work was performed at NASA Goddard Space Flight Center and at the University of the Colorado Boulder under NASA Grant 80NSSC21K0699.

# Astrodynamics Convention and Modeling Reference for Lunar, Cislunar, and Libration Point Orbits

Version 1.1, December 1, 2022

## Contents

<b>1</b>	<b>Introduction</b>	<b>7</b>
<b>2</b>	<b>Definitions of Selected Reference Systems and Frames</b>	<b>10</b>
2.1	Fundamental Terminology . . . . .	10
2.2	International Celestial Reference System . . . . .	12
2.3	Selected Earth-Centered Systems . . . . .	13
2.3.1	Earth-Centered Inertial Systems . . . . .	13
2.3.2	International Terrestrial Reference System . . . . .	14
2.3.3	World Geodetic System 1984 . . . . .	14
2.4	Selected Moon-Centered Systems . . . . .	15
2.4.1	Moon-Inertial System . . . . .	15
2.4.2	Moon-Fixed Systems . . . . .	16
2.5	Selected Synodic Frames . . . . .	18
2.5.1	Earth-Moon Rotating Frame . . . . .	18
2.5.2	Sun-Earth-Moon Rotating Frame . . . . .	18
2.5.3	Sun-Earth Rotating Frame . . . . .	19
2.5.4	Geocentric Solar Ecliptic . . . . .	19
2.6	Selected Spacecraft-Centered Systems . . . . .	19
2.6.1	Local Vertical, Local Horizontal System . . . . .	19
2.6.2	Velocity, Normal, Co-Normal Axes . . . . .	20
2.7	Describing the State of a Spacecraft in Cislunar Space using Two-Line Elements . . . . .	20
<b>3</b>	<b>Definitions of Common Time Systems</b>	<b>22</b>
3.1	International Atomic Time (TAI) . . . . .	22
3.2	Terrestrial Time (TT) . . . . .	22
3.3	Geocentric Coordinate Time (TCG) . . . . .	23
3.4	Barycentric Dynamical Time (TDB) . . . . .	23

3.5	Barycentric Coordinate Time (TCB) . . . . .	24
3.6	Universal Time (UT1) . . . . .	24
3.7	Coordinated Universal Time (UTC) . . . . .	24
3.8	Time Formats . . . . .	25
3.9	GPS times . . . . .	25
3.10	Navigation Considerations and Relativistic Effects . . . . .	25
<b>4</b>	<b>Overview of Common Coordinate System Transformations</b>	<b>29</b>
4.1	Transformation Background . . . . .	29
4.2	Transformation Roadmap . . . . .	31
4.3	Transforming Between Earth-Centered Inertial and Body-Fixed Systems . . . . .	31
4.3.1	Precession-Nutation . . . . .	32
4.3.2	Sidereal Motion . . . . .	34
4.3.3	Polar Motion . . . . .	36
4.3.4	Transformations Between GCRF and ITRF . . . . .	37
4.3.5	Transformations Between GCRF and Mean Equator and Equinox at J2000 . . . . .	37
4.4	Transforming Between Inertial Systems with Distinct Origins . . . . .	39
4.4.1	Transformations Between GCRF and ICRF . . . . .	39
4.4.2	Transformations Between GCRF and Moon-Centered Inertial System . . . . .	40
4.5	Transforming Between Moon-Centered Systems . . . . .	41
4.6	Transforming Between Inertial and Synodic Systems . . . . .	45
4.6.1	General Procedure . . . . .	45
4.6.2	Transformations Between GCRF and Earth-Moon Rotating Frame . . . . .	48
4.6.3	Transformations Between Moon Inertial and Earth-Moon Rotating Frame . . . . .	49
4.6.4	Transformations Between GCRF and Sun-Earth Rotating Frame . . . . .	49
4.6.5	Transformations Between GCRF and Geocentric Solar Ecliptic Frame . . . . .	50
<b>5</b>	<b>Numerically Generating Trajectories</b>	<b>52</b>
5.1	Numerical Integration of the Equations of Motion . . . . .	52
5.1.1	Euler Methods . . . . .	52
5.1.2	Nomenclature . . . . .	53
5.1.3	Runge-Kutta Methods . . . . .	54
5.1.4	Adams-Basforth-Moulton Methods . . . . .	57
5.1.5	Other Methods . . . . .	58

5.2	Solving Two-Point Boundary Value Problems . . . . .	59
5.2.1	Shooting Methods . . . . .	59
5.2.2	Collocation . . . . .	62
5.2.3	Continuation . . . . .	64
5.2.4	Optimal Trajectories . . . . .	66
<b>6</b>	<b>Preliminary Modeling of Cislunar Space and Definitions</b>	<b>68</b>
6.1	Fundamental Assumptions . . . . .	68
6.2	Nondimensionalization Scheme . . . . .	69
6.3	Circular Restricted Three-Body Problem Equations of Motion . . . . .	70
6.4	Jacobi Constant . . . . .	71
6.5	Fundamental Solutions . . . . .	71
6.6	Equilibrium Points . . . . .	72
6.7	Regions of Allowable Motion . . . . .	72
6.8	Region Nomenclature . . . . .	73
6.9	Periodic Orbit Stability . . . . .	75
6.10	Computing Families of Periodic Orbits . . . . .	76
6.11	Periodic Orbit Families . . . . .	80
6.11.1	Common $L_1$ , $L_2$ and $L_3$ Periodic Orbit Families . . . . .	84
6.11.2	Common $L_4$ and $L_5$ Periodic Orbit Families . . . . .	87
6.11.3	Common Moon-Centered Periodic Orbit Families . . . . .	88
6.11.4	Common Resonant Periodic Orbit Families . . . . .	89
6.12	Quasi-Periodic Orbits . . . . .	89
6.13	Hyperbolic Invariant Manifolds . . . . .	91
6.14	Heteroclinic and Homoclinic Connections . . . . .	93
6.15	Correcting a Transfer in the CR3BP . . . . .	93
<b>7</b>	<b>Higher-Fidelity Modeling of Cislunar Space</b>	<b>95</b>
7.1	Point Mass Gravitational Interactions . . . . .	95
7.2	Higher-Order Gravitational Models . . . . .	95
7.3	Solar Radiation Pressure . . . . .	96
7.4	Atmospheric Drag . . . . .	97
7.5	Propulsion Systems . . . . .	98
7.6	Relative Contributions of Each Force . . . . .	99

7.6.1	Earth-Moon Point Mass Gravitational Interactions . . . . .	99
7.6.2	Higher-Order Gravitational Models . . . . .	100
7.6.3	Point Mass Gravitational Influence of the Sun . . . . .	103
7.6.4	Solar Radiation Pressure . . . . .	104
7.6.5	Summary . . . . .	105
7.7	Useful Heuristics for Defining High-Fidelity Dynamical Models . . . . .	107
<b>8</b>	<b>Use Case and Practical Considerations</b>	<b>108</b>
8.1	Scenario Overview . . . . .	108
8.2	Constructing a Reference Mission Orbit . . . . .	109
8.2.1	Rapid Preliminary Analysis in a Low-Fidelity Model . . . . .	109
8.2.2	Relevant State Transformations . . . . .	114
8.2.3	Recovering a Nearby Trajectory in an Ephemeris Model via Single Shooting in GMAT . . . . .	116
8.2.4	Recovering a Nearby Trajectory in an Ephemeris Model via Multiple Shooting in Custom Codes	123
8.3	Designing a Transfer to the Mission Orbit . . . . .	127
8.3.1	Designing a Direct Transfer: Single-Shooting Backward in Time . . . . .	129
8.3.2	Designing a Direct Transfer: Single-Shooting Forward in Time . . . . .	135
8.3.3	Designing an Indirect Transfer: Single-Shooting Backward in Time . . . . .	141
8.4	Station-Keeping Near the Mission Orbit . . . . .	146
<b>9</b>	<b>Summary</b>	<b>151</b>

## 1 Introduction

Of paramount importance to the planning of robotic and human missions to various Earth-Moon (cislunar), libration, and lunar regions is to document established and demonstrated conventions and applications that are necessary to achieve such missions. It is also important to provide these standards and conventions to the at large astrodynamics community for general purpose and consistency in successful mission design, navigation, and operational support endeavors.

The purpose and direction of the Astrodynamics Convention and Modeling Reference for Lunar, Cislunar, and Libration Point Orbits technical document is to provide U.S. government agencies, specifically National Aeronautics and Space Administration (NASA) and Department of Defense (DoD) space related centers including NGA and commercial entities with a foundational summary of astrodynamics concepts for trajectory design and operations in the Earth-Moon system. The contents of this document are based on decades of previous coordinate system definitions specified by NASA and more recent development on multi-body dynamics by the astrodynamics community. This document is meant to fulfill a basic understanding of coordinate systems and transformations that can be applied to complex trajectory designs. In addition, with many missions now using similar coordinate systems and dynamics to accomplish challenging designs, an example mission scenario is constructed to provide basic guidance in order to meet performance and mission requirements for new environments.

With applications to cislunar, lunar, and libration point orbits, this document includes seven technical sections which address: the definitions of standard and unique coordinate systems for positioning, navigation, timing, and targeting (PNT), definition of common time systems, overview of common coordinate system transformations, overview of approaches for numerical generating trajectories, preliminary modeling of cislunar space via the circular restricted three-body problem, the description of higher-fidelity models of cislunar space, and the application of these concepts to trajectory and maneuver design for a sample mission concept in these regions of space.

The authors would like to acknowledge that the contents of this document are dependent upon the advancements made by the world-wide astrodynamics community for the general knowledge, guidance, and algorithms employed and discussed herein. A list of numerous references is offered, though there are many other peer reviewed materials, guides, documents, and books which are available to assist in understanding these topics in greater detail. Embedded within each section are blue colored call-out boxes that supply the reader with insight, guidelines, and information based on past mission operations and research findings within the astrodynamics community. In addition, the equations and definitions developed in earlier sections are used in the Use Case and Practical Considerations section.

Section 2 supplies an overview of reference systems and frames that are commonly used by NASA GSFC for operational support of missions operating in the cislunar, lunar, and libration point regions. It describes the fundamental terminology and the definitions and construction of selected Earth and Moon centered systems. These systems include inertial and fixed frames along with synodic frames. Specific coordinate systems that are used to describe the state of an object with respect to a central body or reference location are defined. While there are various useful coordinate systems

for various applications and analysis tasks, those that are most applicable to regions beyond geosynchronous orbit (GEO), including the cislunar, lunar, and libration point regions, are covered. In this section, the coordinate frame descriptions follow both NASA standards of practice and terminology that are widely used throughout the astrodynamics community.

Section 3 describes the definitions of time standards that are critical for coordinate system definition as well as operational, navigation, and scientific purposes. For navigation solutions, time errors directly translate into position and velocity errors, influencing the resulting prediction. Furthermore, scientists not only need to accurately locate collected data but also accurately time-tag it. There are a wide array of useful time systems for various applications and data analysis tasks, as outlined in many well-known textbooks and in the references listed in this document. A time system used for a specific application must be appropriate for the orbital regime and central body, and must properly account for relativistic effects. Accordingly, this section presents a brief overview of the time systems that are, at the time of writing, most applicable to coordinate system definitions and spacecraft operations within cislunar, lunar, and libration point regions. This section may be updated and expanded in subsequent editions following current work within the technical community to prepare improved time standards for cislunar operations. These common time scales tend to be defined using various initial epochs and one of the following physical phenomena: atomic transitions, sidereal motion of the Earth, the rotation of pulsars, or the motion of celestial bodies. This section also addresses at a high level the incorporation of relativistic effects.

Section 4 focuses on state transformations between two coordinate systems for an object in cislunar space, libration orbits, and lunar orbits. It requires a combination of some or all of the following steps: rotation between distinct axes, translation of the origin, a conversion between distinct types of coordinates, and a transformation between quantities expressed in distinct units or scales. A rotation is required when transforming, for example, between body-fixed and inertial coordinate systems or between inertial and synodic coordinates. When the coordinate systems use distinct origins, such as the center of the Earth or Moon or the barycenter of the Earth-Moon system, a translation must also be performed using knowledge of their relative position vectors, typically calculated using ephemerides. The subsections present common foundational concepts used across the presented transformations and are described not only with common equations and notations but also using figures to display the rotation directions and angles and any translations.

Section 5 summarizes methods used to numerically generate satellite trajectories. In the context of this document, a trajectory reflects the path a satellite (natural or human-made) follows in space over a specified time interval. The goal of this section is to present a high-level overview of commonly-used numerical approaches to compute trajectories and the associated challenges, with a focus on applicability to the lunar/cislunar region. Subsections address several well-known approaches to solving initial value problems. Common approaches to solving two point boundary value problems as described, including shooting and continuation methods that are routinely used for trajectory design or targeting for orbit maintenance. Collocation and optimization techniques are also addressed at a high level.

Section 6 discusses low-fidelity modeling of cislunar space and key technical concepts. Spacecraft operating in

cislunar space are significantly influenced by a wide variety of forces, including, but not limited to: the irregular gravitational fields of the Earth and Moon, the gravitational influence of the Sun and other celestial bodies throughout the solar system, solar radiation pressure, and relativistic effects. Analyzing the structure of the cislunar dynamical environment when incorporating all of these force contributions is challenging, numerically intensive, and limits the discovery of fundamental insights into the solution space. NASA and the astrodynamics community often use an approximate dynamical model labeled the circular restricted three-body problem (CR3BP) for a preliminary exploration of cislunar space and construction of an initial guess prior to higher-fidelity analyses. This dynamical model seeds much of the terminology used to describe regions of cislunar space and fundamental motions. This section presents a brief summary with the goal of supplying a high level understanding of the foundational theoretical insights derived from this low-fidelity model of cislunar space; references to more detailed discussions are provided throughout the text for the interested reader. A subsection is also devoted to the computation of well-known families of periodic orbits throughout the Earth-Moon CR3BP. Similar concepts can be applied to other multi-body systems such as the Sun-Earth system.

Section 7 focuses on higher-fidelity modeling of cislunar space. Modeling the motion of a spacecraft at a high fidelity involves constructing a dynamical model that approximates the true environment as closely as possible. This section summarizes the most significant forces that may be modeled and impart an acceleration on a spacecraft, including: gravity, solar radiation pressure, atmospheric drag, and thrust applied by a propulsion system. Beyond simply including these forces in a dynamical model, deviations from the true environment still exist due to uncertainty in the parameters governing each force. Additional accelerations impacting the path of the spacecraft include random perturbations such as those that might occur due to regular momentum unloads. This section also provides data on the relative contributions of each force and a comparison of these accelerations that can be used to gauge their importance in modeling the cislunar and libration orbit dynamics.

The final section demonstrates the practical implementation of and considerations required in using the outlined coordinate systems, transformations, time descriptions, numerical methods and modeling approaches in the context of a mission concept. This mission concept involves a spacecraft operating as a lunar communications relay; such a concept has been explored from a mission and trajectory design perspective by NASA GSFC. This section specifically focuses on the following aspects of this use case: 1) designing a feasible mission orbit in cislunar space subject to hardware and mission requirements, from preliminary analysis in a low-fidelity model to high-fidelity analysis in NASA GSFC's General Mission Analysis Tool (GMAT); 2) designing a transfer from the Earth to the selected mission orbit; and 3) designing station-keeping maneuvers to maintain the path in the vicinity of a reference orbit. These examples are designed for the non-expert to understand and implement.

In summary, this document is intended to be used as a reference in the construction, applications, and modeling of cislunar, libration, and lunar orbits. The contents reflect the general knowledge of the authors who have operational experience that can be directly applied to this challenging dynamical region of space.

## 2 Definitions of Selected Reference Systems and Frames

This section supplies an overview of reference systems and frames that are commonly used by NASA GSFC for operational support of missions in the cislunar, lunar, and libration point regions. First, fundamental terms for specifying a coordinate system are defined. Then, specific coordinate systems that describe the state of an object with respect to a central body or reference location are defined. While there are a larger array of useful coordinate systems for various applications and data analysis tasks, only those that are most applicable to regions beyond geosynchronous orbit (GEO), including the cislunar, lunar, and libration point regions, are covered. In this section, the coordinate frame descriptions follow both NASA standards of practice and terminology that are widely used throughout the astrodynamics community.

### 2.1 Fundamental Terminology

A reference system is a set of “constants, conventions, models, and parameters, which serve as the necessary basis for the mathematical representation of geometric and physical quantities” (Drewes, 2009, pg. 3 [1]). Reference systems are specified by defining an origin (e.g., the center of mass of a celestial body), a set of axes (e.g., a right-handed, orthogonal set of vectors), a scale (the magnitude of the vector defining the axis), an orientation (e.g., the third axis is aligned with a body’s spin axis), and a time evolution (i.e., the time derivatives of the origin, axis orientation, and scale). Furthermore, a datum is a reference system equipped with a reference surface. Examples of a datum are a reference ellipsoid (i.e., a smooth surface that approximates the shape of the Earth), or a geoid (i.e., a model of global mean sea level characterized by points with the same geopotential). An example of a reference ellipsoid is the latest version of the World Geodetic System (WGS), i.e., WGS84. An example of geoid is the EGM2008 that contains geopotential coefficients that define a global potential surface to coincide with mean sea level.

The concept of a ‘coordinate’ characterizes how points are defined in the reference system. In a three-dimensional space, three components of a vector are required to define a position of an object. Hence, a coordinate system is the definition of the three components of a vector that define the position of an object in space with respect to a reference system. Well-known types of coordinate systems include, but are not limited to [2]:

- Cartesian coordinate system: each component is the projection of a vector onto each one of the axes in a reference system
- Spherical coordinate system: two components are the angles that represent the longitude and latitude (or right ascension and declination), and the third component is the distance of the object from the origin
- Elliptic coordinate system: two components are the angles that represent the longitude and latitude, and the third component is the height with respect to a reference ellipsoid

The definition of a reference system does not specify the values of the parameters that characterize it; only their definition. A reference frame is a realization of “the reference system physically, i.e., by a solid materialization of points, and mathematically, i.e., by the determination of parameters (e.g., geometric coordinates)” (Drewes, 2009, pg. 3 [1]).

The parameters of a reference frame are typically characterized by a set of computed coordinates at selected points.

In some reference systems, the associated basis vectors or axes are defined using a meaningful reference plane and direction for the first basis vector. Then, the third basis vector is selected normal to this plane to complete either a right-handed or left-handed triad [3]. Previous definitions of common Earth-centered coordinate systems used several foundational reference planes and directions including:

- The ecliptic plane that is defined, based on recommendations from the International Astronomical Union (IAU) 2006 Resolution B1, as the plane normal to the mean orbital angular momentum vector of the Earth-Moon barycenter relative to the solar system barycenter [4].
- The equatorial plane of a celestial body, i.e., the plane that is normal to the spin axis of the body and passes through its center [3].
- The direction to the vernal equinox, commonly used as a reference direction for defining a basis vector in many coordinate systems. The direction to the vernal equinox is aligned with the ascending node of the ecliptic plane when measured relative to the Earth's equatorial plane [3]. The vernal equinox is not a fixed direction, but drifts by about 1.4 deg/century, with variation in this drift on the order of <1 arc-sec/year [3].
- A local meridian, which corresponds to half a great circle on a celestial body, with a constant longitude.

Due to the complex gravitational environment within our solar system, calculation and specification of these common reference planes and directions typically requires additional terminology. For instance, the rotational axis of a celestial body may experience precession, nutation, and polar motion [5]. Accordingly, calculating an equatorial plane and/or vernal equinox direction requires specification of the model used to capture the orientation of the spin axis of the celestial body in three-dimensional space. For instance, coordinate system specifications that leverage an equatorial plane and include the terminology ‘mean’ in the label indicate that the equatorial plane is calculated using a spin axis that is modeled using only the precession of the celestial body over time [6]. The terminology ‘true’, however, indicates that the equatorial plane is calculated using a spin axis that is modeled with both the precession and nutation of the body [6]. Calculating these planes also requires information about the time instant or interval used to calculate its orientation in three-dimensional space. The terminology ‘of date’ indicates that the plane is calculated using nutation information at each instant of time within a simulation or mission, while ‘of epoch’ indicates that the plane is calculated using nutation information at a fixed, specified epoch [6]. The most common epoch used in reference plane calculation is currently the J2000 epoch, defined as January 1st, 2000, 12:00.000 in Barycentric Dynamical Time (described in Sec. 3.4). However, due to the challenges of consistently expressing and calculating the vernal equinox and equatorial plane of the Earth, an alternative convention was later introduced.

The IAU, International Earth Rotation Service (IERS), and associated technical communities have developed and adopted a set of standards for accurately defining and calculating the transformation between newer Earth-centered reference systems. The associated terminology is not currently widely used in cislunar space exploration beyond

specialized texts. Accordingly, an overview and brief summary of this terminology is presented [7]:

- Celestial Intermediate Pole (CIP): the pole that is normal to the equatorial plane of the Earth calculated using precession and nutation.
- Celestial Intermediate Origin (CIO): a nonrotating axis that lies within the equatorial plane of the Earth, calculated using precession and nutation, and is used to define the first axis of an Earth-centered inertial system
- Terrestrial Intermediate Origin (TIO): the first axis of the Earth-fixed system labeled the Terrestrial Intermediate Reference System, described below.

The well-known coordinate systems that are presented in this section are organized according to their properties. An inertial coordinate system requires a set of basis vectors that are non-rotating and an origin that is non-accelerating. In practice, there are no known precisely inertial coordinate systems but only our best estimate of basis vectors that do not rotate relative to stars. However, the astrodynamics community still denotes these coordinate frame and systems as ‘inertial’; accordingly, this terminology will be used throughout this document. These inertial systems are often used as a basis for constructing and numerically integrating the equations of motion in many simulation tools such as GMAT, where perturbing accelerations from gravitational bodies and spacecraft characteristics (maneuvers, solar radiation pressure, out-gassing) may be added in the same frame to produce a high-fidelity dynamical model. Alternatively, the basis vectors associated with a body-fixed frame rotate with the body, whereas a synodic frame is defined using the motion of two celestial bodies in their orbits.

## 2.2 International Celestial Reference System

The International Celestial Reference Frame (ICRF) is a realization of the International Celestial Reference System (ICRS) that is managed by the IERS [7]. The ICRF uses the solar system barycenter as the origin and axes that are calculated using precise coordinates of extragalactic radio sources to be fixed relative to quasars. Based on recommendations from the IERS, the axes are also defined with the first two unit vectors lying in a plane that is close to the mean equatorial plane of the Earth on the J2000 epoch and the first vector lying close to the vernal equinox on this epoch [7]. There have been multiple realizations of the ICRS, based on improvements and expansion in the data acquired to support calculations. The most recent realization, ICRF3 (referred to in this document as ICRF), which was adopted on January 1, 2019, was constructed using observations of 4,536 extragalactic objects through very long baseline interferometry (VLBI) [8].

### Implementation Note

An important aspect of using the ICRF consistently is specifying the location of the solar system barycenter. The most recent planetary and lunar Development Ephemeris (DE) files, DE440 and DE441, prepared by NASA's Navigation and Ancillary Information Facility (NAIF), calculate the location of the solar system barycenter using "the Sun, barycenters of eight planetary systems, the Pluto system barycenter, 343 asteroids, 30 KBOs [Kuiper Belt Objects], and a KBO ring representing the main Kuiper belt." (Park et al., 2021, pg. 2 [9]). Park et al. note that the solar system barycenter calculated in these most recent ephemerides is displaced by approximately 100 km relative to the value used in the previous DE430 ephemeris file, primarily due to the inclusion of Kuiper belt objects in the calculations [9]. Accordingly, transformations to or from the ICRF between distinct software or users requires specification of the data used to locate the solar system barycenter. In addition, because there are multiple realizations of the ICRF, it is important to identify which version is selected for the various products used to build a coordinate system and ensure that these definitions are consistent with other parameters used such as Earth Orientation Parameters (EOP) and ephemerides. For example, DE440 uses the third realization of the ICRF, i.e., ICRF3, to report the planetary and lunar ephemerides [9].

## 2.3 Selected Earth-Centered Systems

### 2.3.1 Earth-Centered Inertial Systems

There are a wide variety of Earth-centered, equatorial inertial systems that have been used in practice; those that are commonly used are summarized here.

*Geocentric Celestial Reference System:* The Geocentric Celestial Reference Frame (GCRF) is a realization of the Geocentric Celestial Reference System (GCRS). The GCRF is defined using an origin located at the center of the Earth and the same basis vectors as the ICRF [7]. The GCRS is the currently adopted standard for an Earth-centered inertial system due to its independence from definitions of the ecliptic and vernal equinox.

*Earth-Centered Mean Equator and Equinox of the J2000 Epoch (EME) Inertial System:* Also sometimes labeled an Earth-centered inertial (ECI) system or Geocentric Equatorial Inertial (GCI). This system uses the Earth as an origin and basis vectors ( $\hat{x}$ ,  $\hat{y}$ ,  $\hat{z}$ ) that are defined as follows:

- $\hat{x}$ : direction from the center of the Earth to the vernal equinox, evaluated as the intersection of the mean equatorial plane and mean ecliptic plane, on the J2000 epoch.
- $\hat{y}$ : perpendicular to both the  $\hat{x}$  and  $\hat{z}$  axes, forming a right-handed triad.
- $\hat{z}$ : normal to the Earth's mean equatorial plane at the J2000 epoch.

*True of Date (TOD) Equatorial Earth-Centered System:* The TOD Earth-centered system uses the true equator and true vernal equinox at each epoch in a simulation or mission. This system uses an origin placed at the center of the Earth and

basis vectors ( $\hat{x}$ ,  $\hat{y}$ ,  $\hat{z}$ ) that are defined as follows:

- $\hat{x}$ : direction from the center of the Earth to the true vernal equinox at the current epoch.
- $\hat{y}$ : perpendicular to both the  $\hat{x}$  and  $\hat{z}$  axes, forming a right-handed triad.
- $\hat{z}$ : normal to the Earth's true equatorial plane at the current epoch.

*Mean of Date (MOD) Equatorial Earth-Centered System:* The MOD Earth-centered system uses a mean equator and mean equinox at each epoch in a simulation or mission. This system uses an origin at the center of the Earth and basis vectors ( $\hat{x}$ ,  $\hat{y}$ ,  $\hat{z}$ ) that are defined as follows:

- $\hat{x}$ : direction from the center of the Earth to the mean vernal equinox at the current epoch.
- $\hat{y}$ : perpendicular to both the  $\hat{x}$  and  $\hat{z}$  axes, forming a right-handed triad.
- $\hat{z}$ : normal to the Earth's mean equatorial plane at the current epoch.

### 2.3.2 International Terrestrial Reference System

The International Terrestrial Reference Frame (ITRF) is a realization of the International Terrestrial Reference System (ITRS) that is managed by the IERS and calculated using information about sites located on the Earth's surface [7]. The Earth-fixed ITRF uses as an origin the center of the Earth system (including the oceans and atmosphere). The three basis vectors for defining the axes of the ITRF rotate with the Earth and are selected to ensure that there is no net rotation relative to horizontal plate motion on the Earth; these axes are regularly updated with improved modeling of ground stations due to plate tectonics. For recent realizations of the ITRS, these axes are also selected to ensure close alignment with previous realizations [7].

### 2.3.3 World Geodetic System 1984

The US military employs a specified set of reference coordinate systems. Information pertaining to a position on the Earth or in the Earth's atmosphere uses the standard geospatial reference frame defined by the World Geodetic System 1984 (WGS 84) and maintained by the NGA [10]. Information referring to a position in space must be expressed in terms of the Celestial Reference Frame (CRF), defined by the U.S. Naval Observatory (USNO). References to time must be provided in the standard temporal reference defined by Coordinated Universal Time (UTC) and maintained by the USNO master clock [11].

On pg. 27, the Time, Frequency, Ephemeris, Geodesy and Weather Reference and Guidance Handbook [12] provides the following criteria for the WGS 84, quoted directly here:

- “It is geocentric, the center of mass being defined for the whole Earth including oceans and atmosphere” [12]
- “Its scale is that of the local Earth frame, in the meaning of a relativistic theory of gravitation” [12]
- “Its orientation was initially given by the Bureau International de l'Heure (BIH) orientation of 1984.0” [12]
- “Its time evolution in orientation will create no residual global rotation with regards to the crust” [12]

- “The WGS 84 Coordinate System is a right-handed, Earth-fixed orthogonal coordinate system” [12]

Within the WGS 84 standard, the reference system uses an origin placed at the center of the Earth and basis vectors ( $\hat{x}$ ,  $\hat{y}$ ,  $\hat{z}$ ) that are defined as follows [10]:

- $\hat{x}$ : intersection of the IERS reference meridian and the plane normal to the IERS reference pole
- $\hat{y}$ : perpendicular to both the  $\hat{x}$  and  $\hat{z}$  axes, forming a right-handed triad
- $\hat{z}$ : parallel to the IERS reference pole, essentially the axis of rotation of a WGS84 ellipsoid model of the Earth.

To support expressing the position of an object in geodetic coordinates, a geocentric, equipotential ellipsoid is often employed. The WGS 84 ellipsoid is defined to possess a semi-major axis of 6378.137 km and a flattening of 1/298.257223563; the gravitational constant is  $3.986004418 \times 10^{14} m^3/s^2$  and the angular rotational velocity is  $7.292115 \times 10^{-5}$  rad/s [10].

The WGS 84 uses various geoids, such as the Earth Gravitational Model 1996 (EGM 96), EGM 2008, and EGM 2020, depending on the user’s intended application. Reference [12] provides guidance to military users on which reference frame and EGM to use, depending on the application. Refer to Section 6 of reference [12] for more information.

## 2.4 Selected Moon-Centered Systems

### 2.4.1 Moon-Inertial System

One definition of a Moon-inertial system uses the Moon center as the origin and three basis vectors that are set equal to the axes associated with the most recent realization of the ICRF, as described in Sec. 2.2 [9].

When locating an object in a Moon-inertial system, it may be useful to use selenocentric, spherical coordinates: the selenocentric longitude is measured positive eastward as the angle from the  $x$ -axis of a Moon-centered frame to a vector from the center of mass of the Moon to the object; the selenocentric latitude is measured as the north-south angle from the  $xy$ -plane of a Moon-centered frame to a vector directed from the center of mass of the Moon to the object; and the distance is measured from the center of mass of the Moon to the object.

### Implementation Note

Although we use a specific definition throughout this document, alternate definitions for the axes of a Moon-inertial system may be used in practice and constructed using the axes associated with various Earth-centered inertial systems. For instance, GMAT offers an option for defining right-handed body-inertial systems (associated with celestial bodies that are not the Earth) with the following default configuration: using the intersection of the body's equatorial plane and the  $xy$ -plane of the Earth-centered mean equator and equinox of the J2000 epoch system to define the first axis  $\hat{x}$  and the spin axis of the body on the J2000 epoch to define the third axis  $\hat{z}$ , with  $\hat{y}$  completing the right-handed triad. [13]. The non-uniqueness of definitions used for an inertial system that is associated with a body that is not the Earth throughout the well-known software and literature may result in differences when expressing the position and velocity vectors for an object in a Moon-inertial system. However, we suggest defining a Moon-inertial coordinate system using the axes associated with the ICRF due to its precision and continued maintenance.

#### 2.4.2 Moon-Fixed Systems

The most common definitions for a Moon-fixed system use the center of the Moon as the origin and rely on two types of axes: the mean-Earth/polar (ME) axes and the Principal Axes (PA). Note that the ME axes are also referred to as mean-Earth/mean-rotation (MER) axes [9].

*Mean-Earth / Polar (ME) Axes:* The ME or MER axes are a Moon-fixed set of basis vectors ( $\hat{x}, \hat{y}, \hat{z}$ ) that are defined as follows [9, 14, 15]:

- $\hat{x}$ : direction from the center of mass of the Moon to the intersection of the Moon's equatorial plane and the Moon's prime meridian. The Moon's prime meridian is calculated as the mean direction to the Earth, consistent with the Moon's rotational period matching its orbital period relative to the Earth [14].
- $\hat{y}$ : perpendicular to both the  $\hat{x}$  and  $\hat{z}$  axes, forming a right-handed triad.
- $\hat{z}$ : aligned with the mean axis of rotation of the Moon.

*Lunar Principal Axes (PA):* The PA axes are a Moon-fixed set of basis vectors ( $\hat{x}, \hat{y}, \hat{z}$ ) that are calculated as the principal axes of the Moon, assuming that its mantle is not distorted due to tides and rotation [9]. As outlined by Park et al., these axes are calculated using data from the Gravity Recovery and Interior Laboratory (GRAIL) mission [9]. Because the Moon is not a perfect synchronously rotating triaxial ellipsoid, the PA and ME axes do not exactly coincide. In fact, these two systems differ by about 1 km at the lunar surface [14].

**Implementation Note**

The PA axes are often updated with new Lunar Laser Ranging (LLR) data as they become available. Use of the PA axes relies on the Moon's orientation information. An approximation of this information is provided in specific DE files prepared by NASA's NAIF and determined using 50+ years of LLR data [16]. Thus, this information must be reported when using the PA axes. For instance, the LRO project used DE421 to define the PA axes [14]. The next recommended baseline after DE421 was DE430, which incorporated five more years of data into its solution. The differences between the two ephemerides are minimal over a 50 year timespan: about 0.5 mas in right ascension and declination and less than 0.25 m in radius [17]. However, there are currently only four LLR stations on Earth and in Northern Hemisphere. In addition, the Apollo sites on the Moon that are lased are necessarily on the Earth-facing side and in or toward the Moon's northern hemisphere. These conditions represent the limitations of the current LLR/DE data set. In addition, the ME axes are defined as a constant rotation from the PA axes. Thus, the specific DE files used to specify the ME axes should also be reported.

When locating an object in a Moon-fixed frame it is common to use selenographic, spherical coordinates: the selenographic longitude is measured positive eastward as the angle from the  $x$ -axis of a Moon-centered frame to a vector that both passes through the projected point and is normal to the surface of a three-dimensional representation of the Moon; the selenographic latitude is measured as the north-south angle from the  $xy$ -plane of a Moon-centered frame to a vector that both passes through the projected point and is normal to the surface of the same three-dimensional representation of the Moon; and the distance is reported using the height of the object above the associated projection onto the surface of the representative shape.

Polar stereographic coordinates [18] are also used by the LRO project to define their lunar digital elevation models (LDEM) [19]. The LRO products use either South pole or North pole stereographic coordinates  $(x, y)$  expressed in a Moon-fixed reference frame with ME axes and a Moon radius of 1737.4 km. For a given set of coordinates  $(x, y)$  on the lunar map, the LDEM product provides the height  $z$  above the assumed Moon radius.

### Implementation Note

The Moon possesses a small flattening coefficient, equal to approximately 0.0012, which is three times smaller than the Earth. Accordingly, the IAU cartographic working group does not recommend using an ellipsoid to represent the Moon [20]; the Moon is often sufficiently approximated using a sphere. Smith et. al. provide a value of the mean Moon radius of 1737.151 km based on data from the Lunar Orbiter Laser Altimeter (LOLA) [19]. When using a spherical model with altitude quantities representing the distance or range, it is important to clearly specify the assumed radius used to calculate this relative quantity, because it varies across products and applications [14]. For example, all LRO map products assume a Moon radius of 1737.4 km, which is the value recommended by the IAU in Table 5 of [15], whereas gravity field parameters use a Moon radius of 1738.0 km [9]. GMAT uses another value, 1737.2 km for its default radius. As the technical community develops new standards for lunar reference frames, a recommended value for the assumed lunar radius should also be specified.

## 2.5 Selected Synodic Frames

Synodic coordinate frames are defined using the motion of two primary bodies. These noninertial frames are commonly employed when studying multi-body gravitational environments where multiple celestial bodies significantly influence the path of an object, particularly when comparing trajectories to known fundamental solutions that exist in low-fidelity models.

### 2.5.1 Earth-Moon Rotating Frame

The Earth-Moon rotating frame uses basis vectors ( $\hat{x}$ ,  $\hat{y}$ ,  $\hat{z}$ ) that are defined as follows:

- $\hat{x}$ : directed from the center of the Earth to the center of the Moon.
- $\hat{y}$ : perpendicular to both the  $\hat{x}$  and  $\hat{z}$  axes, forming a right-handed triad.
- $\hat{z}$ : parallel to the instantaneous orbital angular momentum vector of the Moon relative to the Earth.

The origin used for specifying the position of an object is the Earth-Moon barycenter. For libration point missions or missions operating close to one celestial body, variations on this frame use the same axes but a different origin. For an origin located at a libration point, the associated frame is often labeled a Rotating Libration Point (RLP) frame.

### 2.5.2 Sun-Earth-Moon Rotating Frame

The Sun-Earth-Moon rotating frame uses basis vectors ( $\hat{x}$ ,  $\hat{y}$ ,  $\hat{z}$ ) that are defined as follows:

- $\hat{x}$ : directed from the center of the Sun to the instantaneous Earth-Moon barycenter.
- $\hat{y}$ : perpendicular to both the  $\hat{x}$  and  $\hat{z}$  axes, forming a right-handed triad.
- $\hat{z}$ : parallel to the instantaneous orbital angular momentum vector of the Earth-Moon barycenter relative to the center of the Sun

The origin used for specifying the position of an object is the system barycenter. For libration point missions or missions operating close to one celestial body, variations on this frame, e.g., an RLP frame, use the same axes but a different origin, e.g., a libration point.

### 2.5.3 Sun-Earth Rotating Frame

The Sun-Earth rotating frame uses basis vectors ( $\hat{x}$ ,  $\hat{y}$ ,  $\hat{z}$ ) that are defined as follows:

- $\hat{x}$ : directed from the center of the Sun to the center of the Earth
- $\hat{y}$ : perpendicular to both the  $\hat{x}$  and  $\hat{z}$  axes, forming a right-handed triad.
- $\hat{z}$ : parallel to the instantaneous orbital angular momentum vector of the Earth relative to the center of the Sun.

The origin used for specifying the position of an object is the Sun-Earth barycenter. For libration point missions or missions operating close to one celestial body, variations on this frame, e.g., an RLP frame, use the same axes but a different origin, e.g., a libration point.

### 2.5.4 Geocentric Solar Ecliptic

The Geocentric Solar Ecliptic (GSE) system is a type of synodic reference system that is defined using the motion of the Sun and Earth; however, its definition differs from a traditional Sun-Earth rotating frame as defined above. The GSE system uses an origin placed at the center of the Earth and basis vectors ( $\hat{x}$ ,  $\hat{y}$ ,  $\hat{z}$ ) that are defined as follows:

- $\hat{x}$ : directed from the center of the Earth to the center of the Sun.
- $\hat{y}$ : perpendicular to both the  $\hat{x}$  and  $\hat{z}$  axes, forming a right-handed triad.
- $\hat{z}$ : normal to the ecliptic plane.

## 2.6 Selected Spacecraft-Centered Systems

The following spacecraft-centered systems use the spacecraft location as the origin, with axes defined using information about the spacecraft state.

### 2.6.1 Local Vertical, Local Horizontal System

The local vertical, local horizontal (LVLH) system is often used in relative motion applications. With an origin at the spacecraft, the basis vectors ( $\hat{x}$ ,  $\hat{y}$ ,  $\hat{z}$ ) are defined as follows:

- $\hat{x}$ : aligned with the position vector from a central body to the spacecraft; also often labeled the radial direction
  - $\hat{y}$ : perpendicular to both the  $\hat{x}$  and  $\hat{z}$  axes, forming a right-handed triad; also often labeled the along-track direction
  - $\hat{z}$ : aligned with the orbital angular momentum vector of the spacecraft; also often labeled the cross-track direction.
- and requires specification of the associated central body for a complete definition.

## 2.6.2 Velocity, Normal, Co-Normal Axes

The velocity, normal, co-normal (VNC) axes are often used in defining maneuver directions. The basis vectors ( $\hat{V}$ ,  $\hat{N}$ ,  $\hat{C}$ ) are defined as follows:

- $\hat{V}$ : aligned with the instantaneous velocity vector of the spacecraft relative to a central body
- $\hat{N}$ : normal to the orbit plane
- $\hat{C}$ : perpendicular to both the  $\hat{V}$  and  $\hat{N}$  axes, forming a right-handed triad; also often labeled the co-normal direction.

and requires specification of the associated central body for a complete definition.

## 2.7 Describing the State of a Spacecraft in Cislunar Space using Two-Line Elements

Two line elements (TLE) are derived based on a paired down force model and require a specific propagator referred to as SGP (Simplified General Perturbation). TLE were developed in the 1960's and are still widely used for Earth object tracking [21, 22]. NORAD provides regular updates of its Earth space object catalog using TLE based on tracking data [22]. TLE data is publicly available on the <https://www.celestrak.com/> website. These elements are useful in that they can be propagated analytically to estimate a spacecraft state much faster than if using a full ephemeris force model. It is worth noting with the improvement made in computer performance, the propagation performance gain from TLE is not as much a driver as it used to be when the TLE were first developed. However, moving away from a TLE-based formulation requires a significant re-architecting of existing tools reliant on that model. Figure 1 provides a high level description of the current version of the TLE.

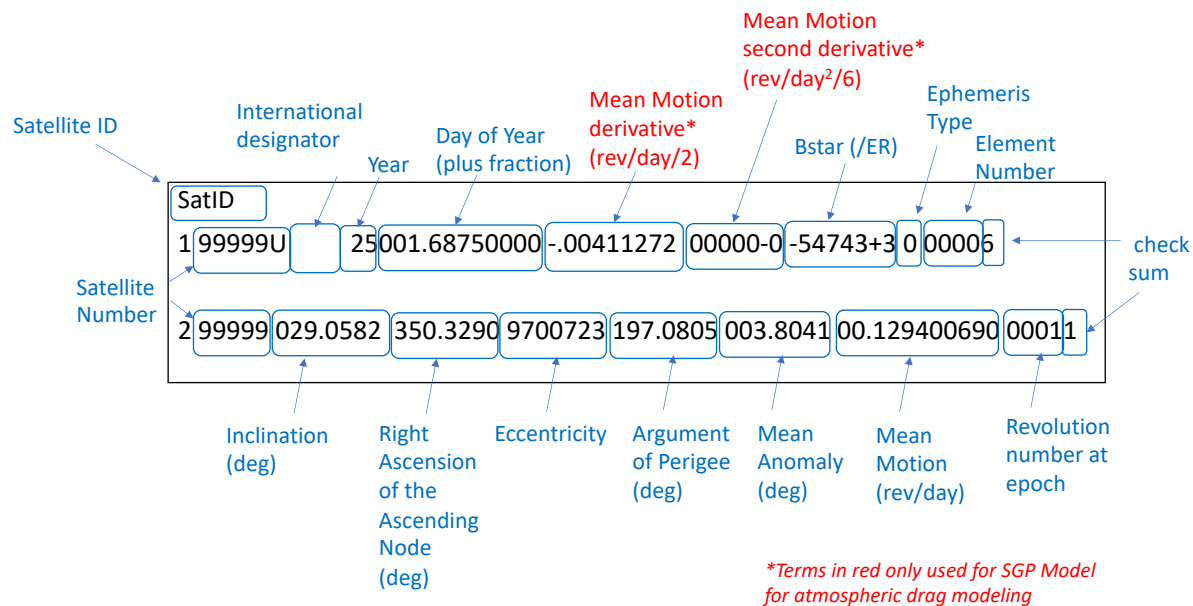


**Fig. 1** Definition of the two-line element set.

The TLE data generated can be used to obtain approximate location of mission assets even international ones without direct information on their current operations. With the increased number of mission in the cislunar/lunar domain, the question rose as to whether the TLE generated for these missions can be used to estimate asset location in that regime. Indeed since TLE assume a certain force model (Main Earth zonal harmonics up to J5, simplified drag model/third body and solar radiation pressure), their accuracy and applications are mainly limited to Earth orbiting objects although some development was done to cover more deep space applications [21, 23]. A new and improved model (SGP4-XP) has been derived and published to provide higher accuracy in applications with higher altitudes relative to the Earth and still allow for fast propagation [24]. However this new formulation is not compatible with the previous model or TLEs. Another limitation of the TLE formulation is that it is lacking covariance information which is key to certain applications such as conjunction assessment. Accordingly, TLEs may be supplemented with Vector Covariance Messages (VCMs). In addition, because TLEs are derived from tracking data which can be sparse, unknown maneuvers especially of large magnitude can be hard to resolve. Finally, it is possible to use TLE information outside the confine of the general perturbation model by converting them to osculating elements and fitting the converted TLE over a certain period [25]. This fitted osculating state can then be propagated in a full ephemeris model.

### 3 Definitions of Common Time Systems

Time standards are critical for coordinate system definition as well as operational, navigation, and scientific purposes. For navigation solutions, time errors directly translate into position and velocity errors, influencing the resulting prediction. Furthermore, scientists not only need to accurately locate collected data but also accurately time-tag it. There are a wide array of useful time systems for various applications and data analysis tasks, as outlined in many well-known textbooks and comprehensive references [3, 5, 6, 26]. However, the time system used for a specific application must be appropriate for the orbital regime and central body. In addition, the time system selected must properly account for relativistic effects. Accordingly, this section presents a brief overview of the time systems that are, at the time of writing, most applicable to coordinate system definitions and spacecraft operations within cislunar, lunar, and libration point regions. This section may be updated and expanded in subsequent editions following current work within the technical community to prepare improved time standards for cislunar operations. These common time scales tend to be defined using various initial epochs and one of the following physical phenomena: atomic transitions, sidereal motion of the Earth, the rotation of pulsars, or the motion of celestial bodies [26]. Ref [27] provides an additional overview of the various time scales and their relationships. Finally, this section also covers the incorporation of relativistic effects.

#### 3.1 International Atomic Time (TAI)

TAI is an atomic time standard that is computed by the International Bureau of Weights and Measures as a realization of terrestrial time [7, 28]. TAI is computed using a weighted average of over 400 atomic clocks distributed throughout the world, without astronomical corrections. This time system uses as a fundamental unit the Système International (SI) second at sea level on the Earth, defined by the International Bureau of Weights and Measures as “equal to the duration of 9,192,631,770 periods of the radiation corresponding to the transition between the two hyperfine levels of the unperturbed ground state of the [cesium-133] atom” (Bureau International des Poids et Mesures, [28]). Note that worldwide synchronization is to within a couple tenths of a nanosecond [29].

#### 3.2 Terrestrial Time (TT)

TT (formerly Terrestrial Dynamic Time, TDT) is used as an independent variable for geocentric ephemerides and defined with a fundamental unit equal to the SI second on a geoid [7, 13, 27]; because it serves an independent variable in the equations of motion for an object, it is a form of dynamical time [6]. TT also replaces the former standard for an astronomical time scale, labeled ephemeris time (ET). TT is related to TAI via the following relationship:

$$TT = TAI + 32.184\text{sec} \quad (1)$$

The origin of this time scale, i.e., the "time zero" is defined by a reference epoch. One commonly used reference epoch for TT is the J2000.0 epoch, defined as 2000 January 1, 12:00:00.000 Barycentric Dynamical Time (which is defined in an upcoming subsection).

### 3.3 Geocentric Coordinate Time (TCG)

TCG is the time coordinate in the GCRS [5–7, 27]. Because TCG is a theoretical time scale, TCG is typically calculated directly from TT via the following expression:

$$TCG = TT + \frac{L_g}{1 - L_g} \times (JD_{TT} - 2443144.5) \times 86400 \text{ seconds} \quad (2)$$

where  $L_g = 6.969290134 \times 10^{-10}$  and  $JD_{TT}$  indicates the Julian Date in TT [3, 6, 7, 26].

### 3.4 Barycentric Dynamical Time (TDB)

TDB is a dynamical time system that is used as an independent variable in the equations of motion for celestial objects as formulated relative to the solar system barycenter and includes relativistic corrections [3, 6, 30]. TDB deviates from TT by a periodic oscillation of less than 2 msec [30] and their relationship is approximated by the following expression [3, 6, 13]:

$$TDB \approx TT + 0.001658 \sin(M_E) + 0.000014 \sin(2M_E) \text{ seconds} \quad (3)$$

where  $M_E$  is the mean anomaly of the Earth, calculated as:

$$M_E = 357.53 + 0.9856003(JD_{TT} - 2451545.0) \text{ degrees} \quad (4)$$

and  $JD_{TT}$  is the Julian date in TT. For increased accuracy, more complex expressions are available [3, 30]. For example, Eq. 9.6 in Ref. [26] presents an expression for TDB in terms of TT and the number of Julian centuries in TT from the J2000 reference epoch; this expression results in errors below 10 microseconds from 1600 to 2200. An even more precise expression appears in Ref. [31]

#### Implementation Note

For cislunar applications, TDB is recommended as it is the most accurate convention, particularly for navigation analyses where time accuracy is critical. This time convention is used in the lunar and planetary ephemerides published by NASA's NAIF, which include past and future states of a variety of celestial bodies. These files are used as part of high precision propagations or to determine shadows, sensor occultation, solar array illuminations, or thermal analysis.

### 3.5 Barycentric Coordinate Time (TCB)

TCB is the time coordinate used in the solar system barycentric celestial reference system [5, 7, 27]. TDB and TCB coincided on January 1, 1977 and now differ by approximately 9.3 seconds. Because TCB is a theoretical time scale, TCB is typically calculated directly from TDB as [7]:

$$TCB = TDB + L_b \times (JD_{TAI} - 2443144.5) \times 86400 + P_0 \text{ seconds} \quad (5)$$

where  $L_b = 1.550519768 \times 10^{-8}$ ,  $JD_{TAI}$  is the Julian date in TAI, and  $P_0 \approx 6.55 \times 10^{-5}$  s. Note that some physical constants possess slightly different values when expressed in TCB. Furthermore, the rate difference between TCB and TDB may become significant in long term measurements.

### 3.6 Universal Time (UT1)

UT1 is a realization of universal time that captures the Earth's rotation about the CIP and is independent of observing location [3, 5, 6, 27]. UT1 represents the mean solar time at  $0^\circ$  longitude and is calculated using very long baseline interferometry observations and Global Positioning System (GPS) satellites [3, 27]. UT1 can be understood as a time determined by the rotation of the Earth, and it is described by the following linear relationship with the Earth rotation angle (ERA)  $\theta_{ERA}$  in radians:

$$\theta_{ERA} = 2\pi \left( \theta_0 + \frac{d\theta_0}{dt} (JD_{UT1} - 2451545.0) \right) \quad (6)$$

where  $\theta_0 = 0.7790572732640$  rev is the ERA at J2000.0 in revolutions (units of  $2\pi$  radians),  $d\theta_0/dt = 1.00273781191135448$  rev/UT1 day is the rate of advance of ERA in revolution per UT1 day, and  $JD_{UT1}$  is the Julian date in UT1 (see Refs. [7, 30] for further details).

### 3.7 Coordinated Universal Time (UTC)

UTC is a time system that uses the SI second as a fundamental unit but is defined to remain within 0.9 seconds of UT1, which is governed by the Earth's rotation, through the insertion of leap seconds [6, 27, 30]. The relationship between UTC and TAI is defined as follows [6, 30]:

$$UTC = TAI - (\text{Number of leap seconds}) \quad (7)$$

where the leap seconds are provided by the IERS as needed (usually on June 30th or December 31st) [32].

**Implementation Note**

UTC is the time system commonly used for many data products and on-board spacecraft. Spacecraft time is used for executing on-board commands such as maneuvers. Current Earth networks—including the space surveillance network—have also adopted UTC as their time convention. However, the incorporation of leap seconds into UTC may complicate operations due to the need to track the leap seconds used. For this reason, a more universal time standard that does not rely on leap seconds, such as TAI, is recommended.

**3.8 Time Formats**

The most common calendar to represent time is the Gregorian calendar: a solar calendar with 12 months of 28–31 days each, along with a rule for leap years. In addition to the well-known Gregorian format, another common time format for expressing an epoch is the Julian date (JD), which reports the number of days from the reference epoch of January 1, 4713 BC at 12:00.000 [6]. Because the Julian dates for modern epochs are large quantities, a Modified Julian Date (MJD) is often employed. One common definition for an epoch in MJD format, given an epoch in JD format is [6]:

$$MJD = JD - 2,400,000.5 \quad (8)$$

**Implementation Note**

Equation 8 is not the only definition of an MJD. For instance, in the GMAT software, the same epoch in JD and MJD form differ by 2,430,000 [13]. Thus, it is important to specify or confirm the definition of MJD in software or data reporting.

**3.9 GPS times**

GPS time is the time provided as part of GPS ephemeris information. It is based on a time “0” of midnight on January 6th, 1980 (UTC time) and uses the SI second as a fundamental unit of time. Other types of Global Navigation Satellite System (GNSS) ephemeris broadcasts have their own time “0” and hence a unique offset from TAI, including:

- GPS Time (GPST) = TAI-19 sec
- GLONASS Time (GLONASST) = TAI - 34 sec
- Galileo System Time (GST) = TAI - 19 sec
- BeiDou Time (BDT) = TAI - 33 sec

**3.10 Navigation Considerations and Relativistic Effects**

For navigation applications involving ‘one-way’ measurement (where time of flight is a driver), there is a need for extra precise knowledge of the relative time of emission and arrival of some feature of the signal. For example, for GPS

applications, timing error on the order of 1 nanosecond will lead to position errors of 30 cm [33, 34]. This drives some applications towards the need for Ultra-Stable Oscillators (USO), or even atomic clocks. In addition, there is a need to accurately and precisely identify the relationship between the signal transmitting and signal receiving sources as well as the stability of those respective clocks over the duration of signal transit and measurement integration interval. Consequently, clock parameters are modeled as part of the estimation process. The fidelity of the clock model depends on the requirement of the user for state knowledge (orbiting or surface). Solving for updates to the clock parameters depends on the ability of the measurement set to provide adequate observability of those parameters.

When operating a mission in the cislunar or lunar regions and beyond, it is important to select a time convention that takes into account relativistic effects to ensure the high accuracy required for navigation estimation is met. This is especially true with on-board time management. On-board USO drift and stability need to take into account general relativistic effects that include gravity. These relativistic effects are needed to synchronize clocks; that is, to relate the times measured by the observers on their watches due to their motion to a common clock. The times measured by the observers on their clocks are referred to as proper times. The time measured on this common clock is, by definition, a time that has the same value for a given event independently of where it is measured [35]. This reference clock defines a time coordinate system referred to as coordinate time. In addition, two clocks with proper times  $t_1$  and  $t_2$  are synchronized if their values agree in a common time coordinate system. For the remainder of this discussion, this common time coordinate system is assumed to be TCG, and this time is linked to the ECI reference frame.

In general, the elapsed TCG coordinate time  $\Delta T$  corresponding to the measured elapsed time of a clock moving under the gravity potential  $U$  between the proper times  $t_1$  and  $t_1$  with speed  $V$  is equal to [35, 36]:

$$\Delta T = \int_{t_0}^{t_1} \left( 1 + \frac{1}{c^2} U + \frac{1}{2c^2} V^2 \right) d\tau_p \quad (9)$$

where  $c$  is the speed of light. As a result, note that the relationship between coordinate time and proper time depends on the speed of the clock and the gravitational potential at the location of the clock.

Considering the case of a clock on or in the vicinity of the Earth, the gravitational potential  $U$  is a function of the distance  $r$  to the origin of the ECI reference frame, and the geocentric latitude  $\phi$ , and longitude  $\lambda$ , i.e.,  $U = U(r, \phi, \lambda)$ . For practical applications, the gravitational potential  $U$  may be truncated to include only the  $J_2$  term [6] as:

$$U(r, \phi, \lambda) = \frac{GM_E}{r} \left[ 1 + J_2 \left( \frac{R_E}{r} \right)^2 \frac{1}{2} \left( 1 - 3 \sin^2 \phi \right) \right] \quad (10)$$

Now consider two use cases: the case of a clock at rest on the surface of the Earth's geoid, and the case of a clock on satellite in a Keplerian orbit around the Earth. For these two use cases, their associated proper times differ from the TCG time due to the relativistic effects.

Assuming a clock on the geoid, note that it moves with respect to the ECI reference (and also with respect to the coordinate time) with velocity  $\mathbf{V}_E = \boldsymbol{\omega} \times \mathbf{R}$ , where  $\boldsymbol{\omega}$  is the angular velocity of the Earth, and  $\mathbf{R}$  is the position vector of the clock in the ECI frame. Hence, the elapsed coordinate time is:

$$\Delta T = \int_{t_0}^{t_1} \left( 1 + \frac{1}{c^2} U + \frac{1}{2c^2} \|\boldsymbol{\omega} \times \mathbf{R}\|^2 \right) d\tau_p = \int_{t_0}^{t_1} \left( 1 + \frac{1}{c^2} W \right) d\tau_p \quad (11)$$

where  $W = U + (1/2)\|\boldsymbol{\omega} \times \mathbf{R}\|^2$ . Following [37], consider  $W$  constant because the gravity potential on the geoid is constant by definition. Evaluating  $W$  at the equator (this is,  $\phi = 0^\circ$ ) offers a sufficient approximation for practical purposes. The best estimate of this quantity as of today is  $W_0 = 6.2636856 \times 10^7 \text{ m}^2/\text{s}^2$  [37]. As a result:

$$\Delta T = \left( 1 + \frac{W_0}{c^2} \right) \Delta \tau_p = (1 + L_G) \Delta \tau_p \quad (12)$$

where  $L_G$  is a unitless constant that relates TT with TCG as defined in subsection 3.3. The relationship between a clock measuring time in TT to the TCG coordinate time is defined as  $TT = (1 - L_G)TCG$ .

The same reasoning enables estimation of the coordinate time of a satellite in a Keplerian orbit around the Earth. For a Keplerian orbit, it is known that the energy is conserved as:

$$E = \frac{1}{2} V_S^2 - U = -\frac{GM_E}{2a} \quad (13)$$

where  $a$  is the semimajor axis of the orbit. Accordingly, the term  $\frac{1}{2}V_S^2$  may be expressed as a function of the potential  $U$  and the semimajor axis  $a$ . Then, the coordinate time  $\Delta T$  of a clock in a Keplerian orbit between the proper times  $t_0$  and  $t_1$  is:

$$\Delta T = \int_{t_0}^{t_1} \left( 1 + \frac{2}{c^2} U - \frac{1}{c^2} \frac{GM_E}{a} \right) d\tau_p \quad (14)$$

This integral admits an approximated closed-form expression as follows [38]:

$$\Delta T = \left( 1 + \frac{3}{2c^2} \frac{GM_E}{a} \right) \Delta \tau_p + \frac{2}{c^2} e \sin(E) \sqrt{GM_E a} \quad (15)$$

where  $e$  is the orbit's eccentricity and  $E$  is the eccentric anomaly.

These results enable comparison between the proper times of a clock on a satellite to a clock at rest on the geoid. The main idea is to convert the time to  $TT$ , and the relationship between the two proper times is:

$$\Delta \tau_G = \left( 1 + \frac{3}{2c^2} \frac{GM_E}{a} - \frac{1}{c^2} W_0 \right) \Delta \tau_S + \frac{2}{c^2} e \sin(E) \sqrt{GM_E a} \quad (16)$$

where  $\Delta \tau_G$  and  $\Delta \tau_S$  are the proper times recorded by a clock in the geoid and in a satellite respectively, and  $R_E$  is the

radius of the Earth. The details of this derivation can be found in [38]. Finally, further guidance and recommendations on how to compare clocks on the Earth's surface or satellites orbiting within the solar system in several reference frames can also be found in [38].

## 4 Overview of Common Coordinate System Transformations

Transforming between two coordinate systems used to describe the state of an object in cislunar space requires a combination of some or all of the following steps: rotation between distinct axes, translation of the origin or basepoint, a conversion between distinct types of coordinates, and a transformation between quantities expressed in distinct units or scales. A rotation is required when transforming, for example, between body-fixed and inertial coordinate systems or between inertial and synodic coordinates. When the coordinate systems use distinct origins, such as the center of the Earth or Moon or the barycenter of the Earth-Moon system, a translation must also be performed using knowledge of their relative position vectors, typically calculated using ephemerides.

### 4.1 Transformation Background

This subsection presents common foundational concepts used across the presented transformations. First, the following general mathematical notation is used to describe the position vector of a point  $b$  relative to another point  $a$  in the axes of a coordinate system  $c$ :  $\mathbf{r}_{a,b}^c$ . The associated velocity vector,  $\mathbf{v}_{a,b}^c$ , is calculated as the time derivative of the position vector assuming an observer fixed in coordinate system  $c$ .

To transform the position and velocity vectors for an object  $p$  from one coordinate system (labeled with the superscript  $i$ ) with origin  $O_i$  to another coordinate system (labeled with the superscript  $f$ ) with the origin  $O_f$  and distinct axes, the following general expressions are used:

$$\mathbf{r}_{O_f,p}^f = [{}^f \mathbf{R}^i(t)] \mathbf{r}_{O_i,p}^i + \mathbf{r}_{O_f,O_i}^f \quad (17)$$

$$\mathbf{v}_{O_f,p}^f = [{}^f \mathbf{R}^i(t)] \mathbf{v}_{O_i,p}^i + [{}^f \dot{\mathbf{R}}^i(t)] \mathbf{r}_{O_i,p}^i + \mathbf{v}_{O_f,O_i}^f \quad (18)$$

where  $[{}^f \mathbf{R}^i(t)]$  represents a general rotation matrix from coordinate system  $i$  to coordinate system  $f$  and  $[{}^f \dot{\mathbf{R}}^i(t)]$  is its time derivative. Then,  $\mathbf{r}_{O_f,O_i}^f$  and  $\mathbf{v}_{O_f,O_i}^f$  are the relative position and velocity vectors, respectively of the origin  $O_i$  relative to  $O_f$ , expressed in coordinate system  $f$ . In this general scenario, the transformation includes terms that reflect both the rotation between axes that do not coincide and translation to a distinct origin.

The transformation step of performing a rotation between two axes is typically described using a rotation matrix. One approach to forming a rotation matrix for a complex rotation is to decompose it into a sequence of simple rotations, each describing rotation about a single intermediate axis by an angle. The rotation matrix corresponding to a simple rotation about each of the first, second and third axes in a system are, respectively, equal to the following for a general

angle  $\phi$  [6]:

$$[\mathbf{R}_1(\phi)] = \begin{bmatrix} 1 & 0 & 0 \\ 0 & \cos(\phi) & \sin(\phi) \\ 0 & -\sin(\phi) & \cos(\phi) \end{bmatrix} \quad (19)$$

$$[\mathbf{R}_2(\phi)] = \begin{bmatrix} \cos(\phi) & 0 & -\sin(\phi) \\ 0 & 1 & 0 \\ \sin(\phi) & 0 & \cos(\phi) \end{bmatrix} \quad (20)$$

$$[\mathbf{R}_3(\phi)] = \begin{bmatrix} \cos(\phi) & \sin(\phi) & 0 \\ -\sin(\phi) & \cos(\phi) & 0 \\ 0 & 0 & 1 \end{bmatrix} \quad (21)$$

The transformations associated with each of these simple rotations is displayed graphically in Fig. 2 from the black axes  $(\hat{x}_1, \hat{y}_1, \hat{z}_1)$  to the blue axes  $(\hat{x}_2, \hat{y}_2, \hat{z}_2)$ . These three simple rotation matrices may be used to form a complex rotation matrix through multiplication in the correct order. Because each of these matrices is orthogonal, the inverse of a simple rotation matrix is written as either the transpose of the matrix or the matrix evaluated using the negative of the angle, i.e.,  $[\mathbf{R}_i(\phi)]^{-1} = [\mathbf{R}_i(\phi)]^T = [\mathbf{R}_i(-\phi)]$ . Another well-known approach to constructing a rotation matrix includes directly writing the basis vectors of coordinate system  $f$  in terms of their components in coordinate system  $i$  and using those expressions to form the rows or columns of the rotation matrix.

Calculating the position and velocity vectors of the origin of a new coordinate system relative to a distinct origin of another coordinate system requires accurate knowledge of their relative states. For some origins, such as those that are located at the center of a celestial body or barycenter of a system, this relative state information may be accessed

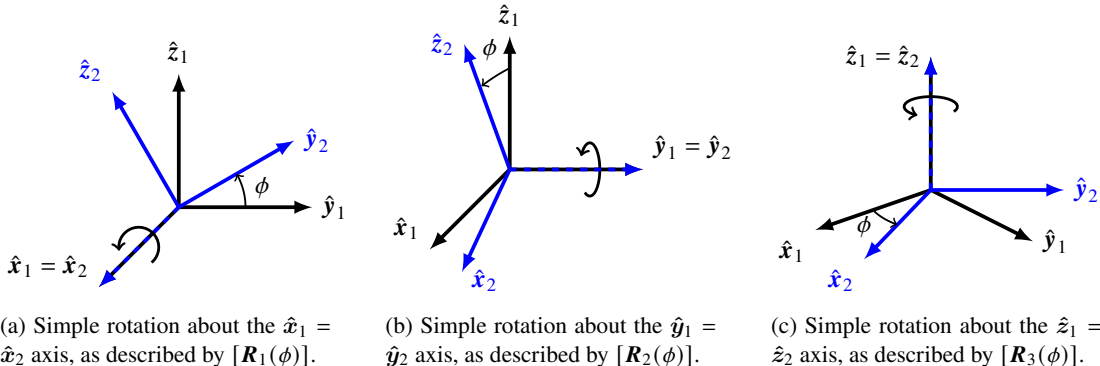


**Fig. 2 Transformations from  $(\hat{x}_1, \hat{y}_1, \hat{z}_1)$  to  $(\hat{x}_2, \hat{y}_2, \hat{z}_2)$  axes, corresponding to a simple rotation about each of the first, second and third axes by an angle  $\phi$ .**

using ephemerides available in DE data files, made available by NASA's NAIF [9, 39]. However, accessing these data involves specifying key information such as [40]:

- the desired coordinate frame, requiring careful analysis of the documentation to understand the definition and, sometimes, additional transformations to a desired frame
- the two origins for calculating the relative state vector, requiring careful analysis of documentation to understand any assumptions in calculation
- the epoch specified in the required format, and any aberration corrections, e.g., light time and stellar aberration

The resulting relative position and velocity vectors might also depend on:

- the ephemeris file that is used to supply this information, these may be compiled from different sources or correspond to different versions
- the interpolation scheme used to calculate state information
- the availability of ephemeris data for the original and/or new origins at a specific epoch

New versions of the DE are regularly published using new planetary and LLR measurements; the latest version and the completed revision information of these ephemerides may be found at Ref. [41]. Additional sources for lunar and planetary ephemerides include: (1) INPOP which produces ephemerides within 5 cm of the DE 430 and (2) Ephemeris of Planets and the Moon (EPM) [42, 43]. For origins that correspond to calculated locations, such as the Lagrange points, the position and velocity vectors relative to the barycenter of a system or center of a celestial body may be influenced by the masses of the celestial system associated with the Lagrange points and the normalization schemes used if their location is originally calculated in nondimensional coordinates. Slight differences of the specifications in either of these scenarios between distinct software or users may produce slight differences in the position and velocity vectors calculated via a coordinate system transformation and, potentially, grow over time with numerical integration.

## 4.2 Transformation Roadmap

Figure 3 supplies an overview of the coordinate transformations presented in this chapter, organized by their origin and type. This diagram includes the well-known reference systems and frames, along with the rotation matrices and, where relevant, translation steps that relate them; the arrows indicate directionality of the transformation that is described by the annotated rotation matrices. A condensed version of this diagram is also used throughout the remaining subsections to supply context to the reader.

## 4.3 Transforming Between Earth-Centered Inertial and Body-Fixed Systems

The procedure for performing a transformation between body-fixed and inertial coordinate systems using the same origin is sometimes also referred to as ‘reduction’ [6, 13]. The procedure for transforming between these systems has changed over time as the IAU’s definition of an inertial or celestial system has evolved along with Earth orientation

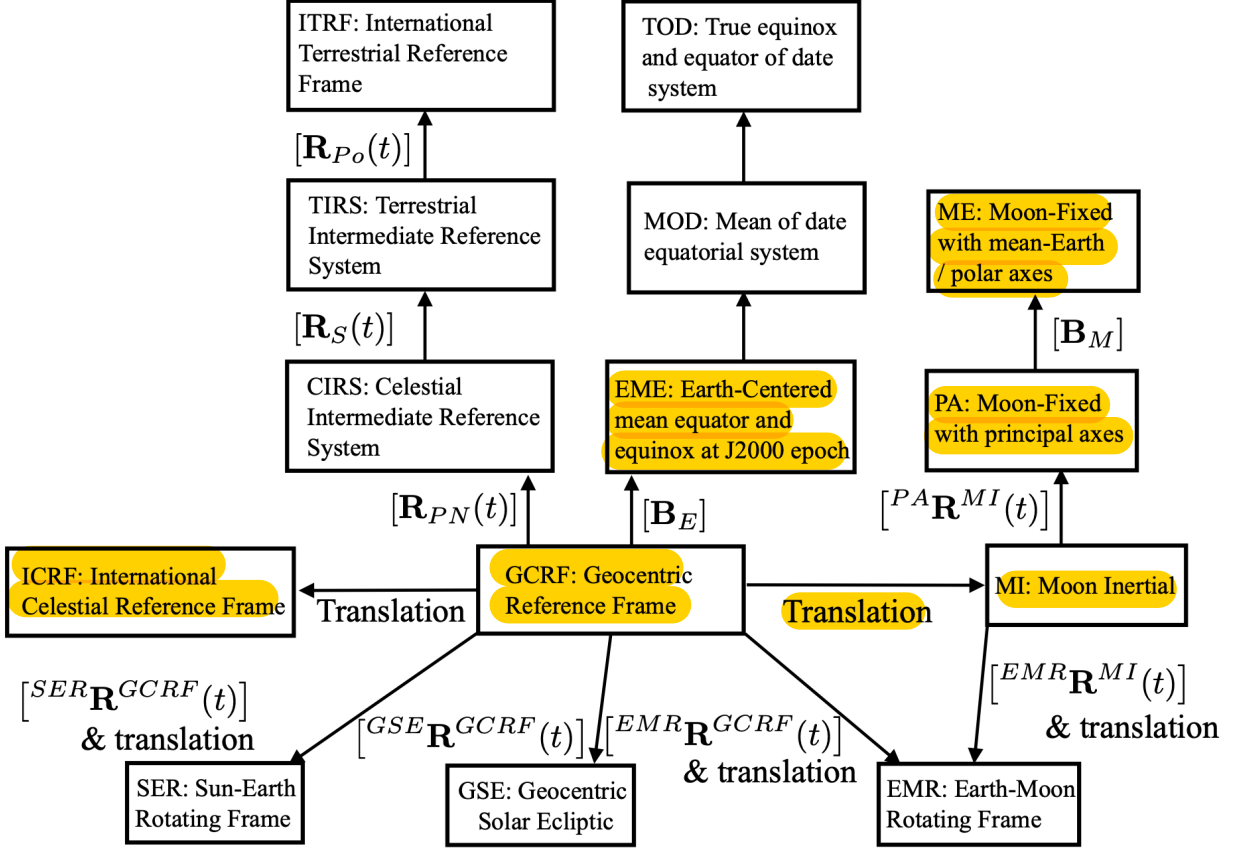


Fig. 3 Roadmap of the transformations covered within this section; matrices are defined throughout the text.

modeling convention [44]. Current convention adopted by the IAU eliminates previous dependencies on the ecliptic of date [44] to use a non-rotating origin; this newer approach is sometimes referred to as a CIO-based approach as opposed to the equinox-based approach previously employed [7, 44]. The current CIO-based convention for transforming between Earth-centered inertial and body-fixed coordinate systems includes three fundamental components:

- 1) Capturing the precession-nutation of the Celestial Intermediate Pole (CIP) in inertial space
- 2) Capturing the rotation of the body about the CIP, often labeled sidereal motion
- 3) Modeling polar motion, which reflects the shift of the CIP relative to surface of the body

This section delves deeper into each of these contributions. Recall the specialized terminology commonly employed in the definition of and transformation between coordinate systems is summarized in Section 2.1. These steps, as highlighted in Figure 4, are combined to transform between the GCRF and the ITRF.

#### 4.3.1 Precession-Nutation

The ‘precession-nutation’ component of the conventional transformation between body-fixed and inertial coordinate systems focuses on modeling the motion of the CIP in inertial space. Recall that the CIP is the pole that is normal to the

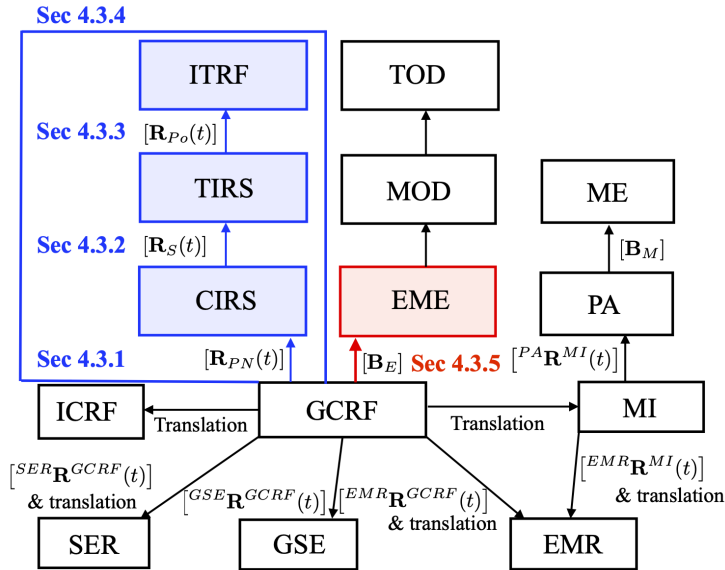


**Fig. 4** Highlighted segments of the transformation roadmap are covered in Sec 5.3.

equatorial plane of the Earth when only precession and nutation are modeled. This motion includes both periodic effects with a period greater than two days in the inertial system and secular effects [7]. The physical phenomena that contribute to precession and nutation of the CIP in inertial space include: the gravitational influence of the Sun, Moon and other planets; the irregular shape and gravitational distribution of the Earth; and the evolution of the Moon's orbit [6].

This ‘precession-nutation’ component of the transformation is summarized by a single, time-dependent rotation matrix,  $[R_{PN}(t)]$ , that explicitly depends on both the location of the CIO (i.e., the first axis of the GCRF) within the equatorial plane (i.e., the plane that is perpendicular to the CIP) as well as the components of the CIP as expressed in the inertial reference frame [7]. When this rotation is performed for geocentric reference frames, this rotation matrix transforms a position vector from the GCRS, a celestial or inertial reference system, to an intermediate system labeled the Celestial Intermediate Reference System (CIRS). The IERS defines the CIRS as a system that differs from the GCRS by modeling the spin axis using only precession-nutation, rendering it similar to an Earth-centered true of date equinox and equator system but with the first axis directed along the CIO as opposed to the vernal equinox [7, 13]. A similar rotation may be used for systems where the celestial body used to define the origin is not the Earth, with an update to the naming of each coordinate system to reflect that they are not geocentric.

There are a variety of approaches to computing the rotation matrix that captures the ‘precession-nutation’ component of the transformation between body-fixed and inertial coordinate systems, based on distinct sequences of simple rotations and input parameters. However, a simplified expression for this rotation matrix, from the GCRF to the CIRS that is also

used in the GMAT software is written as [7, 13]:

$$[\mathbf{R}_{PN}(t)] = [\mathbf{R}_3(-s)] \begin{bmatrix} 1 - aX^2 & -aXY & -X \\ -aXY & 1 - aY^2 & -Y \\ X & Y & 1 - a(X^2 + Y^2) \end{bmatrix} \quad (22)$$

where  $a$  is equal to:

$$a = \frac{1}{1 + \sqrt{1 - X^2 - Y^2}} \quad (23)$$

The quantities  $X(t)$  and  $Y(t)$  are the first two components of a unit vector aligned with the CIP expressed in the GCRF. Then, the scalar, time-varying quantity  $s(t)$  locates the CIO within the equatorial plane in the GCRF [7]; this quantity is often labeled the CIO locator. This quantity uses the right ascension of the ascending node for the equatorial plane measured relative to the plane formed by the first two axes of the GCRF. The quantity  $s(t)$  then reflects the difference between the right ascension measured from the first axis of the GCRS and that measured from the CIO. [7, 45, 46]. This difference is incorporated via the transformation matrix  $[\mathbf{R}_3(-s)]$  which is a time-dependent simple rotation matrix about the 3rd axis by an angle  $s$ . This step of the transformation, between GCRF and CIRS, is graphically represented in Fig. 5a) using the same notation as in this section.

Throughout the simplified expression for  $[\mathbf{R}_{PN}(t)]$ , three time-dependent quantities are required:  $X(t)$ ,  $Y(t)$ , and  $s(t)$ . These quantities may be calculated for a specific epoch using complex expressions that are each composed of a polynomial in time and a series expansion to reflect frame bias terms, precession and nutation [7]. Truncation of this series expansion influences the accuracy of the values used for these three quantities [47]. High-order truncations of these expressions may be performed using IAU Standards of Fundamental Astronomy (SOFA) routines available online at [www.iausofa.org](http://www.iausofa.org) [45]. However, the GMAT documentation notes that using these routines may become computationally expensive. Instead, GMAT leverages an alternative approach that is discussed by Seago and Vallado and Coppola, Seago and Vallado [44, 48]: interpolating between values of  $X(t)$ ,  $Y(t)$ , and  $s(t)$  computed at one day time intervals. GMAT performs this interpolation using a 9-th order Lagrange interpolation [13]. Bradley, Sibois and Axelrad present an assessment of the accuracy associated with alternative interpolation schemes for various regimes near the Earth, along with a set of recommendations for suitable interpolation schemes that meet desired accuracy requirements [49].

#### 4.3.2 Sidereal Motion

The sidereal motion component of the adopted procedure for transforming between body-fixed and inertial coordinate systems focuses on capturing the rotation of the Earth around the CIP. This single component of the transformation is summarized by a single, time-dependent rotation matrix,  $[\mathbf{R}_S(t)]$ , that explicitly depends on the Earth rotation angle,

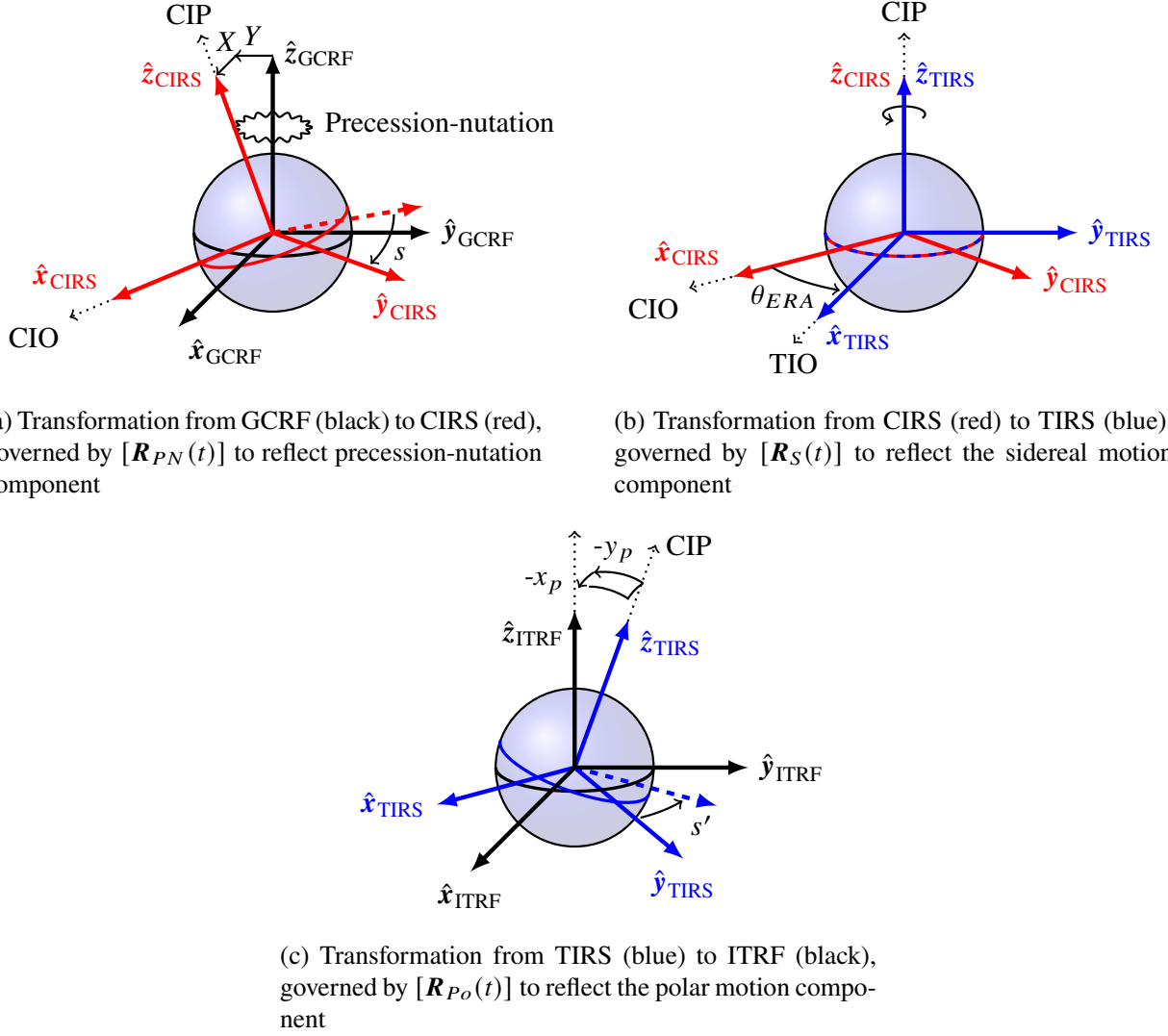


**Fig. 5 Transformation between the GCRF and the ITRF, decomposed into a sequence of three rotations. Note: angles between axes may be exaggerated for visual clarity.**

$\theta_{ERA}$ . This step reflects one simple rotation about the third axis from the CIRS to a system labeled the Terrestrial Intermediate Reference System (TIRS) [7]. This rotation matrix is expressed as [7]:

$$[R_S(t)] = [R_3(\theta_{ERA})] \quad (24)$$

In this expression, the Earth rotation angle is calculated in radians as [7]:

$$\theta_{ERA} = 2\pi (0.7790572732640 + 1.00273781191135448 (JD_{UT1} - 2451545.0)) \quad (25)$$

where  $JD_{UT1}$  is the Julian date in UT1. The rotation matrix from the CIRS to the TIRS possesses a nonzero time derivative. Accordingly, its time derivative is equal to:

$$\left[ \dot{\mathbf{R}}_S(t) \right] = \begin{bmatrix} -\omega_E \sin(\theta_{ERA}) & \omega_E \cos(\theta_{ERA}) & 0 \\ -\omega_E \cos(\theta_{ERA}) & -\omega_E \sin(\theta_{ERA}) & 0 \\ 0 & 0 & 0 \end{bmatrix} \quad (26)$$

where  $\omega_E$  is the rotation rate of the Earth [6, 44]. This step of the transformation, between CIRS and TIRS, is graphically represented in Fig. 5b) using the same notation as in this section.

#### 4.3.3 Polar Motion

The polar motion component of the adopted procedure for transforming between body-fixed and inertial coordinate systems focuses on capturing the shift of the CIP relative to the surface of the body. This single component of the transformation is summarized by a single, time-dependent rotation matrix,  $[\mathbf{R}_{Po}(t)]$ , that explicitly depends on both the location of the CIP expressed in the ITRS and the location of the Terrestrial Intermediate Origin (TIO), which is the first axis of the ITRS [7]. Using this information, the associated complex rotation from the TIRS to the ITRF to capture polar motion is written using a sequence of simple rotations as [7]:

$$[\mathbf{R}_{Po}(t)] = [\mathbf{R}_1(-y_p)] [\mathbf{R}_2(-x_p)] [\mathbf{R}_3(s')] \quad (27)$$

In this expression, the scalar variable  $s'$  is labeled the TIO locator. The TIO locator is analogous to the CIO locator, but reflects the location of the TIO within the equatorial plane [7]. This quantity,  $s'$ , is approximated as [7]:

$$s' \approx (-47\mu\text{as})t \quad (28)$$

where  $t$  is the time after JD 2,451,545.0 TT expressed in Julian TT century format [13]. This expression for  $s'$  is calculated via a linear fit to capture the mean amplitudes of variations in  $s'$  derived from measurements [50]. Then, the quantities  $x_p$  and  $y_p$  are coordinates of the CIP in the ITRS. The values of these coordinates may be calculated using parameters published by the IERS, with additional corrections as needed to accommodate the influence of ocean tides as well as libration effects with periods that are greater than two days and not included in the nutation model [7]. GMAT accesses discrete values from IERS and then performs a third-order Lagrange interpolation [13]. This step of the transformation, between TIRS and ITRF, is graphically represented in Fig. 5c) using the same notation as in this section.

#### 4.3.4 Transformations Between GCRF and ITRF

The rotation matrices presented for each of the three components of the conventional CIO-based approach are multiplied in the correct order to form a single transformation matrix between the GCRF, an inertial system, and the ITRF, a body-fixed system with a common origin at the center of the Earth. To transform the position vector of an object  $p$  from the GCRF to the ITRF, the following expression is used:

$$\mathbf{r}_{E,p}^{ITRF} = [ITRF \mathbf{R}^{GCRF}(t)] \mathbf{r}_{E,p}^{GCRF} = [\mathbf{R}_{Po}(t)] [\mathbf{R}_S(t)] [\mathbf{R}_{PN}(t)] \mathbf{r}_{E,p}^{GCRF} \quad (29)$$

The time derivative of this expression supplies the transformation for the velocity vector. When applying the product rule during differentiation, software such as GMAT assumes that the only matrix that possesses a significant time derivative is  $[\mathbf{R}_S(t)]$  [13, 44]. Thus, the transformation for the velocity vector of an object  $p$  from the GCRF to the ITRF uses the following expression:

$$\mathbf{v}_{E,p}^{ITRF} = [\mathbf{R}_{Po}(t)] [\mathbf{R}_S(t)] [\mathbf{R}_{PN}(t)] \mathbf{v}_{E,p}^{GCRF} + [\mathbf{R}_{Po}(t)] [\dot{\mathbf{R}}_S(t)] [\mathbf{R}_{PN}(t)] \mathbf{r}_{E,p}^{GCRF} \quad (30)$$

Alternatively, to transform the position vector of an object  $p$  from the ITRF to the GCRF, the following expression is used:

$$\mathbf{r}_{E,p}^{GCRF} = [GCRF \mathbf{R}^{ITRF}(t)] \mathbf{r}_{E,p}^{ITRF} = [\mathbf{R}_{PN}(t)]^T [\mathbf{R}_S(t)]^T [\mathbf{R}_{Po}(t)]^T \mathbf{r}_{E,p}^{ITRF} \quad (31)$$

Following the same procedure as above to take the time derivative of this expression, the transformation for the velocity vector of an object  $p$  from the ITRF to the GCRF uses the following expression:

$$\mathbf{v}_{E,p}^{GCRF} = [\mathbf{R}_{PN}(t)]^T [\mathbf{R}_S(t)]^T [\mathbf{R}_{Po}(t)]^T \mathbf{v}_{E,p}^{ITRF} + [\mathbf{R}_{PN}(t)]^T [\dot{\mathbf{R}}_S(t)]^T [\mathbf{R}_{Po}(t)]^T \mathbf{r}_{E,p}^{ITRF} \quad (32)$$

Together, these expressions supply a transformation of the state vector for an object between the inertial GCRF and body-fixed ITRF systems.

#### 4.3.5 Transformations Between GCRF and Mean Equator and Equinox at J2000

Transforming between the GCRF and Earth-Centered Mean Equator and Equinox at J2000 inertial system relies on a time-independent frame bias matrix that reflects the constant angular offset between two sets of axes. To transform a position vector from the GCRF to the Mean Equator and Equinox at J2000 inertial system (indicated by the label MJ2000), the following expression is used:

$$\mathbf{r}_{E,p}^{MJ2000} = [MJ2000 \mathbf{R}^{GCRF}] \mathbf{r}_{E,p}^{GCRF} = [\mathbf{B}_E] \mathbf{r}_{E,p}^{GCRF} \quad (33)$$

where the rotation matrix is set equal to the frame bias matrix,  $[\mathbf{B}_E]$ . The frame bias matrix is a function of three parameters [6, 13]:  $\xi_0 = -16.6170 \text{ mas} = -8.0561 \times 10^{-8} \text{ rad}$  and  $\eta_0 = -6.8192 \text{ mas} = -3.3060 \times 10^{-8} \text{ rad}$  reflect the angular deviations between the CIP on the J2000 epoch and the third axis of the GCRS, and  $d\alpha_0 = -14.6 \text{ mas} = 7.0783 \times 10^{-8} \text{ rad}$  captures the deviation between the first axes of the two systems [6, 7, 13, 30]. Note that mas is an abbreviation for milliarcseconds. This transformation is displayed graphically in Fig. 6. The exact expression for the frame bias matrix to convert from the GCRF to the Earth-Centered Mean Equator and Equinox at J2000 inertial system is written as:

$$[\mathbf{B}_E] = [\mathbf{R}_1(-\eta_0)] [\mathbf{R}_2(\xi_0)] [\mathbf{R}_3(d\alpha_0)] \quad (34)$$

However, there are two widely-used approximations of the frame bias matrix, with different levels of accuracy. A first-order approximation of the frame bias matrix is written as [30]:

$$[\mathbf{B}_E] \approx \begin{bmatrix} 1 & d\alpha_0 & -\xi_0 \\ -d\alpha_0 & 1 & -\eta_0 \\ \xi_0 & \eta_0 & 1 \end{bmatrix} \quad (35)$$

while a second-order approximation of the frame-bias matrix is equal to [30]:

$$[\mathbf{B}_E] \approx \begin{bmatrix} 1 - 0.5(d\alpha_0^2 + \xi_0^2) & d\alpha_0 & -\xi_0 \\ -d\alpha_0 - \eta_0\xi_0 & 1 - 0.5(d\alpha_0^2 + \eta_0^2) & -\eta_0 \\ \xi_0 - \eta_0d\alpha_0 & \eta_0 + \xi_0d\alpha_0 & 1 - 0.5(\eta_0^2 + \xi_0^2) \end{bmatrix} \quad (36)$$

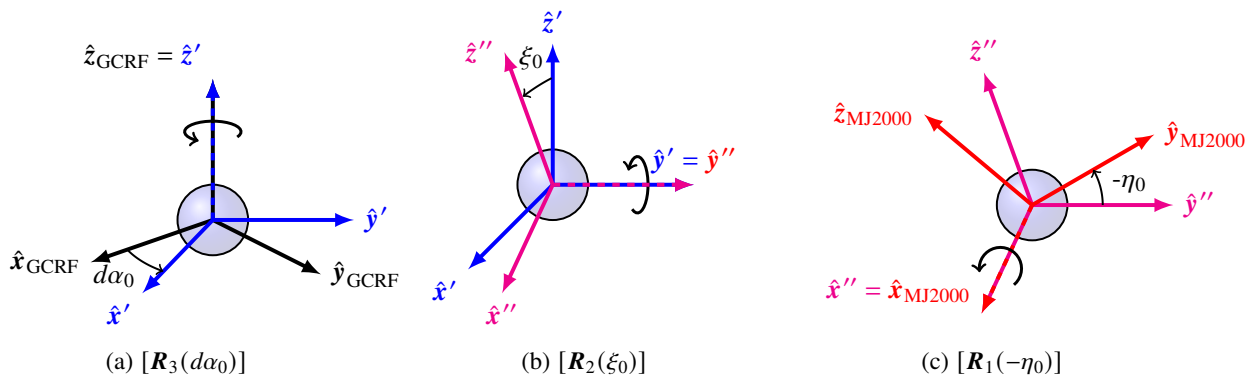


**Fig. 6** Conceptual representation of the simple rotations captured within the frame bias matrix to transform from the GCRF to the Earth-Centered Mean Equator and Equinox at J2000 inertial system.

The GMAT software uses the second-order approximation of the frame-bias matrix [13]. Because this matrix does not vary with time, the velocity vector is transformed from the GCRF to the Earth-centered Mean Equator and Equinox at J2000 inertial system via the following expression:

$$\mathbf{v}_{E,p}^{MJ2000} = [{}^{MJ2000}\mathbf{R}^{GCRF}] \mathbf{v}_{E,p}^{GCRF} = [\mathbf{B}_E] \mathbf{v}_{E,p}^{GCRF} \quad (37)$$

To transform the position and velocity vectors from the Earth-centered Mean Equator and Equinox at J2000 inertial system to the GCRF, i.e., perform the inverse transformation, the following expressions are used:

$$\mathbf{r}_{E,p}^{GCRF} = [\mathbf{B}_E]^{-1} \mathbf{r}_{E,p}^{MJ2000} \quad (38)$$

$$\mathbf{v}_{E,p}^{GCRF} = [\mathbf{B}_E]^{-1} \mathbf{v}_{E,p}^{MJ2000} \quad (39)$$

#### Implementation Note

While there is a small angular offset between the axes of the Earth-centered Mean Equator and Equinox at J2000 inertial system and the GCRF, they are often used interchangeably for applications such as trajectory design where the magnitude of the difference does not noticeably impact the results. This assumption is reasonable because the J2000 mean pole differs by about 18 mas from the ICRS pole, as determined by VLBI observations, while LLR observations have revealed that right ascensions to the first axes of the J2000 and ICRS differ by about 15 mas [51]. The overall difference in orientation is about 24 mas. Such a difference between these two sets of axes would translate to about 50 m at the lunar orbit radius when measured from the center of the Earth and 0.5 m on the Moon surface when measured from the center of the Moon.

## 4.4 Transforming Between Inertial Systems with Distinct Origins

This subsection focuses on transformations between inertial systems with the same axis definitions but distinct origins, requiring only a translation. The transformations summarized in this subsection are highlighted in Figure 7.

### 4.4.1 Transformations Between GCRF and ICRF

The transformation between the GCRF and ICRF coordinate systems includes only a translation component because the axes associated with ICRF are used as the axes for the GCRF. This translation shifts the origin between the solar system barycenter (indicated by the label SSB) and the center of the Earth (indicated by the label E). Accordingly, the transformation of the position and velocity vectors of an object  $p$  from the GCRF to ICRF is written as:

$$\mathbf{r}_{SSB,p}^{ICRF} = \mathbf{r}_{E,p}^{GCRF} + \mathbf{r}_{SSB,E}^{ICRF} \quad (40)$$

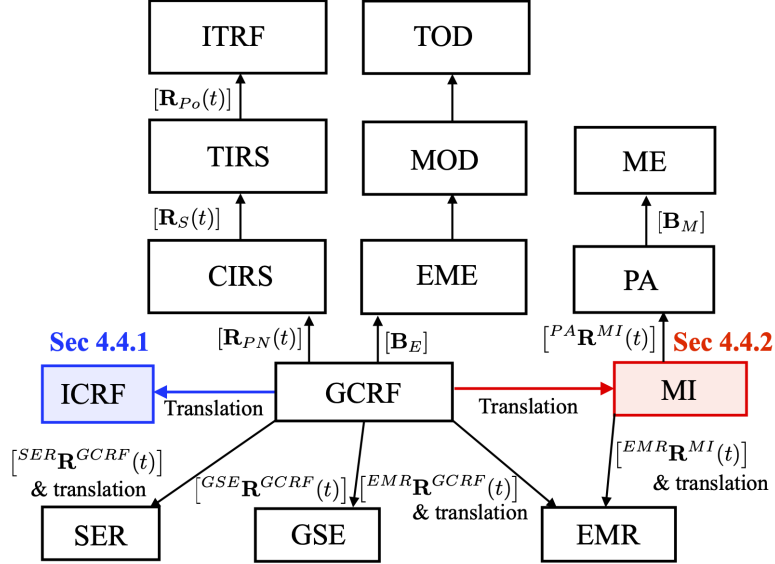


**Fig. 7** Highlighted segments of the transformation roadmap are covered in the labeled subsections.

$$\mathbf{v}_{SSB,p}^{ICRF} = \mathbf{v}_{E,p}^{GCRF} + \mathbf{v}_{SSB,E}^{ICRF} \quad (41)$$

where  $\mathbf{r}_{SSB,E}^{ICRF}$  and  $\mathbf{v}_{SSB,E}^{ICRF}$  are the position and velocity vectors of the center of the Earth relative to the solar system barycenter. The inverse transformation, from the ICRF to GCRF is written as:

$$\mathbf{r}_{E,p}^{GCRF} = \mathbf{r}_{SSB,p}^{ICRF} + \mathbf{r}_{E,SSB}^{GCRF} \quad (42)$$

$$\mathbf{v}_{E,p}^{GCRF} = \mathbf{v}_{SSB,p}^{ICRF} + \mathbf{v}_{E,SSB}^{GCRF} \quad (43)$$

Note that the relative position and velocity vectors between the center of the Earth and solar system barycenter are epoch dependent; they may be calculated using planetary ephemerides.

#### 4.4.2 Transformations Between GCRF and Moon-Centered Inertial System

The transformation between the GCRF and Moon-centered inertial coordinate systems, following the definitions in Section 2, includes only a translation component because the axes of each system are equal to the axes associated with the ICRF. This translation shifts the origin between the center of the Moon (labeled M) and the center of the Earth (indicated by the label E). Accordingly, transformation of the position and velocity vectors of an object  $p$  from the GCRF to Moon-centered inertial system (labeled using the superscript MI) is written as:

$$\mathbf{r}_{M,p}^{MI} = \mathbf{r}_{E,p}^{GCRF} + \mathbf{r}_{M,E}^{MI} \quad (44)$$

$$\mathbf{v}_{M,p}^{MI} = \mathbf{v}_{E,p}^{GCRF} + \mathbf{v}_{M,E}^{MI} \quad (45)$$

where  $\mathbf{r}_{M,E}^{MI}$  and  $\mathbf{v}_{M,E}^{MI}$  are the position and velocity vectors of the center of the Earth relative to the center of the Moon. The opposite transformation, from the Moon-centered inertial system to the GCRF is written as:

$$\mathbf{r}_{E,p}^{GCRF} = \mathbf{r}_{M,p}^{MI} + \mathbf{r}_{E,M}^{GCRF} \quad (46)$$

$$\mathbf{v}_{E,p}^{GCRF} = \mathbf{v}_{M,p}^{MI} + \mathbf{v}_{E,M}^{GCRF} \quad (47)$$

Note that the relative position and velocity vectors between the centers of the Earth and Moon are epoch dependent; they may be calculated using planetary and lunar ephemerides.

#### 4.5 Transforming Between Moon-Centered Systems

Transforming between the Moon inertial coordinate system and a Moon-fixed system that uses either the ME or PA axes relies on the use of Euler angles describing the time-dependent orientation of the principal axes of the Moon. A realization of these parameters at the time of publication is available in the planetary and lunar ephemerides files made available by NASA's NAIF, e.g., DE440 and DE441 [9]. This subsection presents an overview of this process as well as the procedure for calculating spherical coordinates for mapping applications. The transformations presented in this subsection are highlighted in Figure 8.

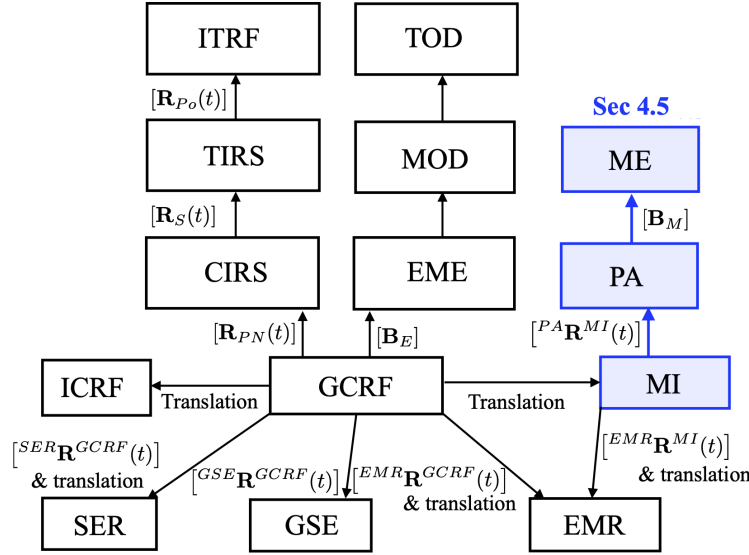


**Fig. 8** Highlighted segments of the transformation roadmap are covered in this subsection.

To transform a position vector for an object  $p$  from the Moon inertial system (labeled as MI) to a Moon-fixed system that uses the PA axes (labeled as PA), the following expression is used:

$$\mathbf{r}_{M,p}^{PA} = [{}^P\mathbf{A}\mathbf{R}^{MI}(t)] \mathbf{r}_{M,p}^{MI} \quad (48)$$

where the subscript  $M$  indicates the center of the Moon. The rotation matrix  $[{}^P A \mathbf{R}^{MI}(t)]$  is written in terms of three Euler angles [9]:

- $\psi_m$ : the angle from the intersection of the mantle equator and the  $xy$ -plane of the Moon inertial system to the Moon's prime meridian, measured within the mantle's equatorial plane
- $\theta_m$ : the angular tilt of the mantle's equatorial plane relative to the  $xy$ -plane of the Moon inertial system
- $\phi_m$ : the angle from the first axis of the Moon inertial system to intersection of the mantle equator and the  $xy$ -plane of the Moon inertial system, measured within the  $xy$ -plane of the Moon inertial system

Using these Euler angles, the rotation matrix  $[{}^P A \mathbf{R}^{MI}(t)]$  is calculated using a sequence of simple rotations as [9]:

$$[{}^P A \mathbf{R}^{MI}(t)] = [\mathbf{R}_3(\psi_m)] [\mathbf{R}_1(\theta_m)] [\mathbf{R}_3(\phi_m)] \quad (49)$$

This complex transformation, formed through a sequence of three simple rotations, is displayed graphically in Fig. 9 and relates the black axes of the Moon inertial system to the blue PA axes. The dotted circles indicate the  $\hat{x}\hat{y}$ -plane of each system. Taking the time derivative of Eq. 48, the expression governing the transformation of the velocity vector from the Moon inertial system to a Moon-fixed system with PA axes is then written as:

$$\mathbf{v}_{M,p}^{PA} = [{}^P A \mathbf{R}^{MI}(t)] \mathbf{v}_{M,p}^{MI} + [{}^P A \dot{\mathbf{R}}^{MI}(t)] \mathbf{r}_{M,p}^{MI} \quad (50)$$

where the time derivative of the rotation matrix,  $[{}^P A \dot{\mathbf{R}}^{MI}(t)]$  is calculated exactly as:

$$[{}^P A \dot{\mathbf{R}}^{MI}(t)] = [\dot{\mathbf{R}}_3(\psi_m)] [\mathbf{R}_1(\theta_m)] [\mathbf{R}_3(\phi_m)] + [\mathbf{R}_3(\psi_m)] [\dot{\mathbf{R}}_1(\theta_m)] [\mathbf{R}_3(\phi_m)] + [\mathbf{R}_3(\psi_m)] [\mathbf{R}_1(\theta_m)] [\dot{\mathbf{R}}_3(\phi_m)]$$

However, the GMAT software assumes that  $[\dot{\mathbf{R}}_1(\theta_m)]$  and  $[\dot{\mathbf{R}}_3(\phi_m)]$  are equal to the  $3 \times 3$  zero matrices [13] such that:

$$[{}^P A \dot{\mathbf{R}}^{MI}(t)] \approx [\dot{\mathbf{R}}_3(\psi_m)] [\mathbf{R}_1(\theta_m)] [\mathbf{R}_3(\phi_m)]$$

where

$$[\dot{\mathbf{R}}_3(\psi_m)] = \begin{bmatrix} -\dot{\psi}_m \sin(\psi_m) & \dot{\psi}_m \cos(\psi_m) & 0 \\ -\dot{\psi}_m \cos(\psi_m) & -\dot{\psi}_m \sin(\psi_m) & 0 \\ 0 & 0 & 0 \end{bmatrix}$$

and  $\dot{\psi}_m$  is equivalent to the  $\dot{W}$  quantity presented in the GMAT Mathematical Specifications document [13].

To transform a position vector for an object  $p$  from a Moon-fixed system that uses the PA axes to one that uses the

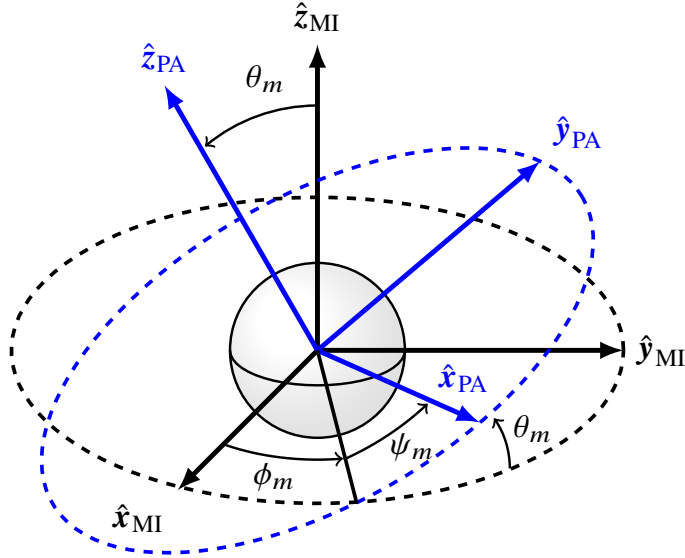


**Fig. 9 Transformation between the axes of the Moon inertial system (black) to the PA axes (blue) decomposed into a sequence of three rotations.**

ME axes, as calculated using DE421 ephemerides, a single time-independent frame bias matrix is employed:

$$\mathbf{r}_{M,p}^{ME} = [{}^{ME}\mathbf{R}^{PA}] \mathbf{r}_{M,p}^{PA} = [\mathbf{B}_M] \mathbf{r}_{M,p}^{PA} \quad (51)$$

where the frame bias matrix is equal to the following product of simple rotations [9]:

$$[\mathbf{B}_M] = [\mathbf{R}_1(-0.2785 \text{ arcsec})] [\mathbf{R}_2(-78.6944 \text{ arcsec})] [\mathbf{R}_3(-67.8526 \text{ arcsec})] \quad (52)$$

and the argument of each simple rotation is calculated using the coordinates of retroreflectors on the Moon's surface in each of the PA and ME axes. Note that the ME axes are calculated using the DE421 ephemerides which were used by the LRO. Then, the transformation for the velocity vector from a Moon-fixed system that uses the PA axes to one that uses the ME axes, as calculated using DE421 ephemerides, is expressed as

$$\mathbf{v}_{M,p}^{ME} = [{}^{ME}\mathbf{R}^{PA}] \mathbf{v}_{M,p}^{PA} = [\mathbf{B}_M] \mathbf{v}_{M,p}^{PA} \quad (53)$$

because the frame bias matrix is time-independent.

Combining these transformations, position and velocity vectors expressed in the Moon inertial system are transformed to a Moon-fixed system that uses ME axes via the following expressions:

$$\mathbf{r}_{M,p}^{ME} = [\mathbf{B}_M] [\mathbf{R}_3(\psi_m)] [\mathbf{R}_1(\theta_m)] [\mathbf{R}_3(\phi_m)] \mathbf{r}_{M,p}^{MI} \quad (54)$$

$$\mathbf{v}_{M,p}^{ME} = [\mathbf{B}_M] [\mathbf{R}_3(\psi_m)] [\mathbf{R}_1(\theta_m)] [\mathbf{R}_3(\phi_m)] \mathbf{v}_{M,p}^{MI} + [\mathbf{B}_M] \left[ {}^{PA} \dot{\mathbf{R}}^{MI}(t) \right] \mathbf{r}_{M,p}^{MI} \quad (55)$$

The inverse transformation for position and velocity vectors expressed in a Moon-fixed system that uses ME axes to the Moon inertial system is written as:

$$\mathbf{r}_{M,p}^{MI} = [{}^{MI} \mathbf{R}^{ME}] \mathbf{r}_{M,p}^{ME} = [\mathbf{R}_3(-\phi_m)] [\mathbf{R}_1(-\theta_m)] [\mathbf{R}_3(-\psi_m)] [\mathbf{B}_M]^{-1} \mathbf{r}_{M,p}^{ME} \quad (56)$$

$$\mathbf{v}_{M,p}^{MI} = [\mathbf{R}_3(-\phi_m)] [\mathbf{R}_1(-\theta_m)] [\mathbf{R}_3(-\psi_m)] [\mathbf{B}_M]^{-1} \mathbf{v}_{M,p}^{ME} + [{}^{MI} \dot{\mathbf{R}}^{ME}] \mathbf{r}_{M,p}^{ME} \quad (57)$$

When spherical coordinates are used, the selenocentric longitude, latitude and distance may be directly calculated from a Cartesian state expressed in a Moon-fixed frame; typically, these spherical coordinates are expressed in a Moon-fixed frame with ME axes [14]. To demonstrate the procedure for calculating spherical coordinates, consider a Cartesian position vector  $\mathbf{r}_{M,p}^{ME} = x\hat{x} + y\hat{y} + z\hat{z}$  of an object  $p$  relative to the center of the Moon and expressed in a Moon-fixed coordinate system with ME axes. Then, the selenocentric longitude,  $\lambda_{sc}$ , is calculated as:

$$\lambda_{sc} = \tan^{-1} \left( \frac{y}{x} \right) \quad (58)$$

with values in the range  $[-180, 180]$  degrees. The selenocentric latitude,  $\phi_{sc}$ , is calculated as:

$$\phi_{sc} = \tan^{-1} \left( \frac{z}{\sqrt{x^2 + y^2}} \right) \quad (59)$$

and possesses values within the range  $[-90, 90]$  degrees. Finally, the distance  $r_{sc}$  from the center of the Moon to the object is calculated as:

$$r_{sc} = \sqrt{x^2 + y^2 + z^2} \quad (60)$$

The position vector of the object in the Moon-fixed coordinate system with ME axes (denoted  $\hat{x}, \hat{y}, \hat{z}$ ) is calculated from the spherical coordinates  $\lambda_{sc}, \phi_{sc}, r_{sc}$  as [52]:

$$\mathbf{r}_{M,p}^{ME} = r_{sc} \cos(\phi_{sc}) \cos(\lambda_{sc}) \hat{x} + r_{sc} \cos(\phi_{sc}) \sin(\lambda_{sc}) \hat{y} + r_{sc} \sin(\phi_{sc}) \hat{z} \quad (61)$$

For a given set of stereographic coordinates  $(x, y)$  expressed in the Moon-fixed reference frame with ME axes and a height  $z$  above the Moon radius of 1737.4 km, these coordinates are transformed to selenocentric spherical coordinates  $(\phi, \lambda, R_M + z)$  as follows:

$$\rho = \sqrt{x^2 + y^2} \quad (62)$$

$$c = 2 \tan^{-1} \left( \frac{\rho}{2R_M} \right) \quad (63)$$

$$\phi = \sin^{-1} \left( \cos(c) \sin(\phi_0) + \frac{\cos(\phi_0)y \sin(c)}{\rho} \right) \quad (64)$$

$$\lambda = \lambda_0 + \tan^{-1} \left( \frac{x \sin(c)}{\cos(\phi_0)\rho \cos(c) - \sin(\phi_0)y \sin(c)} \right) \quad (65)$$

where  $\phi_0$  and  $\lambda_0$  are the latitude and longitude, respectively, of the projection pole when  $x = y = 0$ .

#### 4.6 Transforming Between Inertial and Synodic Systems

Another type of transformation focuses on relating inertial and synodic coordinate systems. As described in 2.5, a synodic coordinate system is defined using the motion of two massive bodies (each labeled the larger and smaller primary according to their mass); thus, a rotation must be performed during the transformation. The matrix governing this transformation is typically calculated directly from the relative state of the two primary bodies. In addition, the origin of a synodic system is often located at a calculated point such as the barycenter of the primary system or a Lagrange point; in some cases, the origin may be selected as one of the primary bodies. If the origin of a specific inertial system does not coincide with the origin of the synodic coordinate system, a translation must also be performed. This subsection supplies an overview of the general procedure for implementing this transformation; this procedure is then applied to specific synodic systems. The specific transformations summarized in this subsection are highlighted in Figure 10.

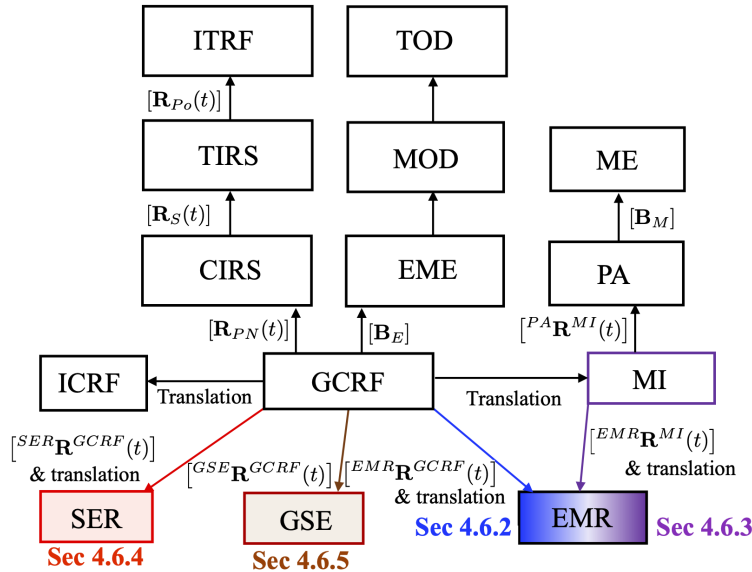


**Fig. 10** Highlighted segments of the transformation roadmap are covered in this subsection.

##### 4.6.1 General Procedure

Consider two primary bodies,  $P_1$  and  $P_2$ , used to define a  $P_1$ - $P_2$  synodic system with axes  $(\hat{x}, \hat{y}, \hat{z})$  and origin  $O_s$ . In the case of the Earth-Moon and Sun-Earth rotating frames, the three axes are commonly defined as follows:  $\hat{x}$  is

directed from the larger primary  $P_1$  to the smaller primary  $P_2$ ,  $\hat{z}$  is aligned with the orbit angular momentum vector for the primary system, and  $\hat{y}$  completes the right-handed triad. Note that in some groups, a modification to this definition is employed: the first axis is directed from the smaller primary to the larger primary; this difference also occurs for the Geocentric Solar Ecliptic frame. An inertial coordinate system is also denoted using the axes  $(\hat{X}, \hat{Y}, \hat{Z})$  and origin  $O_i$ .

The rotation matrix governing the transformation from an inertial system to a synodic system is calculated using the position and velocity vectors of  $P_2$  relative to  $P_1$  in the inertial frame. These vectors are labeled  $\mathbf{R}_{12}$  and  $\mathbf{V}_{12}$ , respectively, and are typically calculated using ephemerides. The rotation matrix,  $[{}^S\mathbf{R}^I(t)]$ , governing the rotation from the axes  $(\hat{X}, \hat{Y}, \hat{Z})$  of the inertial frame to the axes  $(\hat{x}, \hat{y}, \hat{z})$  of the rotating frame about a common origin, are then written as [13]:

$$[{}^S\mathbf{R}^I(t)] = \begin{bmatrix} \hat{x}^T \\ \hat{y}^T \\ \hat{z}^T \end{bmatrix} \quad (66)$$

where the following column vectors are written using components in the inertial frame:

$$\hat{x} = \frac{\mathbf{R}_{12}}{\|\mathbf{R}_{12}\|}$$

$$\hat{z} = \frac{\mathbf{R}_{12} \times \mathbf{V}_{12}}{\|\mathbf{R}_{12} \times \mathbf{V}_{12}\|}$$

$$\hat{y} = \hat{z} \times \hat{x}$$

Thus, a position vector  $\mathbf{r}_{O_I,p}^I$  that locates an object  $p$  and is expressed in the inertial coordinate system is transformed to a position vector  $\mathbf{r}_{O_S,p}^S$  in a synodic system via the following expression:

$$\mathbf{r}_{O_S,p}^S = [{}^S\mathbf{R}^I(t)] \mathbf{r}_{O_I,p}^I + \mathbf{r}_{O_S,O_I}^S \quad (67)$$

where  $\mathbf{r}_{O_S,O_I}^S$  is the position vector of the origin of the inertial system relative to the origin of the synodic system and expressed in the synodic frame, capturing the necessary translation step when the origins of the two coordinate systems do not coincide. Because the matrix  $[{}^S\mathbf{R}^I(t)]$  is orthogonal, transformation of a position vector  $\mathbf{r}_{O_S,p}^S$  in the synodic coordinate system to a position vector  $\mathbf{r}_{O_I,p}^I$  in an inertial system is calculated as

$$\mathbf{r}_{O_I,p}^I = [{}^S\mathbf{R}^I(t)]^T \mathbf{r}_{O_S,p}^S + \mathbf{r}_{O_I,O_S}^I \quad (68)$$

using the transpose of the rotation matrix in Eq. 66 and  $\mathbf{r}_{O_I,O_S}^I$ , which is the position vector of the origin of the synodic system relative to the origin of the inertial system and expressed in the inertial frame.

One approach to transforming the velocity vector of an object from the synodic coordinate system to the inertial coordinate system involves directly calculating the time derivative of the rotation matrix. This time derivative of the rotation matrix governing the rotation from the axes  $(\hat{X}, \hat{Y}, \hat{Z})$  of the inertial frame to the axes  $(\hat{x}, \hat{y}, \hat{z})$  of the synodic frame about a common origin is calculated as [13]:

$$\left[ {}^S \dot{\mathbf{R}}^I(t) \right] = \begin{bmatrix} \left( \frac{d\hat{x}}{dt} \right)^T \\ \left( \frac{d\hat{y}}{dt} \right)^T \\ \left( \frac{d\hat{z}}{dt} \right)^T \end{bmatrix} \quad (69)$$

The time derivatives of the first and second axes of the synodic frame are column vectors written using components in the inertial frame and are calculated as:

$$\begin{aligned} \frac{d\hat{x}}{dt} &= \frac{\mathbf{V}_{12}}{||\mathbf{R}_{12}||} - \hat{x} \left( \frac{\hat{x} \cdot \mathbf{V}_{12}}{||\mathbf{R}_{12}||} \right) \\ \frac{d\hat{y}}{dt} &= \frac{d\hat{z}}{dt} \times \hat{x} + \hat{z} \times \frac{d\hat{x}}{dt} \end{aligned}$$

The GMAT software then calculates the time derivative of the  $\hat{z}$  axis by assuming that the  $\hat{z}$ -axis associated with the synodic frame does not shift significantly relative to the inertial frame. The result is that:

$$\frac{d\hat{z}}{dt} \approx 0$$

This assumption is reasonable in the Sun-Earth and Earth-Moon rotating frames. However, for a higher-fidelity transformation, the Goddard Trajectory Determination System (GTDS) and the Systems Tool Kit (STK) software both report using an exact expression for the time derivatives of the three axes of the synodic frame written using components in the inertial frame [52, 53]. This expression is derived by directly taking the time derivative of the expression for  $\hat{z}$  to produce:

$$\frac{d\hat{z}}{dt} = \frac{\mathbf{R}_{12} \times \mathbf{A}_{12}}{||\mathbf{R}_{12} \times \mathbf{V}_{12}||} - \frac{[(\mathbf{R}_{12} \times \mathbf{A}_{12}) \cdot (\mathbf{R}_{12} \times \mathbf{V}_{12})] (\mathbf{R}_{12} \times \mathbf{V}_{12})}{||\mathbf{R}_{12} \times \mathbf{V}_{12}||^3}$$

where the variable  $\mathbf{A}_{12}$  is the acceleration of  $P_2$  relative to  $P_1$ , i.e., the time derivative of the velocity vector for an observer fixed in the inertial frame. If  $\mathbf{R}_{12}$  and  $\mathbf{V}_{12}$  are calculated using ephemerides, this acceleration vector may be approximated using equations of motion that sufficiently reflect the dynamical environment governing the motion of  $P_2$  relative to  $P_1$  to a desired accuracy level.

The transformation for the velocity vector from the inertial coordinate system to the synodic system is written to incorporate both the rotation and translation components. Specifically, the velocity vector for an object  $p$  in the synodic

coordinate system is calculated using state information in the inertial coordinate system as:

$$\mathbf{v}_{O_S,p}^S = [{}^S \mathbf{R}^I(t)] \mathbf{v}_{O_I,p}^I + [{}^S \dot{\mathbf{R}}^I(t)] \mathbf{r}_{O_I,p}^I + \mathbf{v}_{O_S,O_I}^S \quad (70)$$

where  $\mathbf{v}_{O_S,O_I}^S$  is the velocity of the origin of the inertial frame relative to the origin of the synodic frame and expressed in the synodic frame. In addition, the transformation for the velocity vector from the synodic to inertial coordinate systems is written as:

$$\mathbf{v}_{O_I,p}^I = -[{}^S \mathbf{R}^I(t)]^T [{}^S \dot{\mathbf{R}}^I(t)] [{}^S \mathbf{R}^I(t)]^T \mathbf{r}_{O_S,p}^S + [{}^S \mathbf{R}^I(t)]^T \mathbf{v}_{O_S,p}^S + \mathbf{v}_{O_I,O_S}^I \quad (71)$$

This transformation is calculated by writing Eq. 67 and 70 in matrix form and performing an inversion that is written in terms of the submatrices. However, this transformation may also be expressed in a similar form to Eq. 67 and 70 by starting with the transformation matrix  $[{}^I \mathbf{R}^S(t)]$  that is calculated as the transpose of  $[{}^S \mathbf{R}^I(t)]$ .

#### 4.6.2 Transformations Between GCRF and Earth-Moon Rotating Frame

To transform the position and velocity vectors of an object  $p$  from the GCRF, an Earth-inertial frame, to the Earth-Moon rotating frame (indicated by the superscript EMR), the following expressions are used:

$$\mathbf{r}_{EMB,p}^{EMR} = [{}^{EMR} \mathbf{R}^{GCRF}(t)] \mathbf{r}_{E,p}^{GCRF} + \mathbf{r}_{EMB,E}^{EMR} \quad (72)$$

$$\mathbf{v}_{EMB,p}^{EMR} = [{}^{EMR} \dot{\mathbf{R}}^{GCRF}(t)] \mathbf{r}_{E,p}^{GCRF} + [{}^{EMR} \mathbf{R}^{GCRF}(t)] \mathbf{v}_{E,p}^{GCRF} + \mathbf{v}_{EMB,E}^{EMR} \quad (73)$$

where  $[{}^{EMR} \mathbf{R}^{GCRF}(t)] = [{}^{GCRF} \mathbf{R}^{EMR}(t)]^T$  and the subscript  $E$  indicates the Earth center and  $EMB$  corresponds to the Earth-Moon barycenter. Although the Earth-Moon barycenter is considered the traditional origin for an Earth-Moon rotating frame, alternative origins are often employed when analyzing trajectories in a multi-body systems; in that case, the subscript  $EMB$  would be replaced with an alternative subscript such as  $E$ ,  $M$  or  $L_i$  to indicate the origin as the Earth, Moon or an Earth-Moon Lagrange point, respectively. The relationship between these two frames is depicted graphically in Fig. 11.

The inverse transformation for the position and velocity vectors, from the Earth-Moon rotating frame to the GCRF is written as:

$$\mathbf{r}_{E,p}^{GCRF} = [{}^{EMR} \mathbf{R}^{GCRF}(t)]^T \mathbf{r}_{EMB,p}^{EMR} + \mathbf{r}_{E,EMB}^{GCRF} \quad (74)$$

$$\mathbf{v}_{E,p}^{GCRF} = -[{}^{EMR} \mathbf{R}^{GCRF}(t)]^T [{}^{EMR} \dot{\mathbf{R}}^{GCRF}(t)] [{}^{EMR} \mathbf{R}^{GCRF}(t)]^T \mathbf{r}_{EMB,p}^{EMR} + [{}^{EMR} \mathbf{R}^{GCRF}(t)]^T \mathbf{v}_{EMB,p}^{EMR} + \mathbf{v}_{E,EMB}^{GCRF} \quad (75)$$

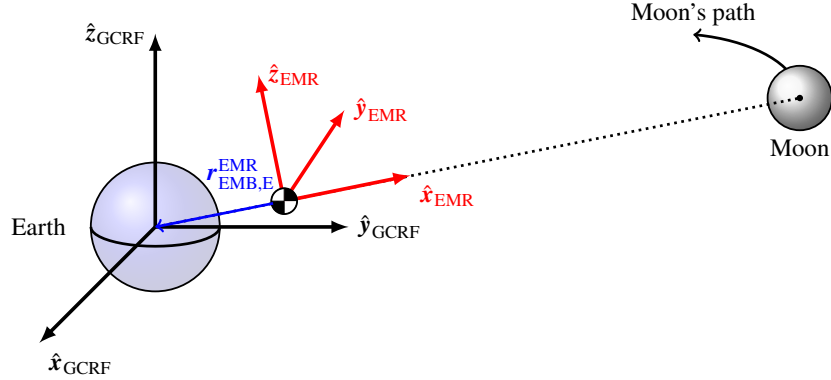


**Fig. 11** Conceptual representation of the relationship between the GCRF and Earth-Moon rotating frame. Note: distances and angles may be exaggerated for visual clarity.

#### 4.6.3 Transformations Between Moon Inertial and Earth-Moon Rotating Frame

To transform the position and velocity vectors of an object  $p$  from a Moon-centered inertial frame (indicated by the superscript MI) to the Earth-Moon rotating frame (indicated by the superscript EMR), the following expressions are used:

$$\mathbf{r}_{EMB,p}^{EMR} = [{}^{EMR}\mathbf{R}^{MI}(t)] \mathbf{r}_{M,p}^{MI} + \mathbf{r}_{EMB,M}^{EMR} \quad (76)$$

$$\mathbf{v}_{EMB,p}^{EMR} = [{}^{EMR}\dot{\mathbf{R}}^{MI}(t)] \mathbf{r}_{M,p}^{MI} + [{}^{EMR}\mathbf{R}^{MI}(t)] \mathbf{v}_{M,p}^{MI} + \mathbf{v}_{EMB,M}^{EMR} \quad (77)$$

where the subscript  $M$  indicates the Moon center and  $EMB$  corresponds to the Earth-Moon barycenter. Although the Earth-Moon barycenter is considered the traditional origin for an Earth-Moon rotating frame, alternative origins may be employed; in that case, the subscript  $EMB$  would be replaced with an alternative subscript such as  $E$ ,  $M$  or  $L_i$  to indicate the origin as the Earth, Moon or an Earth-Moon Lagrange point, respectively.

The inverse transformation for the position and velocity vectors, from the Earth-Moon rotating frame to the Moon-centered inertial frame is written as:

$$\mathbf{r}_{M,p}^{MI} \equiv [{}^{EMR}\mathbf{R}^{MI}(t)]^T \mathbf{r}_{EMB,p}^{EMR} + \mathbf{r}_{M,EMB}^{MI} \quad (78)$$

$$\mathbf{v}_{M,p}^{MI} \equiv [{}^{EMR}\mathbf{R}^{MI}(t)]^T [{}^{EMR}\dot{\mathbf{R}}^{MI}(t)] [{}^{EMR}\mathbf{R}^{MI}(t)]^T \mathbf{r}_{EMB,p}^{EMR} + [{}^{EMR}\mathbf{R}^{MI}(t)]^T \mathbf{v}_{EMB,p}^{EMR} + \mathbf{v}_{M,EMB}^{MI} \quad (79)$$

#### 4.6.4 Transformations Between GCRF and Sun-Earth Rotating Frame

To transform the position and velocity vectors of an object  $p$  from the GCRF to the Sun-Earth rotating frame (indicated by the superscript SER), the following expression is used:

$$\mathbf{r}_{SEB,p}^{SER} = [{}^{SER}\mathbf{R}^{GCRF}(t)] \mathbf{r}_{E,p}^{GCRF} + \mathbf{r}_{SEB,E}^{SER} \quad (80)$$

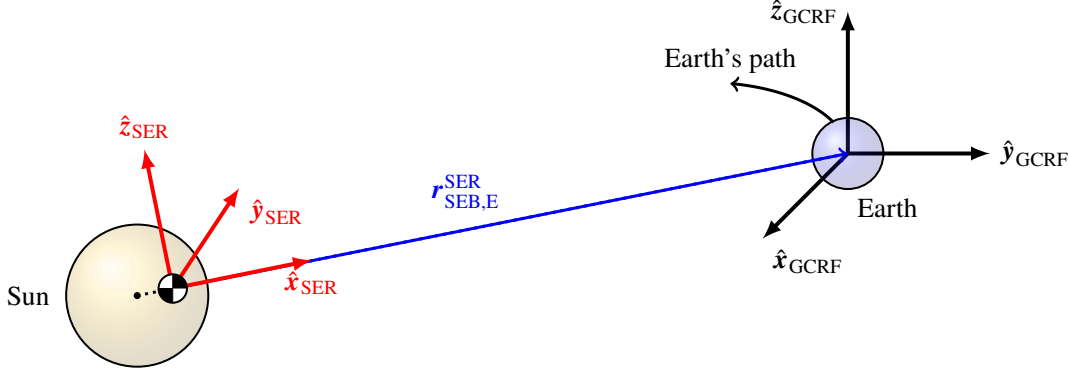


**Fig. 12** Conceptual representation of the relationship between the GCRF and Earth-Moon rotating frame. Note: distances and angles may be exaggerated for visual clarity.

$$\mathbf{v}_{SEB,p}^{SER} = [^{SER}\dot{\mathbf{R}}^{GCRF}(t)] \mathbf{r}_{E,p}^{GCRF} + [^{SER}\mathbf{R}^{GCRF}(t)] \mathbf{v}_{E,p}^{GCRF} + \mathbf{v}_{SEB,E}^{SER} \quad (81)$$

where the subscript  $E$  indicates the Earth center and  $SEB$  corresponds to the Sun-Earth barycenter. Although the Sun-Earth barycenter is considered the traditional origin for a Sun-Earth rotating frame, alternative origins may be employed; in that case, the subscript  $SEB$  would be replaced with an alternative subscript such as  $S$ ,  $E$  or  $L_i$  to indicate the origin as the Sun, Earth or a Sun-Earth Lagrange point, respectively. The relationship between these two frames is depicted graphically in Fig. 12.

The inverse transformation for the position and velocity vectors, from the Sun-Earth rotating frame to the GCRF is written as:

$$\mathbf{r}_{E,p}^{GCRF} = [^{SER}\mathbf{R}^{GCRF}(t)]^T \mathbf{r}_{SEB,p}^{GCRF} + \mathbf{r}_{E,SEB}^{GCRF} \quad (82)$$

$$\mathbf{v}_{E,p}^{GCRF} = -[^{SER}\mathbf{R}^{GCRF}(t)]^T [^{SER}\dot{\mathbf{R}}^{GCRF}(t)] [^{SER}\mathbf{R}^{GCRF}(t)]^T \mathbf{r}_{SEB,p}^{SER} + [^{SER}\mathbf{R}^{GCRF}(t)]^T \mathbf{v}_{SEB,p}^{SER} + \mathbf{v}_{E,SEB}^{GCRF} \quad (83)$$

#### 4.6.5 Transformations Between GCRF and Geocentric Solar Ecliptic Frame

To transform the position and velocity vectors of an object  $p$  from the GCRF to the Geocentric Solar Ecliptic frame (indicated by the superscript GSE), the mathematical foundation presented in Section 4.6 is employed with some modifications. Specifically, the three column vectors for the axes of the GSE frame are calculated using the position vector from the Earth to the Sun (as opposed to the vector from the Sun to the Earth in the Sun-Earth rotating frame) such that:

$$\hat{x} = \frac{\mathbf{R}_{ES}}{||\mathbf{R}_{ES}||}$$

$$\hat{z} = \frac{\mathbf{R}_{ES} \times \mathbf{V}_{ES}}{||\mathbf{R}_{ES} \times \mathbf{V}_{ES}||}$$

$$\hat{y} = \hat{z} \times \hat{x}$$

where the subscript  $E$  indicates the Earth center and  $S$  indicates the Sun center, such that  $\mathbf{R}_{ES}$  and  $\mathbf{V}_{ES}$  are the position and velocity vectors of the Sun center relative to the Earth center, expressed in the Earth-inertial system. In addition, the origin of the GSE system is the Earth center. Accordingly, the transformation between the GSE and Earth-centered inertial frames does not require a translation. With these modifications to the approach used in Section 4.6, the following expression is used:

$$\mathbf{r}_{E,p}^{GSE} = [{}^{GSE}\mathbf{R}^{GCRF}(t)] \mathbf{r}_{E,p}^{GCRF} \quad (84)$$

$$\mathbf{v}_{E,p}^{GSE} = [{}^{GSE}\dot{\mathbf{R}}^{GCRF}(t)] \mathbf{r}_{E,p}^{GCRF} + [{}^{GSE}\mathbf{R}^{GCRF}(t)] \mathbf{v}_{E,p}^{GCRF} \quad (85)$$

A similar transformation may be constructed from an inertial coordinate system that uses the Sun or Moon as an origin; in that case, a translation term must be included in these expressions.

The inverse transformation for the position and velocity vectors, from the GSE system to the GCRF is written as:

$$\mathbf{r}_{E,p}^{GCRF} = [{}^{GSE}\mathbf{R}^{GCRF}(t)]^T \mathbf{r}_{E,p}^{GSE} \quad (86)$$

$$\mathbf{v}_{E,p}^{GCRF} = -[{}^{GSE}\mathbf{R}^{GCRF}(t)]^T [{}^{GSE}\dot{\mathbf{R}}^{GCRF}(t)] [{}^{GSE}\mathbf{R}^{GCRF}(t)]^T \mathbf{r}_{E,p}^{GSE} + [{}^{GSE}\mathbf{R}^{EI}(t)]^T \mathbf{v}_{E,p}^{GSE} \quad (87)$$

which possesses a similar form as in the Sun-Earth rotating frame but with modifications outlined at the beginning of this subsection.

## 5 Numerically Generating Trajectories

This section summarizes methods used to numerically generate satellite trajectories. In the context of this document, a trajectory reflects the path a satellite (natural or human-made) follows in space over a specified time interval. The goal of this section is to present a high-level overview of commonly-used numerical approaches to computing trajectories and the associated challenges, with a focus on applicability to a satellite that is already in space and located within the lunar and cislunar regions. Hence, we will not discuss the generation of trajectories from the launch pad to the injection orbit.

### 5.1 Numerical Integration of the Equations of Motion

A common task in studying the motion of a spacecraft in cislunar space is solving the equations of motion numerically to closely approximate a true solution. These equations of motion govern the motion of a satellite experiencing an acceleration  $\mathbf{a}$  that captures the forces acting on it and, potentially, frame transformation terms. To solve the equations of motion numerically, information about the state, reflected by the position and velocity vectors  $\mathbf{r}$  and  $\mathbf{v}$ , at an initial time  $t_0$  is required, i.e.,  $\mathbf{r}(t_0) = \mathbf{r}_0$ , and  $\mathbf{v}(t_0) = \mathbf{v}_0$ . Then, the goal is to generate a solution to the following system of first-order differential equations that is associated with the specified set of initial conditions

$$\begin{aligned}\dot{\mathbf{r}}(t) &= \mathbf{v}(t) \\ \dot{\mathbf{v}}(t) &= \mathbf{a}(t, \mathbf{r}, \mathbf{v}) \\ \mathbf{r}(t_0) &= \mathbf{r}_0, \quad \mathbf{v}(t_0) = \mathbf{v}_0\end{aligned}\tag{88}$$

This problem is often labeled an Initial Value Problem (IVP), and the rest of this section focuses on numerical approaches to solving this problem. This section uses the following notation: given an IVP as in Eq. (88) for a state vector  $\mathbf{x}(t) = [\mathbf{r}(t), \mathbf{v}(t)]^T$ ,  $\mathbf{x}_k = \mathbf{x}(t_k)$  is the solution of the state vector at time  $t_k$ . With this definition, consider a general and compact representation of an IVP that is written as follows:

$$\begin{aligned}\dot{\mathbf{x}}(t) &= \mathbf{f}(t, \mathbf{x}) \\ \mathbf{x}(t_0) &= \mathbf{x}_0\end{aligned}\tag{89}$$

where  $\mathbf{x} \in \mathbb{R}^n$ , and  $\mathbf{f} : \mathbb{R} \times \mathbb{R}^n \rightarrow \mathbb{R}^n, n \geq 1$  is a smooth enough function.

#### 5.1.1 Euler Methods

When the time stepsize  $h_0 \in \mathbb{R}^+$  is small enough,  $\dot{\mathbf{x}}$  may be approximated (to first order) as:

$$\dot{\mathbf{x}}(t_0) \approx \frac{\mathbf{x}(t_0 + h_0) - \mathbf{x}(t_0)}{h_0}\tag{90}$$

Noting that  $\dot{\mathbf{x}} = \mathbf{f}(t, \mathbf{x})$ , defining  $t_1 = t_0 + h_0$ , and rearranging Eq. (90), the following expression for approximating  $\mathbf{x}_1 = \mathbf{x}(t_1)$  is obtained:

$$\mathbf{x}_1 = \mathbf{x}_0 + h_0 \mathbf{f}(t_0, \mathbf{x}_0)$$

Then, at the  $k$ -th step, the following expression is obtained for  $\mathbf{x}_{k+1}$ :

$$\mathbf{x}_{k+1} = \mathbf{x}_k + h_k \mathbf{f}(t_k, \mathbf{x}_k) \quad (91)$$

This general expression reveals that the state at a nearby, future time  $t_{k+1}$  may be approximated by updating the current state at  $t_k$  using the product of the time step size with the evaluation of the vector field  $\mathbf{f}(t_k, \mathbf{x}_k)$ ; this relationship is used to form a foundational numerical integration scheme for solving an IVP that is labeled the forward Euler method. The (local) error  $\epsilon_k(h) = \mathbf{x}_k(t_k) - \tilde{\mathbf{x}}(t_k)$ , where  $\tilde{\mathbf{x}}(t_k)$  is the actual state at time  $t_k$ , is  $\epsilon_k(h) \sim O(h^2)$  for this method. This mathematical expression means that for this particular numerical integration scheme, the error in the state approximation that it produces is on the order of the time step size squared. In general, if the error is  $\epsilon_k(h) \sim O(h^{p+1})$ , then the numerical integration method is labeled an order- $p$  method.

Other numerical integration schemes can be derived by approximating  $\dot{\mathbf{x}}$  in a different manner. For instance, an alternative approximation of the state derivative at a time  $t_k$  is written as:

$$\dot{\mathbf{x}}(t_k) \approx \frac{\mathbf{x}(t_k) - \mathbf{x}(t_k - h_k)}{h_k}$$

and, more generally at the  $(k + 1)$ -th step:

$$\mathbf{x}_{k+1} = \mathbf{x}_k + h_k \mathbf{f}(t_{k+1}, \mathbf{x}_{k+1}) \quad (92)$$

Unlike Eq. (91), the unknown state  $\mathbf{x}_{k+1}$  is calculated from the state at  $t_k$  by evaluating the vector field at the future time  $t_{k+1}$  with  $\mathbf{x}_{k+1}$ . Given that  $\mathbf{x}_{k+1}$  is the variable of interest, this method is labeled a backward or implicit Euler method and is usually solved by iteration.

### 5.1.2 Nomenclature

These two examples of distinct types of Euler methods support defining important concepts for describing numerical integration schemes that solve ordinary differential equations in general:

- 1) The stepsize  $h_k$  does not need to be constant at each step. Methods that maintain a constant stepsize are labeled fixed-stepsize methods, as opposed to variable-stepsize methods.
- 2) Methods that compute the state  $\mathbf{x}_{k+1}$  at time  $t_{k+1}$  as a function of only the previous state  $\mathbf{x}_k$  are called single-step

methods, whereas multiple-step methods compute  $\mathbf{x}_{k+1}$  as a function of multiple earlier  $\mathbf{x}_k, \dots, \mathbf{x}_{k-s}$  for  $s > 0$ .

- 3) In Eq. (91), the unknown state  $\mathbf{x}_{k+1}$  can be solved explicitly, meaning that it does not appear in the right side of the equation within a term such as  $f(\mathbf{x}_{k+1})$ . Methods with this property are called explicit methods. On the other hand, as in Eq. (92), the unknown state also appears in  $f(\mathbf{x}_{k+1})$  on the right hand side. Methods with this property are labeled implicit methods.

These three properties of numerical integration methods that solve ordinary differential equations supply a useful categorization scheme: fixed-stepsize vs. variable-stepsize, single-step vs. multiple-step, and explicit vs. implicit. In the following paragraphs, some of the most popular families of methods are presented.

### 5.1.3 Runge-Kutta Methods

The numerical integration schemes in the Runge-Kutta family are single-step and variable-stepsize methods that can be formulated as either explicit or implicit. This section summarizes the main principles of Runge-Kutta methods with a focus on explicit methods.

The classical explicit Runge-Kutta method computes the state at time  $t_{k+1} = t_k + h$  from a state  $\mathbf{x}_k$  at time  $t_k$  that is known to solve the IVP in Eq. (89) using an expression of the form (see [54]):

$$\mathbf{x}_{k+1} = \mathbf{x}_k + h \sum_{i=1}^s b_i \mathbf{k}_i = \mathbf{x}_k + h \Phi(t_k, \mathbf{x}_k; h) \quad (93)$$

where the integer  $s \geq 1$  is the number of stages of the method. These stages reflect the number of evaluations of the vector field  $f$  across the time interval from  $t_k$  to  $t_{k+1}$ , captured by the vectors  $\mathbf{k}_i$  as follows:

$$\begin{aligned} \mathbf{k}_1 &= f(t_k, \mathbf{x}_k) \\ \mathbf{k}_2 &= f(t_k + \alpha_2 h, \mathbf{x}_k + h \beta_{21} \mathbf{k}_1) \\ \mathbf{k}_3 &= f(t_k + \alpha_3 h, \mathbf{x}_k + h(\beta_{31} \mathbf{k}_1 + \beta_{32} \mathbf{k}_2)) \\ &\vdots \\ \mathbf{k}_s &= f(t_k + \alpha_s h, \mathbf{x}_k + h(\beta_{s1} \mathbf{k}_1 + \cdots + \beta_{s,s-1} \mathbf{k}_{s-1})) \end{aligned} \quad (94)$$

In Eqs. (93) and (94), the coefficients  $b_1, \dots, b_s, \alpha_2, \dots, \alpha_s, \beta_{ij}$ ,  $1 < i \leq s, 0 < j \leq s$  are real numbers. A convenient

way to display these coefficients is through the use of a Butcher table:

0					
$\alpha_2$	$\beta_{21}$	$\beta_{22}$			
$\vdots$	$\vdots$		$\dots$		
$\alpha_s$	$\beta_{s1}$	$\beta_{s2}$	$\dots$	$\beta_{s,s-1}$	
	$b_1$	$b_2$	$\dots$	$b_{s-1}$	$b_s$

Examples on how to determine these parameters for different stages appear in [55–57]; the following paragraphs present some examples.

As a first example, consider the Butcher table for  $s = 1$ :

0				
				1

which produces the forward Euler method because  $\Phi(t_k, \mathbf{x}_k; h) = f(t_k, \mathbf{x}_k)$ . Hence, the Euler method belongs to the Runge-Kutta family. Note that there is an important observation about the relationship between the order of the method ( $p$ ) and number of stages ( $s$ ): in general, given an order  $p$ ,  $s \geq p$ , and  $s \geq p + 1$  if  $p \geq 5$  (see [57]). Accordingly, it is not possible for a Runge-Kutta implementation to possess an order higher than the number of vector field evaluations. However, the higher the order, the more expensive the method is in terms of computational time.

An example of a fourth-order Runge-Kutta with four stages is described by the following Butcher table (see [57]):

0					
$\frac{1}{2}$		$\frac{1}{2}$			
$\frac{1}{2}$		0	$\frac{1}{2}$		
1	0	0	1		
	$\frac{1}{6}$	$\frac{1}{3}$	$\frac{1}{3}$	$\frac{1}{6}$	

Note that, given a fixed number of stages  $s$ , the coefficients that characterize a Runge-Kutta integrator are not unique.

Another example of a fourth-order Runge-Kutta with four stages is described by the following Butcher table (see [57]):

	0			
	$\frac{1}{2}$	$\frac{1}{4}$		
	$\frac{1}{2}$	0	$\frac{1}{2}$	
	1	1	-2	2
		$\frac{1}{6}$	0	$\frac{2}{3}$
				$\frac{1}{6}$

These are two examples of Butcher tables for fourth order Runge-Kutta methods, but of course there are higher order versions (see, for example, [56]). Typically, for astrodynamics applications, seventh order methods or higher are used if a Runge-Kutta method is employed.

Based on this foundation in defining Runge-Kutta methods, a natural question is to define which stepsize to use for every step. The next paragraphs describe the *Runge-Kutta-Felhberg* method, a member of the Runge-Kutta family that is very popular in the astrodynamics community in its higher order version due to its adaptive stepsize selection.

The Runge-Kutta-Felhberg method uses two Runge-Kutta instantiations, one of order  $p$ , and another of order  $p + 1$ . Together, these integration schemes are summarized as:

$$\begin{aligned}\tilde{\mathbf{x}}_{k+1} &= \mathbf{x}_k + h\Phi_1^p(t_k, \mathbf{x}_k, h) \\ \bar{\mathbf{x}}_{k+1} &= \mathbf{x}_k + h\Phi_2^{p+1}(t_k, \mathbf{x}_k, h)\end{aligned}$$

where  $\Phi_1^p(t_k, \mathbf{x}_k, h)$  (resp.  $\Phi_2^{p+1}(t_k, \mathbf{x}_k, h)$ ) corresponds to the  $p$ -order (resp.  $(p + 1)$ -order) Runge-Kutta scheme. See [57] for a discussion on how the coefficients that characterize  $\Phi_1^p$  and  $\Phi_2^{p+1}$  are selected to ensure that the evaluations of the vector field needed for  $\Phi_1^p$  can be reused for  $\Phi_2^{p+1}$ . With two approximations of the state that solve the IVP at  $t_k$ , given by  $\mathbf{x}_{k+1}^{p+1}$  and  $\mathbf{x}_{k+1}^p$ , stepsize control is performed using the difference between the two solutions,  $\delta(h) = \|\mathbf{x}_{k+1}^{p+1} - \mathbf{x}_{k+1}^p\|$ , and a user-defined tolerance  $\varepsilon > 0$ . If  $\delta(h) < \varepsilon$ , then the current stepsize value is used. If on the other hand,  $\delta(h) \geq \varepsilon$ , then the stepsize is adjusted via the following formula:

$$h_{new} = 0.9h \left( \frac{\varepsilon}{\delta(h)} \right)^{\frac{1}{p+1}} \quad (95)$$

where  $h_{new}$  is the updated stepsize, and 0.9 is a safety factor. This formula can also be used to increase the step size when the error is too small. See [54] for the derivation of Eq. (95).

### 5.1.4 Adams-Bashforth-Moulton Methods

This section discusses two families of multi-step methods: the Adams-Bashforth and Adams-Moulton methods. As discussed in Sec. 5.1, a multi-step method computes the state  $\mathbf{x}_{k+s} = \mathbf{x}(t_{k+s})$ ,  $s \geq 1$  of the IVP problem in Eq. (89) based on  $s$  previous known states  $\mathbf{x}_k, \mathbf{x}_{k+1}, \dots, \mathbf{x}_{k+s-1}$ . In this section, assume that all states are equidistant in time, i.e.,  $t_{k-i} - t_{k-i-1} = h$ ,  $i = 0, 1, \dots, s-1$  for a fixed stepsize.

In its general form, a multi-step method predicts the state  $\mathbf{x}_{k+s}$  as follows:

$$\mathbf{x}_{k+s} = \mathbf{x}_{k+s-1} + h \sum_{i=0}^s \beta_i f(t_{k+i}, \mathbf{x}_{k+i}) \quad (96)$$

where

$$\beta_i = \int_0^1 \prod_{j=0, j \neq i}^s \frac{r - (s-j-1)}{i-j} dr \quad (97)$$

The formulae for the coefficients  $\beta_i$ ,  $i = 0, 1, \dots, s$  in Eq. (97) are based on the Lagrange interpolation formula. (See [54, 58] for a complete derivation of the method.) Consider the particular case where  $\beta_s = 0$  and  $\beta_0 \neq 0$ . In this case, the method is explicit, meaning that the unknown  $\mathbf{x}_{k+s}$  does not appear on the right side of Equation (96). This implementation is known as the Adams-Bashforth method. On the other hand, if  $\beta_s \neq 0$  and  $\beta_0 = 0$ , the method is implicit, and leads to the Adams-Moulton method. As an example, the  $\beta$ -coefficients for  $s = 4$  are presented in Table 1 (see [58].)

	Adams-Bashforth	Adams-Moulton
$\beta_0$	$\frac{55}{24}$	—
$\beta_1$	$-\frac{59}{24}$	$\frac{9}{24}$
$\beta_2$	$\frac{37}{24}$	$\frac{19}{24}$
$\beta_3$	$-\frac{9}{24}$	$-\frac{5}{24}$
$\beta_4$	—	$\frac{1}{24}$

**Table 1**  $\beta$ -coefficients for the Adams-Bashforth and Adams-Moulton formulae for  $s = 4$

For implicit methods, a natural question is how to solve these expressions given that the unknown cannot be explicitly isolated. Typically these equations are solved by means of an iterative scheme, which at the  $j$ -th update, is expressed as:

$$\mathbf{x}_{k+s}^{(j+1)} = \mathbf{x}_{k+s-1}^{(j)} + \beta_s f(t_{k+s}^{(j)}, \mathbf{x}_{k+s}^{(j)}) + h \sum_{i=0}^{s-1} \beta_i f(t_{k+i}, \mathbf{x}_{k+i}) \quad (98)$$

for  $j=0, 1, 2, \dots$ . There are two notable considerations for implementing the iterative scheme described by this expression: how to initialize the iteration, and when to stop iterating. The initial guess is required to be good enough to ensure convergence. This initial guess, or prediction, is formed using the Adams-Bashforth explicit method. With this initial guess, the implicit Adams-Moulton corrects the prediction by applying the iteration scheme in Eq. (98). The correction

process terminates when the state difference between two consecutive iterations is below a user-defined threshold, usually after one or two iterations. Such a scheme is often labeled a predictor-corrector method. Finally, it is worth noting that the requirement of a fixed step-size can be relaxed. See [58] for an example of a fourth-order predictor-corrector multistep method with variable step-size derived from the classical Adams-Basforth and Adams-Moulton formulae.

### 5.1.5 Other Methods

The numerical integration schemes described in Sec. 5.1.3 and 5.1.4 are amongst the most popular methods used in astrodynamics. For example, popular tools for mission design such as GMAT, FreeFlyer, and STK offer all or some of these methods in their standard set of integrators while allowing the user to select the absolute and/or relative tolerances that govern variable stepsize schemes. There are, however, other families of methods that are worth briefly summarizing: the Taylor method, and symplectic integrators.

#### The Taylor Method

Consider the IVP in Eq. (89) and a solution at time  $t_k$ ,  $\mathbf{x}_k = \mathbf{x}(t_k)$ . Fixing a stepsize  $h$  such that  $t_{k+1} = t_k + h$ , the state  $\mathbf{x}_{k+1} = \mathbf{x}(t_{k+1}) = \mathbf{x}(t_k + h)$  can be approximated by its Taylor series around  $t_k$  as:

$$\mathbf{x}_{k+1} = \mathbf{x}(t_k + h) = \mathbf{x}(t_k) + h \left. \frac{d\mathbf{x}}{dt} \right|_{t=t_k} + \frac{h^2}{2} \left. \frac{d^2\mathbf{x}}{dt^2} \right|_{t=t_k} + \cdots + \frac{h^p}{p!} \left. \frac{d^p\mathbf{x}}{dt^p} \right|_{t=t_k}$$

where, by definition:

$$\begin{aligned} \left. \frac{d\mathbf{x}}{dt} \right|_{t=t_k} &= \mathbf{f}(t_k, \mathbf{x}_k) \\ \left. \frac{d^2\mathbf{x}}{dt^2} \right|_{t=t_k} &= \left. \frac{\partial \mathbf{f}}{\partial \mathbf{x}} \right|_{t=t_k} \mathbf{f}(t_k, \mathbf{x}_k) + \left. \frac{\partial \mathbf{f}}{\partial t} \right|_{t=t_k} \end{aligned}$$

These definitions can be continued until order  $p$ . Note that to construct high-order Taylor integrators, high-order derivatives of  $\mathbf{f}$  are required; however, their computation may not be practical. This limitation may be overcome by using automatic differentiation. Details on how to implement automatic differentiation are out of the scope of this document, but an introduction and links to a publicly available software package appears in [59]. Although automatic differentiation mitigates the challenges of calculating higher-order derivatives, only functions that belong to a special class can benefit from this advantage. Many functions that appear in the mathematical models used in astrodynamics (e.g., the two-body problem, or the circular restricted three body problem) belong to this class. However, when the models use, for example, functions reflecting gravitational acceleration or interpolate ephemeris states, using automatic differentiation in a Taylor method is not useful. This is usually the case for practical mission design.

#### Symplectic Integrators

Symplectic integrators are a family of methods used exclusively in the context of Hamiltonian dynamical systems. These dynamical systems are relevant because a lot of the models considered in astrodynamics and celestial mechanics

(e.g., the  $n$ -body problem, or the circular restricted three body problem) can be formulated under the Hamiltonian formalism. The detailed description of Hamiltonian systems and their properties is out of the scope of this document. The interested reader is referred to [60] for a introduction on Hamiltonian systems and their application to celestial mechanics. However, the main property exploited in the symplectic integrators is the fact that the flow  $\phi$  of a Hamiltonian system preserves the symplectic structure of the phase space (see [60]). In the language of Hamiltonian mechanics, this means that the flow defines a *canonical transformation*. In other words: the flow  $\phi$  defines a coordinate change that preserves the Hamiltonian structure. Hence, the idea behind the symplectic integrators is to find a numerical solution to a Hamiltonian system that is a symplectic transformation for sufficiently small stepsizes.

This type of integrator is used in celestial mechanics for long-term integrations. However, they are limited in application to Hamiltonian systems. Models used in practical mission design usually consider non-conservative forces, hence they do not fall under the umbrella of the Hamiltonian systems and symplectic integrators are not useful. References [61, 62] provide good introduction to this family of integrators.

## 5.2 Solving Two-Point Boundary Value Problems

A common problem in astrodynamics is solving a Two-Point Boundary Value Problem (TPBVP). Solving a TPBVP involves calculating a solution to the equations of motion,  $\dot{\mathbf{x}} = \mathbf{f}(t, \mathbf{x})$ , over a time interval  $[t_0, t_f]$  given a set of boundary conditions  $\mathbf{G}(\mathbf{x}_0, \mathbf{x}_f) = \mathbf{0}$  that are a function of information at the beginning and/or end of the time interval [63]. Such a problem is encountered, for example, in the preliminary design of a spacecraft trajectory from one position vector to another in cislunar space. While the equations of motion may be known, a trajectory that connects these two position vectors may not be known. In this example, the goal is to find the initial velocity vector and, potentially the flight time, that produces a trajectory connecting these two position vectors (if such a trajectory exists). When there are multiple solutions that satisfy this TPBVP, an analyst may be interested in generating either an array of solutions or one solution that also minimizes or maximizes a specified objective function. This subsection presents an overview of shooting methods and collocation, each used to solve a TPBVP. Then, well-known continuation schemes that are used to generate an array of solutions are presented, followed by a brief overview of constrained optimization.

### 5.2.1 Shooting Methods

Shooting methods recast the process for solving a TPBVP into an initial value problem by focusing on identifying a state at the beginning of the time interval that, when propagated using the equations of motion over the time interval of interest, satisfy the specified boundary conditions [63]. This approach is useful in recovering either natural trajectories or those that use impulsive or continuous control. There are two fundamental types of shooting methods: single-shooting and multiple-shooting.

In a single-shooting method, displayed conceptually in Fig. 13 a), a trajectory is represented by a single arc across

the time interval  $[t_0, t_f]$  and described by its initial state  $\mathbf{x}(t_0)$ . An initial guess for the initial state  $\mathbf{x}(t_0)$  might produce the black arc in Fig. 13 a) over an integration time  $t_f - t_0$ . However, consider a scenario where a trajectory is sought that satisfies boundary conditions such as possessing a state at the end of the arc equal to  $\mathbf{x}_{des}(t_f)$ ; the trajectory that satisfies this constraint is displayed in blue. Then, in a single-shooting scheme, the initial state and/or integration time of the arc are updated from the black initial guess until they produce a trajectory that is sufficiently close to the blue arc.

Multiple-shooting, however, discretizes a trajectory into multiple sequential arcs spanning smaller time intervals within  $[t_0, t_f]$  [64]. A conceptual representation of a multiple-shooting approach appears in Fig. 13 b) with an initial guess for the trajectory comprised of multiple, potentially discontinuous arcs, in black. The  $i$ -th arc along the trajectory is then described by the initial state  $\mathbf{x}_{i,0}$ , the integration time  $\Delta t_i$ , and/or any other parameters necessary to uniquely specify the arc. The solution of interest may, however, need to satisfy constraints at the boundaries of the larger time interval, such as possessing a desired state at the end of the arc equal to  $\mathbf{x}_{des}(t_f)$ . Due to the discretization of the trajectory, continuity constraints must also be satisfied between neighboring arcs that comprise the larger trajectory. For a natural trajectory, such a continuity constraints may be described as follows: the state  $\mathbf{x}_{i,f}$  at the end of the  $i$ -th arc must equal the state  $\mathbf{x}_{i+1,0}$  at the beginning of the  $i + 1$ -th arc. This desired solution, satisfying the continuity constraints and boundary condition, is displayed in blue. In a multiple-shooting scheme, the initial states, integration times, and any additional parameters describing all of the arcs are simultaneously updated until satisfying all of the boundary, continuity and additional constraints to within a specified tolerance. The resulting solution then lies sufficiently close to the desired solution over the interval  $[t_0, t_f]$ . Although single-shooting usually supports a simpler problem specification and implementation, multiple-shooting often reduces the sensitivity associated with iteratively adjusting the free variable vector to produce shorter arcs that together form a trajectory in a complex, nonlinear dynamical system.

One approach to implementing a shooting method to solve a TPBVP involves converting it into a vectorial root-finding problem through the definition of a free variable vector,  $\mathbf{V}$ , and a constraint vector,  $\mathbf{F}(\mathbf{V})$  [54]. The  $(n \times 1)$ -dimensional free variable vector reflects the  $n$  problem variables such as the initial state and integration time and is defined as:

$$\mathbf{V} = [V_1, V_2, \dots, V_{n-1}, V_n]^T \quad (99)$$

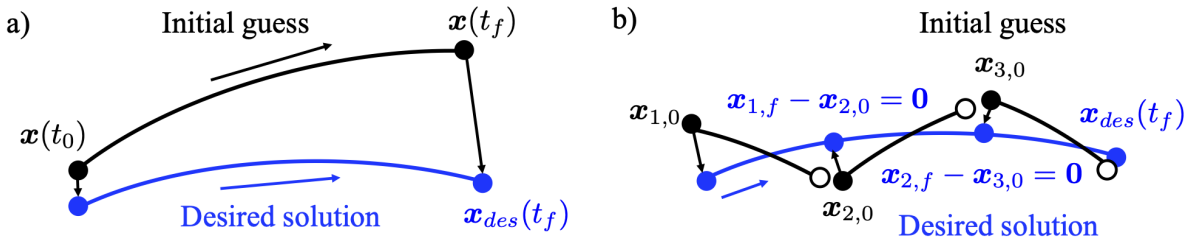


**Fig. 13** Conceptual representation of a) single-shooting and b) multiple-shooting approaches to compute solutions to a two-point boundary value problem.

where  $V_i$  is the  $i$ -th free variable in the problem. Next, an  $(m \times 1)$ -dimensional constraint vector captures the boundary conditions and any other constraints that the trajectory must satisfy. The constraint vector, which is a function of the free variable vector, is defined as:

$$\mathbf{F}(\mathbf{V}) = [F_1, F_2, \dots, F_{m-1}, F_m]^T \quad (100)$$

where  $F_j$  is the  $j$ -th scalar constraint, expressed as a function of the free variables to equal 0 when satisfied. Then, the goal in a shooting method is to calculate the free variable vector  $\mathbf{V}_d$  producing  $\mathbf{F}(\mathbf{V}_d) = \mathbf{0}$  to within a specified tolerance. However, in a nonlinear dynamical model, the relationship between the two vectors may be quite complex, meaning that identifying a solution to such a problem is often nontrivial. Thus, iterative numerical procedures are often used to gradually adjust a guess for the free variable vector until it sufficiently satisfies the constraints.

In one approach to identifying a solution that satisfies the constraints, the free variable vector is iteratively updated from an initial guess using a multivariate Newton's method. Assuming that the initial guess for the free variable vector,  $\mathbf{V}_0$ , lies sufficiently close to  $\mathbf{V}_d$ , a first-order Taylor series expression approximates the relationship between these two vectors as:

$$\mathbf{0} \approx \mathbf{F}(\mathbf{V}_0) + [\mathbf{DF}(\mathbf{V}_0)] (\mathbf{V}_d - \mathbf{V}_0) \quad (101)$$

where  $[\mathbf{DF}(\mathbf{V})]$  is the  $(m \times n)$  Jacobian matrix composed of the partial derivatives of each constraint with respect to each free variable [54]:

$$[\mathbf{DF}(\mathbf{V})] = \frac{\partial \mathbf{F}(\mathbf{V})}{\partial \mathbf{V}} = \begin{bmatrix} \frac{\partial F_1}{\partial V_1} & \dots & \frac{\partial F_1}{\partial V_n} \\ \vdots & \dots & \vdots \\ \frac{\partial F_m}{\partial V_1} & \dots & \frac{\partial F_m}{\partial V_n} \end{bmatrix} \quad (102)$$

The individual partial derivatives of  $[\mathbf{DF}(\mathbf{V})]$  may be computed using analytical expressions, finite-difference approximations or automatic differentiation. This relationship between the initial guess and desired solution to the TPBVP is generalized to produce an update equation that is used at the  $i$ -th iteration to update the current guess for the free variable vector with the goal of bringing the guess gradually closer to an unknown solution that is assumed to be located nearby. If there are more free variables than independent constraints (i.e.,  $m < n$ ), the update equation at the  $i$ -th iteration is commonly written using a minimum-norm formulation as

$$\mathbf{V}_{i+1} = \mathbf{V}_i - [\mathbf{DF}(\mathbf{V}_i)]^T \left( [\mathbf{DF}(\mathbf{V}_i)][\mathbf{DF}(\mathbf{V}_i)]^T \right)^{-1} \mathbf{F}(\mathbf{V}_i) \quad (103)$$

If the number of independent constraints equals the number of free variables (i.e.  $m = n$ ), the update equation at the  $i$ -th iteration is written in a simpler form

$$\mathbf{V}_{i+1} = \mathbf{V}_i - [\mathbf{DF}(\mathbf{V}_i)]^{-1} \mathbf{F}(\mathbf{V}_i) \quad (104)$$

One of these update equations is then applied to iteratively update the initial guess for the free variable vector until either  $\|F(V_i)\| = 0$  to within a desired tolerance or any additional termination criteria are satisfied.

### Implementation Note

Given this formulation of a shooting method to leverage a multi-variate Newton's method, conditions that are required for quadratic convergence to a solution include [65]:

- 1) The initial guess for the free variable vector lies ‘sufficiently’ close to the actual solution,  $V_d$ , that satisfies the constraints and produces  $F(V_d) = \mathbf{0}$  to within a specified tolerance.
- 2) The Jacobian matrix of the constraint vector with respect to the free variable vector is always full-rank.
- 3) The constraint vector is a continuous function of the free variable vector.

As a result, the performance and success of shooting methods in recovering solutions to a TPBVP depends on the initial guess for the free variable vector and the problem formulation. When designing trajectories that satisfy a desired set of boundary conditions in cislunar space, constructing an initial guess that lies ‘sufficiently’ close to a true solution that is not known a priori is sometimes a significant challenge. In some cases, it also challenging to define a suitable problem formulation that does not unnecessarily overconstrain the trajectory.

## 5.2.2 Collocation

Collocation is another technique for identifying a solution to a TPBVP and relies on translating a TPBVP into a nonlinear programming (NLP) problem via transcription. To describe the result of the transcription process, consider the problem of recovering a controlled trajectory that uses a continuous acceleration at all instants of time. Note, however, similar problems can be constructed to recover natural trajectories or trajectories with impulsive maneuvers. Collocation then uses polynomial approximations of multiple arcs along a solution that satisfies the equations of motion as well as the boundary constraints  $G(x_0, x_f) = \mathbf{0}$  and any additional path equality/inequality constraints. In this problem, the free variable vector  $X \in \mathbb{R}^N$  contains all the states, controls and any other parameters necessary for fully specifying motion in the dynamical model of interest for a set of  $M$  instants of time  $t_i, i = 1, \dots, M$  where  $t_0 \leq t_1 < t_2 < \dots < t_M = t_f$ . Hence, if we define the states as  $x_i = x(t_i) \in \mathbb{R}^n, i = 1, \dots, M$ , the control vectors as  $u_i = u(t_i) \in \mathbb{R}^m, i = 1, \dots, M$ , and fix the instants of time at which these states and controls apply, the free variable vector becomes  $X^T = [x_0^T, \dots, x_M^T, u_0^T, \dots, u_M^T] \in \mathbb{R}^N$ , and  $N = M \times (m + n)$ .

The first step of transcription is to divide a trajectory into phases. Using different phases enables the definition of different dynamics, state representations, coordinate frames, etc, in each phase. Hence, the use of phases to break down the trajectory provides a framework for combining problems that span a variety of regimes or descriptions into a single TPBVP. For example, in the case of a lunar mission, the trajectory could be divided in three phases: launch and early orbit, transfer trajectory, and lunar insertion. For the sake of providing a brief overview, this section will assume one

phase, and explain how to rewrite a TPBVP as a NLP problem.

A phase is first discretized into  $M$  segments,  $S_1, S_2, \dots, S_M$  defined as  $S_i = [t_{i-1}, t_i], i = 1, \dots, M$ . The boundaries of the segments,  $t_{i-1}, t_i, i = 1, \dots, M$ , are called the nodes. Note that in the case where there is more than one phase, two adjacent phases share one node. By imposing specific conditions on those nodes, the transition between phases can be smooth. Next, in each segment  $S_i$ , both the state and the control components are approximated by polynomials of a pre-defined degree  $d$ . In other words, if  $\xi^i$  is an arbitrary component of the state or control vector in the segment  $S_i$ , its polynomial approximation is written as  $\xi^i = a_0^i + a_1^i s + \dots + a_d^i s^d, s \in S_i, i = 1, \dots, M$ . Accordingly, the problem of calculating time-dependent functions  $\mathbf{x}$  and  $\mathbf{u}$  is reduced to finding the polynomial coefficients that approximate each of their components. As a result, approximations of  $\mathbf{x}(t)$  and  $\mathbf{u}(t)$  are fully characterized by a finite number of coefficients. This means not having to solve for functions that, in general, will not have closed analytical expressions.

The next step in the transcription process is to define the conditions on points in a segment to ensure that the dynamics are captured. This procedure requires, first, an initial guess of the solution. Consider a collocation problem that uses  $d = 3$ , i.e., approximating the components of the state and control vectors with cubic polynomials. For the sake of simplifying the notation, and without loss of generality, time is normalized to produce boundary conditions such that  $t_0 = 0$ , and  $t_M = 1$ , i.e., time along the segment spans the unit interval  $[0, 1]$ . From here on, the superscript  $i$  is dropped from  $\xi^i$  for conciseness, and simply represents an arbitrary component of the state or control vector. Then, nodes are defined along the unit interval  $s_0 = 0, s_1 = 1$  by imposing the following conditions:

$$\begin{aligned} \xi(0) &= a_0 = \xi_0 \\ \frac{d\xi}{ds}|_{s=0} &= a_1 = \xi'_0 \\ \xi(1) &= a_0 + a_1 + a_2 + a_3 = \xi_1 \\ \frac{d\xi}{ds}|_{s=1} &= a_1 + 2a_2 + 3a_3 = \xi'_1 \end{aligned} \tag{105}$$

where  $\xi_0, \xi'_0, \xi_1, \xi'_1$  are specified, initially, by the initial guess. Note that Eq. (105) defines a system of linear equations that can be solved to obtain the coefficients  $a_0, \dots, a_3$ . Hence,  $\xi$  is generated via the cubic polynomial that is calculated based on the values of the points  $\xi_0, \xi'_0, \xi_1, \xi'_1$ :

$$\tilde{\xi}(s) = a_0 + a_1 s + a_2 s^2 + a_3 s^3, s \in [0, 1]$$

This approach is completed for all the components of the state and control vectors, producing the state and control vectors  $\tilde{\mathbf{x}}(s), \tilde{\mathbf{u}}(s), s \in [0, 1]$ .

The state description enables measurement of how this approximation compares to the actual solution to the dynamics by incorporating knowledge about how the system evolves with respect to time, i.e., via the equations of

motion. Consider the state vector and the control vector at  $s_{\frac{1}{2}} = 1/2$ , i.e.,  $\tilde{\mathbf{x}}(s_{\frac{1}{2}})$  and  $\tilde{\mathbf{u}}(s_{\frac{1}{2}})$ . The polynomial expression for the state vector also enables calculation of the approximation of the state derivative: taking the derivative of the polynomial expression for the state vector with respect to time and evaluating the resulting polynomial description for the state derivative at  $s_{\frac{1}{2}} = 1/2$  produces  $\tilde{\mathbf{x}}'(s_{\frac{1}{2}})$ . Next, the equations of motion are evaluated using the state approximation at the center of the segment, producing the vector  $f_\xi$  for component  $\xi$ :  $f_\xi = f(\tilde{\mathbf{x}}(s_{\frac{1}{2}}), \tilde{\mathbf{u}}(s_{\frac{1}{2}}))|_\xi$ . This quantity is used to define the quantity  $\Delta_\xi = f_\xi - \tilde{\mathbf{x}}'(\frac{1}{2})$  which estimates the error in capturing the dynamics at the center of the segment induced through the polynomial approximation. This quantity is often labeled the defect at  $s_{\frac{1}{2}}$ . To produce an approximation of a solution to the equations of motion, collocation requires the constraint that  $\Delta_\xi = 0$ . Note that the previous discussion can be generalized to states and controls approximated using polynomials of odd degree  $d = 2k + 1, k \in \mathbb{N}$ . In that general case, the collocation problem relies on information at  $k$  instants of time to calculate the polynomial coefficient and  $k - 1$  defect points to apply the defect constraints. Figure 14 provides a visual representation of the relationship between the estimated component  $\xi$  and the dynamical model defined by  $f_\xi$ .

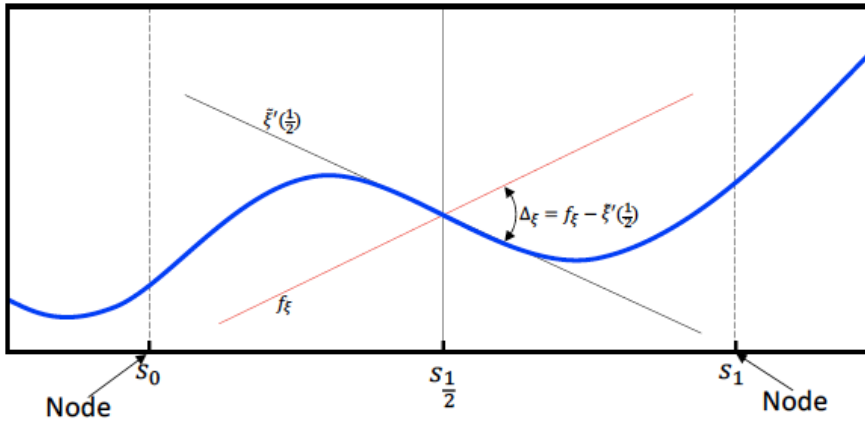


**Fig. 14** Visual representation of the interplay between the estimated components and dynamical model. (Figure inspired by [70].)

Based on this brief summary in the context of a single phase, an NLP problem may be formally stated. The goal in a collocation approach to solving a TPBVP is to solve for the free variable vector  $X^T = [\mathbf{x}_0^T, \dots, \mathbf{x}_M^T, \mathbf{u}_0^T, \dots, \mathbf{u}_M^T] \in \mathbb{R}^N$  that satisfies the constraints  $h_j(X) = \Delta_{x_j} = (\Delta_{x_{j,0}}, \dots, \Delta_{x_{j,n}}) = 0, j = 0, \dots, M$  along with the boundary conditions  $\mathbf{G}(\mathbf{x}_0, \mathbf{x}_f) = \mathbf{0}$  and any additional path constraints. This problem is typically solved by iteratively refining an initial guess until the constraints are met through techniques such as Newton's method.

### 5.2.3 Continuation

In some cases, solutions to a TPBVP are not unique and, rather, exist in continuous families. Such a scenario is commonly encountered when calculating trajectories with various flight times between two position vectors or

families of fundamental solutions that exist in an autonomous dynamical model. Solutions that exist within continuous families may be computed efficiently from other known solutions along the same family using numerical continuation methods. Two continuation schemes that are commonly used in astrodynamics are natural parameter continuation and pseudo-arclength continuation. These continuation schemes are used in the same fundamental structure: given a known solution, new solutions are predicted and then corrected via techniques such as shooting methods or collocation to solve a particular TPBVP while also satisfying the constraints imposed on the difference between the known and new solution. This procedure is applied repeatedly until a desired number of solutions along the family are calculated, the family is completely traversed, or some other termination criteria are satisfied. However, the two continuation schemes differ in their approaches to predicting the description of a new solution that lies near the known solution as well as constraining some properties of that solution to effectively step along the family.

In natural parameter continuation, a new solution along a family is computed from a single, known solution by incrementally calculating solutions that possess a desired change in a single parameter [66]. In trajectory design, such parameters for continuation may be related to state information, time, energy or other characteristics. To summarize this process consider a value of a selected parameter,  $p_{j-1}$ , evaluated along at the  $j - 1$ -th known solution within this family. At the  $j$ -th step of the continuation process, the goal is to calculate a nearby solution along the family that possesses a value of that same parameter equal to:

$$p_j = p_{j-1} + \Delta p \quad (106)$$

where  $p_j$  is the desired value of the parameter evaluated along the new solution and  $\Delta p$  is a sufficiently small step along parameter to ensure convergence of the TPBVP solver to recover a new solution [66]. The desired parameter value is typically included in the formulation of the TPBVP via the addition of the equality constraint  $p_j - (p_{j-1} + \Delta p) = 0$ . Although this approach is relatively straightforward to implement, natural parameter continuation is known to fail at turning points in the natural parameter space, i.e., when a solution along the family possessing a parameter of  $p_{j-1} + \Delta p$  no longer exists nearby; in this case, a smaller  $\Delta p$  or a different natural parameter may be manually selected to continue along the family. For this reason, a priori knowledge of the solution space of the orbit family is helpful for selection of a useful natural parameter and step direction.

In pseudo-arclength continuation, the local gradient of the solution curve is used to predict and identify a nearby member of the family [66]. As a result, this particular continuation method tends to succeed in computing members along a family that possess turning points along the solution curve in a natural parameter space [67]. At each step of pseudo-arclength continuation, a small step is taken along the tangent to the solution curve, evaluated at the location of a known solution, to predict a nearby solution along the family. A corrections scheme, such as a shooting method or collocation, is then applied to solve the TPBVP using this prediction as an initial guess. However, often during corrections, a solution is sought that simultaneously satisfies the constraints of the TPBVP as well as an additional

constraint: the projection of the difference between the known and new solution onto the approximated tangent to the family is equal to a desired step size. When computing the  $j$ -th member of the family, this scalar constraint is expressed mathematically as

$$(\mathbf{V}_j - \mathbf{V}_{j-1})^T \mathbf{n}_j - \Delta s = 0 \quad (107)$$

where  $\mathbf{V}_j$  reflects the variables describing the  $j$ -th solution,  $\mathbf{V}_{j-1}$  reflects the variables describing the known  $j-1$ -th solution,  $\mathbf{n}_j$  is a unit vector that is tangent to the family at the location of the  $j-1$ -th solution and pointed in the desired direction for continuation, and  $\Delta s$  is the stepsize. Of course, an important step in implementing this procedure is calculating the tangent to the solution curve. In a free variable and constraint formulation of a shooting method or collocation, this tangent direction may be evaluated using the nullspace of a matrix that reflects the sensitivity of the constraints to the free variables, e.g.,  $D\mathbf{F}(\mathbf{V}_{j-1})$ . This process is repeated to compute each new solution along the family. When using pseudo-arc length continuation, the step size is typically selected to balance taking small enough steps to ensure new solutions may be corrected to lie within the same family as the known solution with taking large enough steps to limit the number of continuation steps needed to generate solutions along a family. Advanced implementations of pseudo-arc length continuation often include an adaptive stepsize, reducing the step size near regions of the family that are sensitive and increasing the step size in regions where the gradient of the solution curve is sufficiently close to linear.

#### 5.2.4 Optimal Trajectories

In scenarios where multiple solutions to a TPBVP exist, one or more of those solutions may be locally optimal solutions that minimize or maximize a desired objective. In trajectory design applications, such solutions may minimize propellant mass usage, minimize the transfer time or, as a result of their trajectory, maximize observation of a specific region in the configuration space. Although optimal trajectories may be natural or controlled, this overview will focus on controlled trajectories for the sake of generality. Under this assumption, an optimal control problem may be formulated using the following definitions [68]: let  $\mathbf{x}(t) \in \mathbb{R}^n$  be a trajectory,  $\mathbf{u}(t) \in \mathbb{R}^m$  a control vector, and  $\mathbf{p} \in \mathbb{R}^p$  a constant vector of parameters. The goal in an optimal control problem is to determine a trajectory  $\mathbf{x}(t)$  over the time interval  $[t_0, t_f]$  as well as the associated control vector  $\mathbf{u}(t)$  that minimizes the following objective function

$$J = \Psi(\mathbf{x}(t_0), t_0, \mathbf{x}(t_f), t_f; \mathbf{p}) + \int_{t_0}^{t_f} \mathcal{L}(\mathbf{x}(t), \mathbf{u}(t), t; \mathbf{p}) dt \quad (108)$$

where  $\Psi$  is the cost at the beginning and the end of the time interval, and the integral expression is the cost over the trajectory characterized by the function  $\mathcal{L}$ . The solution  $\mathbf{x}(t)$  also satisfies the equations of motion:

$$\dot{\mathbf{x}}(t) = f(\mathbf{x}(t), \mathbf{u}(t), \mathbf{p}) \quad (109)$$

while subject to a set of equality and inequality constraints at the boundaries and/or along the path:

$$\mathbf{G}(\mathbf{x}(t), \mathbf{u}(t), \mathbf{p}) = \mathbf{0} \quad \mathbf{H}(\mathbf{x}(t), \mathbf{u}(t), \mathbf{p}) \leq 0 \quad (110)$$

This problem is often labeled a constrained optimization problem and multiple solutions may potentially exist.

The current state of the art in solving optimal control problems includes approaches that may be divided into three categories: indirect methods, direct methods, and global optimization methods. Indirect methods are based on variational techniques to find the necessary conditions (Euler-Lagrange equations and Pontryagin's maximum principle) that produce values of  $\mathbf{x}(t)$ ,  $t_0$ ,  $\mathbf{u}(t)$ , and  $t_f$  corresponding to a local minimum. This approach formulates the problem analytically, and it is typically solved numerically. This approach often requires initial guesses for co-states, which are non-intuitive parameters to select. On the other hand, direct methods discretize the original problem so it is transcribed to an NLP problem. Once the problem is formulated as a NLP, it is then solved using optimization techniques. Finally, global optimization methods are algorithms designed to find global minimum. The survey papers [68–71] discuss each of these families of methods in detail along with their advantages and disadvantages.

## 6 Preliminary Modeling of Cislunar Space and Definitions

Spacecraft operating in cislunar space are significantly influenced by a wide variety of forces, including, but not limited to: the irregular gravitational fields of the Earth and Moon, the gravitational influence of the Sun and other celestial bodies throughout the solar system, solar radiation pressure, and relativistic effects. Analyzing the structure of the cislunar dynamical environment when incorporating all of these force contributions is challenging, numerically intensive, and limits the discovery of fundamental insights into the solution space. Rather, NASA and the astrodynamics community often uses an approximate dynamical model labeled the circular restricted three-body problem (CR3BP) for a preliminary exploration of cislunar space and construction of an initial guess prior to higher-fidelity analyses. This dynamical model seeds much of the terminology used to describe regions of cislunar space and fundamental motions. This section presents a brief summary with the goal of supplying a high level understanding of the foundational theoretical insights derived from this low-fidelity model of cislunar space; references to more detailed discussions are provided throughout the text for the interested reader.

### 6.1 Fundamental Assumptions

The circular restricted three-body problem relies on the use of the following fundamental assumptions [72]:

- Only two primary bodies (the Earth and Moon) are modeled as point masses gravitationally interacting with an object such as a spacecraft or small celestial body. Modeling the motion of the spacecraft under the influence of only the Earth and Moon contributes to the ‘three-body problem’ component of the CR3BP name. Of course, this assumption neglects the gravitational influence of the Sun, which may significantly impact the path of the spacecraft and required maneuvers.
- The spacecraft is assumed to possess a negligible mass relative to the Earth and Moon, contributing the term ‘restricted’ to the CR3BP name. The mass of the Earth is  $\tilde{M}_1 \approx 5.97 \times 10^{24}$  kg and the mass of the Moon is  $\tilde{M}_2 \approx 7.35 \times 10^{22}$  kg [6]; thus, this assumption is reasonable subject to current spacecraft technology standards. Due to this assumption, the Earth and Moon are modeled as an isolated two-body problem.
- The Earth and Moon travel on circular orbits around their mutual barycenter, contributing the term ‘circular’ to the CR3BP name. This assumption is crucial for simplifying visualization and analysis while also removing an explicit time dependency from the dynamics. Given that the eccentricity of the Moon’s orbit relative to the Earth is approximately 0.055 [6], this assumption is a reasonable, but not perfect, starting point. In fact, for a semi-major axis of 384,400 km, the distance of the Moon from the Earth when modeled using an elliptical orbit in the two-body problem, varies by approximately 42,284 km. Such variance between the actual path of the Moon and its assumed circular orbit relative to the Earth may impact the identification of some trajectories in a high-fidelity model with a similar geometry to those that exist in the CR3BP, particularly trajectories with a close passage of the Moon.

A medium fidelity dynamical model that incorporates the eccentricity of the Moon's orbit is the elliptic restricted three-body problem (ER3BP) [72]. Another medium fidelity dynamical model that incorporates the Sun's gravity is the bicircular restricted four-body problem (BC4BP). However, both of these models are time-dependent, which significantly increases the complexity of analysis. Fortunately, many of the fundamental solutions and insights into the solution space gained via analysis of the CR3BP offer a sufficient starting point for analysis in higher-fidelity models of cislunar space either with or without maneuvers. Thus, it is from this approximate model that many fundamental definitions and concepts emerge, and that astrodynamicists and trajectory designers often begin their design process.

## 6.2 Nondimensionalization Scheme

In the astrodynamics community, it is common to use nondimensionalized state vectors and system parameters. This nondimensionalization reduces the potential for poor conditioning between quantities of distinct orders of magnitude as well as the comparison between systems where the primary bodies have a similar relative mass. The constants used to normalize length, mass and time quantities are labeled characteristic quantities and are typically designated as follows:

- $l^*$ : set equal to an assumed constant distance between the Earth and Moon, used to normalize length quantities.
- $m^*$ : set equal to the sum of the masses of the Earth and Moon, used to normalize mass quantities.
- $t^*$ : produces a mean motion for the Earth and Moon that is equal to unity and is calculated as:

$$t^* = \left( \frac{(l^*)^3}{\tilde{G}m^*} \right)^{1/2}$$

where  $\tilde{G}$  is the universal gravitational constant.

When this normalization is performed, a mass ratio is defined as  $\mu = \tilde{M}_2/(\tilde{M}_1 + \tilde{M}_2)$  and influences the solution space.

### Implementation Note

When studying the solution space derived from the CR3BP or recovering nearby geometrically-similar trajectories in an ephemeris model, the values of the characteristic quantities may influence the analysis. Accordingly, these parameters should be reported whenever nondimensionalization influences the analysis, as well as their source. An example set of values for each of these quantities appears in Table 2. The mass values are calculated using gravitational parameters in the DE421 SPICE ephemerides and used in GMAT [13, 73]. The length value is calculated as the average semi-major axis of the Moon's orbit. Note that in a chaotic dynamical model, reporting these quantities and state vector components to 15 significant figures is common.

Parameter	Value
$\tilde{G}\tilde{M}_1$	$3.986004415000000 \times 10^5 \text{ kg}$
$\tilde{G}\tilde{M}_2$	$4.902800582147800 \times 10^3 \text{ kg}$
$I^*$	$3.84400 \times 10^5 \text{ km}$
$\mu$	$1.215058535056245 \times 10^{-2}$
$t^*$	$3.751902588926273 \times 10^5 \text{ s}$

**Table 2 Example values of system parameters for the Earth-Moon CR3BP**

### 6.3 Circular Restricted Three-Body Problem Equations of Motion

The equations of motion for a spacecraft in the Earth-Moon CR3BP are typically written in nondimensional form in the rotating frame. Recall that the Earth-Moon rotating frame is commonly defined using the Earth-Moon barycenter as the origin and with axes constructed such that the Earth and Moon appear fixed when their orbits are modeled as circular [72]. In nondimensional coordinates and in this rotating frame, the Earth is located at  $(-\mu, 0, 0)$  while the Moon is located at  $(1 - \mu, 0, 0)$ . A depiction of the rotating frame is displayed in Figure 15 relative to a set of axes  $(\hat{X}\hat{Y}\hat{Z})$  from an inertial frame such as the GCRF. In the Earth-Moon CR3BP, the state vector of a spacecraft is expressed in nondimensional components defined in the rotating frame as  $\mathbf{x} = [x, y, z, \dot{x}, \dot{y}, \dot{z}]^T$ . The nondimensional equations of

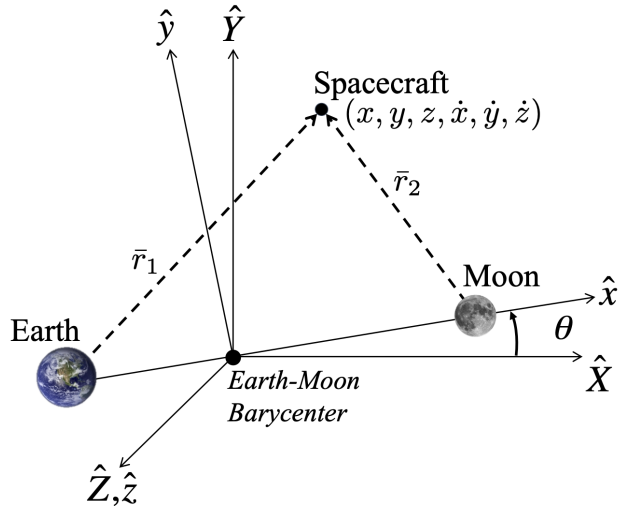


**Fig. 15** Conceptual representation of the rotating frame commonly used to define a state vector in the CR3BP; note that the Earth and Moon locations and radii are not drawn to scale for clarity.

motion for the spacecraft in the rotating frame are:

$$\begin{aligned}\ddot{x} &= 2\dot{y} + x - \frac{(1-\mu)(x+\mu)}{r_1^3} - \frac{\mu(x-1+\mu)}{r_2^3} \\ \ddot{y} &= -2\dot{x} + y - \frac{(1-\mu)y}{r_1^3} - \frac{\mu y}{r_2^3} \\ \ddot{z} &= -\frac{(1-\mu)z}{r_1^3} - \frac{\mu z}{r_2^3}\end{aligned}\tag{111}$$

where  $r_1 = \sqrt{(x+\mu)^2 + y^2 + z^2}$  and  $r_2 = \sqrt{(x-1+\mu)^2 + y^2 + z^2}$  are the distances between the spacecraft and the Earth and Moon, respectively [72]. Detailed derivations of these equations of motion appear throughout the literature: from Szebehely's foundational text on the CR3BP [72], to modern textbooks such as those by Vallado [6] and Koon, Lo, Marsden and Ross [74], to PhD dissertations [75].

#### 6.4 Jacobi Constant

In the CR3BP, there exists a constant of motion commonly labeled the Jacobi constant  $C_J$ , written as a function of the nondimensional state vector and mass ratio as:

$$C_J = (x^2 + y^2) + \frac{2(1-\mu)}{r_1} + \frac{2\mu}{r_2} - \dot{x}^2 - \dot{y}^2 - \dot{z}^2\tag{112}$$

Detailed derivations of this quantity appear throughout the literature [72, 74]. The Jacobi constant is constant along a natural trajectory generated in the CR3BP. As a result, this quantity is also valuable in validating numerical integration in the CR3BP and selecting suitable tolerances. Although this quantity is not constant along a general trajectory in a higher-fidelity model, it supports preliminary insight into the accessibility of the cis-lunar environment for a spacecraft at a given state. For instance, when the Jacobi constant decreases, the spacecraft energy increases and the spacecraft may potentially travel through a wider region of the phase space.

#### 6.5 Fundamental Solutions

At a single value of the Jacobi constant, a wide variety of fundamental solutions exist in the Earth-Moon CR3BP: equilibrium points; periodic orbits that exactly repeat after a minimal time labeled the period,  $T$ , in the rotating frame; quasi-periodic orbits that correspond to bounded but not periodic motion in the rotating frame; and hyperbolic (i.e., stable or unstable) invariant manifolds that capture motion asymptotically approaching or departing an equilibrium point, periodic or quasi-periodic orbit. Fundamental solutions that exist in the CR3BP are valuable for preliminary analysis of cis-lunar space: unlike a general solution to a nonlinear system that can only be analyzed over the time interval that it is numerically propagated, a fundamental solution supplies insight into the behavior of the trajectory for all time or, in the case stable or unstable manifolds, as time approaches either positive or negative infinity.

## 6.6 Equilibrium Points

In the Earth-Moon CR3BP, there are five equilibrium points that correspond to locations in the rotating frame where a spacecraft may remain indefinitely with zero velocity [72]. These equilibrium points are displayed and labeled in Figure 16 and are commonly also known as Lagrange points or libration points.  $L_1$ ,  $L_2$  and  $L_3$  are denoted collinear equilibrium points because they lie along the  $\hat{x}$ -axis of the rotating frame. In the Earth-Moon CR3BP, a stability analysis reveals that the collinear equilibrium points admit stable and unstable modes within the Earth-Moon plane as well as two sets of oscillatory modes: one within the plane of the primaries and one out of the plane of the primaries [74]. As a result, the collinear equilibrium points admit both stable and unstable manifolds (corresponding to natural motion that asymptotically approaches the equilibrium point in forwards and backwards time, respectively) as well as nearby bounded motions (e.g., periodic and quasi-periodic orbits).  $L_4$  and  $L_5$  are commonly labeled triangular or equilateral points because they lie at the vertices of equilateral triangles formed with the Earth and Moon. In the Earth-Moon CR3BP, a stability analysis reveals that the triangular equilibrium points admit only oscillatory modes that indicate the existence of a wide variety of bounded motions in its vicinity. The five equilibrium points of the CR3BP do not exactly exist in models of cislunar space that are of a higher fidelity; however, many of the orbits that exist in their vicinity are approximately retained, either with or without regular maneuvers, and they still influence the characteristics of cislunar trajectories as well as common terminology.

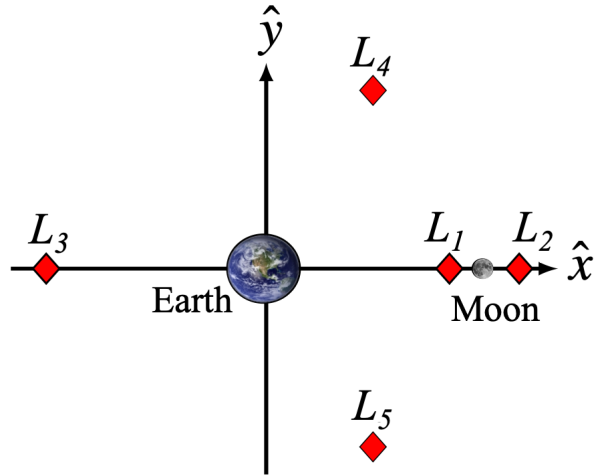


**Fig. 16** Conceptual representation of location and terminology for the five equilibrium points in the CR3BP; Earth and Moon displayed using 10x scale.

## 6.7 Regions of Allowable Motion

One useful insight that emerges from the CR3BP is the definition of regions of allowable motion. For a given Jacobi constant—or, analogously, the spacecraft energy—a spacecraft may only be located in certain regions of the system, described by the configuration space variables  $x, y, z$  in the rotating frame. The configuration space variables that

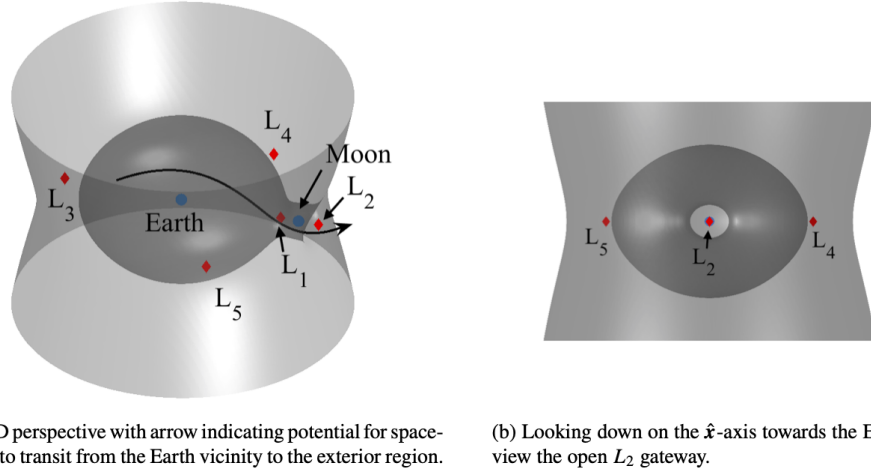


**Fig. 17 Sample zero velocity surfaces at a single value of the Jacobi constant.**

correspond to the spacecraft possessing a real-valued speed in the CR3BP at a specified value of the Jacobi constant define ‘regions of allowable motion’. If a given combination of position variables at a specific Jacobi constant only corresponds to an imaginary-valued speed in the CR3BP, then a spacecraft cannot be located at that position without a change in energy (e.g., via a propulsion system, solar sail, solar radiation pressure acting on an object with evolving attitude, etc); the collection of these position vectors defines a ‘forbidden region’. The forbidden and allowable regions are separated by zero velocity surfaces, i.e., a point along the zero velocity surface possesses a velocity vector equal to the zero vector, but the acceleration vector may be nonzero [74]. Figure 17 displays in gray an example set of zero velocity surfaces at a selected value of the Jacobi constant, with the Earth and Moon indicated as blue circles and the equilibrium points labeled with red diamonds.

The zero velocity surfaces evolve as the Jacobi constant changes [74]. For example, Figure 18 displays the intersection of the zero velocity surfaces with the  $xy$ -plane (i.e., the orbital plane of the Earth and Moon) to produce zero velocity curves at selected values of the Jacobi constant. As the spacecraft energy increases—and Jacobi constant decreases—the forbidden regions (gray) shrink in the plane and the allowable regions (white) become connected. When the Jacobi constant decreases further, these surfaces exist further away from the plane and allow higher inclination motion. The spacecraft may not cross the zero velocity surface along a natural trajectory. As a result, the spacecraft can move within and between connected regions of allowable motion. When two regions are not connected at a specific energy level, the spacecraft is constrained to remain within the vicinity of one or more primaries or outside the zero velocity surfaces.

## 6.8 Region Nomenclature

Common terminology for regions of cislunar space is defined graphically in Figure 19 using the zero velocity surfaces to form the boundaries. For instance, the regions that lie inside the zero velocity curves at low energy levels are generally labeled the interior regions near the Earth or Moon; similarly, a spacecraft within these regions may

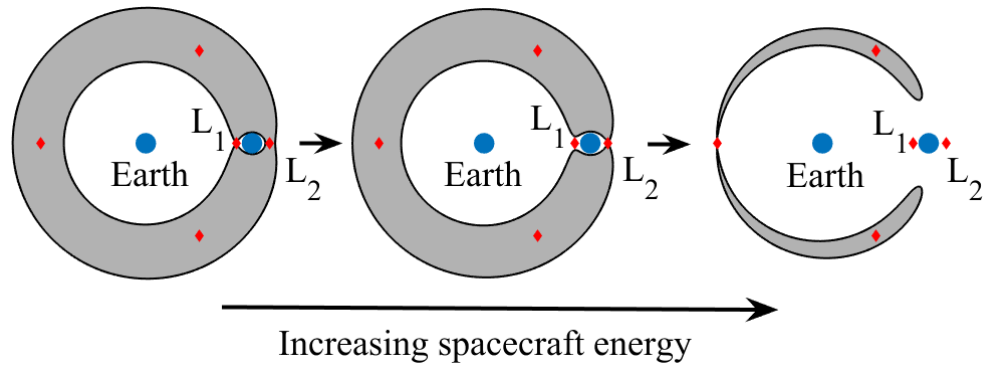


**Fig. 18** Zero velocity curves at decreasing values of the Jacobi constant or increasing spacecraft energy, creating larger and connected regions of allowable motion within the Earth-Moon plane. Primaries not drawn to scale.

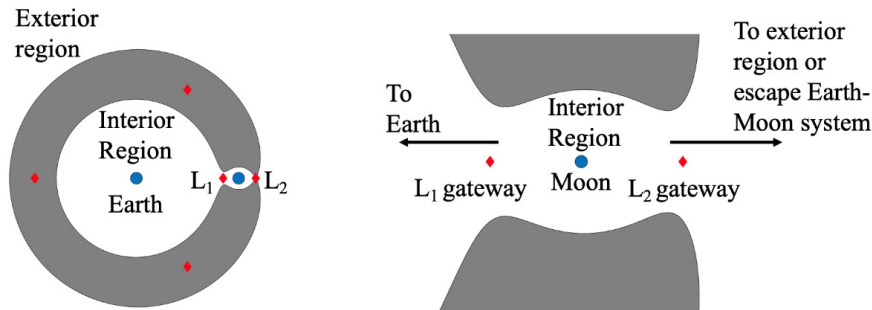


**Fig. 19** Terminology for regions within cislunar space, derived from the CR3BP [94].

be referred to as being located in the Earth or Moon vicinity. The exterior region lies outside of the zero velocity curves. The connections between the interior and exterior regions of allowable motion occur near the equilibrium points, defining the well-known  $L_1$ ,  $L_2$  or  $L_3$  ‘gateways’. These gateways enable a spacecraft to transfer between the vicinity of each of the Earth and Moon and/or the exterior region. At the Jacobi constant of one of the collinear equilibrium points, the zero velocity surfaces meet at the equilibrium point; below the Jacobi constant evaluated at one of these three collinear equilibrium points, the zero velocity surfaces meet at the equilibrium point; below the Jacobi constant evaluated at one of these three collinear equilibrium points, the spacecraft may pass through the gateway. In addition, the result that  $C_J(L_1) > C_J(L_2) > C_J(L_3)$  reveals that as the Jacobi constant is decreased or the spacecraft energy increases, the  $L_1$  gateway opens first, to allow passage between the Earth and Moon vicinities, followed by the  $L_2$  and then  $L_3$  gateway.

#### Implementation Note

The region terminology is clear to visualize in the Earth-Moon plane at relatively low spacecraft energies. However, as the spacecraft energy increases and the zero velocity surfaces no longer intersect the Earth-Moon orbital plane, these distinctions become unclear. As a result, there is not currently a single, established set of definitions for region nomenclature in cislunar space; rather, such standards are a work in progress within the astrodynamics and space communities.

## 6.9 Periodic Orbit Stability

The stability of a periodic orbit reflects the behavior of nearby trajectories and supplies insight into the existence of nearby fundamental solutions such as hyperbolic invariant manifolds or invariant tori. Assessing orbital stability typically relies on the use of a state transition matrix that is evaluated along the periodic orbit and then decomposed into its eigenvalues and eigenvectors.

When evaluated along a single reference trajectory, the state transition matrix (STM) produces a linear mapping from a variation in an initial state  $\delta\mathbf{x}(t_0)$  to a variation in the state  $\delta\mathbf{x}(t)$  at a later instant of time  $t$ . The state transition matrix along a trajectory, generated from an initial time,  $t_0$ , to a final time,  $t$ , is labeled in this document as  $[\Phi(t, t_0)]$ . Thus,  $\delta\mathbf{x}(t) = [\Phi(t, t_0)] \delta\mathbf{x}(t_0)$ . The evolution of the state transition matrix along a reference trajectory is governed by the following matrix differential equation [76]:

$$[\dot{\Phi}(t, t_0)] = [A(t)]|_{ref} [\Phi(t, t_0)] \quad (113)$$

where  $[A(t)]|_{ref} = \partial\dot{\mathbf{x}}/\partial\mathbf{x}|_{ref}$  is evaluated along the reference trajectory. From this differential equation, the state transition matrix is generated by simultaneously integrating Eq. (113) along with the 6 first-order differential equations derived from the second-order equations of motion in Eq. 111 using an augmented state comprised of the state vector and the state transition matrix unpacked into a vector form. The initial condition of a trajectory is equal to its initial state while the initial condition for the state transition matrix,  $[\Phi(t_0, t_0)]$ , is the  $6 \times 6$  identity matrix.

The state transition matrix evaluated for one period of a periodic orbit and from a selected initial state, i.e.,  $[\Phi(t_0 + T, t_0)]$ , is labeled the monodromy matrix,  $M$ , and is used to assess orbital stability [74]. Following the application of Floquet theory, the eigenvalues of the monodromy matrix predict the stability of the periodic orbit and the behavior of motion in its vicinity [74]. Because of the Hamiltonian structure of the CR3BP, several properties of the eigenvalues,  $\lambda_i$  for  $i = [1, 6]$ , of the monodromy matrix are known. First, each monodromy matrix produces two trivial eigenvalues equal to unity [77]. The remaining four nontrivial eigenvalues exist in either a complex-conjugate pair as  $\lambda_{i,j} = a \pm bi$  or a real-valued inverse pair as  $\lambda_i = a$ ,  $\lambda_j = 1/a$ . The form of the eigenvalues in each nontrivial pair indicates the orbital stability:

- A real eigenvalue with a magnitude of  $|\lambda_i| < 1$  corresponds to the stable mode of a periodic orbit. In the local vicinity of the periodic orbit, motion exciting only a stable mode asymptotically approaches the periodic orbit.
- A real eigenvalue with magnitude  $|\lambda_j| > 1$  corresponds to an unstable mode. Motion exciting only this mode asymptotically departs the periodic orbit.
- Complex conjugate eigenvalue pairs that lie on the unit circle correspond to the oscillatory mode of the periodic orbit. One type of trajectory that exists in the associated center eigenspace is a quasi-periodic orbit that produces bounded but non-repeating motion.

- A spiral mode is indicated by a complex conjugate eigenvalue pair that does not lie on the unit circle. Although this type of mode is generally less common, it does occur for some periodic orbits in the Earth-Moon system.

## 6.10 Computing Families of Periodic Orbits

An infinite variety of periodic orbits exist throughout the Earth-Moon system in continuous families; and family of solutions is essentially a set of solutions with a continuously varying set of properties. A single periodic orbit may be calculated by solving a boundary value problem using numerical methods such as a shooting scheme. Then, additional members of the family may be calculated from this first member using continuation methods. This subsection presents an example procedure for generating periodic orbits along a family in the CR3BP via a shooting method and pseudo-arclength continuation; both single- and multiple-shooting schemes are summarized here. In each approach, an initial guess for the periodic orbit is required. This initial guess may be generated via linearization near an equilibrium point, from a bifurcation that occurs along another periodic orbit family, using a Poincaré map, or via continuation from another system or dynamical model. This initial guess is corrected until a solution to the boundary value problem is recovered. Note that there are a variety of alternative formulations for a useful shooting scheme that recovers a periodic orbit; this subsection simply presents one of the most straightforward formulations. This shooting scheme is then augmented to implement pseudo-arclength continuation.

Consider one example formulation of a single shooting scheme to compute a periodic orbit in the CR3BP. A conceptual illustration of the application of single shooting to this problem is included in Figure 20. In this figure, an initial guess for a periodic orbit is represented as the nonperiodic black arc. This initial guess is defined by an initial guess for an initial state,  $x_0$ , and the orbit period,  $T$ . In this example, consider the following  $7 \times 1$  free variable vector that is formulated to contain these quantities as follows:

$$\mathbf{V} = \begin{bmatrix} \mathbf{x}_0 \\ T \end{bmatrix}$$

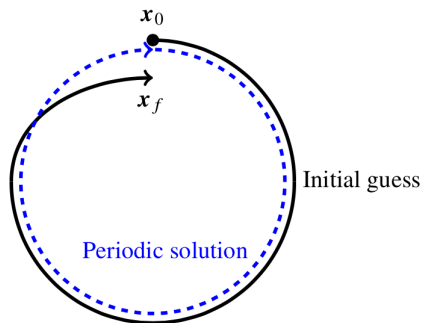


**Fig. 20** Conceptual illustration of single shooting formulation to computing a periodic orbit.

Because the goal in solving the corrections problem is to recover a trajectory that corresponds to a periodic orbit, the initial state and the state,  $\mathbf{x}_f$ , generated by propagating forward for  $T$  along the trajectory must be equal, i.e.  $\mathbf{x}_f = \mathbf{x}_0$ ; this constraint is often referred to as a state continuity constraint. The associated constraint vector is written as the following  $6 \times 1$  vector:

$$\mathbf{F}(\mathbf{V}) = [\mathbf{x}_f - \mathbf{x}_0]$$

Depending on the formulation of the shooting method, one or more periodic orbit solutions may exist that satisfy the constraint formulation, to within a specified tolerance. For this example, a Jacobian matrix that captures the partial derivatives of the constraints with respect to the free variables is equal to

$$[\mathbf{D}\mathbf{F}(\mathbf{V})] = \begin{bmatrix} \frac{\partial \mathbf{x}_f - \mathbf{x}_0}{\partial \mathbf{x}_0} & \frac{\partial \mathbf{x}_f - \mathbf{x}_0}{\partial T} \end{bmatrix} = \begin{bmatrix} [\Phi(t_0 + T, t_0)] - [\mathbf{I}_6] & \dot{\mathbf{x}}_f \end{bmatrix}$$

where  $[\Phi(t_0 + T, t_0)]$  is the state transition matrix generated along the trajectory associated with the current guess for  $\mathbf{x}_0$  at  $t_0$  and the orbit period. The free variables are iteratively updated using Eq. 103 until the norm of the constraint vector equals zero to within a selected tolerance. This solution produces a close approximation (to within numerical integration error and the selected numerical tolerance) of a periodic orbit, represented in Figure 20 as the dashed blue line. Of course, there are alternative formulations of a single shooting scheme, such as those that use the mirror theorem or incorporate implicit state constraints such as those due to conservation of the Jacobi constant along a trajectory. Such schemes may reduce sensitivity during corrections, reduce the required computational load, or limit overconstraining the problem when additional constraints are desired.

Recall that multiple shooting focuses on calculating the solution to a boundary value problem by dividing a trajectory into several arcs. Figure 21 illustrates the concept of using multiple shooting to recover a periodic orbit, represented as the closed blue dashed curve, given a discontinuous initial guess, represented as several black arcs. In multiple shooting, the discontinuous arcs are simultaneously updated via a multi-variate Newton's method to recover the continuous trajectory that is also periodic. In practice, a multiple-shooting scheme often produces a less sensitive corrections problem, at the expense of a slightly more complex implementation [75]. This characteristic may motivate using a shooting method to recover complex or long-duration trajectories, or trajectories with varying levels of sensitivity over time (e.g., a trajectory possessing a close flyby of a gravitational body).

Consider a simple formulation of a multiple shooting scheme to compute a periodic orbit in the CR3BP. In particular, consider a trajectory discretized into  $N$  arcs, each with a common integration time of  $t_{\text{int}}$ . The  $i$ -th arc is then completely defined by its initial state,  $\mathbf{x}_{0,i}$ , and  $t_{\text{int}}$ . The free variable vector that captures the initial state of all  $N$  arcs and the

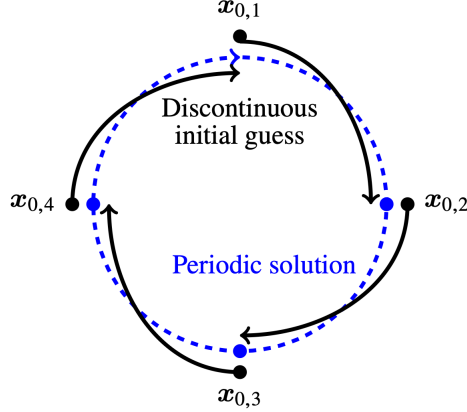


**Fig. 21** Conceptual illustration of multiple shooting to target a periodic orbit.

common integration time is then expressed as:

$$\mathbf{V} = \left[ \mathbf{x}_{0,1}^T, \quad \mathbf{x}_{0,2}^T, \quad \dots, \quad \mathbf{x}_{0,N-1}^T, \quad \mathbf{x}_{0,N}^T, \quad t_{\text{int}} \right]^T$$

and possesses a dimension of  $(6N + 1) \times 1$ . The constraint vector is formulated to enforce full state continuity between neighboring arcs. Accordingly, for the  $i$ th arc, its final state,  $\mathbf{x}_{f,i}$ , must equal the initial state of the  $i + 1$ -th arc,  $\mathbf{x}_{0,i+1}$  (or the first arc if  $i = N$ ). By applying this full state continuity constraint to all neighboring arcs, periodicity is also enforced. The full constraint vector is then written as

$$\mathbf{F}(\mathbf{V}) = \left[ \mathbf{x}_{f,1}^T - \mathbf{x}_{0,2}^T, \quad \mathbf{x}_{f,2}^T - \mathbf{x}_{0,3}^T, \quad \dots, \quad \mathbf{x}_{f,N-1}^T - \mathbf{x}_{0,N}^T, \quad \mathbf{x}_{f,N}^T - \mathbf{x}_{0,1}^T \right]^T$$

with a dimension of  $(6N) \times 1$ . For this definition of the free variable and constraint vectors, the corresponding Jacobian matrix,  $[D\mathbf{F}(\mathbf{V})]$ , is equal to

$$[D\mathbf{F}(\mathbf{V})] = \begin{bmatrix} [\Phi(t_{f,1}, t_{0,1})] & -[\mathbf{I}_6] & \mathbf{0}_6 & \dots & \mathbf{0}_6 & \mathbf{0}_6 & \dot{\mathbf{x}}_{f,1} \\ \mathbf{0}_6 & [\Phi(t_{f,2}, t_{0,2})] & -[\mathbf{I}_6] & \dots & \mathbf{0}_6 & \mathbf{0}_6 & \dot{\mathbf{x}}_{f,2} \\ \vdots & \vdots & \vdots & \ddots & \vdots & \vdots & \vdots \\ \mathbf{0}_6 & \mathbf{0}_6 & \mathbf{0}_6 & \dots & [\Phi(t_{f,N-1}, t_{0,N-1})] & -[\mathbf{I}_6] & \dot{\mathbf{x}}_{f,N-1} \\ -[\mathbf{I}_6] & \mathbf{0}_6 & \mathbf{0}_6 & \dots & \mathbf{0}_6 & [\Phi(t_{f,N}, t_{0,N})] & \dot{\mathbf{x}}_{f,N} \end{bmatrix}$$

where  $\mathbf{I}_6$  is the  $6 \times 6$  identity matrix,  $t_{0,i}$  is the time at the beginning of an arc, and  $t_{f,i}$  is the time at the end of the arc, equal to  $t_{f,i} = t_{0,i} + t_{\text{int}}$ . For this example, the  $[D\mathbf{F}(\mathbf{V})]$  matrix possesses a dimension of  $(6N) \times (6N + 1)$ . Notably, this matrix is calculated using the state transition matrix evaluated along each arc, consistent with the STM reflecting the

sensitivity of a perturbation from a trajectory at the end of the time interval of interest to perturbations in the initial state. Because the number of free variables is one less than the number of independent constraints, a one-parameter family of solutions exist. The update equation in Eq. (103) is used to iteratively update the free variables from an initial guess using Newton's method until a solution is found that satisfies the constraint vector to within a specified tolerance. Of course, as with single shooting, multiple shooting may be implemented using a variety of formulations, tailored to the specific application as well as to limit sensitivity during corrections or overconstrained problem formulation as desired.

Once a single periodic orbit has been calculated, continuation enables other members of the family to be computed more efficiently. Consider, for example, the use of pseudo-arc length continuation in combination with the previously-described multiple-shooting scheme. In this case, the free variable vector is unchanged in definition. An initial guess for this free variable vector is calculated by stepping along the tangent,  $\mathbf{n}_j$ , to the solution curve at a known solution,  $\mathbf{V}_j$ , by a stepsize  $\Delta s$ . One approach to calculating this tangent direction is to use a unit vector that lies in the nullspace of the Jacobian matrix evaluated using the known solution, i.e.,  $[DF(\mathbf{V}_j)]$ . Given that the Jacobian matrix formulated in the last paragraph possesses a dimension of  $(6N) \times (6N + 1)$ , the nullspace is one-dimensional. The direction of the unit vector that lies in the nullspace is selected according to the desired direction for stepping along the family. Then, the initial guess for a new periodic orbit along the family is calculated as  $\mathbf{V}_{j+1} = \mathbf{V}_j + \Delta s \mathbf{n}_j$ . An augmented constraint vector, denoted  $\mathbf{H}(\mathbf{V})$ , is constructed by combining the constraints that the desired solution must satisfy,  $\mathbf{F}(\mathbf{V})$ , with the pseudo-arc length continuation constraint; this augmented constraint vector is written as [78]

$$\mathbf{H}(\mathbf{V}) = \begin{bmatrix} \mathbf{F}(\mathbf{V}) \\ (\mathbf{V}_{j+1} - \mathbf{V}_j)^T \mathbf{n}_j - \Delta s \end{bmatrix} \quad (114)$$

The Jacobian matrix composed of the partial derivatives of the augmented constraint vector with respect to the free variables is then equal to

$$[D\mathbf{H}(\mathbf{V})] = \begin{bmatrix} [DF(\mathbf{V})] \\ (\mathbf{n}_j)^T \end{bmatrix} \quad (115)$$

This Jacobian is square and full-rank, indicating that a single solution exists. Accordingly, the update equation of each iteration of the corrections scheme is described by Eq. (104). The update equation is then applied iteratively with the goal of recovering a free variable vector,  $\mathbf{V}$ , that describes a new orbit in the family that satisfies  $\mathbf{H}(\mathbf{V}) = \mathbf{0}$  to within a desired tolerance. Using this solution, the nullspace of the Jacobian matrix,  $[DF(\mathbf{V})]$ , is recalculated to generate the tangent direction to the family at the new solution. This process is repeated to compute additional orbits along the family.

## 6.11 Periodic Orbit Families

Families of periodic orbits contribute to an underlying dynamical structure that governs natural transport throughout the Earth-Moon CR3BP. Although there are an infinite variety of orbit families, consistent with the occurrence of bifurcations in a chaotic dynamical system, astrodynamicists commonly leverage well-known families during trajectory design and analysis; these families have been computed, characterized and used extensively in astrodynamics and celestial mechanics [72, 79–81]. This subsection supplies a brief overview of several well-known families of periodic orbits, with the caveat that this is not an exhaustive or complete overview. This overview is organized according to a general classification defined by the associated equilibrium point, region of existence, or generating resonance [79]. Within each subsection, selected members of each family are displayed in the nondimensional configuration space of the Earth-Moon rotating frame. In these figures, the color of each orbit reflects the orbital stability of the selected periodic orbit in the rotating frame, thereby indicating the behavior of nearby trajectories: purple periodic orbits admit only oscillatory modes that indicate the existence of nearby bounded motions such as quasi-periodic orbits; light blue periodic orbits possess both oscillatory modes as well as stable and unstable modes, indicating the existence of both nearby bounded motions as well as stable and unstable manifolds; and royal blue periodic orbits admit only stable and unstable manifolds. Selected states and orbit periods for one member of each family in the Earth-Moon CR3BP appear in Tables 3-6 to assist the interested reader in calculating these periodic orbit families. Note that this data is truncated for brevity and is calculated using the system parameters presented in Table 2 with a specific numerical integration scheme. Thus, corrections will be required to recover a periodic orbit from this information in the reader's custom codes.

Orbit family	Period (nondim.)	Period (days)	Jacobi constant	Example state vector (nondim.)
$L_1$ Lyapunov	3.071168	13.334	3.107961	[0.807303, 0, 0, 0.298948, 0] <sup>T</sup>
$L_1$ northern halo	2.760344	11.985	3.151498	[0.823969, 0, 0.053194, 0, 0.163217, 0] <sup>T</sup>
	1.868528	8.113	3.003577	[0.906618, 0, 0.203669, 0, 0.169171, 0] <sup>T</sup>
$L_1$ southern halo	2.760344	11.985	3.151498	[0.823969, 0, -0.053194, 0, 0.163217, 0] <sup>T</sup>
	1.868528	8.113	3.003577	[0.906618, 0, -0.203669, 0, 0.169171, 0] <sup>T</sup>
$L_1$ vertical	3.961489	17.200	3.001662	[0.861879, 0, 0, 0.085903, 0.432614] <sup>T</sup>
$L_1$ axial	4.003592	17.383	3.007163	[0.913013, 0, 0, -0.313025, 0.434375] <sup>T</sup>
$L_2$ Lyapunov	3.727062	16.182	3.072614	[1.062267, 0, 0, 0.470321, 0] <sup>T</sup>
$L_2$ northern halo	3.366323	14.616	3.128090	[1.174193, 0, 0.076230, 0, -0.182432, 0] <sup>T</sup>
	2.269175	9.852	3.015746	[1.075397, 0, 0.202158, 0, -0.192618, 0] <sup>T</sup>
$L_2$ southern halo	3.366323	14.616	3.128090	[1.174193, 0, -0.076230, 0, -0.182432, 0] <sup>T</sup>
	2.269175	9.852	3.015746	[1.075397, 0, -0.202158, 0, -0.192618, 0] <sup>T</sup>
$L_2$ vertical	3.708580	16.102	3.087212	[1.133881, 0, 0, 0, -0.059618, 0.292024] <sup>T</sup>
$L_2$ axial	4.335199	18.823	3.002210	[1.038680, 0, 0, 0, 0.466570, 0.466012] <sup>T</sup>
$L_2$ northern butterfly	2.796694	12.143	3.061834	[1.038394, 0, 0.173741, 0, -0.078548, 0] <sup>T</sup>
$L_3$ Lyapunov	6.230086	27.050	2.677460	[-0.463824, 0, 0, -1.388737, 0] <sup>T</sup>
$L_3$ northern halo	6.233248	27.064	1.999059	[-1.415165, 0, 1.065337, 0, 1.065076, 0] <sup>T</sup>
$L_3$ southern halo	6.233248	27.064	1.999059	[-1.415165, 0, -1.065337, 0, 1.065076, 0] <sup>T</sup>
$L_3$ vertical	6.250683	27.139	2.472376	[-1.003671, 0, 0, 0.267975, 0.684081] <sup>T</sup>
$L_3$ axial	6.263619	27.195	1.151029	[-1.765916, 0, 0, 1.724945, 0.356883] <sup>T</sup>

**Table 3** Nondimensional state in the Earth-Moon rotating frame, period, and Jacobi constant for selected periodic orbits in well-known  $L_1$ ,  $L_2$ , and  $L_3$  orbit families.

Orbit family	Period (nondim.)	Period (days)	Jacobi constant	Example state vector (nondim.)
$L_4$ short period	6.581383	28.575	2.986425	[0.416475, 0.866025, 0, -0.045831, 0.054473, 0] <sup>T</sup>
$L_4$ long period	21.134919	91.764	2.989588	[0.401123, 0.866025, 0, -0.051838, 0.027839, 0] <sup>T</sup>
$L_4$ vertical	6.285140	27.289	2.848918	[0.503828, 0.856388, 0, 0.059258, -0.034869, 0.366554] <sup>T</sup>
$L_4$ axial	6.287950	27.301	2.054761	[0.570828, 0.522879, 0, -0.015379, -0.156282, 1.038768] <sup>T</sup>
	5.222033	22.673	2.847428	[0.715919, 0.111984, 0, -0.246533, 0.534722, 0.309278] <sup>T</sup>
$L_5$ short period	6.581275	28.575	2.986295	[0.554935, -0.866025, 0, -0.041453, -0.060038, 0] <sup>T</sup>
$L_5$ long period	21.087959	91.560	2.988246	[0.450191, -0.866025, 0, 0.023670, 0.014418, 0] <sup>T</sup>
$L_5$ vertical	6.283895	27.283	2.937495	[0.493855, -0.862446, 0, -0.021646, -0.012396, 0.223342] <sup>T</sup>
$L_5$ axial	6.290729	27.313	2.021197	[0.445443, -1.067760, 0, -0.698239, -0.184929, 0.718757] <sup>T</sup>
	3.084440	13.392	2.925097	[1.093283, -0.069113, 0, 0.146971, -0.414519, 0.240964] <sup>T</sup>

Table 4 Nondimensional state in the Earth-Moon rotating frame, period, and Jacobi constant for selected periodic orbits in well-known  $L_4$  and  $L_5$  orbit families.

Orbit family	Period (nondim.)	Period (days)	Jacobi constant	Example state vector (nondim.)
Distant prograde orbit	1.573499	6.832887	3.169904	[1.061162, 0, 0, 0, 0.358303, 0] <sup>T</sup>
Low prograde orbit	1.570473	6.819749	3.187006	[1.012458, 0, 0, 0, 0.868239, 0] <sup>T</sup>
Distant retrograde orbit	1.572685	6.829354	3.000353	[0.885102, 0, 0, 0, 0.470647, 0] <sup>T</sup>

Table 5 Nondimensional state in the Earth-Moon rotating frame, period, and Jacobi constant for selected periodic orbits in well-known Moon-centered orbit families.

Orbit family	Period (nondim.)	Period (days)	Jacobi constant	Example state vector (nondim.)
2:1 planar resonant orbit family	6.180165	26.837242	3.078721	$[0.391571, 0, 0, 0, 1.417418, 0]^T$
3:1 planar resonant orbit family	6.262867	27.196372	3.170384	$[-0.790514, 0, 0, 0, 0.080413, 0]^T$
1:2 planar resonant orbit family	10.962937	47.606335	2.828255	$[0.902405, 0, 0, 0, 0.656333, 0]^T$
2:3 planar resonant orbit family	16.608901	72.123819	2.897540	$[0.937401, 0, 0, 0, 0.737256, 0]^T$
4:3 planar resonant orbit family	16.123301	70.015108	2.939696	$[1.062927, 0, 0, 0, -0.592894, 0]^T$
3:4 planar resonant orbit family	25.547545	110.939699	2.573128	$[0.475766, 0, 0, 0, 1.322852, 0]^T$

**Table 6** Nondimensional state in the Earth-Moon rotating frame, period, and Jacobi constant for selected periodic orbits in well-known planar resonant orbit families. Selected orbits are not located at the exact resonance, but exist in the same family.

### 6.11.1 Common $L_1$ , $L_2$ and $L_3$ Periodic Orbit Families

In the vicinity of the two collinear equilibrium points near the Moon,  $L_1$  and  $L_2$ , there are several well-known periodic orbit families; selected families in the Earth-Moon CR3BP are displayed in Figs. 22 and 23, respectively.

The Lyapunov orbit families are composed of orbits that remain within the Earth-Moon plane and emanate from the equilibrium points, exhibiting clockwise motion about the equilibrium points. Along these families, these orbits evolve away from the equilibrium points and eventually exhibit close passes to the primaries, i.e., the Earth and Moon. The vertical orbit families emanate away from the equilibrium point, but out of the Earth-Moon plane. Close to the equilibrium point, and at low  $z$ -amplitudes in the Earth-Moon rotating frame, these orbits resemble a figure-eight

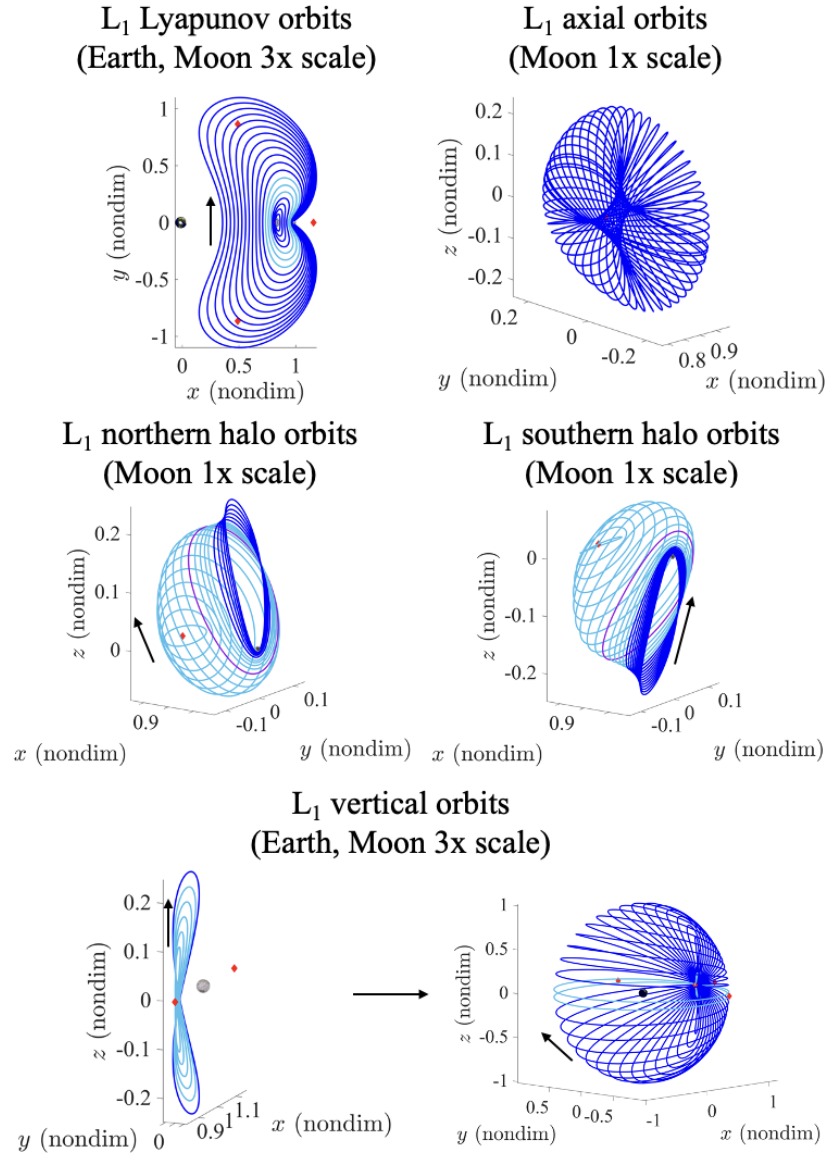


**Fig. 22** Selected well-known periodic orbit families near  $L_1$  in the Earth-Moon CR3BP.

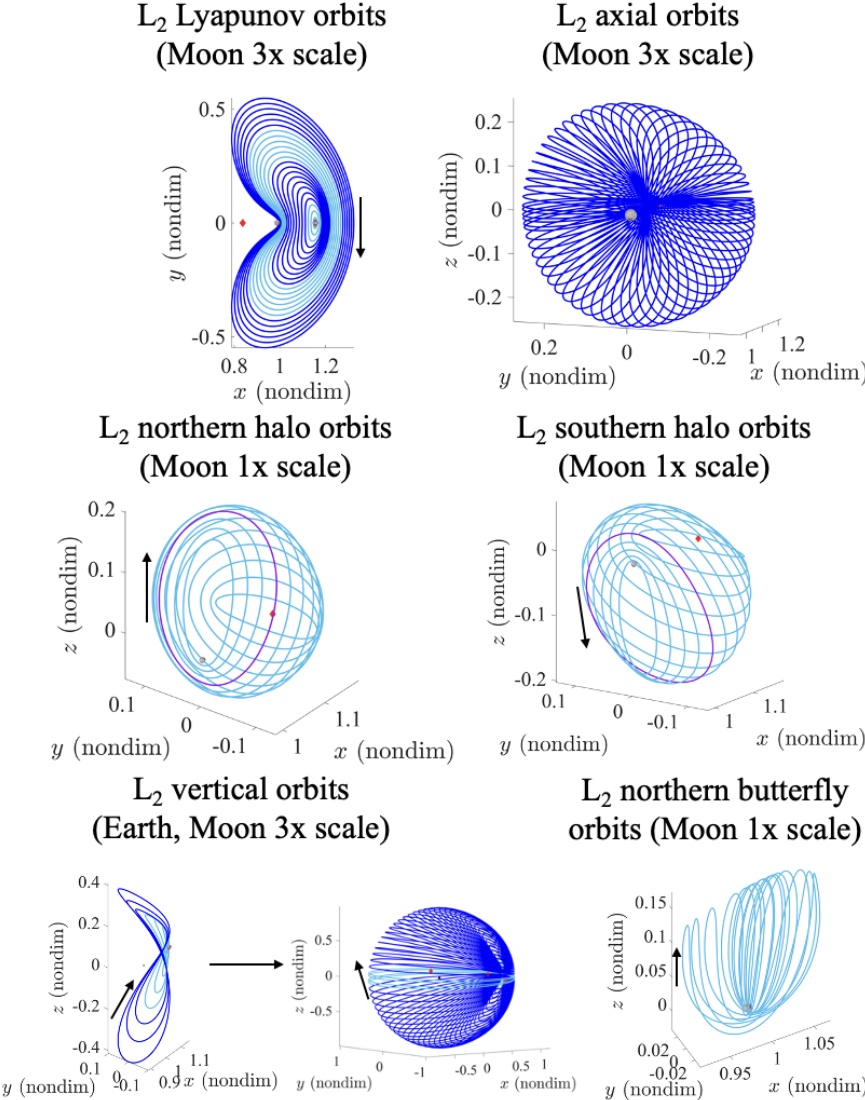


**Fig. 23 Selected well-known periodic orbit families near  $L_2$  in the Earth-Moon CR3BP.**

and are symmetric about the Earth-Moon plane. As members along each of the vertical families evolve away from the equilibrium point, each half of the orbit grows in size to envelope the Earth and eventually meet to produce two revolutions around a large and near-circular orbit in the Earth-Moon plane. Bifurcations that occur along the Lyapunov orbit families correspond to an intersection with the three-dimensional halo and axial orbit families. The halo orbit families each consist of two branches with members that are symmetric about the  $xy$ -plane: a southern branch and a northern branch. The northern (southern) branch corresponds to orbits for which the maximum extension out of the Earth-Moon plane occurs for positive (negative) values of  $z$ . As orbits along each branch of the  $L_1$  and  $L_2$  families evolve away from their bifurcation with the Lyapunov orbit family, they evolve towards the Moon to possess a low perilune, high eccentricity and high inclination relative to the Earth-Moon plane. Members along the  $L_1$  and  $L_2$  halo

orbit families that are stable or nearly stable have recently been labeled ‘near-rectilinear halo orbits’ (NRHOs). The axial orbit families are a closed family that intersect both the Lyapunov orbit families and the vertical orbit families. More complex periodic orbits also exist in the vicinity of  $L_1$  and  $L_2$  due to the occurrence of bifurcations along the family. A well-known example includes the  $L_2$  butterfly orbit family, which intersects the  $L_2$  halo orbit family at period-doubling bifurcations. Members of the  $L_2$  butterfly orbit family possess two branches, a northern and southern branch. Along each orbit, there are two halves with a high  $z$ -extension on each of the  $L_1$  and  $L_2$  sides of the Moon and a low perilune.

Similar families exist near  $L_3$  as displayed in Fig. 24. Notably, however, motion along the  $L_3$  Lyapunov orbit is still clockwise around the equilibrium point but the family evolves to possess a close pass to the Earth. Similarly, halo orbits exist due to a bifurcation along the  $L_3$  Lyapunov orbit family and capture motion throughout a wider region of the

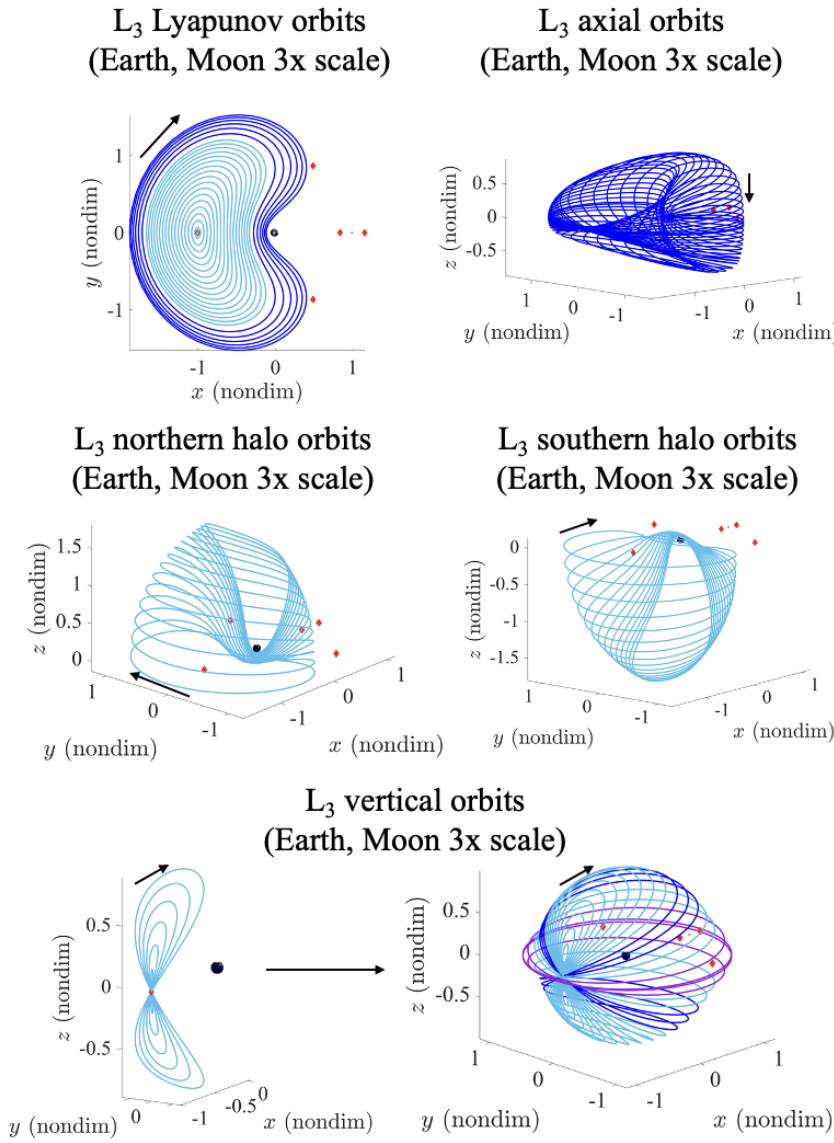


**Fig. 24** Selected well-known periodic orbit families near  $L_3$  in the Earth-Moon CR3BP.

Earth-Moon system than the  $L_1$  and  $L_2$  halo orbits. Stepping along the  $L_3$  southern or northern halo orbit branches and away from the bifurcation with the  $L_3$  Lyapunov family, members eventually possess a low perigee and high inclination.

### 6.11.2 Common $L_4$ and $L_5$ Periodic Orbit Families

In the Earth-Moon CR3BP, the  $L_4$  and  $L_5$  equilibrium points possess only oscillatory modes, indicating the existence of two planar periodic orbit families and one three-dimensional periodic orbit family; these families in the Earth-Moon CR3BP are displayed in Fig. 25. The periodic orbits associated with  $L_4$  may be reflected about the  $y$ -axis to produce the periodic orbits associated with  $L_5$ . The planar periodic orbits associated with each of  $L_4$  and  $L_5$  are labeled the

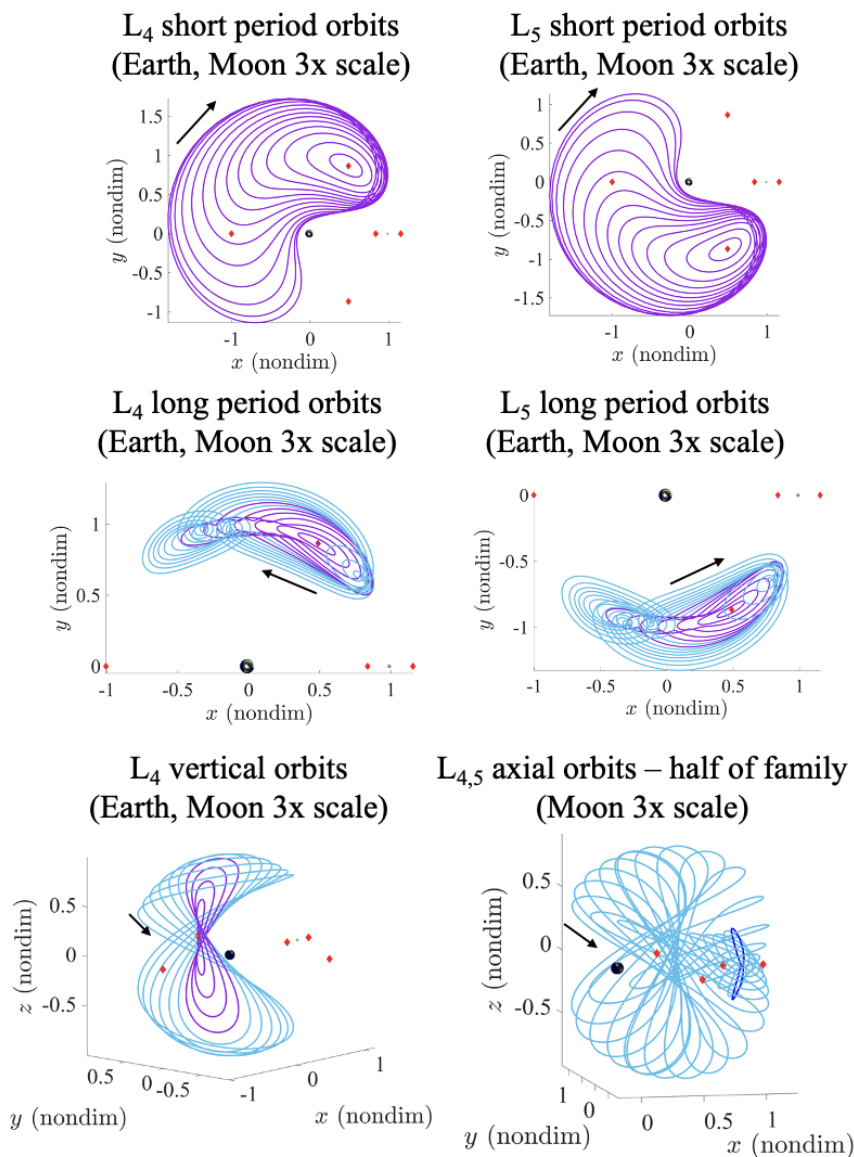


**Fig. 25 Examples of well-known periodic orbit families near the  $L_4$  and  $L_5$  equilibrium points in the Earth-Moon CR3BP.**

short period and long period orbits, consistent with the relative periods of the orbits and, therefore, distinctly different frequencies of each oscillatory mode. Spatial vertical orbits exist near each of  $L_4$  and  $L_5$ , with a shape that resembles a figure-eight. An additional well-known family of spatial periodic orbits are the axial orbits; these orbits exist in a closed family that possesses a bifurcation with the  $L_4$  and  $L_5$  vertical orbit families and also with the  $L_1$  northern and southern halo orbits. Unfortunately, some of these periodic orbits do not admit nearby natural trajectories in an ephemeris model of cislunar space.

### 6.11.3 Common Moon-Centered Periodic Orbit Families

In the vicinity of the Moon, there are well-known periodic orbit families that are labeled according to the direction of motion along a range of members; these families in the Earth-Moon CR3BP are displayed in Fig. 26. For instance, the distant retrograde orbits (DROs) possess planar members that encircle the Moon in a retrograde direction relative to the Moon, i.e., clockwise when looking down on the Earth-Moon plane from the  $+z$  direction. The DROs evolve away from near-circular retrograde orbits that exist close to the Moon to grow and eventually exhibit a close pass to the Earth. A spatial DRO family exists due to a bifurcation along the standard planar DRO family and its members evolve out of the Earth-Moon plane. Distant prograde orbits (DPOs) are planar members that are named for the direction of motion along the majority of members as prograde relative to the Moon, i.e., counterclockwise when looking down on the

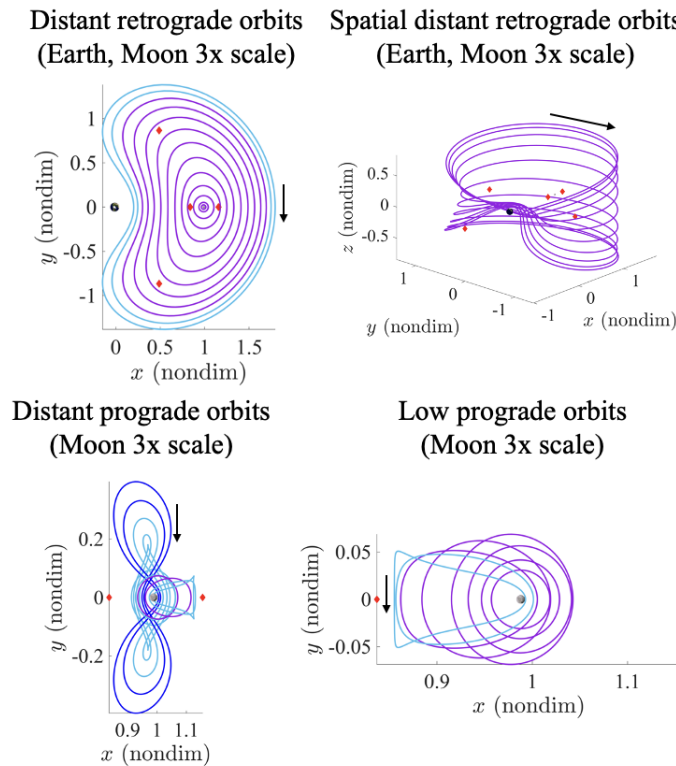


**Fig. 26 Examples of well-known periodic orbit families near the Moon in the Earth-Moon CR3BP.**

Earth-Moon plane from the  $+z$  direction. Some members of these family appear nearly elliptical in the Earth-Moon rotating frame. As members evolve away from this type of orbit in one direction of the family, the perilune lowers and apolune increasingly shifts towards  $L_2$ , with additional apses occurring along some members. Along the other direction of the family, the members extend further away from the  $x$ -axis and develop loops that correspond to a temporary change in the direction of motion relative to the Moon and in the Earth-Moon rotating frame. Finally, the low prograde orbits correspond to motion that is predominantly prograde relative to the Moon. The orbits evolve away from near-circular prograde orbits that exist close to the Moon to eventually admit a low perilune and apolune near  $L_1$ . Some members of these families do not admit nearby natural trajectories in an ephemeris model of cislunar space.

#### 6.11.4 Common Resonant Periodic Orbit Families

Resonant orbit families include a periodic orbit that possesses an orbital resonance with the primary system [82]. Along a  $p : q$  resonant orbit, a spacecraft completes  $p$  revolutions around the Earth in the inertial frame in the same interval of time that the Moon completes  $q$  revolutions. Along a resonant orbit family, members evolve away from this condition to possess periods that are not in an orbital resonance with the Moon and potentially significant changes in the geometry and/or direction of motion along some segments of the orbit. Interior resonant orbits possess  $p > q$  and typically revolve predominantly around the Earth. Exterior resonant orbits possess  $p < q$  and typically revolve around both primaries [82]. Selected members of some planar resonant orbit families appear in Fig. 27. Many resonant orbit families also admit a bifurcation with spatial periodic orbit families and/or nearby quasi-periodic orbits that may be useful in trajectory design or mission orbit selection; for instance, the Transiting Exoplanet Survey Satellite (TESS) and Interstellar Boundary Explorer (IBEX) missions followed bounded motions near 2:1 and 3:1 interior resonances, respectively [83–85].

## 6.12 Quasi-Periodic Orbits

A quasi-periodic trajectory exhibits nonperiodic, bounded motion that traces out the surface of an invariant torus [86, 87]. A torus exists near a periodic orbit with a set of oscillatory modes and the associated trajectory is governed by a finite number of incommensurate fundamental frequencies. These quasi-periodic orbits exist within continuous families, inheriting the geometric characteristics of nearby periodic orbits but potentially evolving significantly along the family. Examples of tori associated with well-known families of quasi-periodic orbits are displayed in Figure 28. On the left is a torus traced out by a quasi-halo orbit that exists near an  $L_2$  southern halo orbit. On the right is a set of tori that exist at the same energy level as nearby  $L_2$  Lyapunov and vertical orbits. At this energy level, tori exist in a continuous set that collapse to each of the nearby periodic orbits at their boundaries. The quasi-periodic orbits tracing these tori are often labeled Lissajous orbits. Although they are not periodic, their boundedness often renders them suitable candidates for mission orbit selection. However, the existence of quasi-periodic orbits in multi-dimensional families as well as their

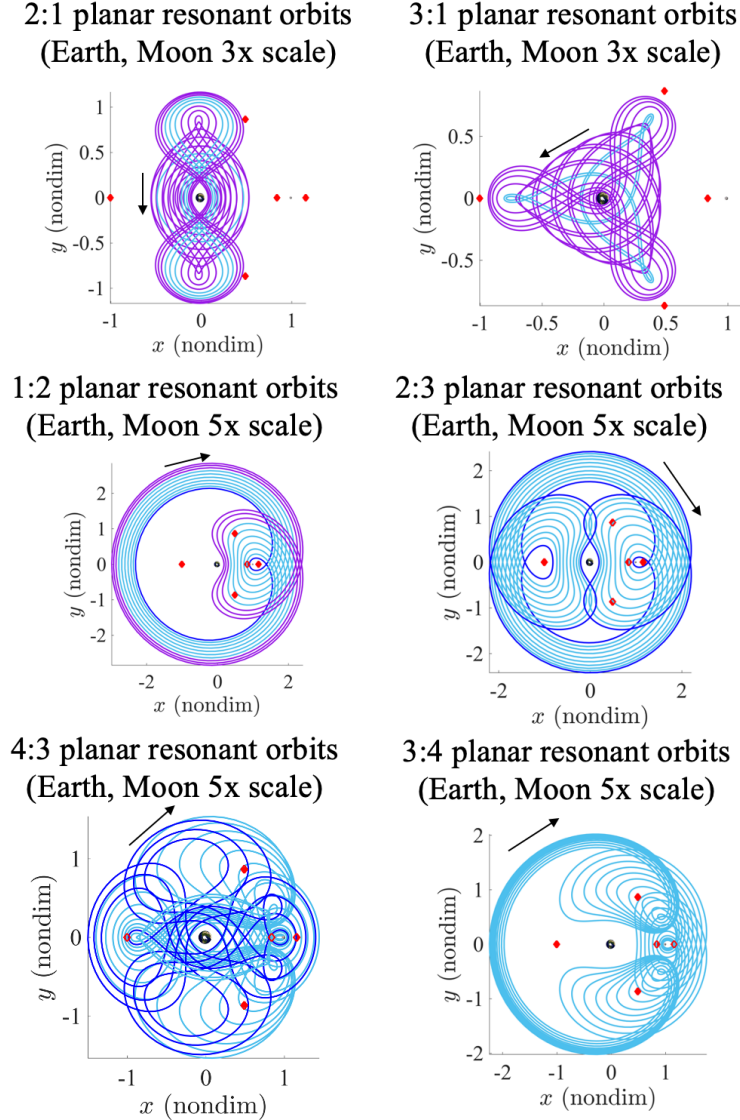


**Fig. 27 Examples of well-known planar periodic orbit families near orbital resonances in the Earth-Moon CR3BP.**

complex description often results in a more complex computation and analysis than periodic orbit families.

Well-known approaches used throughout the astrodynamics community to compute approximations to quasi-periodic orbits include, but are not limited to:

- Using a Poincaré map: quasi-periodic orbits can be identified from an appropriately-constructed Poincaré map as a closed curve (or chain of closed curves). In this case, a state that lies on the closed curve may be directly integrated to generate the associated quasi-periodic orbit [86]. Identifying these closed curves to locate spatial quasi-periodic orbits can sometimes be challenging, particularly when the map captures higher-dimensional information.
- Using multiple-shooting to compute a trajectory that resembles a quasi-periodic orbit: given an initial guess for a quasi-periodic orbit, a trajectory that is simply bounded over a suitable time horizon and resembles a quasi-periodic

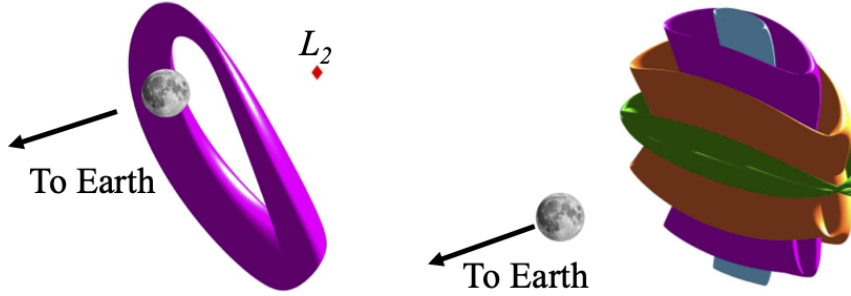


**Fig. 28 Examples of tori associated with well-known families of quasi-periodic orbits.**

orbit is computed using multiple-shooting [88]. This trajectory is continuous over a time interval equal to several revolutions, but is not necessarily confirmed or constrained to lie along a torus. In some mission design examples or analyses, such a trajectory may sufficiently approximate a nearby quasi-periodic orbit.

- Directly computing a close approximation to a torus as opposed to a single trajectory along the torus. Such approaches have been developed by Olikara and Scheeres, Schilder et al., Gómez and Mondelo, Jorba, and Kolemen et al. [89–92].
- Using reduction to the center manifold of an equilibrium point or periodic orbit, a process that involves a transformation to a set of canonical coordinates in the vicinity of the reference orbit [93].
- Using a series expansion to approximate a quasi-periodic orbit: analytical expressions developed by Richardson and Cary are useful for generating approximations to motion in the vicinity of  $L_1$  and  $L_2$  in terms of two frequencies and may be useful for forming an initial guess for a quasi-periodic orbit prior to additional corrections [74].

### 6.13 Hyperbolic Invariant Manifolds

Hyperbolic invariant manifolds are a set of states within the phase space that remain within that set for all time when subject to the flow of the dynamical system and either approach or depart a specific fundamental solution [87], e.g., an equilibrium point, periodic orbit, or quasi-periodic orbit. A stable manifold corresponds to trajectories that approach the associated fundamental solution as time tends forwards towards infinity. However, an unstable manifold corresponds to trajectories that approach the associated fundamental solution as time tends backwards towards negative infinity. Hyperbolic invariant manifolds are associated with fundamental solutions that admit stable and unstable modes, governing natural transport throughout a system in the CR3BP. For instance, the hyperbolic invariant manifolds of periodic and quasi-periodic orbits near  $L_1$  and  $L_2$  govern natural transport through the  $L_1$  and  $L_2$  gateways [74]. Figure 29 displays an example of this concept: a trajectory that lies within the stable manifold associated with an  $L_1$  Lyapunov orbit in the six-dimensional phase space passes through the  $L_1$  gateway in forward time, enabling a spacecraft

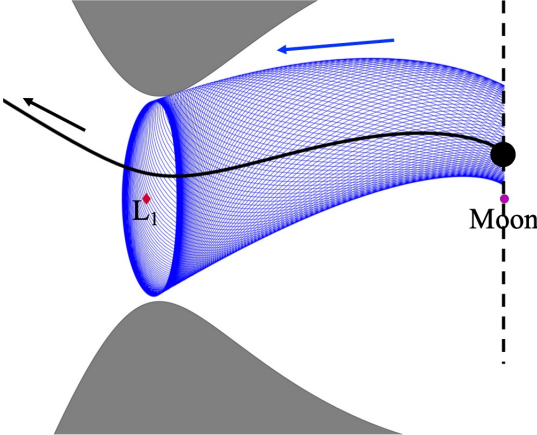


**Fig. 29 Example of a trajectory inside the stable manifold of an  $L_1$  Lyapunov orbit, passing through the  $L_1$  gateway in forward time [94].**

to naturally depart from the vicinity of the Moon and approach the Earth vicinity at that specific Jacobi constant. Thus, hyperbolic invariant manifolds play an important role in examining natural transport in a multi-body system, as well as in the design of initial guesses for trajectories that use a low-thrust propulsion system or small impulsive maneuvers.

When a periodic orbit admits stable or unstable modes, an approximation of the stable or unstable manifold is typically generated using the following procedure [74]:

- Sample a selected number of states along the periodic orbit.
- Calculate the monodromy matrix associated with each state,  $\mathbf{x}_{PO}$ , as the STM generated over one orbital period.
- Decompose the monodromy matrix into six eigenvalues and eigenvectors. A stable (or unstable) mode corresponds to a real-valued eigenvalue with a magnitude less than (or greater than) unity.
- A state  $\mathbf{x}_{S/U}$  that lies in the stable (or unstable) eigenspace of the periodic orbit is calculated by perturbing a state along the periodic orbit in the direction of the stable (or unstable) eigenvector  $\mathbf{v}_{S/U}$  by a small value  $d$ :

$$\mathbf{x}_{S/U} = \mathbf{x}_{PO} + \pm d\mathbf{v}_{S/U} \quad (116)$$

The plus or minus sign indicates that the perturbation may be applied in the  $+\mathbf{v}_{S/U}$  or  $-\mathbf{v}_{S/U}$  direction to generate each half-manifold that comprises a global stable or unstable manifold. Often, the eigenvector  $\mathbf{v}_{S/U}$  is normalized to ensure that the magnitude of the first three elements equals unity, giving the value of  $d$  physical meaning as the magnitude of the position components of the perturbation from the state along the periodic orbit.

- Propagate each state  $\mathbf{x}_{S/U}$  that lies in the stable (or unstable) eigenspace of the periodic orbit backward (or forward) in time using the equations of motion to generate a single trajectory along the global stable (or unstable) manifold.

**Implementation Note**

This step  $d$  must be selected to be sufficiently small to ensure that the linear approximation used to identify the stable (or unstable) eigenspace is reasonable, but not too small to ensure that a trajectory requires a large time interval to depart the periodic orbit in backward (or forward time). To justify that a selected value of  $d$  produces a state that lies sufficiently close to the stable (or unstable) manifold, common checks include propagating the state forward (or backward) in time to verify that the associated trajectory approaches the periodic orbit over a finite time and examining the change in the Jacobi constant across the step into the eigenspace.

**6.14 Heteroclinic and Homoclinic Connections**

Trajectories that lie along stable and unstable manifolds of either the same or different periodic orbits may intersect; the result is two types of fundamental natural transfers [74, 87]. A homoclinic connection is a natural trajectory that lies on both the stable and unstable manifolds associated with the same dynamical structure, e.g., a periodic orbit. A heteroclinic connection is a natural trajectory that lies on both the stable manifold associated with one dynamical structure and the unstable manifold associated with a different dynamical structure. These trajectories insert into and depart the associated periodic orbits after an infinite time when propagating forwards or backwards in time. Although theoretical, these two types of fundamental transfers are useful for predicting the geometry of natural transfers in higher-fidelity models and as an initial guess for designing controlled trajectories that require little propellant to depart from and arrive into specific orbits in a finite duration.

**6.15 Correcting a Transfer in the CR3BP**

One approach to computing a transfer between two states in the CR3BP with or without maneuvers uses a multiple-shooting scheme. In a foundational formulation of a multiple-shooting scheme, consider a trajectory that is discretized into  $N$  arcs with one impulsive maneuver allowed between the end of the second arc and beginning of the third arc. The  $i$ -th arc is defined by the initial state,  $\mathbf{x}_{0,i}$ , and integration time  $t_i$  for  $i = [1, N - 1]$ ; the  $N$ -th state is the final state along the trajectory and does not require an integration time. One formulation for a free variable vector that captures these states and integration times is:

$$\mathbf{V} = \left[ \mathbf{x}_{0,1}^T, \quad t_1 \quad \mathbf{x}_{0,2}^T, \quad t_2 \quad \dots, \quad \mathbf{x}_{0,N-1}^T, \quad t_{N-1} \quad \mathbf{x}_{0,N}^T \right]^T$$

and possesses a dimension of  $(7N - 1) \times 1$ . The constraint vector is formulated to enforce full state continuity between neighboring arcs that are not separated by a maneuver and continuity in position vectors, labeled  $\mathbf{r}$ , only between arcs

that are separated by impulsive maneuver. The full constraint vector is then written as

$$\mathbf{F}(\mathbf{V}) = \left[ \mathbf{x}_{f,1}^T - \mathbf{x}_{0,2}^T, \quad \mathbf{r}_{f,2}^T - \mathbf{r}_{0,3}^T, \quad \mathbf{x}_{f,3}^T - \mathbf{x}_{0,4}^T, \quad \dots, \quad \mathbf{x}_{f,N-1}^T - \mathbf{x}_{0,N}^T \right]^T$$

Additional boundary conditions may be added as needed. Furthermore, the constraint vector may possess slightly different forms when maneuvers are allowed between distinct combinations of neighboring arcs. Because the number of free variables is less than the number of independent constraints, infinite solutions may exist. The update equation in Eq. (103) is used to iteratively update the free variables from an initial guess using Newton's method until a solution is found that satisfies the constraint vector to within a specified tolerance.

#### Implementation Note

One challenge to implementing this approach is selecting the discretization of the trajectory via the number of arcs and their integration times in a manner that balances: selecting enough arcs to reduce sensitivity during corrections, not selecting too many arcs to increase the computational load, and the location of initial states along arcs in the sensitive and complex environment of cislunar space. Another significant challenge is constructing an initial guess that lies sufficiently close to the desired solution to ensure that corrections are successful.

## 7 Higher-Fidelity Modeling of Cislunar Space

Modeling the motion of a spacecraft at a high fidelity involves constructing a dynamical model that approximates the true environment as closely as possible. This environment is used to form a second-order vector differential equation that is used to generate the path of a spacecraft via numerical integration. This differential equation typically reflects the acceleration acting on the spacecraft relative to a selected central body, e.g., the Earth or Moon, in the constructed dynamical model. This section summarizes the most significant forces that may be modeled and impart an acceleration on a spacecraft, including: gravity, solar radiation pressure, atmospheric drag, and thrust applied by a propulsion system. Beyond simply including these forces in a dynamical model, deviations from the true environment still exist due to uncertainty in the parameters governing each force. Additional accelerations impacting the path of the spacecraft include random perturbations such as those that might occur due to regular momentum unloads.

### 7.1 Point Mass Gravitational Interactions

A higher-fidelity model of the dynamical environment governing a spacecraft often incorporates the point mass gravitational influence of  $N$  celestial bodies, following paths modeled using their ephemerides. Consider a spacecraft with a state vector  $\mathbf{X} = [X, Y, Z, \dot{X}, \dot{Y}, \dot{Z}]$  expressed in the GCRF, with the time derivatives calculated using an inertial observer. The acceleration  $\mathbf{a}_{pm}$  acting on the spacecraft and relative to the Earth due to the point mass gravitational influence of the Earth and  $N - 1$  additional celestial bodies is written as:

$$\mathbf{a}_{pm} = \ddot{\mathbf{R}}_{E,sc} = -G(M_E + M_{sc}) \left( \frac{\mathbf{R}_{E,sc}}{R_{E,sc}^3} \right) + G \sum_{i=1}^{N-1} M_i \left( \frac{\mathbf{R}_{sc,i}}{R_{sc,i}^3} - \frac{\mathbf{R}_{E,i}}{R_{E,i}^3} \right) \quad (117)$$

where  $G$  is the universal gravitational constant,  $M_i$  is the mass of the  $i$ -th celestial body,  $\mathbf{R}_{i,j}$  is the position vector from the center of body  $i$  to the center of body  $j$  and the subscripts ‘sc’ and ‘E’ denote the spacecraft and Earth, respectively. In reality, there are many celestial objects in the solar system that might influence the path of the spacecraft. However, some of these objects will impart a negligibly small acceleration on the spacecraft. As a result, the number of celestial bodies,  $N$  included in a high-fidelity model is often set as a finite value that is reasonably small, selected to capture only the celestial bodies that impart a significant acceleration on the spacecraft. In addition, this expression requires knowledge of the position vectors for each of the  $N$  celestial bodies. These position vectors are typically accessed using a specified DE file generated by NASA’s NAIF. Note that in these DE files, the axes of the ICRF or GCRF and the ECI system are assumed to be aligned.

### 7.2 Higher-Order Gravitational Models

Celestial bodies typically possess a gravitational model that is distinct from that of a point mass. One approach to modeling an irregular gravity field is to write the acceleration acting on the spacecraft using a spherical harmonics

expansion. Then, the acceleration acting on the spacecraft in an inertial frame is written as the vector derivative of a potential function,  $U_{grav,i}$ , such that:

$$\boldsymbol{a}_{grav,i} = \nabla U_{grav,i}$$

where  $\nabla$  is a vector derivative with respect to position coordinates, e.g.,  $\nabla(\cdot) = (\partial(\cdot)/\partial X)\hat{X} + (\partial(\cdot)/\partial Y)\hat{Y} + (\partial(\cdot)/\partial Z)\hat{Z}$ . One form of the potential function for a spacecraft due to the irregular gravity field of celestial body  $i$  is written as:

$$U_{grav,i} = \frac{GM_i}{r} \left[ 1 + \sum_{l=1}^{\infty} \sum_{m=0}^l \left( \frac{R_i}{R} \right)^l P_{l,m} (\sin(\phi)) (C_{l,m} \cos(m\lambda) + S_{l,m} \sin(m\lambda)) \right] \quad (118)$$

where  $l$  and  $m$  are integers for the ‘degree’ and ‘order’ of the model,  $R_i$  is the mean radius of body  $i$ ,  $P_{l,m}$  is an associated Legendre function,  $\phi$  and  $\lambda$  are the planetocentric latitude and longitude of the spacecraft, and  $C_{l,m}$  and  $S_{l,m}$  are the coefficients of the expansion [6]. Analysis of this expression reveals that modeling the higher-order gravitational field of a central body requires knowledge of its mean radius as well as the expansion coefficients. These coefficients are typically calculated in the scientific community using data generated from on-orbit gravity field measurements and, as a result, are only made available to a finite degree and order. This finite degree and order of the gravitational model are typically specified during modeling, along with the specific data set used to access the coefficients.

### 7.3 Solar Radiation Pressure

Solar radiation pressure (SRP) is caused by the pressure exerted on the surface of a spacecraft due to the impact of photons from the Sun. Preliminary analyses often approximate the spacecraft as a sphere, corresponding to a constant cross-sectional area facing the Sun. In this simplified model of solar radiation pressure and the spacecraft, the expression for the acceleration acting on a spacecraft due to solar radiation pressure is written as:

$$\boldsymbol{a}_{SRP,c} = \nu P_{SRP} \frac{C_R A \boldsymbol{R}_{S,sc}}{M_{sc} R_{S,sc}} \quad (119)$$

where  $\nu$  is an eclipse factor equal to 1 when the spacecraft is located in direct sunlight, 0 if the spacecraft is in shadow and in the range  $[0, 1]$  if the spacecraft is located in penumbra [6, 52]. In addition,  $P_{SRP}$  is the force per unit area due to solar radiation pressure at 1 AU,  $C_R$  is the coefficient of reflectivity with values in the range  $[0, 2]$  depending on the surface material,  $A$  is the cross-sectional area facing the Sun,  $\boldsymbol{R}_{S,sc}$  is the position vector from the Sun to the spacecraft, and  $M_{sc}$  is the mass of the spacecraft.

The acceleration due to solar radiation pressure may be calculated to a higher fidelity by modeling the spacecraft as a collection of  $P$  flat plates and with a more complex reflection model. Specifically, the accelerations due to absorption, specular reflection and diffuse reflection are modeled; for the  $i$ -th flat plate, their relative contributions are defined by the coefficients  $\rho_a^i, \rho_s^i, \rho_d^i$ , respectively, which sum to 1. Using these definitions, the cumulative acceleration due to

solar radiation pressure acting on a spacecraft, modeled as the collection of  $p$  flat plates, is:

$$\boldsymbol{a}_{SRP,f\,p} = \frac{P_{SRP}}{M_{sc}} \sum_{i=1}^p A_i \cos(\theta_i) \left[ (1 - \rho_s^i) \frac{\boldsymbol{R}_{S,sc}}{R_{S,sc}} + 2 \left( \rho_s^i \cos(\theta_i) + \frac{\rho_d^i}{3} \right) \hat{\mathbf{n}}_i \right] H(\theta_i) \quad (120)$$

where  $A_i$  is the surface area of the  $i$ -th flat plate,  $\hat{\mathbf{n}}_i$  is the unit vector perpendicular to the outward-facing surface or reflective side of the flat plate, and  $\theta_i$  is the angle between  $\hat{\mathbf{n}}_i$  and  $\boldsymbol{R}_{S,sc}$  [95, 96]. The binary function  $H(\theta_i)$  captures whether the reflective side of the flat plate is facing the Sun, i.e.,  $H(\theta_i) = 1$  when  $\cos(\theta_i) < 0$  and  $H(\theta_i) = 0$  otherwise.

Solar sails leverage this force contribution to adjust the path of a spacecraft by using a sail of significant surface area to increase the value of the cross-sectional area facing the Sun and with a high coefficient of reflectivity. By changing the attitude of the solar sail, the direction of the acceleration imparted by solar radiation pressure may be used for control.

### Implementation Note

Calculating solar radiation pressure to a high level of accuracy is complex for several reasons. First, the eclipse factor requires the accurate computation of shadow regions, using epoch-dependent calculations from the location of nearby celestial bodies. In addition, the solar flux, used to calculate the value of  $P_{SRP}$ , varies in a manner that is epoch-dependent and difficult to accurately predict. Furthermore, sufficient knowledge of the attitude and model of the spacecraft are required to accurately calculate the cross-sectional area of the spacecraft facing the Sun or, similarly, the angle between each component of the spacecraft model and the vector from the Sun to spacecraft. Finally, the coefficients that govern the reflectivity and/or absorption must be estimated using information about the surface of the spacecraft, which may change post-launch.

## 7.4 Atmospheric Drag

Atmospheric drag is the force acting on a spacecraft due to the friction of the gas in the atmosphere with the satellite. Drag is a non-conservative force that acts opposite to the motion of the spacecraft relative to the atmosphere, and is only significant when a spacecraft is located within the atmosphere of a central body. The acceleration due to atmospheric drag acting on the spacecraft may be written as:

$$\boldsymbol{a}_{drag} = -\rho V_{rel} \frac{C_D A_d \boldsymbol{V}_{rel}}{2M_{sc}} \quad (121)$$

where  $C_D$  is the drag coefficient for the spacecraft,  $\boldsymbol{V}_{rel}$  is the velocity vector of the spacecraft relative to the atmosphere,  $A_d$  is the cross-sectional area of the spacecraft that is perpendicular to  $\boldsymbol{V}_{rel}$ , and  $\rho$  is the density of the atmosphere at the location of the spacecraft [6].

### Implementation Note

Calculating the atmospheric drag acting on a spacecraft to a high accuracy is complex for several reasons. First, the coefficient of drag for a spacecraft must be estimated. Second, the cross-sectional area of the spacecraft must be calculated using information about the attitude and shape model of the spacecraft. In addition, calculating the velocity of the spacecraft relative to the atmosphere depends on atmospheric and wind models. Finally, the time-dependent density of the atmosphere depends on the altitude of the spacecraft, temperature, temporal and spatial variations in the atmosphere, solar variations, winds, tides, and magnetic fields [6].

## 7.5 Propulsion Systems

Thrusters are used to adjust a spacecraft trajectory with two types often modeled: impulsive and finite-duration thrust. Impulsive maneuvers supply a high thrust over a negligibly small time interval. Impulsive maneuvers are often approximated to first order as instantaneous changes of velocity whereas short, finite burns model the maneuver in higher-fidelity analyses. Finite-duration thrust maneuvers, however, supply thrust over a finite and non-negligible duration. Through each of these maneuvers, the mass of the spacecraft decrements with propellant use. One approach to modeling both the acceleration and the mass flow rate involves modeling each of the thrust and specific impulse, i.e.,  $I_{sp}$ , as polynomials that depend on the thruster pressure and temperature [13]. The thrust magnitude equals:

$$F_T = C_1 + C_2 P + \left( C_3 + C_4 P + C_5 P^2 + C_6 P^{C_7} + C_8 P^{C_9} + C_{10} P^{C_{11}} + C_{12} C_{13}^{C_{14} P} \right) \left( \frac{T}{T_{ref}} \right)^{1+C_{15}+C_{16}P} \quad (122)$$

where  $T$  is the temperature in Celsius,  $T_{ref}$  is a reference temperature in Celsius,  $P$  is the pressure in kPa, and  $C_i$  are coefficients associated with specific engine models. The specific impulse, calculated in seconds, is equal to:

$$I_{sp} = K_1 + K_2 P + \left( K_3 + K_4 P + K_5 P^2 + K_6 P^{K_7} + K_8 P^{K_9} + K_{10} P^{K_{11}} + K_{12} K_{13}^{K_{14} P} \right) \left( \frac{T}{T_{ref}} \right)^{1+K_{15}+K_{16}P} \quad (123)$$

where  $K_i$  are coefficients associated with specific engine models. Using these quantities, the mass flow rate in kg/s is:

$$\dot{m} = f_d \frac{F_T}{I_{sp} g} \quad (124)$$

where  $f_d$  is the duty cycle factor, the fraction of the maneuver time that thrusters are activated, and  $g$  is the gravitational acceleration on the Earth's surface,  $9.81 m/s^2$ . The acceleration imparted by the propulsion system equals:

$$\mathbf{a}_{thrust} = \frac{f_s f_d F_T}{M_{sc}} \hat{\mathbf{u}} \quad (125)$$

where  $f_s$  is the thrust scale factor and  $\hat{\mathbf{u}}$  is the thrust direction in the coordinate frame of interest.

## 7.6 Relative Contributions of Each Force

When modeling the motion of a spacecraft in cislunar space, the analyst must construct a dynamical model of desired fidelity, dependent on the application or task. For instance, during trajectory design, the analyst might first select candidate mission orbits or construct an initial guess for a trajectory in a low-fidelity model to facilitate rapid analysis and then use a high-fidelity model to accurately compute a trajectory and maneuvers. To construct a suitable dynamical model, it is helpful to first assess the relative contributions of the most significant forces acting on a spacecraft located within cislunar space. To reduce the complexity of this analysis, this section presents a preliminary and limited visual assessment of the magnitudes of the acceleration due to each of: the combined point mass gravity of the Earth and Moon, higher-order gravitational models of the Earth and Moon, the point mass gravity of the Sun, and SRP. Throughout this section, the magnitude of the acceleration due to the each of the selected forces is calculated using GMAT for a variety of position vectors, defined relative to the Earth-Moon barycenter in the Earth-Moon rotating frame, at a single epoch of January 1st, 2025 00:00:00.000 UTC [13]. The components of these position vectors are defined within the following ranges:

$$x \in [-4.5 \times 10^5, 5.5 \times 10^5] \text{ km} = [-1.179, 1.441] \text{ nondim.}$$

$$y \in [-5 \times 10^5, 5 \times 10^5] \text{ km} = [-1.310, 1.310] \text{ nondim.}$$

$$z \in [-5 \times 10^5, 5 \times 10^5] \text{ km} = [-1.310, 1.310] \text{ nondim.}$$

Absolute or relative magnitudes of the acceleration vectors at these position vectors are then visualized using a blue to yellow color scale on a two-dimensional contour plot. For each plot, position vector components within the Earth-Moon plane are represented on the vertical and horizontal axes and nondimensionalized by the instantaneous separation between the Earth and Moon at the specified epoch, i.e., in a pulsating Earth-Moon rotating frame where the locations of the Earth and Moon are fixed.

### 7.6.1 Earth-Moon Point Mass Gravitational Interactions

First, consider the acceleration of a spacecraft due to the combined point mass gravity of the Earth and the Moon for an Earth-centered model and a Moon-centered model, i.e., when the acceleration is expressed relative to either celestial body. Recall that the inertial acceleration of a spacecraft due to the point mass gravitational influence of the Earth and Moon relative to the Earth is:

$$\mathbf{a}_{pm,E} = \ddot{\mathbf{R}}_{E,sc} = -G(M_E + M_{sc}) \left( \frac{\mathbf{R}_{E,sc}}{R_{E,sc}^3} \right) + GM_M \left( \frac{\mathbf{R}_{sc,M}}{R_{sc,M}^3} - \frac{\mathbf{R}_{E,M}}{R_{E,M}^3} \right)$$

For a Moon-centered model, the inertial acceleration of a spacecraft due to the point mass gravitational influence of the Earth and Moon is:

$$\mathbf{a}_{pm,M} = \ddot{\mathbf{R}}_{M,sc} = -G(M_M + M_{sc}) \left( \frac{\mathbf{R}_{M,sc}}{R_{M,sc}^3} \right) + GM_E \left( \frac{\mathbf{R}_{sc,E}}{R_{sc,E}^3} - \frac{\mathbf{R}_{M,E}}{R_{M,E}^3} \right)$$

Each of these equations is evaluated for various position vectors that are defined in the Earth-Moon rotating frame with  $z = 0$ , using DE421 ephemerides to calculate the distance between the Earth and Moon on January 1st, 2025 00:00:00.000 UTC. The magnitudes of  $\mathbf{a}_{pm,E}$  and  $\mathbf{a}_{pm,M}$  are then plotted in Figure 30a) and b), respectively. In each plot, contours of the magnitude of the acceleration are represented using a logarithmic scale. The Earth and Moon are indicated using black markers and the equilibrium points are plotted as red markers. The relative acceleration due to the point mass gravitational interactions of both the Earth and Moon is symmetric about  $\hat{x}$ , regardless of whether it is measured from the Earth or Moon. However, differences in the acceleration magnitudes are most apparent near the  $L_1$  and  $L_2$  gateways.

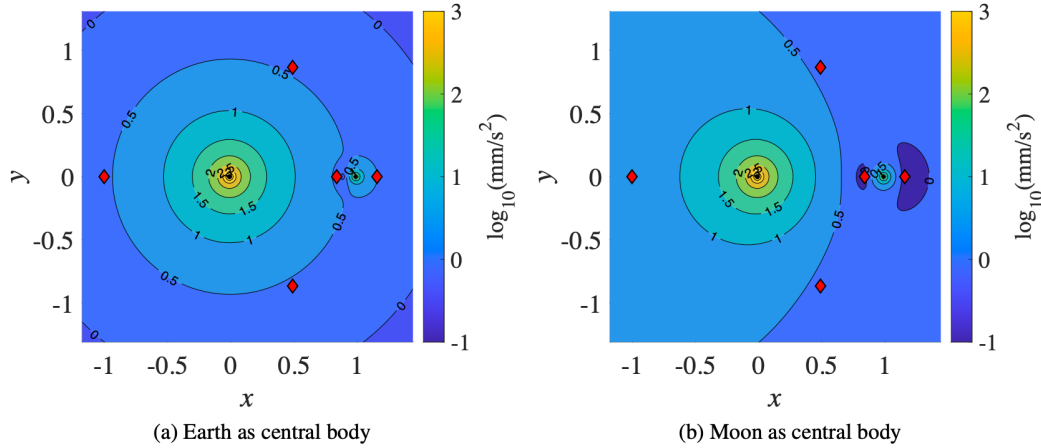


**Fig. 30 Magnitude of the point mass gravitational acceleration of the Earth and Moon, measured relative to either the Earth or the Moon.**

### 7.6.2 Higher-Order Gravitational Models

Some astrodynamics packages support modeling a higher-order gravitational model of only the central body, e.g., integrating the state of a spacecraft with respect to the Earth using a higher-order gravitational model of the Earth and a point mass model of the Moon. In this case, for the analysis of a trajectory that travels between the vicinity of the Earth and Moon, it may be desirable to switch the central body for numerical integration, and thus, the higher-order gravitational model, for different regions of the trajectory. Thus, the analyst may need to determine when to perform this switch. Alternatively, the analyst may simply wish to define a model of sufficient fidelity when generating an entire trajectory. To support such an analysis, this subsection examines the contribution of higher-order gravitational models

of the Earth and Moon to the acceleration of a spacecraft in the Earth-Moon system.

The acceleration of a spacecraft due to higher-order gravitational models of the Earth and Moon are evaluated as percentages of the combined point mass gravitational influence of the Earth and Moon. These percentages, labeled  $\delta_E$  and  $\delta_M$  for a higher-order gravitational model of the Earth and Moon, respectively, are defined as:

$$\delta_E = \frac{\|\mathbf{a}_{grav,E} - \mathbf{a}_{pm,E}\|}{\|\mathbf{a}_{pm,E}\|} \times 100\%$$

$$\delta_M = \frac{\|\mathbf{a}_{grav,M} - \mathbf{a}_{pm,M}\|}{\|\mathbf{a}_{pm,M}\|} \times 100\%$$

where  $\mathbf{a}_{grav,i}$  is the acceleration of a spacecraft due to a higher-order gravitational model of the central body and point mass model of the second body. Acceleration data is generated in GMAT for an Earth-centered model with a  $36 \times 36$  gravity field model of the Earth and for a Moon-centered model with a  $100 \times 100$  gravity field model of the Moon. These acceleration vectors are calculated for a variety of position vectors in each of the  $xy$  and  $xz$  planes of the Earth-Moon rotating frame using DE421 ephemerides [13]. Using this approach, the relative contribution of the higher-order gravitational model of the Earth,  $\delta_E$ , is plotted in Figure 31 using a logarithmic scale, including views of along each of the  $xy$  and  $xz$  planes of a pulsating Earth-Moon rotating frame. Next, the contribution of the higher-order gravitational model of the Moon,  $\delta_M$ , is plotted in Figure 32 using a coloring scheme consistent with Figure 31. Examination of these plots reveals that the acceleration due to higher-order gravitational models of the central body is generally much smaller than the acceleration due to the combined point mass gravity of the Earth and Moon. In general, the percentage of the magnitude of the higher-order gravitational models of the central body is greatest at small separations from the central body, and is smallest at small separations from the secondary body.

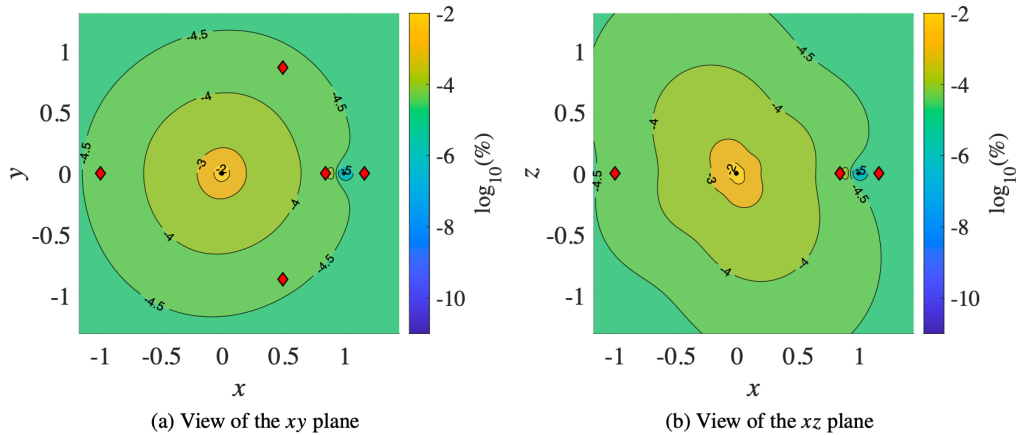


**Fig. 31 Magnitude of the change in the acceleration, measured relative to the Earth, due to the higher-order gravity field of the Earth as a percentage of the combined point mass gravitational acceleration of the Earth and Moon.**

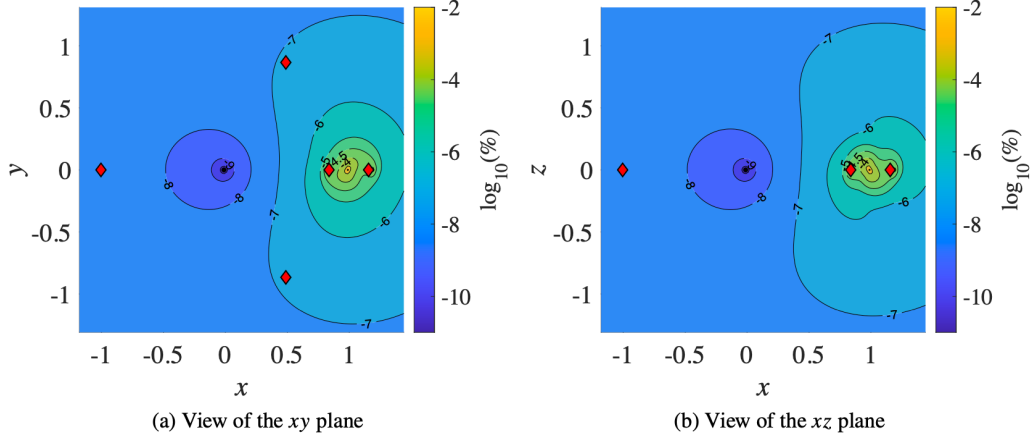


**Fig. 32 Magnitude of the change in the acceleration, measured relative to the Moon, due to the higher-order gravity field of the Moon as a percentage of the combined point mass gravitational acceleration of the Earth and Moon.**

To assess regions where the relative contribution of the higher-order gravitational model of the Earth is greater than the higher-order gravitational model of the Moon, and vice versa, the ratio of the two percentages are evaluated. This ratio is defined as  $\delta_E/\delta_M$  and is plotted using a logarithmic scale in Fig. 33, including views of the  $xy$  and  $xz$  planes of the pulsating Earth-Moon rotating frame. Note, however, that these two relative acceleration contributions are measured from distinct bodies. In Fig. 33, a contour line of 2 indicates where  $\delta_E$  is 100 times greater than  $\delta_M$ . Conversely, a contour line of -2 indicates where  $\delta_M$  is 100 times greater than  $\delta_E$  whereas the contour at zero indicates where  $\delta_E = \delta_M$ . These contour lines may support decision making related to determining when to model the Earth or Moon as the central body with a higher-order gravitational model in different regions of the Earth-Moon system. For the explored epoch and subset of the solution space, the region where the relative contribution of the higher-order gravitational model of

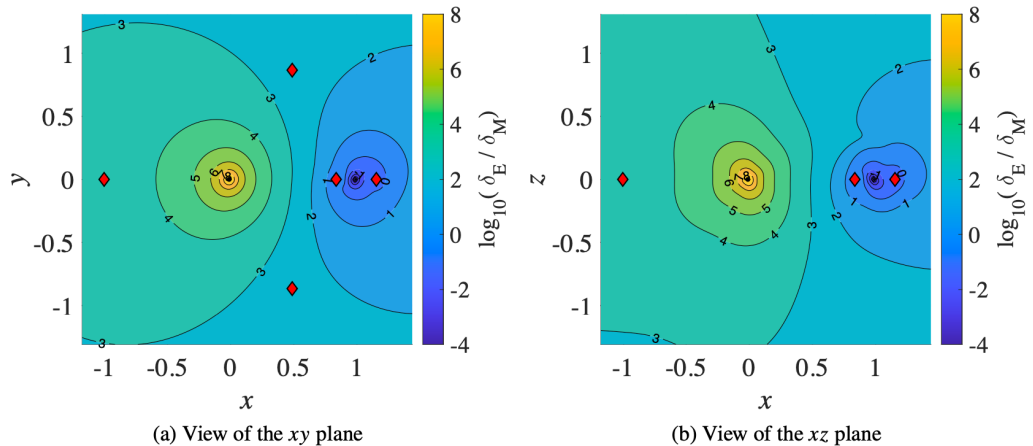


**Fig. 33 Ratio of the magnitudes of the acceleration changes due to the higher-order gravity field of the Earth and Moon.**

the Moon is greater than the higher-order gravitational model of the Earth, i.e.,  $\delta_M > \delta_E$ , encompasses the Moon asymmetrically and extends further from the Moon on the opposite side to the Earth, slightly beyond  $L_2$ .

### 7.6.3 Point Mass Gravitational Influence of the Sun

The magnitude of the acceleration of a spacecraft relative to the Earth or Moon due to the point mass gravity of the Sun depends on the specific central body due to the indirect gravitational interactions of the Sun, Earth, and Moon [6]. For an Earth-centered model, the contribution to the acceleration of a spacecraft due to the point mass gravity of the Sun is equal to

$$\mathbf{a}_{add,S,E} = GM_S \left( \frac{\mathbf{R}_{sc,S}}{R_{sc,S}^3} - \frac{\mathbf{R}_{E,S}}{R_{E,S}^3} \right)$$

The magnitude of this acceleration across the Earth-Moon system is plotted in Fig. 34, including views of both the  $xy$  and  $xz$  planes of the Earth-Moon rotating frame. For a Moon-centered model, the contribution to the acceleration of a spacecraft due to the point mass gravity of the Sun is equal to

$$\mathbf{a}_{add,S,M} = GM_S \left( \frac{\mathbf{R}_{sc,S}}{R_{sc,S}^3} - \frac{\mathbf{R}_{M,S}}{R_{M,S}^3} \right)$$

The magnitude of this acceleration is plotted in Figure 35 using a color scale consistent with Fig. 34. On the selected epoch of January 1st, 2025 00:00:00.000 UTC, the Sun is located approximately -13.904 degrees from the  $x$ -axis, measured counterclockwise, and 4.9442 degrees above the  $xy$ -plane. As depicted in Figs. 34 and 35, the magnitude of the acceleration due to the point mass gravity of the Sun is similar for similar deviations from each central body in the two models. As expected, the contribution of the point mass gravity of the Sun is smallest close to the central body and greater at larger distances from the central body. Accordingly, increased sensitivity may be observed during numerical corrections of continuous trajectories in an ephemeris model at greater distances from the central body when using an initial guess generated without considering the gravitational influence of the Sun.

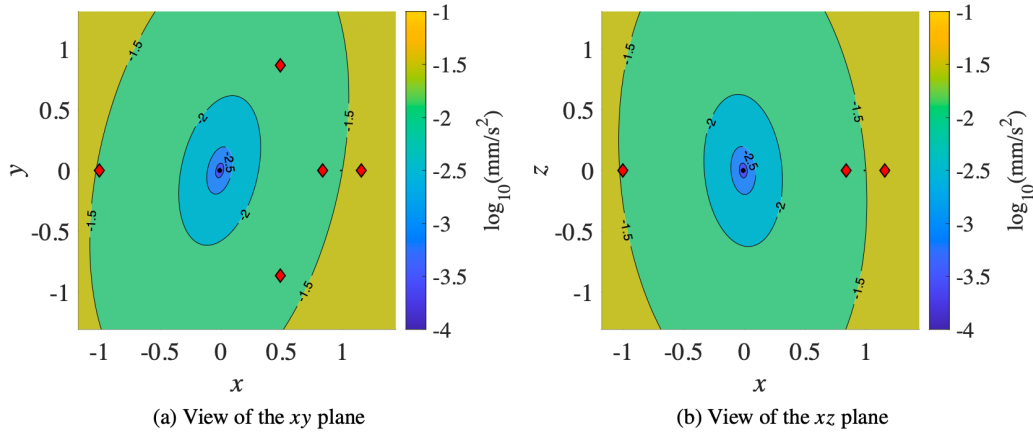


**Fig. 34 Magnitude of the point mass gravity of the Sun in the Earth-Moon system for an Earth-centered model.**

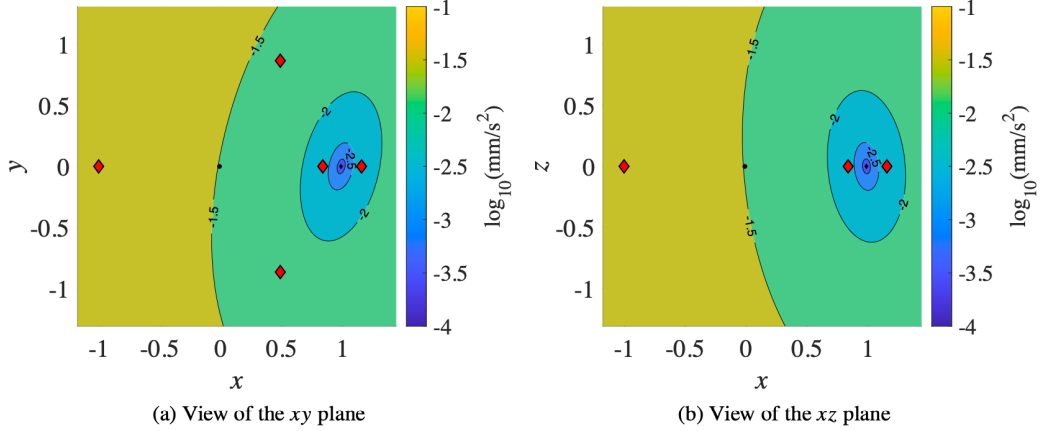


**Fig. 35 Magnitude of the point mass gravity of the Sun in the Earth-Moon system for a Moon-centered model.**

#### 7.6.4 Solar Radiation Pressure

The acceleration of a spacecraft due to an approximate cannonball model of SRP is independent of the central body of numerical integration [13]. The presented analysis considers a 500 kg spacecraft with an effective surface area of  $10 \text{ m}^2$  and coefficient of reflectivity of 1.8. Eclipse modeling of the Earth and Moon is performed in GMAT using a dual cone approximation [97]. The magnitude of the acceleration of the spacecraft with the defined properties due to SRP is plotted in Fig. 36. Compared to the other higher-fidelity model accelerations, the acceleration due to SRP varies less within the vicinity of the Earth-Moon system, of course, with the exception of within the shadows of the Earth and Moon. However, this acceleration is generally on the order of  $10^{-4}$ : orders of magnitude less than the gravitational influence of the Sun beyond the close vicinity of each central body, but on a similar order of magnitude at small distances from either the Earth or Moon. This value is also orders of magnitude lower than the acceleration due to the point mass gravitational interactions of the Earth and Moon beyond the vicinity of each central body.

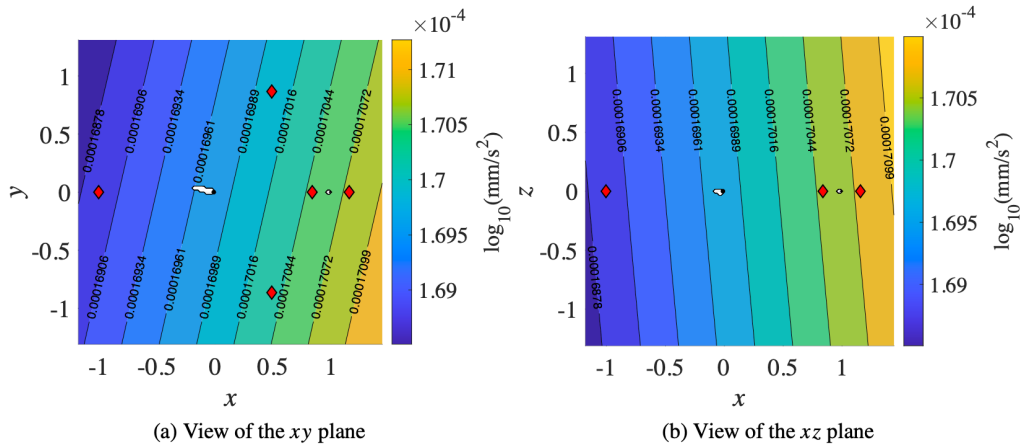


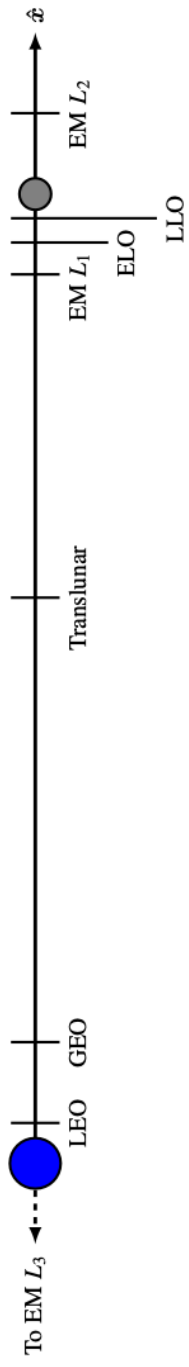
**Fig. 36 Magnitude of the acceleration due to SRP in the Earth-Moon system.**

### 7.6.5 Summary

To compare the relative contribution of each investigation higher-fidelity model force in more detail, the magnitude of the acceleration of a spacecraft due to each force is sampled at various locations within the Earth-Moon system. Table 7 lists the magnitude of the acceleration of a spacecraft due to each of the explored higher-fidelity model forces, indicating the central body of the dynamical model. Solar radiation pressure is modeled using the same spacecraft parameters listed in Section 7.6.4. Each sample is taken along the  $\hat{x}$  axis, with the exception of  $L_4$  and  $L_5$ , which possess nonzero values of  $y$  in the Earth-Moon rotating frame. Also illustrated in Table 7 are the approximate locations, to scale, of the sample points within the Earth-Moon system; however, the sizes of the Earth and Moon and the relative distances are not drawn to scale. This figure uses the following abbreviations: low Earth orbit (LEO), geostationary Earth orbit (GEO), low lunar orbit (LLO), elliptical lunar orbit (ELO).

**Table 7** Magnitude of the contribution to the acceleration measured at various locations in the Earth-Moon system at an epoch of January 1st, 2025 00:00:00 UTC. All data reported in units of mm/s<sup>2</sup>. Diagram of approximate locations of sample locations.

Sample location	Earth-centered model			Moon-centered model		
	Earth-Moon point mass	Earth gravity field	Sun point mass	Earth-Moon point mass	Moon gravity field	Sun point mass
LEO	8.676 × 10 <sup>3</sup>	1.122 × 10 <sup>1</sup>	5.528 × 10 <sup>-4</sup>	8.674 × 10 <sup>3</sup>	3.398 × 10 <sup>-9</sup>	3.070 × 10 <sup>-2</sup>
GEO	2.242 × 10 <sup>2</sup>	7.485 × 10 <sup>-3</sup>	3.440 × 10 <sup>-3</sup>	2.215 × 10 <sup>2</sup>	4.152 × 10 <sup>-9</sup>	2.781 × 10 <sup>-2</sup>
Translunar	1.084 × 10 <sup>1</sup>	1.781 × 10 <sup>-5</sup>	1.560 × 10 <sup>-2</sup>	8.071 × 10 <sup>0</sup>	1.360 × 10 <sup>-8</sup>	1.565 × 10 <sup>-2</sup>
ELO	4.679 × 10 <sup>0</sup>	1.460 × 10 <sup>-6</sup>	2.920 × 10 <sup>-2</sup>	7.448 × 10 <sup>0</sup>	9.127 × 10 <sup>-6</sup>	2.054 × 10 <sup>-3</sup>
LLO	1.223 × 10 <sup>3</sup>	1.137 × 10 <sup>-6</sup>	3.109 × 10 <sup>-2</sup>	1.226 × 10 <sup>3</sup>	2.396 × 10 <sup>-1</sup>	1.643 × 10 <sup>-4</sup>
EM L <sub>1</sub>	2.351 × 10 <sup>0</sup>	2.142 × 10 <sup>-6</sup>	2.652 × 10 <sup>-2</sup>	4.179 × 10 <sup>-1</sup>	3.619 × 10 <sup>-7</sup>	4.732 × 10 <sup>-3</sup>
EM L <sub>2</sub>	3.234 × 10 <sup>0</sup>	5.985 × 10 <sup>-7</sup>	3.652 × 10 <sup>-2</sup>	4.647 × 10 <sup>-1</sup>	2.446 × 10 <sup>-7</sup>	5.268 × 10 <sup>-3</sup>
EM L <sub>3</sub>	2.749 × 10 <sup>0</sup>	1.145 × 10 <sup>-6</sup>	3.080 × 10 <sup>-2</sup>	5.518 × 10 <sup>0</sup>	8.202 × 10 <sup>-10</sup>	6.205 × 10 <sup>-2</sup>
EM L <sub>4</sub>	2.769 × 10 <sup>0</sup>	1.225 × 10 <sup>-6</sup>	1.783 × 10 <sup>-2</sup>	2.769 × 10 <sup>0</sup>	3.355 × 10 <sup>-9</sup>	2.472 × 10 <sup>-2</sup>
EM L <sub>5</sub>	2.769 × 10 <sup>0</sup>	1.122 × 10 <sup>-6</sup>	2.462 × 10 <sup>-2</sup>	2.769 × 10 <sup>0</sup>	3.600 × 10 <sup>-9</sup>	1.795 × 10 <sup>-2</sup>



## 7.7 Useful Heuristics for Defining High-Fidelity Dynamical Models

Building upon the analysis performed within this chapter, Table 8 lists heuristics for defining high-fidelity dynamical models for a spacecraft at various locations within cislunar space.

**Table 8 Recommended gravity fields for various orbit regimes.**

Orbit Regime	Center	Radius $r$ (km)	Earth gravity field	Moon gravity field	Other bodies' gravity fields
Earth LEO	Earth	$r \lesssim 8,371$	$\geq 36 \times 36$	point mass	point mass
Earth GEO	Earth	$8,371 \lesssim r \lesssim 42,162$	$\geq 21 \times 21$	point mass	point mass
Cislunar	Earth	$42,162 \lesssim r \lesssim 323,000$	$8 \times 8$ to $21 \times 21$	point mass	point mass
Lunar (EML1)	Moon	$2,231 \lesssim r \lesssim 61,350$	$8 \times 8$	point mass	point mass
Lunar (low orbit)	Moon	$r \lesssim 2,231$	$8 \times 8$	$\geq 100 \times 100$	point mass
Translunar (EML2)	Moon	$2,231 \lesssim r \lesssim 61,350$	$8 \times 8$	point mass	point mass
Lunar (elliptical)	Moon	$r \lesssim 10,000$	$8 \times 8$	$\geq 100 \times 100$	point mass

## 8 Use Case and Practical Considerations

This section demonstrates the practical implementation of some of the outlined coordinate systems, transformations, time descriptions, numerical methods and modeling approaches in the context of a cislunar mission concept to reach a libration point orbit. This use case is modeled after a mission concept that involves a spacecraft operating as a lunar communications relay; such a concept has previously been explored from a mission design perspective by NASA GSFC. This section specifically focuses on the following aspects of this use case:

- Establishing the scenario and presenting sample mission requirements that govern trajectory and maneuver design.
- Designing a mission orbit near a libration point in cislunar space subject to hardware and mission requirements: from preliminary analysis in a low-fidelity model to higher-fidelity analysis in NASA GSFC's GMAT software.
- Designing straightforward transfer options from a low Earth orbit to the selected mission orbit using NASA GSFC's GMAT.
- Designing maneuvers to maintain the path in the vicinity of the selected mission orbit.

In the current version of this document, these aspects of the use case are discussed and solved using approaches that are designed to be implemented by a non-expert; more complex strategies or advanced analyses will be added as supplements in future versions.

### 8.1 Scenario Overview

Consider a concept involving a lunar relay communications spacecraft, used to support surface operations near the lunar south pole. In this scenario, the spacecraft is assumed to possess an initial wet mass of 500 kg to accommodate a substantial propellant mass and communications instrumentation. The presumed requirements for a mission orbit for this communications relay include:

- Maintaining constant communications with Earth ground stations.
- Ensuring coverage and visibility to a lunar south pole station for at least 50% of the orbit period. Coverage is defined to occur at an elevation angle above 10 deg as measured from the local horizon on the lunar surface to account for crater and other line of sight obstructions.
- Remaining within a range of less than 100,000 km from the lunar south pole station. Such a limitation may be imposed based on both relay spacecraft and lunar base communication systems performance.
- Station-keeping and insertion maneuvers must not exceed a total of 100 m/s and 1 km/s, respectively. These values are derived from previous analyses by NASA GSFC for missions to Earth-Moon  $L_1$  and the THEMIS/ARTEMIS missions. This constraint is also connected with the propulsion system selection, stationkeeping method, and mission lifetime.

## 8.2 Constructing a Reference Mission Orbit

The first analysis in this use case involves selecting a reference mission orbit that satisfies relevant mission requirements. Due to the complexity and sensitivity of the cislunar dynamical environment, the astrodynamics and trajectory design communities often use a rapid and informed procedure that is based on dynamical systems techniques. This approach relies on: an initial analysis of fundamental solutions in the Earth-Moon Circular Restricted Three-Body Problem (CR3BP) or other low to medium-fidelity models, identification of candidate fundamental solutions for further analysis, identification of nearby continuous paths that resemble the candidate orbit/s in an ephemeris model of sufficient fidelity, evaluation of more complex and epoch-dependent constraints, and identification of a reference mission orbit.

### 8.2.1 Rapid Preliminary Analysis in a Low-Fidelity Model

The first step in reference mission orbit design involves examining fundamental solutions in a region of interest in cislunar space for their potential to satisfy high-level geometric requirements. First, a region of interest must be selected. To ensure constant communication with the Earth and to reduce the distance between the Earth and spacecraft for communications, the Earth-Moon  $L_1$  region is examined; note that some motions near  $L_2$  may satisfy the requirements listed in Sec. 8.1, but these orbits exist farther from the Earth than those near  $L_1$  and may influence communications.

In the vicinity of Earth-Moon  $L_1$ , there are a wide variety of bounded motions. To simplify the analysis, it is common to begin by focusing on well-known periodic orbits. Four well-known periodic orbit families from the CR3BP and near Earth-Moon  $L_1$  are analyzed in this example: the Lyapunov, vertical, southern halo, and axial orbits. Selected periodic orbits along each of these families are depicted in Fig. 22 in Sec. 6.11. Note that the northern branch of the  $L_1$  halo orbit family is not examined due to the location of apolune above the lunar equatorial plane, meaning that a spacecraft following a path that resembles an  $L_1$  northern halo orbit in a higher-fidelity model of the Earth-Moon system would spend the majority of each orbit period located above the equatorial plane.

### Implementation Notes: Computing Periodic Orbit Families in the CR3BP

These four periodic orbit families have been computed by first using a corrections algorithm to correct an initial guess in the Earth-Moon CR3BP and in the Earth-Moon rotating frame. These initial guesses, in the form of a state and orbit period, have been identified via linearization of the local neighborhood of an equilibrium point and examining bifurcations along known periodic orbit families. They are then corrected using multiple-shooting in custom codes. Each trajectory is numerically generated using an explicit embedded Runge-Kutta Prince-Dormand (8, 9) method, accessed via C++ using the GNU Scientific Library, for numerical integration with absolute and relative state tolerances of  $10^{-13}$  and  $10^{-14}$ , respectively. Future versions of this document will explain and demonstrate options for selecting numerical integration schemes and tolerances. Following corrections, states and periods that produce a periodic orbit, to within a tolerance of  $10^{-12}$  are recovered. For the reader recreating this example, states and orbit periods for one member along each family appear in Table 3 in Sec. 6.11. Given one corrected periodic orbit, pseudo-arclength continuation is used to generate additional members of a family, as outlined in Section 6.10. Of course, if this process is employed regularly, specialized design tools and databases are useful to reduce the time required to access members of common families. For example, NASA GSFC's Navigation and Mission Design branch uses a catalog of periodic orbits within the Adaptive Trajectory Design (ATD) tool created with Purdue University [79, 98]; researchers in the academic community often create their own databases for internal or external use as well [99].

Let's examine periodic orbits within the four selected families for their potential to satisfy significant high-level geometric requirements; performing this initial analysis in the CR3BP rather than an ephemeris model reduces the complexity and dimensionality of the problem. In this use case, lunar south pole coverage is assessed using a straightforward estimate of the elevation angle from the lunar south pole to states along the periodic orbit, expressed in the Earth-Moon rotating frame. In addition, the range from the lunar south pole is assessed and compared to the associated constraint. To rapidly estimate the elevation angle and range for states along these orbits, the lunar south pole station is initially assumed to lie at a relative position vector of  $[0, 0, -1737]$  km with respect to the Moon. Of course, the lunar equatorial plane is inclined relative to the Earth-Moon plane and this inclination does evolve over time. However, this preliminary estimate of the lunar south pole location simplifies the initial identification of candidate orbits for further analysis within a higher-fidelity model that uses the epoch-dependent and exact location of the lunar south pole. Then, the elevation angle,  $\phi_{el}$ , and range,  $\|r_{SP,sc}\|$ , are defined as displayed graphically in Fig. 37.

Following this simplified approach, the lunar coverage and range is computed for periodic orbits within the four selected families in the Earth-Moon CR3BP. Fig. 38 displays for the  $L_1$  southern halo orbits: a) selected members displayed in the rotating frame and colored by the orbital period, b) curves displaying the elevation angle from the approximate lunar south pole along each orbit and using the same color scheme, and c) a summary of the maximum

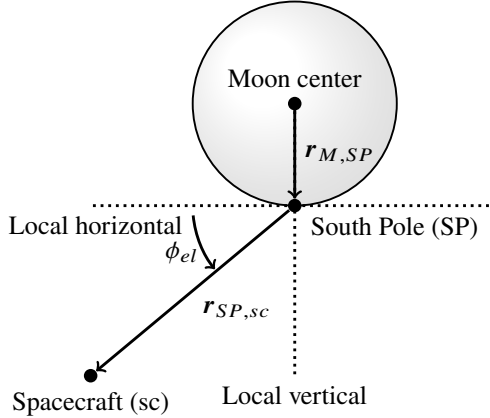


**Fig. 37 Approximating the elevation angle and range of the spacecraft from the south pole.**

range, minimum altitude and visibility of the lunar south pole across the family. Analysis of this figure reveals that members that exist closer to the Moon with a lower perilune admit elevation angles above 10 degrees for a higher fraction of the orbit period. This characteristic is consistent with changes in the geometry along the family. Specifically, members with a higher orbit period that exist close to the bifurcation with the  $L_1$  Lyapunov orbit family lie close to the Earth-Moon plane. As a result, these members possess a negative elevation angle. At the other end of the family, where the  $L_1$  NRHOs exist, members possess a low perilune, high lunar eccentricity and inclination relative to the Earth-Moon plane. As a result, their perilune is located above the northern hemisphere of the Moon and a spacecraft would spend less time at elevation angles below 10 degrees. Fig. 39 displays the periodic orbits and associated elevation angle curves for the Lyapunov, vertical and axial orbit families. The Lyapunov orbits do not provide any south pole coverage, while the vertical and axial orbits do not provide coverage for more than 50% of the orbit period; such a result is expected given their geometry relative to the  $xy$ -plane of the Earth-Moon rotating frame. Based on this analysis, a periodic orbit in the  $L_1$  southern halo family is examined further. Of course, these orbits do not span the full array of candidate orbits for further analysis. For instance, quasi-halo orbits that correspond to bounded motions in the vicinity of the halo orbits, may offer additional candidates. For the purposes of this example and based on the presented analysis, let's select an 11.1 day period southern halo periodic orbit that is estimated to offer 66.6% visibility, i.e., an estimated elevation angle from the south pole of at least 10 deg for 66.6% of the orbit period.

The selected candidate orbit is then used to recover a nearby continuous trajectory in an ephemeris model and its properties are examined in a higher-fidelity model for comparison to the mission constraints. An important part of this step is specifying a suitable dynamical model of sufficient fidelity for further analysis, without dependency on specific spacecraft parameters that may not be selected. For instance, a point mass ephemeris model incorporating the gravity of the Earth, Moon, and Sun captures the most significant components of a high-fidelity model; with an approximate form factor and mass are known, a spherical SRP model is also incorporated. A continuous solution that lies close to

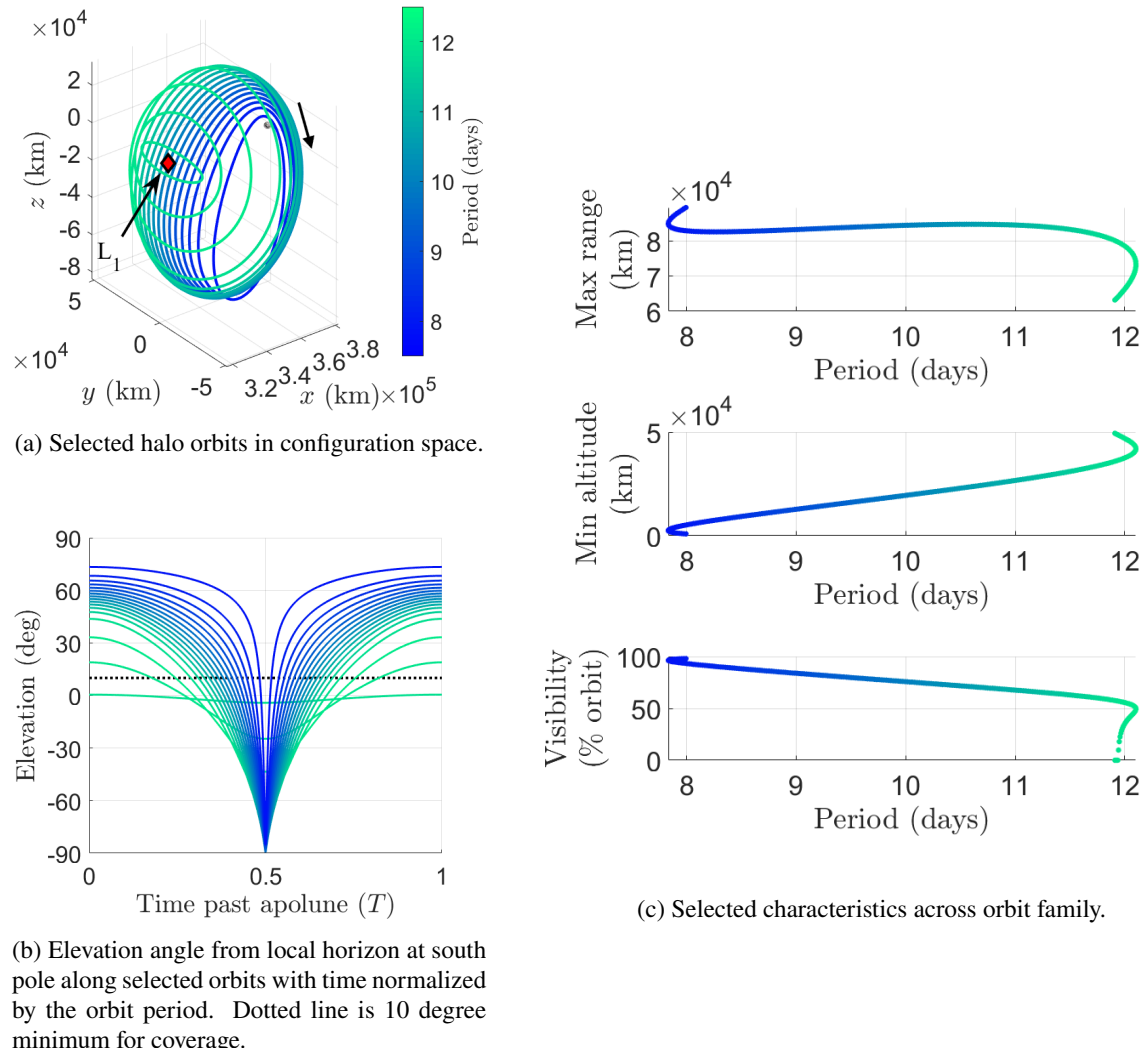


**Fig. 38 Coverage and geometric properties of the  $L_1$  southern halo orbits: a) plotted in the Earth-Moon rotating frame, b) elevation angle along selected members of the family, and c) relevant characteristics across the family.**

the original periodic orbit in the Earth-Moon rotating frame is then recovered in this model. Common approaches to targeting such trajectories in ephemeris models include 1) using a single-shooting scheme in a high-fidelity modeling software such as GMAT, and 2) using a multiple-shooting scheme in custom codes. Alternative approaches exist, such as using collocation in custom codes or in the CSALT tool within GMAT, but are not presented within this version of the document.

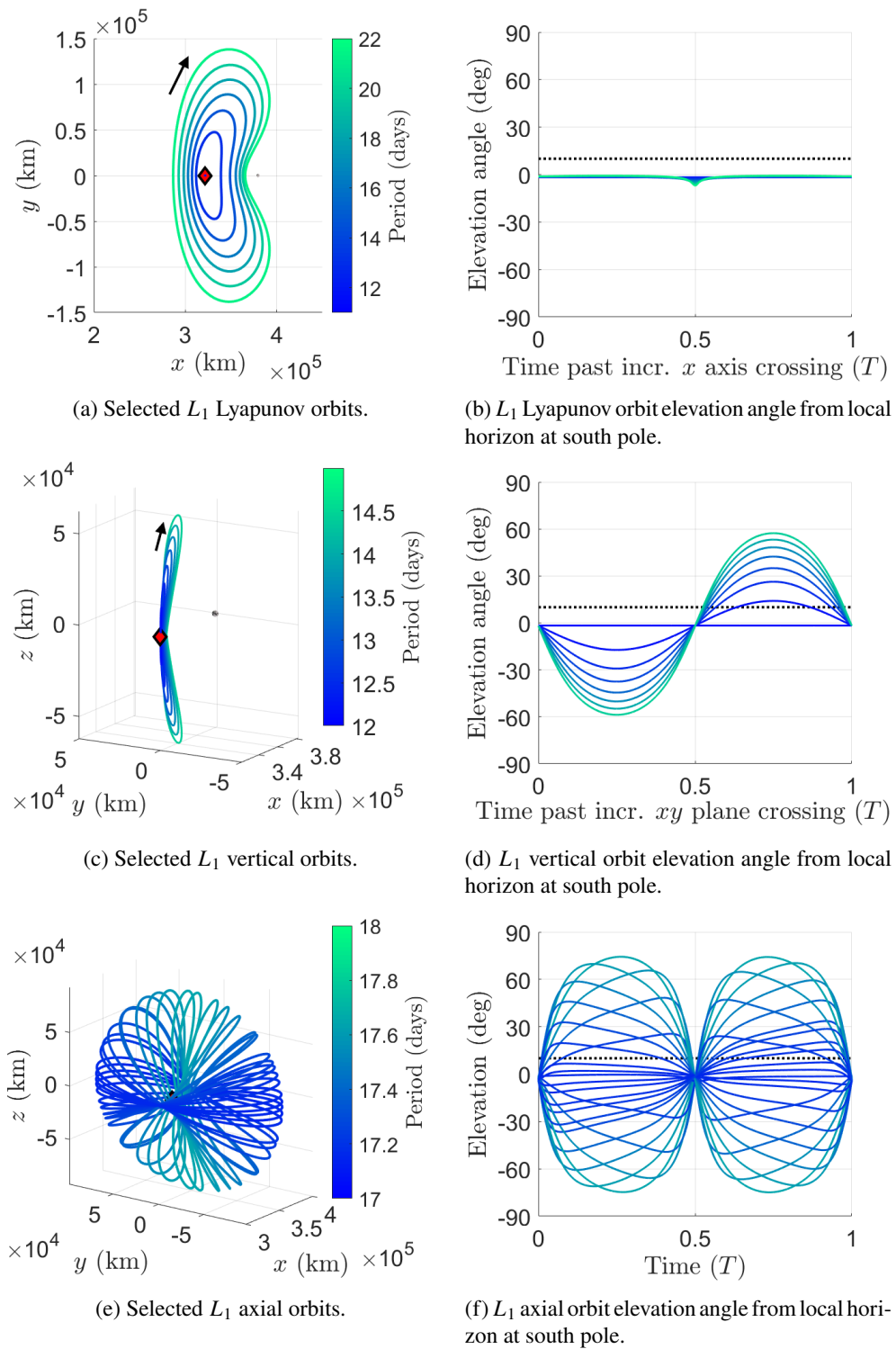


**Fig. 39** Orbits and coverage curves for the  $L_1$ : a,b) Lyapunov, c,d) vertical and e,f) axial periodic orbit families.

### 8.2.2 Relevant State Transformations

Before implementing either of the corrections approaches, nondimensional states along the periodic orbit in the CR3BP are converted into dimensional states in either the Earth-Moon rotating frame or the GCRF to support initial guess construction and targeting in an ephemeris model. To demonstrate these transformation steps, consider a state located at the leftmost  $xz$ -plane crossing of the selected 11.1 day period southern halo orbit in the Earth-Moon rotating frame. The truncated value of this nondimensional state vector is equal to

$$\mathbf{x}_{EMB,PO}^{EMR} = [0.849895, 0, -0.175343, 0, 0.262953, 0]^T$$

in the Earth-Moon rotating frame and relative to the Earth-Moon barycenter. In this example, an initial epoch of 2460676.5 MJD UTC, or January 1, 2025 00:00:00.000 UTC, is assumed.

To convert position and velocity vectors in the Earth-Moon rotating frame to the GCRF, the expressions in Eq. 74 and 75 are used to implement the transformations. Note that the final terms in these equations are the position and velocity vectors of the Earth-Moon barycenter in the GCRF. A simple approach that is often employed is to first rewrite the nondimensional position vector relative to the center of the Earth (as opposed to relative to the Earth-Moon barycenter). This step involves simply adding  $\mu$  to the  $x$ -coordinate of the nondimensional state vector. In addition, the Moon is assumed to follow a perfect circular orbit relative to the Earth, consistent with the assumptions used in the CR3BP. Such an assumption is not employed in software such as GMAT; rather, the final term in Eq. 75 is directly calculated using ephemerides, which reflects the noncircular orbit of the Moon relative to the Earth. As a result, the velocity vectors computed using GMAT or custom codes may slightly differ. If we assume the Moon is instantaneously traveling along a circular orbit, the expressions governing the transformation to the GCRF simplify to:

$$\mathbf{r}_{E,sc}^{GCRF} = [{}^{EMR}\mathbf{R}^{GCRF}(t)]^T \mathbf{r}_{E,sc}^{EMR}$$

$$\mathbf{v}_{E,sc}^{GCRF} = -[{}^{EMR}\mathbf{R}^{GCRF}(t)]^T [{}^{EMR}\dot{\mathbf{R}}^{GCRF}(t)] [{}^{EMR}\mathbf{R}^{GCRF}(t)]^T \mathbf{r}_{E,sc}^{EMR} + [{}^{EMR}\mathbf{R}^{GCRF}(t)]^T \mathbf{v}_{E,sc}^{EMR}$$

One component of evaluating these expressions is calculating the rotation matrix  $[{}^{EMR}\mathbf{R}^{GCRF}(t)]$ . This matrix computation requires the position and velocity vectors of the Moon relative to the Earth in the GCRF, calculated in this example by evaluating the DE421 SPICE ephemerides on the selected epoch of January 1, 2025 00:00:00.000 UTC as:

$$\mathbf{r}_{E,M}^{GCRF} = [1.521169 \times 10^5, -3.077963 \times 10^5, -1.668651 \times 10^5]^T \text{ km}$$

$$\mathbf{v}_{E,M}^{GCRF} = [0.932547, 0.394552, 0.212860]^T \text{ km/s}$$

Although these values are truncated here, more significant figures are typically reported and used for further calculations.

The rotation matrix  $[{}^{EMR}\mathbf{R}^{GCRF}(t)]$  is calculated using the position and velocity vectors of the Moon relative to the Earth by evaluating Eq. 66. On the selected epoch, this rotation matrix equals (in truncated form):

$$[{}^{EMR}\mathbf{R}^{GCRF}(t)] = \begin{bmatrix} 0.398488 & -0.806308 & -0.437122 \\ 0.917173 & 0.350739 & 0.189142 \\ 8.09057 \times 10^{-4} & -0.476288 & 0.879289 \end{bmatrix}$$

In addition, the time derivative of the rotation matrix  $[{}^{EMR}\dot{\mathbf{R}}^{GCRF}(t)]$  on the selected epoch is calculated by evaluating Eq. 69 and is equal to:

$$[{}^{EMR}\dot{\mathbf{R}}^{GCRF}(t)] = \begin{bmatrix} 2.484218 \times 10^{-6} & 9.499983 \times 10^{-7} & 5.123032 \times 10^{-7} \\ -1.079327 \times 10^{-6} & 2.183931 \times 10^{-6} & 1.183971 \times 10^{-6} \\ 0 & 0 & 0 \end{bmatrix}$$

Next, to convert a selected state vector to a dimensional state in the Earth-Moon rotating frame, the position components are multiplied by the instantaneous value of  $l^*$  while the velocity components are multiplied by the instantaneous value  $l^*/t^*$ . The magnitude of the position vector  $\mathbf{r}_{E,M}^{GCRF}$  is used to define the instantaneous value of  $l^* = 3.817357 \times 10^5$  km, and the associated instantaneous value of  $t^* = 3.712963 \times 10^5$  s is calculated as outlined in Sec. 6.2. Using these characteristic quantities, dimensional position and velocity vectors of the selected initial state in the Earth-Moon rotating axes and relative to the Earth equal:

$$\mathbf{r}_{E,sc}^{EMR} = [3.290736 \times 10^5, 0, -6.693448 \times 10^4]^T \text{ km}$$

$$\mathbf{v}_{E,sc}^{EMR} = [0, 2.703462 \times 10^{-1}, 0]^T \text{ km/s}$$

Then, evaluating Eqs. 74 and 75 produces the following position and velocity vectors for the initial state in the GCRF:

$$\mathbf{r}_{E,sc}^{GCRF} = [1.310776 \times 10^5, -2.334545 \times 10^5, -2.027001 \times 10^5]^T \text{ km}$$

$$\mathbf{v}_{E,sc}^{GCRF} = [1.065445, 0.407440, 0.219719]^T \text{ km/s}$$

This same procedure is used to transform multiple states along the periodic orbit in the Earth-Moon CR3BP from the Earth-Moon rotating frame to the GCRF using epoch-dependent information. A similar procedure can also be used to transform states into the Moon inertial frame.

### 8.2.3 Recovering a Nearby Trajectory in an Ephemeris Model via Single Shooting in GMAT

Single shooting offers a straightforward approach to recovering a trajectory in a high-fidelity model of cislunar space to resemble the candidate for a mission orbit selected in Sec. 8.2.1 from the CR3BP.

#### Problem Formulation Example: Recovering a Mission Orbit via Single Shooting in GMAT

**Problem:** Calculate an initial state and regular impulsive maneuvers to produce a bounded trajectory in an ephemeris model that resembles a periodic orbit in the CR3BP by targeting components of the state at the  $xz$ -plane crossings in the Earth-Moon rotating frame

**Known information and constraints:**

- Periodic orbit in the CR3BP with state  $\mathbf{x}_{L1,PO}^{EMR}$  at the leftmost  $xz$ -plane crossing
- Initial epoch  $t_{des}$  and desired number of revolutions around the orbit  $N_r$
- Dynamical model for recovering a trajectory in GMAT
- Impulsive maneuvers applied at  $xz$ -plane crossings near apolune to target state components after one revolution

**Variables to calculate:**

- Initial state  $\mathbf{x}_{L1,0}^{EMR}$  at fixed epoch  $t_{des}$  in an EM  $L_1$ -centered RLP frame
- Impulsive maneuvers  $\Delta\mathbf{v}_i$  for  $i = [1, N_r]$  in Earth-Moon rotating frame for orbit maintenance

**Corrections approach:**

- 1) Correct  $\mathbf{x}_{L1,0}^{EMR}$  at  $t_{des}$  that lies on the  $xz$ -plane and produces a state after one revolution close to  $\mathbf{x}_{L1,PO}^{EMR}$
- 2) Update  $\mathbf{x}_{L1,0}^{EMR}$  at  $t_{des}$  that lies on the  $xz$ -plane to produce a state after two revolutions close to  $\mathbf{x}_{L1,PO}^{EMR}$
- 3) Propagate the corrected initial state  $\mathbf{x}_{L1,0}^{EMR}$  at  $t_{des}$  to the second subsequent  $xz$ -plane crossing
- 4) Calculate the  $i$ -th impulsive maneuver  $\Delta\mathbf{v}_i$  to produce a state after two revolutions that lies on the  $xz$ -plane and sufficiently close to  $\mathbf{x}_{L1,PO}^{EMR}$
- 5) Repeat Steps 3-4 for  $N_r$  revolutions around the orbit

**Why use this approach?** Once a periodic orbit is known, this single-shooting strategy can be straightforwardly implemented in GMAT with limited expertise or specialized custom codes. Targeting the initial state and maneuvers to achieve a desired state after two revolutions encourages the recovery of bounded motion near the reference periodic orbit. Updating the initial state in a two-step approach also limits sensitivity in corrections.

**When to not use this approach?** This corrections approach involves solving smaller corrections problem every revolution, each targeting short-term boundedness only. The individual maneuver magnitudes are not optimized at each step, and may be larger than those calculated using a multiple-shooting scheme. Finally, depending on the orbit or desired number of revolutions considered during targeting at each step, this problem may become very sensitive and difficult to solve with single-shooting.

In the procedure demonstrated here using GMAT, single-shooting is used for both correction of the initial state and calculation of regular impulsive maneuvers at subsequent epochs to produce a trajectory that possesses similar states at each crossing of the  $xz$ -plane to the periodic orbit from the CR3BP. This approach is merely one example of the use of single shooting to produce a trajectory with a desired geometry in a high-fidelity model; other formulations may be implemented to achieve either similar or more complex design goals.

To evaluate the quality of the initial guess, a state that lies along the selected periodic orbit is integrated in the desired ephemeris model. First, this state is selected as the southern crossing of the  $xz$ -plane of the Earth-Moon rotating frame near apolune along the selected periodic orbit in the CR3BP; this nondimensional state,  $\mathbf{x}_{L1,PO}^{EMR}$ , was listed in the Earth-Moon rotating frame in Sec. 8.2.2. This initial state is dimensionalized and then translated to use the axes of the Earth-Moon rotating frame but an origin located at  $L_1$ . The resulting state vector is input to GMAT as the state of a spacecraft in a custom-built coordinate system. Then, a point-mass ephemeris model of the Earth, Moon, and Sun with perturbation from SRP is created in GMAT and trajectories are numerically integrated using an 8th-order Runge-Kutta scheme with a tolerance of  $10^{-11}$  on the state error. In this dynamical model, the trajectory associated with  $\mathbf{x}_{L1,PO}^{EMR}$ , before any corrections, is generated for one revolution and plotted in Fig. 40 in black. This figure also includes EM  $L_1$  as a red diamond and the approximate location of the Moon via a grey-filled circle in the  $L_1$ -centered coordinate system for dimensional perspective. In Fig. 40a), the trajectory is plotted using dimensional quantities relative to  $L_1$  in the non-pulsating Earth-Moon RLP frame. In Fig. 40b), states along this trajectory (black) that is generated in the ephemeris model are nondimensionalized using the instantaneous values of the characteristic quantities, calculated at each epoch, and expressed relative to  $L_1$  in a pulsating Earth-Moon RLP frame. Although the black trajectory is not periodic in the Earth-Moon rotating frame in an ephemeris model, the trajectory shares similar geometric characteristics to the selected

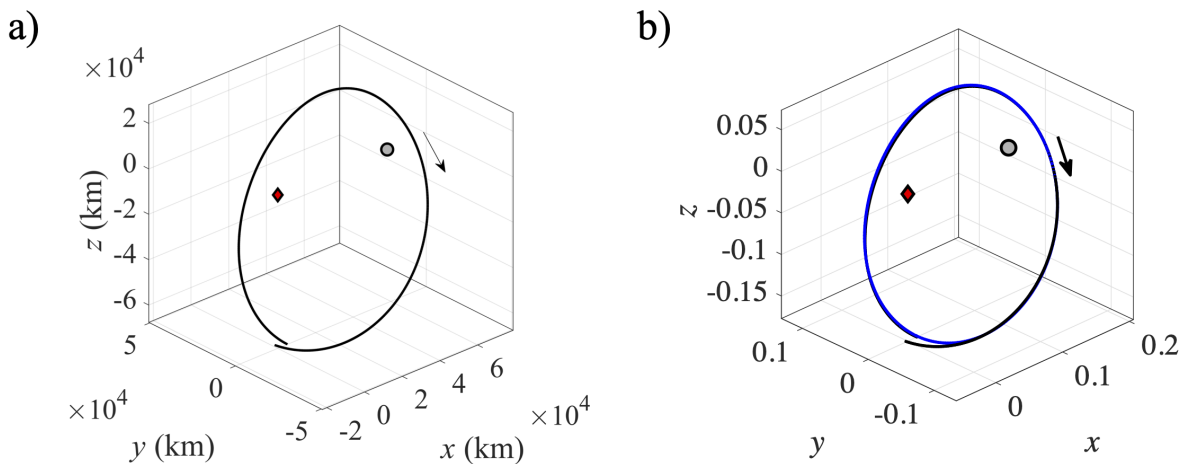


**Fig. 40** Trajectory propagated from the uncorrected initial state in the ephemeris model (blue) and the nearby periodic orbit in the CR3BP (black) in the a) non-pulsating and b) pulsating Earth-Moon RLP frame.

southern halo orbit (blue) from the CR3BP but does possess a noticeable deviation in the configuration space. Thus, the CR3BP has, in this case, supplied a suitable initial guess for corrections to recover additional revolutions of bounded motion in the ephemeris model.

**Implementation Notes: Visualizing Trajectories in a Pulsating or Non-Pulsating Rotating Frame**

When plotting a trajectory in dimensional quantities in the Earth-Moon rotating frame (or an RLP frame,) this trajectory is being viewed in a non-pulsating Earth-Moon rotating frame (or RLP frame) because the Earth and Moon move along the  $x$ -axis in this frame. Thus, the scale in this view in terms of dimensional quantities is unchanged over time. This view reflects how a trajectory generated in an ephemeris model typically appears in an astrodynamics software package such as GMAT. When viewing a trajectory in the Earth-Moon rotating frame (or RLP frame) using nondimensional quantities (nondimensionalized using the instantaneous values of the characteristic quantities calculated at each epoch), the trajectory is being viewed in a pulsating Earth-Moon rotating frame (or RLP frame) because the locations of the Earth and Moon are fixed along the  $x$ -axis in this frame. In this view, the scale changes over time. This pulsating rotating frame enables a better comparison between trajectories in an ephemeris model and periodic orbits in the CR3BP.

Single shooting is used to correct the initial state to produce a trajectory in the ephemeris model that remains close to the reference periodic orbit from the CR3BP for two revolutions. In this step, the corrections process is implemented in two successive applications of single shooting. First, single shooting is implemented to vary the initial conditions on the  $xz$ -plane to target components of the state at a subsequent  $xz$ -plane crossing after one revolution. The results of this corrections process are then used as the initial guess for a second single shooting process that targets state components at an  $xz$ -plane crossing two revolutions later. Separating this corrections process into two successive single shooting processes reduces the sensitivity of the numerical corrections process when compared with targeting the state after multiple subsequent  $xz$ -plane crossings downstream directly from one initial state generated in the CR3BP. This approach also produces an arc that lies close to the reference periodic orbit for more than one revolution.

### Implementation Notes: Formulating Target Conditions for a Trajectory Resembling a Periodic Orbit

The goal of recovering a trajectory that resembles a periodic orbit via single shooting is challenging to translate into a set of analytical criteria that apply to a continuous trajectory. It is common to target components of the states that occur at selected locations along the trajectory that resembles a specific periodic orbit, e.g., targeting components of the state at a crossing of  $xz$ -plane in the Earth-Moon rotating frame, to achieve boundedness. This approach is motivated by a well-known property of symmetric periodic orbits in the CR3BP: they admit two perpendicular crossings of the  $xz$ -plane in the Earth-Moon rotating frame in the CR3BP with  $\dot{x} = 0$ . Although these conditions no longer apply to trajectories in an ephemeris model, they are useful in some cases along with reasonable tolerances to produce a trajectory resembling a periodic orbit from the CR3BP.

The initial state  $\mathbf{x}_{L1,PO}^{EMR}$  is first numerically corrected via single shooting to achieve a crossing of the  $xz$ -plane after one revolution in the ephemeris model that lies within the vicinity of the nearby crossing of the periodic orbit from the CR3BP. For this single shooting scheme, the following components of the initial state that is expressed in dimensional quantities and lies along the  $xz$ -plane are varied:  $x_0, z_0, \dot{x}_0, \dot{y}_0, \dot{z}_0; y_0 = 0$  by definition. This state is integrated for one revolution to produce a state  $\mathbf{x}_{L1,f}^{EMR}$  piercing the  $xz$ -plane. The five listed components of the initial state are varied to achieve the following constraints:  $|z_f - z_{PO}| \leq \text{tol}_r$  and  $|\dot{x}_f| \leq \text{tol}_v$ , where  $z_{PO}$  is the  $z$ -component of  $\mathbf{x}_{L1,PO}^{EMR}$ . For this example, the single shooting process is terminated when the first constraint is satisfied to within  $\text{tol}_r = 1,000$  km and the second constraint is satisfied within  $\text{tol}_v = 1$  m/s. These tolerances are challenging to define, and may be updated iteratively by the trajectory designer based on the orbit, target location, and dynamical model. Furthermore, this subset of target conditions does not guarantee that the trajectory will remain close to the initial guess. Rather, this example demonstrates one straightforward approach that has been used in practice to produce sufficient results in some scenarios. The differential corrector in each step is configured to use a Newton-Raphson method and up to 50 iterations; this maximum number of iterations can be adjusted as needed to limit computational time or accommodate a poor initial guess. In addition, the maximum change in the value of each position component is constrained to 200 km at each iteration. For each velocity component, the value can change by up to 10 m/s with a maximum magnitude of 1 km/s. Using this outlined single shooting formulation and the initial guess from the CR3BP, the free variables are updated over 4 iterations until both constraints are satisfied to within the specified tolerances to produce a new, corrected initial state.

A second single shooting step is implemented to target the selected state components at an  $xz$ -plane crossing two revolutions after the initial state along the trajectory. For this process, the same free variables as the previous single shooting process are used, with the solution of the previous single shooting process used as the initial guess. The constraints, however, are modified to use the state components of the  $xz$ -plane crossing that occurs after two revolutions. The resulting free variables after 5 iterations produce an initial state along a trajectory in the ephemeris model that produces two revolutions of bounded motion in the vicinity of the periodic orbit. Table 9 summarizes the changes in the

free variables and values of the constraints after each corrections step. Figure 41 also displays the results of correcting the initial guess in this manner. First, the trajectory propagated from the initial guess for two revolutions of the reference orbit is plotted in Fig. 41a) in blue, along with the periodic orbit from the CR3BP, in black, in the pulsating  $L_1$ -centered Earth-Moon RLP frame. Clearly, this trajectory does not remain bounded within the vicinity of the periodic orbit from the CR3BP after a second revolution. However, the trajectory generated from the corrected state is plotted in blue in Fig. 41b) in the pulsating  $L_1$ -centered Earth-Moon RLP frame and the reference periodic orbit is displayed in black. This trajectory possesses an  $xz$ -plane crossing after two revolutions that is close to the initial  $xz$ -plane crossing and the entire trajectory generally remains close to the reference periodic orbit across the entire time interval.

Variable	Initial Guess	Value After 1st Corrections Step	Value After 2nd Corrections Step
$x_0$ (km)	4746.469936	4746.469936	4746.469936
$z_0$ (km)	-67585.561767	-67585.561767	-67585.561767
$\dot{x}_0$ (km/s)	0	0.003706	0.007515
$\dot{y}_0$ (km/s)	0.269179	0.267132	0.268892
$\dot{z}_0$ (km/s)	0	0.000868	0.023593
Target Parameter	Target Value	Difference After 1st Corrections Step	Difference After 2nd Corrections Step
$z_f$	-0.175343 nondim	5.360420 km	0.014500 km
$\dot{x}_f$	0	$5.360421 \times 10^{-6}$	$-7.604918 \times 10^{-7}$ km/s

**Table 9 Values of variables and target parameters in the  $L_1$ -centered Earth-Moon rotating frame after each corrections step.**

Next, the corrected initial conditions of the trajectory are integrated for one revolution to an  $xz$ -plane crossing and the first impulsive maneuver is determined to maintain bounded motion in the vicinity of the periodic orbit. A single shooting process is formulated to vary the components of the maneuver in the rotating frame to target selected state components of a southern  $xz$ -plane crossing after two revolutions. The variables that are modified in GMAT

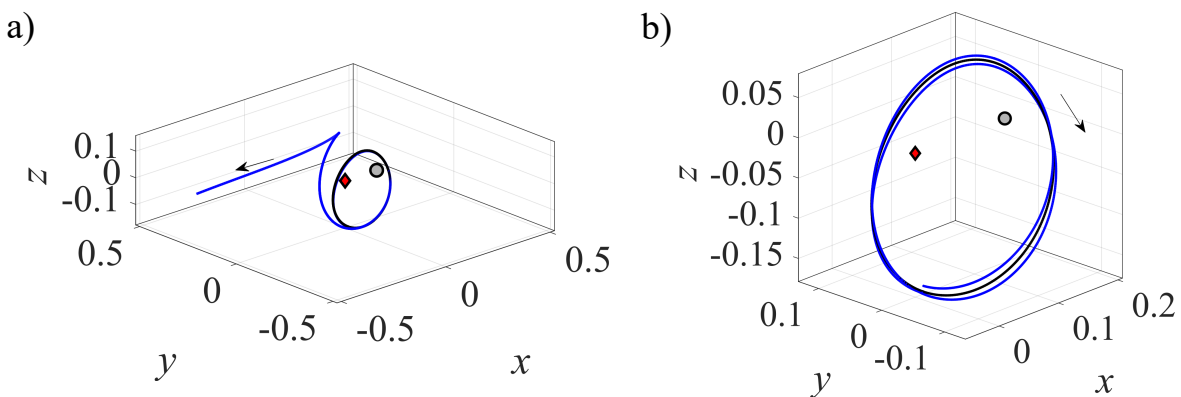


**Fig. 41 Trajectory propagated from initial state that is a) uncorrected and b) corrected to achieve two revolutions of bounded motion in the vicinity of the reference periodic orbit.**

include the three components  $\Delta v_x$ ,  $\Delta v_y$ ,  $\Delta v_z$  of the impulsive maneuver in the  $\hat{x}$ ,  $\hat{y}$ ,  $\hat{z}$  axes of the Earth-Moon rotating frame. The initial guess for the maneuver is selected as 0 km/s for all maneuver components. However, note that some implementations and combinations of variables and constraints may result in numerical issues when a value of zero is used as an initial guess; in those implementations, it may be useful to select a small but nonzero initial guess for a quantity. This state is integrated for two revolutions to produce a state  $\mathbf{x}_{L1,f}^{EMR}$  piercing the  $xz$ -plane near apolune along the periodic orbit. The three components of the maneuver are varied to achieve the following constraints:  $|z_f - z_{PO}| \leq tol_r$  and  $|\dot{x}_f| \leq tol_v$ . For this example, the single shooting process is terminated when the first constraint is satisfied to within  $tol_r = 1,000$  km and the second constraint is satisfied within  $tol_v = 1$  m/s. The differential corrector in each step is configured to use a Newton-Raphson method for up to 50 iterations; this maximum number of iterations can be adjusted as needed to limit computational time or accommodate a poor initial guess. Maximum changes in the value of each variable are also specified as 1 m/s for each maneuver component whereas the maximum magnitude of each component is 100 m/s. Finally, a forward finite differencing method is used to numerically approximate the derivatives of the constraints with respect to each variable. The perturbation size used to calculate the finite difference is equal to the default value in GMAT of  $10^{-5}$ . This value influences the error in the approximation of the derivative and may be updated as needed. This single shooting process produces a solution in a few iterations. Then, the calculated impulsive maneuver is applied, and the trajectory is generated until the next southern  $xz$ -plane crossing. This corrections step is repeated at each subsequent southern  $xz$ -plane crossing to determine the remaining impulsive maneuvers, producing a trajectory that spans a user-specified number of revolutions.

In the presented example, this process is conducted to determine 14 impulsive maneuvers applied at the southern crossings of the  $xz$ -plane of the Earth-Moon rotating frame, for a total of 15 revolutions after the initial state. The total duration of the generated trajectory is approximately 166.5 days. This trajectory is plotted in the rotating frame in Fig. 42a) in blue in the non-pulsating and  $L_1$ -centered Earth-Moon RLP frame with the reference periodic orbit in black. The magnitude of each maneuver is plotted as a function of time, measured along the trajectory, in Fig. 42b). The average maneuver magnitude is approximately 8.3 m/s; the largest maneuver magnitude is approximately 13.7 m/s. Of course, variations in the reference trajectory and single shooting implementation will influence these results. Furthermore, this solution has not been optimized to minimize any cost function, such as minimizing the total maneuver magnitude. Rather, this example simply demonstrates calculation of a point solution. To avoid redundancy in these examples, this trajectory is not compared to the mission constraints; that analysis will be performed in the next subsection following application of multiple shooting.

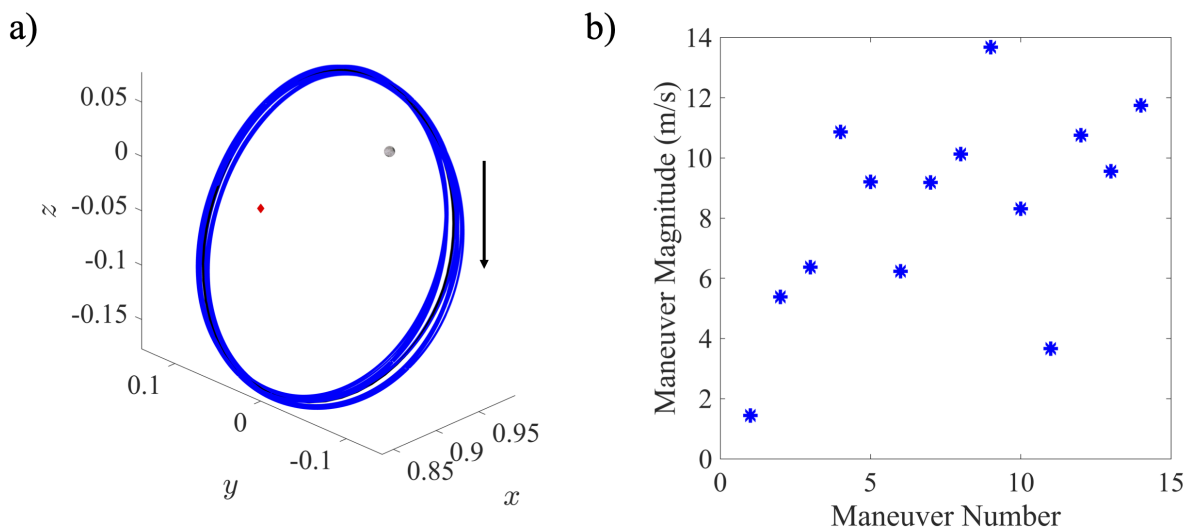


**Fig. 42** a) Mission orbit generated for 15 revolutions in the ephemeris model with b) magnitudes of the impulsive maneuvers applied at each southern  $xz$ -plane crossing to resemble a periodic orbit from the CR3BP.

### 8.2.4 Recovering a Nearby Trajectory in an Ephemeris Model via Multiple Shooting in Custom Codes

An alternative approach to constructing a trajectory in an ephemeris model that resembles a periodic orbit from the CR3BP is to use multiple shooting. Multiple shooting, as summarized in Sec. 5.2.1, focuses on discretizing a trajectory into multiple arcs and simultaneously updating those arcs to produce a continuous trajectory.

#### Problem Formulation Example: Recovering a Mission Orbit via Multiple Shooting

**Problem:** Calculate multiple states and integration times between them along a natural trajectory in an ephemeris model that resembles a periodic orbit in the CR3BP

**Known information and constraints:**

- Periodic orbit in the CR3BP described by state  $\mathbf{x}_{EMB,PO}^{EMR}$  and period  $T_{PO}$  in the Earth-Moon rotating frame
- Initial epoch  $t_{des}$  and dynamical model for recovering a trajectory
- Number of arcs  $N_n$  to discretize each revolution around the orbit and discretization approach, e.g., equal integration time intervals along each arc
- Desired number of revolutions around the orbit  $N_r$

**Variables to calculate:**

- Initial states  $\mathbf{x}_{M,i,0}^{MI}$  and epochs  $t_i$  for  $i = [1, N_t + 1]$  and integration times  $\Delta t_i$  for  $i = [1, N_t]$  where  $N_t = N_r N_n$

**Corrections Approach:**

- 1) Discretize the periodic orbit from the CR3BP into  $N_n$  arcs of equal integration times; repeat for  $N_r$  revolutions.  
Extract the states at the beginning of each arc (and end of the last arc) to supply nondimensional state vectors  $\mathbf{x}_{EMB,i,0}^{EMR}$  in the rotating frame and epochs  $t_i$  for  $i = [1, N_t + 1]$ . Set  $\Delta t_i$  equal to  $T_{PO}/N_n$  for  $i = [1, N_t]$
- 2) Dimensionalize each initial state in the rotating frame using instantaneous characteristic quantities of the Earth-Moon system at  $t_i$  and transform to the Moon inertial frame, producing  $\mathbf{x}_{M,i,0}^{MI}$  for  $i = [1, N_t + 1]$
- 3) Propagate initial state  $\mathbf{x}_{M,i,0}^{MI}$  at epoch  $t_i$  for integration time  $\Delta t_i$  in selected model, where  $i = [1, N_t]$
- 4) Simultaneously update all the initial states  $\mathbf{x}_{M,i,0}^{MI}$  and epochs  $t_i$  for  $i = [1, N_t + 1]$  and integration times  $\Delta t_i$  for  $i = [1, N_t]$  until the trajectory is continuous to within a desired tolerance

**Why use this approach?** Multiple shooting produces a less sensitive corrections problem than single shooting because small errors are distributed along the entire trajectory, as opposed to being concentrated at the end of a time interval. This approach can produce a natural trajectory that lies close to the reference periodic orbit in the CR3BP, if such a trajectory exists. It also does not require definition of specific target conditions.

**Why not to use this approach?** This approach requires sufficient expertise to implement in custom codes.

Let's demonstrate the process for constructing a natural trajectory in the ephemeris model that resembles the selected 11.1 day period Earth-Moon  $L_1$  southern halo orbit from the CR3BP. In this example, the ephemeris model includes the point mass gravitational interaction with the Earth, Moon, and Sun as well as a spherical SRP model. First, consider an initial state that lies at apolune along the periodic orbit at an epoch of January 1st, 2025, 00:00:00.00 UTC; in the CR3BP and Earth-Moon rotating frame, this state  $\mathbf{x}_{PO}$  was presented in Sec. 8.2.2. A similar transformation procedure to Sec. 8.2.2 is used to transform  $\mathbf{x}_{EMB,PO}^{EMR}$  to a dimensional state  $\mathbf{x}_{M,1,0}^{MI}$  in the Moon inertial frame on the selected epoch. Then, the periodic orbit is discretized into  $N_n = 16$  arcs, and the state at the beginning of each arc is transformed into the Moon inertial frame at the associated epoch using a similar process. This process is repeated for a total of  $N_r = 16$  revolutions. This set of states, epochs, and their associated equal integration times of 0.694 days form the initial guess for the trajectory. Integrating state  $\mathbf{x}_{M,i,0}^{MI}$  at the beginning of the  $i$ -th arc forward in time from the associated epoch for 0.694 days in the ephemeris model would not produce a state that coincides with the state at the beginning of the  $i + 1$ -th arc,  $\mathbf{x}_{M,i+1,0}^{MI}$ . Thus, corrections are required to recover a continuous trajectory.

#### Challenge: Selecting a Suitable Discretization and Number of Revolutions along the Orbit

Multiple shooting requires specification of the number of arcs and approach to discretize a trajectory; in this example, dependent on the discretization per revolution and number of revolutions along the orbit. Selecting the discretization per revolution may be an iterative process performed by the analyst: avoiding too many arcs to increase the computational effort required to find a solution but avoiding too few to produce a sensitive corrections problem. In addition, it may be desirable to add or remove arcs near particularly sensitive regions along the trajectory, or modify the discretization approach. Finally, the number of revolutions along the orbit is typically selected to bias the trajectory to remain near the reference periodic orbit and/or satisfy any requirements for the desired integration time along the trajectory.

The multiple shooting scheme is then implemented using a free variable and constraint vector formulation. The free variable vector consists of  $N_t + 1$  nondimensional states in the Moon inertial frame, each labeled  $\mathbf{x}_{M,i,0}^{MI}$ ;  $N_t$  durations for integration along an arc, each labeled  $\Delta t_i$ ; and  $N_t + 1$  epochs, each labeled  $t_i$ , measured from the initial epoch and nondimensionalized using the average characteristic time quantity for the Earth-Moon system. This free variable vector is written mathematically as:

$$\mathbf{V} = \left[ \mathbf{x}_{M,1,0}^{MI}, t_1, \Delta t_1, \dots, \mathbf{x}_{M,N_t,0}^{MI}, t_{N_t}, \Delta t_{N_t}, \mathbf{x}_{M,N_t+1,0}^{MI}, t_{N_t+1} \right]^T$$

Then, the constraint vector is written using the difference between the state  $\mathbf{x}_{M,i,f}^{MI}$  and epoch  $t_{1,0} + \Delta t_1$  at the end of the

$i$ -th arc and the state  $\mathbf{x}_{M,i+1,0}^{MI}$  and epoch  $t_{i+1}$  at the beginning of the  $i + 1$ -th arc. Mathematically, this vector equals:

$$\mathbf{F}(\mathbf{V}) = \left[ \mathbf{x}_{M,1,f}^{MI} - \mathbf{x}_{M,2,0}^{MI}, t_1 + \Delta t_1 - t_2, \dots, \mathbf{x}_{M,N_t,f}^{MI} - \mathbf{x}_{M,N_t+1,0}^{MI}, t_{N_t} + \Delta t_{N_t} - t_{N_t+1}, t_1 \right]^T$$

This problem is composed of  $8N_t + 7$  free variables that can be adjusted to achieve  $7N_t + 1$  constraints; the final constraint fixes the epoch at the beginning of the trajectory. Because there are fewer constraints than variables, the minimum-norm solution in Eq. 103 is used to update the free variable vector. This problem is solved from the defined initial guess using custom codes in MATLAB. An explicit embedded Runge-Kutta Prince-Dormand (8, 9) method, accessed via C++ using the GNU Scientific Library, is used for numerical integration. A total of 10 updates to the free variable occur until the trajectory is continuous to within a tolerance of  $10^{-9}$  nondimensional units. This process, along with the initial guess and corrected trajectories, are displayed graphically in Fig. 43. The trajectory in Step 4 of this figure is natural and closely resembles the periodic orbit displayed in Step 1 of the figure. However, the corrected trajectory does possess state and epoch discontinuities that are less than  $10^{-9}$  nondimensional units approximately every 0.694 days due to the nature of a multiple shooting problem.

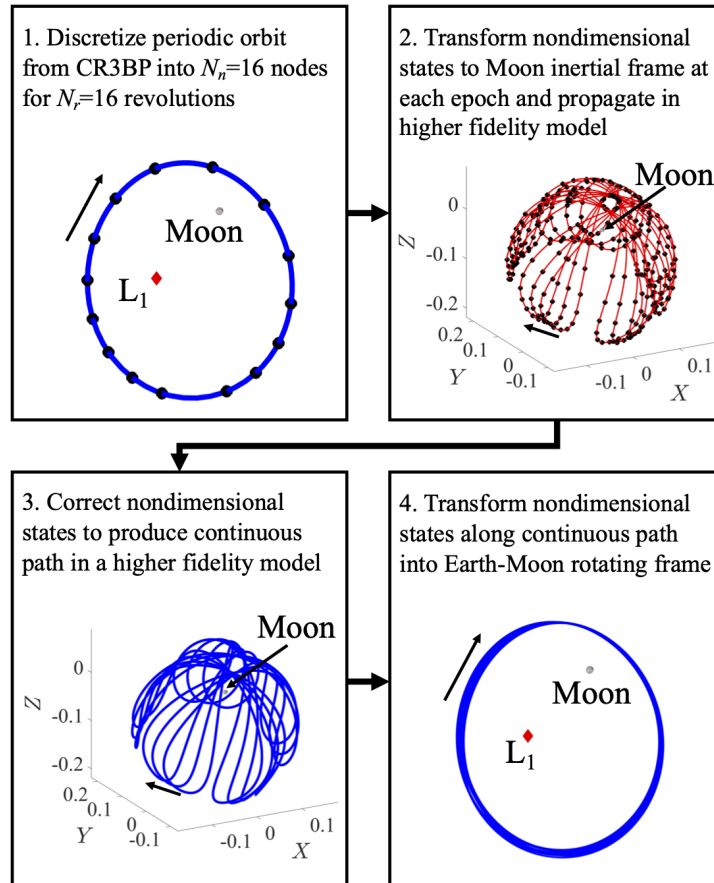


**Fig. 43** Overview of the procedure used to calculate a reference mission orbit in an ephemeris model using multiple shooting along with the results generated in this example.

### Challenge: Does the Solution to a Multiple Shooting Problem Lie Close to a Continuous Trajectory?

Multiple shooting produces a trajectory with small state and epoch discontinuities between arcs along the trajectory. To confirm that this trajectory lies sufficiently close to a solution, one approach is to construct a sequential set of single shooting problems in GMAT: using small maneuvers at the beginning of every arc to target the position vector at the beginning of the next arc and propagating sequentially in the ephemeris model along the entire trajectory. Implementing this approach produces the following trajectory, displayed in Fig. 44, with maneuver magnitudes up to the order of  $10^{-3}$  m/s between each arc for a total of 0.33 m/s over 177.6 days. Because this total maneuver requirement is small, the recovered solution to the multiple shooting problem can be considered to lie sufficiently close to a continuous path in the specified ephemeris model.

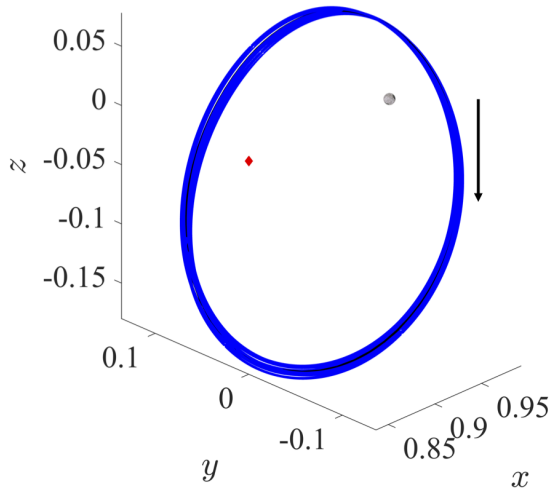


**Fig. 44 Single, continuous trajectory generated in GMAT for 16 revolutions in the ephemeris model using small maneuvers between arcs. This path lies close to the trajectory in Step 4 of Fig. 43 calculated using multiple-shooting.**

Finally, this mission orbit satisfies the following original mission requirements:

- Maintaining constant communications with Earth ground stations: the spacecraft is never obscured by the Moon.
- Ensuring coverage (elevation angle above 10 deg) and visibility to a lunar south pole station for at least 50% of the orbit period: the contact locator function in GMAT reveals coverage for 117.74 days over the span of a total of 177.6 days, i.e., approximately 66% of the integration time, consistent with the original estimate from the CR3BP.
- Remaining within a range of less than 100,000 km from the lunar south pole station: the spacecraft distance from the center of the Earth varies between 24,965.28 km and 88,461.45 km; after deducting the Moon radius from these values, the range satisfies this constraint.

Note that the constraint on the station-keeping and insertion maneuvers is not evaluated in this subsection: the analyst may need to iterate on the mission orbit after designing transfers and station-keeping maneuvers.

### 8.3 Designing a Transfer to the Mission Orbit

The next component of this example involves designing a transfer trajectory for a spacecraft from the vicinity of the Earth to the selected Earth-Moon  $L_1$  southern halo orbit. Trajectory design between and to mission orbits that resemble periodic orbits in cislunar space have been widely studied throughout the astrodynamics community, including strategies incorporating impulsive maneuvers [79, 100–102], low-thrust maneuvers [103, 104], and ballistic lunar capture [105, 106]. These resources demonstrate some of the possible transfer design approaches and geometries to destinations in cislunar space; similar approaches are also helpful in designing transfers to mission orbits near the Sun-Earth equilibrium points [107]. These strategies often initially employ an approximate dynamical model, such as the CR3BP, to rapidly generate an initial guess for a transfer prior to corrections in a higher-fidelity dynamical model. In the astrodynamics community, corrections schemes are often implemented using custom codes. However, simple approaches to correcting a transfer can also be implemented in GMAT using single-shooting; examples are demonstrated in this subsection.

Let's design transfers from a near-circular, parking orbit in LEO to the 11.1-day Earth-Moon  $L_1$  southern halo orbit selected in Sec. 8.2.1. Two types of transfers from LEO to the selected mission orbit are explored in this section:

- A ‘direct transfer’: After a single impulsive maneuver is applied to depart the initial orbit in LEO, the spacecraft coasts until a second and final impulsive maneuver is applied to insert into the mission orbit. A conceptual illustration of a direct transfer geometry appears in Figure 45.

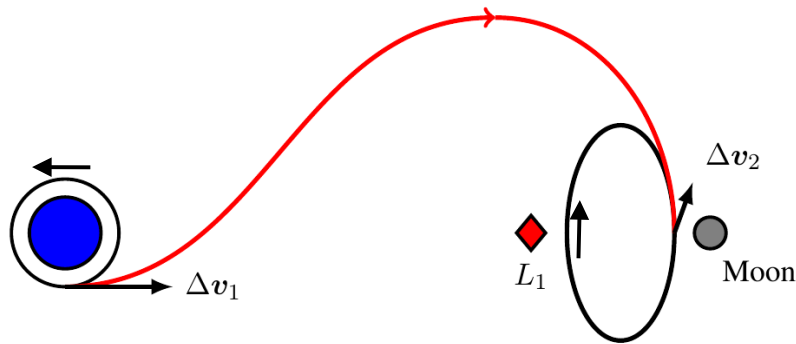


**Fig. 45** Conceptual representation of a direct transfer from the Earth to an EM  $L_1$  southern halo orbit.

- An ‘indirect transfer’: After an initial impulsive maneuver is applied to depart an orbit in LEO, the spacecraft coasts until a second impulsive maneuver is applied near apogee to insert onto an arc that resembles a trajectory on the stable manifold of the periodic orbit in the CR3BP that resembles the mission orbit. A third maneuver inserts the spacecraft into the mission orbit. An illustration of this transfer geometry appears in Figure 46.

As an example, for a spacecraft to transit from LEO to a mission orbit in cislunar space, some transfers can be constructed using the process summarized in the flowchart in Fig. 47. The defined steps provide a basis for transfer design in a higher-fidelity model. However, they do not represent the only approach. Note that the transfers produced by this

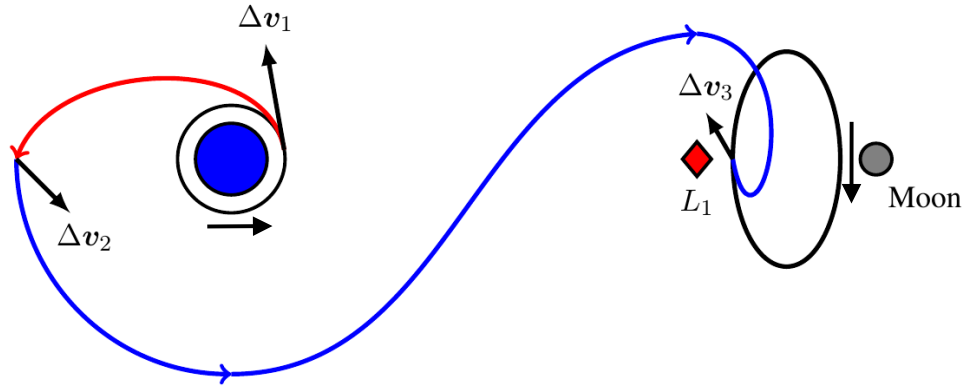


**Fig. 46** Conceptual representation of a direct transfer from the Earth to an EM  $L_1$  southern halo orbit.

process are not optimized in this document to minimize a cost function such as propellant usage or time of flight. Rather, these trajectories represent only point solutions that may be further updated as needed.

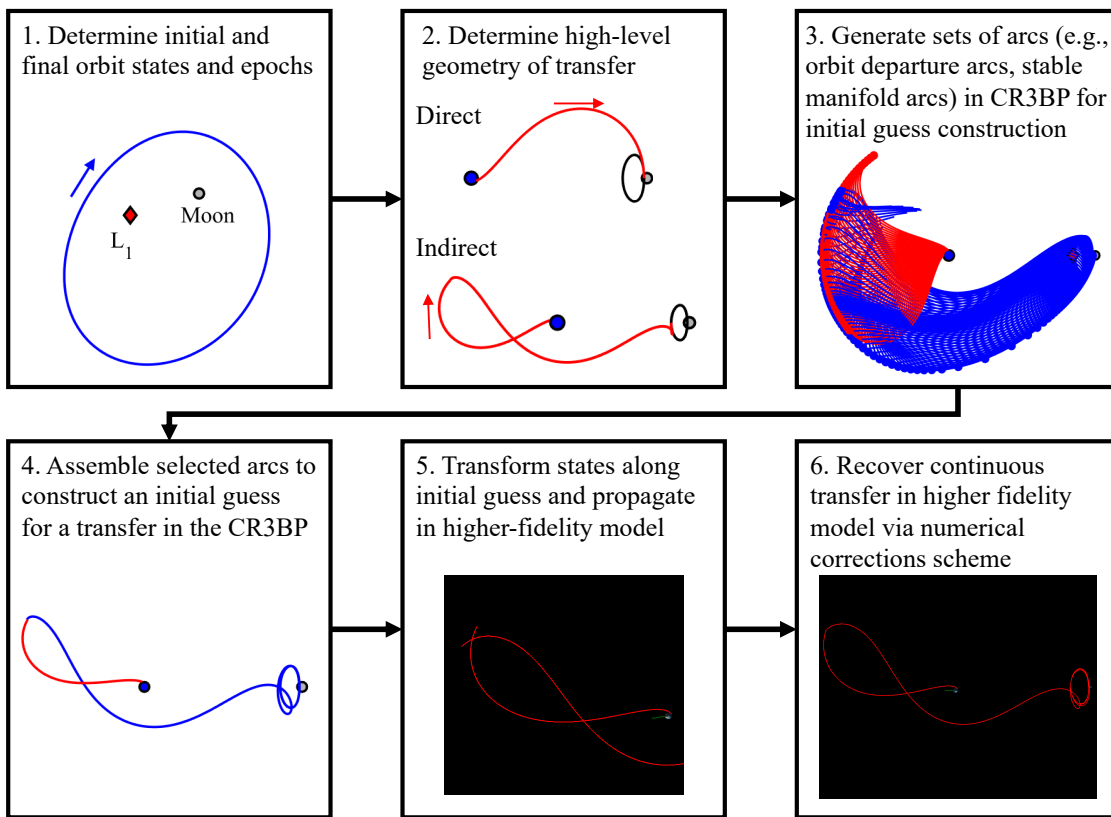


**Fig. 47** Overview of one procedure to design a transfer to the selected mission orbit in an ephemeris model.

### 8.3.1 Designing a Direct Transfer: Single-Shooting Backward in Time

Consider the problem of designing a direct transfer from a circular, low Earth orbit with specified semi-major axis and inclination to a fixed state that lies along the selected mission orbit at a specific epoch. One straightforward approach to designing this transfer in a software package such as GMAT is to solve this problem in backward time.

#### Problem Formulation Example: Designing a Direct Transfer Backward in Time in GMAT

**Problem:** Calculate the Earth departure and orbit insertion maneuvers producing a transfer trajectory with two impulsive maneuvers that, in backward time, reaches the desired low Earth orbit from a fixed state that lies along the desired mission orbit at a specific epoch.

**Known information and constraints:**

- Target state  $\mathbf{x}_{M,des}^{MI}$  in a Moon inertial system and epoch  $t_{des}$  along mission orbit in ephemeris model
- Orbit insertion maneuver  $\Delta v_2$  places the spacecraft near perilune along the mission orbit
- Semi-major axis, eccentricity and inclination (in the GCRF) of low Earth orbit
- LEO departure maneuver  $\Delta v_1$  does not significantly change the inclination of the spacecraft

**Trajectory itinerary in backward time:**

- 1) Integrate spacecraft state backward in time in selected dynamical model from  $\mathbf{x}_{M,des}^{MI}$  at  $t_{des}$  along the mission orbit for a time  $\Delta t_{int}$
- 2) Apply  $\Delta v_2$  that causes the spacecraft to depart the mission orbit in backward time (or insert the spacecraft into the mission orbit in forward time)
- 3) Integrate spacecraft state backward in time in selected dynamical model until the spacecraft reaches perigee
- 4) Apply  $\Delta v_1$  that inserts the spacecraft into the LEO in backward time (or depart the LEO in forward time).

**Variables to calculate:**

- Impulsive maneuver  $\Delta v_1$  to depart the low Earth orbit at epoch  $t_1$
- Impulsive maneuver  $\Delta v_2$  to insert into the mission orbit at epoch  $t_2$
- Time  $\Delta t_{int}$  between impulsive maneuver  $\Delta v_2$  and selected state along the mission orbit

**Why use this approach?** In this problem the final state and epoch are known a priori and the problem is to find the initial state and epoch as well as the maneuvers required along the transfer. By solving the problem backward in time, the final conditions are guaranteed to be satisfied by the computed transfer (if one exists). In addition, it is straightforward to describe the desired LEO and construct targeting conditions. It is more difficult to robustly achieve and describe the target conditions and tolerances for a state along a mission orbit that resembles a periodic orbit from the CR3BP while also computing the transfer itself.

Let's demonstrate the process for solving this two-point boundary value problem in backward time. First, let's

select the target state along the mission orbit that exists in the ephemeris model as the initial state calculated using multiple-shooting in Sec. 8.2.4:

$$\mathbf{x}_{M,des}^{MI} = [-29190.364607\text{km}, 70749.103743\text{km}, -36686.168676\text{km}, 0.119813\text{km/s}, 0.054833\text{km}, -0.008184\text{km}]^T$$

expressed using truncated values in the Moon inertial frame with  $t_{des}$  as January 1st, 2025, 00:00:00.00 UTC. This state is specified here in a Moon inertial frame because 1) the multiple-shooting corrections scheme in Sec. 8.2.4 was implemented to adjust states along a trajectory in the inertial frame, 2) GMAT converts states to an inertial frame during computation, and 3) to avoid any ambiguities that occur due to some differences between distinct astrodynamics software when transforming a state expressed in the inertial frame to a rotating frame. This state occurs near apolune along the mission orbit. For  $\Delta v_2$  to occur approximately near perilune, a good initial guess for the integration time  $\Delta t_{int}$  is half the orbit period, i.e.,  $\Delta t_{int} = -5.55$  days; the negative indicates integration backward in time while half the period is a consequence of the symmetry of the reference periodic orbit in the CR3BP about the  $\hat{x}$ -axis.

Next, GMAT requires maneuvers be specified in a desired set of axes along with initial guesses and boundary constraints on their values. For this example,  $\Delta v_2$  is defined using VNC axes calculated relative to the Moon. These axes offer a heuristic, preliminary interpretation of how the maneuver changes the spacecraft energy and orbit plane. A good initial guess for this maneuver is difficult to determine without a priori expertise. However, the corrections problem presented here and implemented in GMAT can be solved with an initial guess of  $\Delta v_2 = [50, 0, 0]^T$  m/s in VNC axes relative to the Moon; large enough for the trajectory to depart the mission orbit in backward time, but this initial guess can be updated manually as needed. To limit the maneuver magnitude,  $\Delta v_2$  is constrained to possess components each with a magnitude less than 1 km/s and all maneuver components may take nonzero values. Then,  $\Delta v_1$ , the maneuver that is typically supplied by a stage of the launch vehicle, is defined using VNC axes calculated relative to the Earth. The initial guess provided to GMAT is  $\Delta v_1 = [-3.13, 0, 0]^T$  km/s. This initial guess is calculated using a back-of-the-envelope analysis from the two-body problem: 3.13 km/s applied in the velocity direction enables the spacecraft to leave a LEO with the selected altitude and insert onto a conic with a periapsis radius that coincides with the LEO and an apoapsis radius close to the semi-major axis of the Moon's orbit in the two-body problem. Each element of  $\Delta v_1$  is allowed to possess a magnitude that is less than 4 km/s. Finally, the negative value of the first element corresponds to the problem being solved in backward time: for instance, if a maneuver that increases the spacecraft energy in forward time is equal to  $+\Delta v$  in the velocity direction in forward time, then  $-\Delta v$  must be applied in the velocity direction in backward time.

**Challenge: Specifying Initial Guesses for Problem Variables**

The initial guess provided for problem variables can impact the success of a differential corrections scheme but are sometimes difficult to determine. Common approaches for defining initial guesses for parameters include:

- Using heuristics or back-of-the-envelope calculations to guess the order of magnitude of a maneuver. For instance, approximations from the two-body problem or derived from the difference in the Jacobi constant along arcs in the CR3BP can be useful.
- The goal of the maneuver can also be useful for specifying an initial guess for the direction of the maneuver in a VNC frame. For instance, if the goal is to increase (or decrease) the spacecraft energy then a useful starting point might be to place most of the maneuver in the velocity (or anti-velocity direction). If the goal includes changing the orbit plane, it may be useful to guess a nonzero value of the normal component.
- Guess and check: before implementing the corrections scheme, experiment and visualize the influence of some maneuvers in a VNC frame on the resulting path to determine rough orders of magnitude for an initial guess that produces a transfer reaching the desired region or goal.
- To estimate the time along a mission orbit between two locations, consider symmetries that might exist for a similar periodic orbit in the CR3BP to estimate the integration time in terms of the orbit period.
- If a good initial guess for the time along a segment of a trajectory is difficult to determine, consider an alternative specification of the interval for integrating the spacecraft state. For instance, if a good initial guess for the time to reach a periapsis is difficult to determine, integration can be performed until one (or more) periapses occur; in astrodynamics software packages or custom codes, these ‘events’ can be used to specify stopping conditions for integration that are not expressed in terms of time.
- Construct a sequence of progressively difficult corrections problems (with more constraints and/or variables than the previous problem) and use the solutions to one corrections problem to define initial guesses for the next corrections problem.

The constraints and their thresholds for satisfaction must also be specified. Because the problem is solved using single-shooting, only constraints on the initial LEO, or the target orbit at the end of the time interval in backward time, must be specified. Consider a requirement that the initial LEO possess an inclination of 28.5 degrees in the GCRF. The target perigee and apogee radii are both equal to 6578.14 km, corresponding to a circular orbit with a 200 km altitude. The right ascension of the ascending node and location of perigee are allowed to vary in this example (although that may not always be the case if there is a requirement to fly over a specific site on the Earth). The threshold for meeting these three constraints is equal to 0.1 km for the perigee and apogee radii and 0.01 degrees for the inclination. These values are selected to be small; however, in practice, these thresholds may be derived from mission or launch vehicle provider requirements.

**Challenge: Formulating a Corrections Problem that Possesses a Solution**

When designing transfers, it is important to formulate a corrections problem that is solveable. Sometimes we do not know a priori if a solution to a problem that satisfies the dynamics exists. If the corrector does not converge to a solution, one reason could be that a solution does not exist. However, other reasons for failure could be a poor initial guess, a poor problem formulation, large parameter bounds, poor approximations to the derivatives of constraints with respect to variables using finite differencing. It is also a good practice to avoid specifying more constraints than variables to ensure that the problem is not overconstrained.

This two-point boundary value problem is solved in GMAT using a two-step corrections approach. In the first corrections step, the integration time along the mission orbit (that defines the location of  $\Delta v_2$ ) and the  $\Delta v_2$  vector are all varied to achieve the desired periapsis radius and inclination at perigee before the LEO departure maneuver is applied. Thus, four variables are updated to achieve two independent constraints. In the second corrections step, the integration time along the mission orbit  $\Delta t_{int}$ , the  $\Delta v_2$  vector and the  $\Delta v_1$  vector are all varied to achieve the desired periapsis and apoapsis radii and inclination at perigee after the LEO departure maneuver is applied. The initial guesses for  $\Delta t_{int}$  and the  $\Delta v_2$  in the second step are set equal to the values calculated by the first corrections step. One reason to separate out this corrections process into two steps is to reduce the sensitivity of solving a problem where the variables take on values on different orders of magnitude and correspond to motion near two different bodies. The differential corrector in each step is configured to use a Newton-Raphson method for up to 50 iterations; this maximum number of iterations can be adjusted as needed to limit computational time or accommodate a poor initial guess. Maximum changes in the value of each variable are also specified as 0.1 km/s for each maneuver component and 1 hr for  $\Delta t_{int}$ ; these values can be updated if a problem is too sensitive or the initial guess is being updated too many times before reaching a solution. Finally, a forward finite differencing method is used to numerically approximate the derivatives of the constraints with respect to each variable. The perturbations used to calculate the finite difference are equal to the default value in GMAT of  $1 \times 10^{-5}$ . This value influences the error in the approximation of the derivative and may be updated as needed. During both corrections steps, this transfer is modeled using a point mass ephemeris model of the Earth, Moon, and Sun, with SRP and a  $36 \times 36$  higher-order gravity field of the Earth; this additional contribution is included due to the spacecraft passing close to the Earth for a portion of the trajectory.

**Implementation Note: Multi-Step Corrections Process in GMAT**

When implementing a multi-step corrections process in GMAT, it is important to remember to re-initialize the spacecraft to ensure that the spacecraft possesses the same initial state and epoch during each corrections step. One straightforward approach to reinitializing the spacecraft in GMAT involves creating a second clone spacecraft before the first corrections step. Then, the state and epoch of the primary spacecraft are updated during the first corrections steps. The calculated values of the maneuvers and integration time along the mission orbit are saved as variables. Then, the primary spacecraft is reinitialized by setting its properties equal to that of the clone spacecraft. The second corrections step is then applied to the primary spacecraft again. An alternative approach is to run the first corrections scheme, record the initial values and parameters and update them again before adding more variables and/or constraints and re-running the GMAT script.

After implementing this procedure in GMAT, the initial guess and final values at each corrections step are listed in Table 10. The first corrections step requires 11 iterations to meet the required constraints whereas the second step requires 2 iterations. Note that formulating this problem in backward time means that the sign of the maneuvers listed in this Table is opposite the sign of a maneuver that is performed in forward time. The resulting direct transfer, computed in GMAT appears in Fig. 48 in royal blue. 16 revolutions around the mission orbit, as calculated in Sec. 8.2.4 using multiple-shooting, are also added to this figure in dark blue; recall that this mission orbit requires a total maneuver magnitude of approximately 0.33 m/s over 176 days. The magnitude of  $\Delta v_1$  is 3.137 km/s, whereas the magnitude of the second maneuver is 497.18 m/s (which is below the maximum 1 km/s insertion maneuver constraint). The transfer time is 5.59 days between the two maneuvers.

Variable	Initial Guess	Value After 1st Corrections Step	Value After 2nd Corrections Step
$\Delta v_1$ (VNC, km/s)	$\begin{bmatrix} -3.13 \\ 0 \\ 0 \end{bmatrix}$	N/A	$\begin{bmatrix} -3.136597 \\ 7.560 \times 10^{-7} \\ -7.165 \times 10^{-6} \end{bmatrix}$
$\Delta t_{int}$ (days)	-5.55	-5.55	-5.55
$\Delta v_2$ (VNC, km/s)	$\begin{bmatrix} 0.05 \\ 0 \\ 0 \end{bmatrix}$	$\begin{bmatrix} 0.485526 \\ -0.061206 \\ -0.087814 \end{bmatrix}$	$\begin{bmatrix} 0.485524 \\ -0.061139 \\ -0.08782 \end{bmatrix}$
Target Parameter	Target Value	Value After 1st Corrections Step	Value After 2nd Corrections Step
Periapsis radius (km)	6578.14	6578.139994	6578.139511
Apoapsis radius (km)	6578.14	N/A	6578.188845
Inclination (deg)	28.5	28.5	28.5

**Table 10** Values of variables and target parameters after each corrections step when calculating a direct transfer by solving a backward time targeting problem.

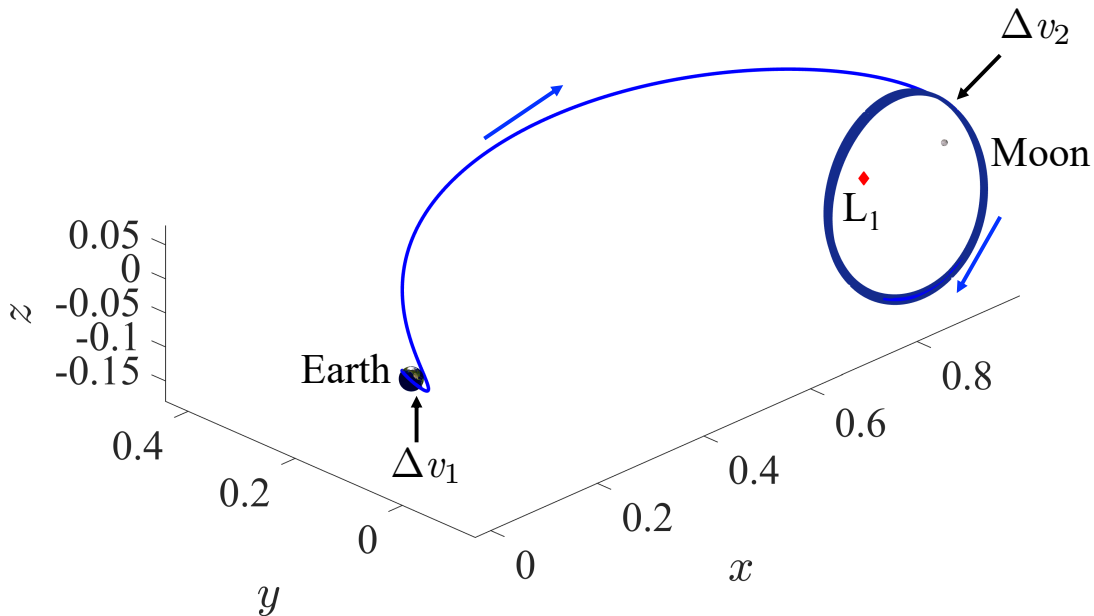


**Fig. 48** Direct transfer generated by solving a backward time targeting problem.

#### Analysis: Why Visualize the Transfer in the Earth-Moon Rotating Frame Using Nondimensional Units?

When visualizing a transfer in the Earth-Moon rotating frame in a software package such as GMAT, the spacecraft trajectory is plotted using dimensional quantities. However, it is common in the astrodynamics community to view trajectories in an Earth-Moon rotating frame with nondimensional units. The position vectors at each epoch along the trajectory are nondimensionalized using the instantaneous distance between the Earth and Moon, i.e., an instantaneous value of  $l^*$ . By visualizing the path of the spacecraft in the resulting pulsating Earth-Moon rotating frame, the locations of the Earth, Moon and  $L_1$  are all fixed over time; this property reduces the complexity of visualizing a path in cislunar space over time in a static 2D plot.

### 8.3.2 Designing a Direct Transfer: Single-Shooting Forward in Time

Consider a different approach to designing a direct transfer from a circular, low Earth orbit at a specific epoch to a state near the reference mission orbit: solving the problem in forward time in GMAT.

#### Problem Formulation Example: Designing a Direct Transfer Forward in Time in GMAT

**Problem:** Calculate the Earth departure and orbit insertion maneuvers producing a transfer that, in forward time, takes the spacecraft from a state that occurs along the transfer immediately after the first maneuver at a specified epoch to a state that produces motion resembling a periodic orbit from the CR3BP.

**Known information and constraints:**

- Semi-major axis, eccentricity and inclination (in the GCRF) of a LEO
- LEO departure maneuver  $\Delta v_1$  does not significantly change the inclination of the spacecraft
- LEO departure maneuver  $\Delta v_1$  is impulsive and occurs at a specified epoch
- Orbit insertion maneuver  $\Delta v_2$  occurs at the  $xz$ -plane of the rotating frame and places the spacecraft along a trajectory that, with regular maneuvers, resembles a selected periodic orbit from the CR3BP

**Trajectory itinerary in forward time:**

- 1) Integrate spacecraft state forward in time in selected model from a state that occurs immediately after the first maneuver for  $\Delta t_{transfer}$ , the time until the spacecraft reaches the  $xz$ -plane of the rotating frame
- 2) Apply  $\Delta v_2$  to produce a spacecraft state that, when integrated to the next  $xz$ -plane crossing, lies sufficiently close to the leftmost  $xz$ -plane crossing of the selected periodic orbit from the CR3BP
- 3) Calculate successive maneuvers at each leftmost  $xz$ -plane crossing to target bounded motion near the selected periodic orbit from the CR3BP

**Variables to calculate:**

- Initial apoapsis radius, right ascension of the ascending node and argument of periapsis after first maneuver
- $\Delta v_1$  to depart the low Earth orbit (calculate after corrections using velocity difference)
- $\Delta v_2$  to insert into a mission orbit on the  $xz$ -plane of the rotating frame
- Time of flight along the transfer  $\Delta t_{transfer}$
- Several impulsive maneuvers, each at leftmost  $xz$ -plane crossing of rotating frame to target mission orbit

**Why use this approach?** Solving the problem forward in time can be conceptually easier to understand. The state immediately after  $\Delta v_1$  is also straightforward to describe and vary using Keplerian orbital elements due to the spacecraft beginning close to the Earth. This approach might also be useful if the epoch of  $\Delta v_1$  is constrained.

**When to not use this approach?** This is a sensitive corrections problem due to the challenges of specifying the target conditions when the epoch at arrival into the mission orbit may vary.

Let's demonstrate the process for solving this two-point boundary value problem in forward time. First, consider the requirement that the spacecraft departs from a circular orbit around the Earth with an inclination of 28.5 deg in the GCRF and an altitude of 200 km. The first impulsive maneuver is assumed to place the spacecraft onto the transfer at perigee with this same inclination. After completing the transfer, a second maneuver places the spacecraft onto a trajectory that resembles the selected Earth-Moon southern  $L_1$  halo orbit with an 11.1 day period. This maneuver is applied at a state that occurs on the  $xz$ -plane of the Earth-Moon rotating frame. Following a similar procedure to calculating the reference mission orbit in the ephemeris model using single-shooting in GMAT, the state at the insertion point is integrated forward in time to the next  $xz$ -plane crossing (near apolune). This state must lie sufficiently close to the leftmost  $xz$ -plane crossing of the periodic orbit in the Earth-Moon rotating frame, equal in nondimensional units to a truncated value of:

$$\mathbf{x}_{EMB,PO}^{EMR} = [0.849895, 0, -0.175343, 0, 0.262953, 0]^T$$

for an orbit period of approximately 11.1 days. Because this state exists in the CR3BP, there is no specific epoch at which this state must be targeted. The transfer that achieves this goal is modeled using a point mass ephemeris model of the Earth, Moon, and Sun, with SRP and a  $36 \times 36$  higher-order gravity field of the Earth.

In this problem formulation, seven variables are modified during corrections including: the apogee radius, right ascension of the ascending node (RAAN) and argument of perigee immediately after the first maneuver, as well as the integration time along the transfer and the insertion maneuver. This corrections problem is designed to begin after the first maneuver to ensure that the maneuver occurs at perigee and does not modify the inclination. This approach also removes three variables from the corrections problem because the resulting tangential first maneuver can be straightforwardly calculated with one nonzero element in the velocity direction: equal to the difference between the speed at the beginning of the transfer and the speed along a circular orbit with the same inclination. For this example, the epoch at the beginning of the transfer is constrained to occur at January 1st, 2025, 00:00:00.00 UTC. Based on this setup, Keplerian orbital elements are modified at the beginning of the transfer, as opposed to the elements of a Cartesian state in an inertial or rotating frame, because some orbital elements are unchanged through the first maneuver that occurs close to the Earth. Through this approach, additional computations or constraints are not required to ensure that the perigee radius and inclination are fixed. In cases like this, alternative state descriptions may simplify the formulation of a corrections problem.

Several constraints are used in the corrections problem. First, the insertion point is constrained to lie on the  $xz$ -plane of the rotating frame by requiring that the  $y$  component of the state equals 0 in the Earth-Moon rotating frame to within a small tolerance of 0.001 km. Then, the state that lies at the subsequent  $xz$ -plane crossing (near apolune) is constrained: the state calculated via GMAT must possess  $x$  and  $z$  components in the rotating frame that match the dimensional values of the associated components of  $\mathbf{x}_{EMB,PO}^{EMR}$  at the same epoch to within a desired tolerance. As a result, the  $x$  and  $z$

components are multiplied by the instantaneous distance between the Earth and Moon at the epoch at the end of the transfer to produce dimensional quantities. The tolerance on meeting this set of position constraints is equal to 500 km. The same procedure is followed to constrain the  $\dot{x}$  value in the rotating frame at this  $xz$ -plane crossing near apolune to equal 0 to within a tolerance of 0.001 km/s. Note that adding constraints on the remaining state components may make it more difficult to recover a solution to this sensitive corrections problem. Furthermore, the tolerance applied to meeting these target conditions may be relaxed to larger values as needed to produce nearby and natural bounded motions in the ephemeris model; selecting these values in an informed manner may require having completed the analysis presented in Sec. 8.2.3 or 8.2.4 to produce bounded motions that resemble nearby orbits from the CR3BP.

### Challenge: Targeting a Mission Orbit with Unconstrained Epoch at the End of the Transfer

Similar to the process for targeting a mission orbit in Sec. 8.2.3, meaningful tolerances on the state components are challenging to determine because a state that lies along a periodic orbit in the CR3BP does not produce similar motion in an ephemeris model. The selected tolerance may influence the success of and number of iterations performed by the corrector as well as the maneuver magnitudes. The location along a periodic orbit that is used as a reference during targeting may also influence the corrections problem in some cases. In this example, motion near perilune, where the spacecraft passes close to the Moon, is sensitive to perturbations. That means the corrections problem can become numerically sensitive when targeting a state to produce a desired mission orbit and the thresholds on reaching those targets can be challenging to select. At apolune, motion is less sensitive to perturbations; this state may offer a less sensitive location for targeting a mission orbit. Due to these challenges, targeting a mission orbit that resembles a periodic orbit from the CR3BP at the end of a transfer might require some iteration from the trajectory designer if using this problem formulation.

One challenge to solving the two-point boundary value problem with this formulation is calculating initial guesses for the problem variables. To define these initial guesses, let's use a preliminary analysis in the CR3BP that resembles a coarse grid search. In this approach, a set of arcs are generated in the CR3BP to depart the LEO. The goal is to find an arc amongst this set that also closely approaches the mission orbit. To reduce the complexity of this analysis, these arcs are first described by Keplerian orbital elements in the GCRF with the periapsis radius and inclination fixed; the transfer is constrained to begin at perigee. The values of the apogee radius, RAAN and argument of perigee at the beginning of the transfer are varied. The resulting orbital element combinations are then used to write a set of initial state vectors in the Earth-Moon rotating frame that are integrated in the CR3BP to produce low-fidelity approximations of potential transfer arcs. To perform these transformations, the orbital element description of the spacecraft is first converted to a Cartesian state description in the GCRF. Then, the Cartesian state is transformed into the Earth-Moon rotating frame. Finally, the position and velocity components of the state vector are nondimensionalized by the characteristic quantities

of the CR3BP computed using the instantaneous distance between the Earth and Moon at the selected initial epoch of January 1st, 2025, 00:00:00.00 UTC.

For the direct transfer, this coarse grid search produces a useful set of initial guesses. First, the characteristic length quantity of the Earth-Moon system supplies a sufficient initial guess for the initial apoapsis radius, i.e.,  $r_a = l^*$ . The initial RAAN in the GCRF of the transfer trajectories is then varied manually to identify trajectories that closely approach the  $L_1$  southern halo orbit. For the selected initial epoch, a value of RAAN = 350 deg appears to supply a good initial guess. Using the selected values of the initial apoapsis radius and RAAN, the initial argument of perigee for the transfer arc is varied between 0 and 360 deg to generate a set of candidate arcs. Each trajectory in the set is propagated in the CR3BP until its first apogee. The generated trajectories are plotted in light red in Fig. 49 and visualized in the Earth-Moon rotating frame. The target Earth-Moon  $L_1$  southern halo orbit from the CR3BP is also plotted in black for reference. From this set, the trajectory that terminates closest to perilune of the halo orbit is selected to form an initial guess for the direct transfer. This trajectory is plotted in dark red in Fig. 49 and possesses an initial argument of perigee of 190.8 deg. Finally, the transfer time  $\Delta t_{transfer}$  is set equal to half the period of a conic with a semi-major axis calculated using the required initial perigee radius and guess for the apogee radius. An alternative method to select suitable initial guesses for these variables may involve a more time-consuming guess and check approach.

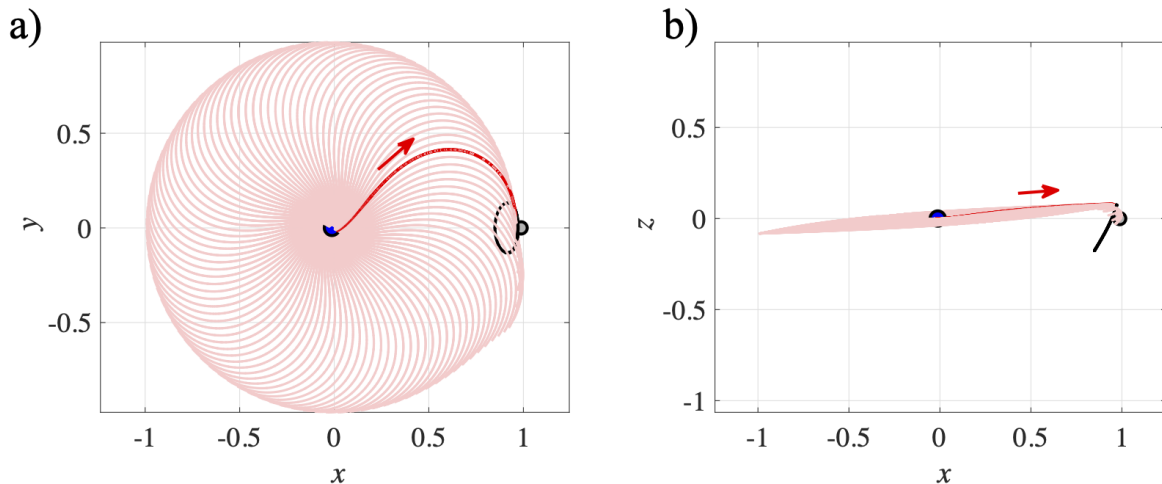


**Fig. 49** Arcs generated with various arguments of perigee in a coarse grid search to construct an initial guess for a direct transfer, to be computed by targeting the mission orbit in forward time.

This two-point boundary value problem is solved in GMAT to determine the transfer time and initial orbital elements that produce a transfer reaching a mission orbit that resembles a periodic orbit from the CR3BP. The differential corrector in each step is configured to use a Newton-Raphson method for up to 50 iterations; this maximum number of iterations can be adjusted as needed to limit computational time or accommodate a poor initial guess. Maximum changes in the value of each variable are also specified as 2000 km for the apogee radius, 1 degree for the RAAN and

argument of perigee, and 0.1 days for the transfer time. These values can be updated if a problem is too sensitive or the initial guess is being updated too many times before reaching a solution. Finally, forward finite differencing is used to approximate the derivatives of the constraints with respect to each variable. The perturbations used to calculate the finite difference in GMAT are set equal to the default values of  $1 \times 10^{-5}$ . This value influences the error in the approximation of the derivative and may be updated as needed. The corrector converges on a solution from the specified initial guess in 18 iterations to produce the values listed in the final column of Table 11. For this transfer, the magnitudes of the impulsive maneuvers are equal to  $\Delta v_1 = 3.131$  km/s and  $\Delta v_2 = 488.2$  m/s. Note that  $\Delta v_1$  is typically supplied by a stage of the launch vehicle. The second maneuver possesses a similar magnitude to the maneuver calculated by solving the problem backward in time and is also less than the 1 km/s insertion maneuver requirement. After the transfer, impulsive maneuvers are calculated at every  $xz$ -plane crossing near perilune of the mission orbit to target states near the rightmost

Initial State Parameters in GCRF	Initial Guess	Corrected Value
Epoch*	January 1st, 2025, 00:00:00.00 UTC	January 1st, 2025, 00:00:00.00 UTC
Time of flight	4.805 days	4.748215 days
Perigee radius*	6578.1363 km	6578.1363 km
Apogee radius	384400 km	384400.027864 km
Inclination*	28.5 deg	28.5 deg
RAAN	350 deg	351.236037 deg
AOP	190.8 deg	188.669103 deg
TA*	0deg	0 deg
Initial State (GCRF)	Value Before Maneuver	Value After Maneuver
$X_0$ (km)	-6559.820246	-6559.820141
$Y_0$ (km)	129.6418534	129.641518
$Z_0$ (km)	-473.105181	-473.106730
$\dot{X}_0$ (km/s)	0.129202	0.181171
$\dot{Y}_0$ (km/s)	-6.862858	-9.623188
$\dot{Z}_0$ (km/s)	-3.672034	-5.148972
Final State (EMR)	Value Before Maneuver	Value After Maneuver
$x_f$ (km)	365846.357902	365846.357902
$y_f$ (km)	$-4.279034 \times 10^{-6}$	$-4.279034 \times 10^{-6}$
$z_f$ (km)	22477.031871	22477.031871
$\dot{x}_f$ (km/s)	0.007159	-0.008611
$\dot{y}_f$ (km/s)	-0.615361	-1.046299
$\dot{z}_f$ (km/s)	0.022091	-0.206798
Maneuvers	Value	
$\Delta v_1$ (VNC, km/s)	$[3.131049, 0, 0]^T$	
$\Delta v_2$ (EMR, km/s)	$[0.015769, 0.430938, 0.228889]^T$	

**Table 11 Problem variables and maneuvers along direct transfer following corrections when solving the targeting problem forward in time (\* = variable fixed during corrections).**

$xz$ -plane crossing along the periodic orbit after two revolutions; this process is performed to calculate 10 impulsive maneuvers that produce a trajectory that remains near the periodic orbit from the CR3BP for 10 revolutions. These maneuvers possess magnitudes between 7 m/s and 23 m/s. The corrected transfer and multiple revolutions along the mission orbit are plotted in blue in Fig. 50 in the Earth-Moon rotating frame.

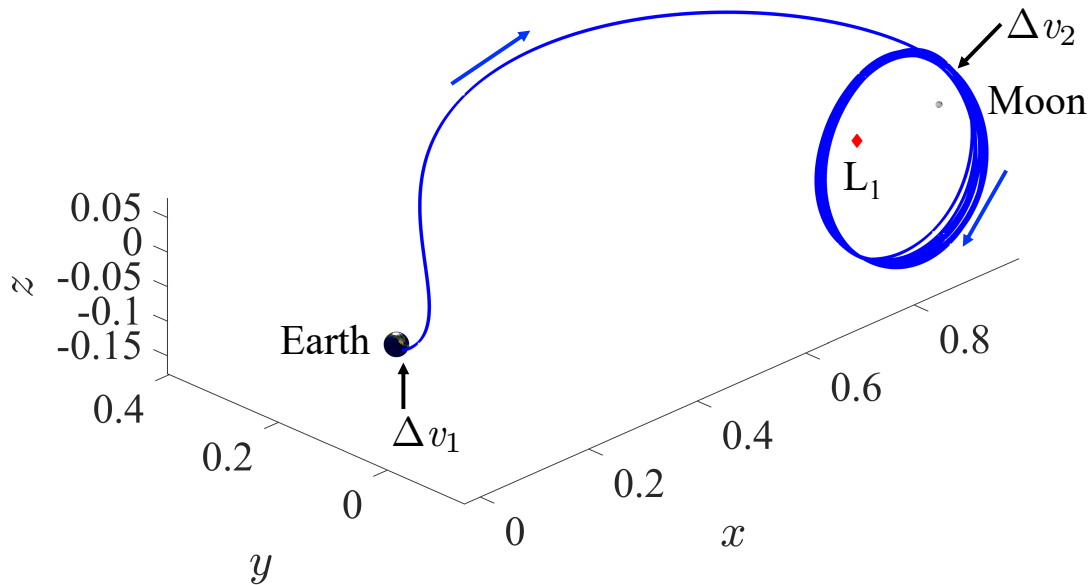


**Fig. 50** Corrected direct transfer from LEO to selected EM  $L_1$  southern halo orbit, calculated by solving the targeting problem in forward time.

### 8.3.3 Designing an Indirect Transfer: Single-Shooting Backward in Time

Consider the problem of designing an indirect transfer from a circular, low Earth orbit with specified semi-major axis and inclination to a fixed state that lies along the selected mission orbit at a specific epoch. One straightforward approach to designing this transfer in a software package such as GMAT is to solve this problem in backward time.

#### **Problem Formulation Example: Designing an Indirect Transfer Backward in Time in GMAT**

**Problem:** Calculate the Earth departure, adjustment and orbit insertion maneuvers producing a transfer trajectory with three impulsive maneuvers that, in backward time, reaches the desired low Earth orbit from a fixed state that lies along the desired mission orbit at a specific epoch.

**Known information and constraints:**

- Target state ( $\mathbf{x}_{M,des}^{MI}$  in a Moon inertial system) and epoch ( $t_{des}$ ) along mission orbit in ephemeris model
- Orbit insertion maneuver  $\Delta v_3$  inserts the spacecraft into the mission orbit
- Path adjustment maneuver  $\Delta v_2$  applied at apogee along the transfer
- Semi-major axis, eccentricity and inclination (in the GCRF) of low Earth orbit
- LEO departure maneuver  $\Delta v_1$  is applied at perigee and does not significantly change the inclination of the spacecraft

**Trajectory itinerary in backward time:**

- 1) Integrate spacecraft state backward in time from  $\mathbf{x}_{M,des}^{MI}$  at  $t_{des}$  along the mission orbit for a time  $\Delta t_{int}$
- 2) Apply  $\Delta v_3$  to insert into the mission in forward time or depart the mission orbit in backward time
- 3) Integrate spacecraft state backward in time until the spacecraft reaches apogee
- 4) Apply  $\Delta v_2$  to adjust the path of the spacecraft at apogee
- 5) Integrate spacecraft state backward in time until perigee
- 6) Apply  $\Delta v_1$  to depart LEO in forward time or insert into the LEO in backward time

**Variables to calculate:**

- Impulsive maneuvers  $\Delta v_1$ ,  $\Delta v_2$ , and  $\Delta v_3$
- Time to reach selected state along the mission orbit after  $\Delta v_3$

**Why use this approach?** In this problem the final state and epoch are known a priori and the problem is to calculate the initial state and epoch as well as the maneuvers required along the transfer. By solving the problem backward in time, the final conditions are guaranteed to be satisfied by the computed transfer (if one exists). In addition, it is straightforward to describe the desired LEO and construct targeting conditions. It is more difficult to robustly achieve and describe the target conditions and tolerances for a state along a mission orbit that resembles a periodic orbit from the CR3BP.

Let's demonstrate the process for solving this two-point boundary value problem in backward time. The target state along the mission orbit in the ephemeris model is the same initial state calculated using multiple-shooting in Sec. 8.2.4:

$$\mathbf{x}_{M,des}^{MI} = [-29190.364607\text{km}, 70749.103743\text{km}, -36686.168676\text{km}, 0.119813\text{km/s}, 0.054833\text{km}, -0.008184\text{km}]^T$$

expressed using truncated values in the Moon inertial frame with  $t_{des}$  as January 1st, 2025, 00:00:00.00 UTC. Note that this is the same target state that is used to construct a direct transfer using a backward time formulation. The goal for this indirect transfer is to depart from a 200 km altitude circular LEO with 28.5 deg inclination in forward time.

Constructing an initial guess for this transfer, which is generated using single shooting, is more challenging than the direct transfer. Let's apply one process for using a fundamental analysis in the CR3BP to construct an initial guess for a transfer: using a set of arcs that lie along the stable manifold of the periodic orbit that is used to design the mission orbit.

A stability analysis of the periodic orbit that exists in the CR3BP reveals that it possesses both a stable mode and unstable mode, indicating the existence of stable and unstable manifolds that govern natural motion that asymptotically approaches and departs the orbit. The orbit also possesses oscillatory modes, indicating the existence of nearby quasi-periodic orbits. Arcs along a stable half-manifold of the selected  $L_1$  southern halo orbit are generated in the CR3BP towards the Earth from fifty states; a projection of these arcs onto the  $xy$ -plane of the Earth-Moon rotating frame is plotted in Fig. 51a) in blue. Each trajectory is integrated backward in time until the first crossing of the  $xz$ -plane that possesses a positive value of  $y$ . This integration time enables visualization of the apogees, indicated by blue circle markers that occur along the arcs.

Next, a set of arcs that depart the LEO is generated to guide specifying initial guesses for the targeting problem. First, an orbital element description is used to specify possible approximations of initial states along the departure arc and following application of the first maneuver. In this analysis, the periapsis radius equals the radius of the LEO whereas the apoapsis radius is assumed to equal 340,000 km consistent with the radii of some of the apogees that occur

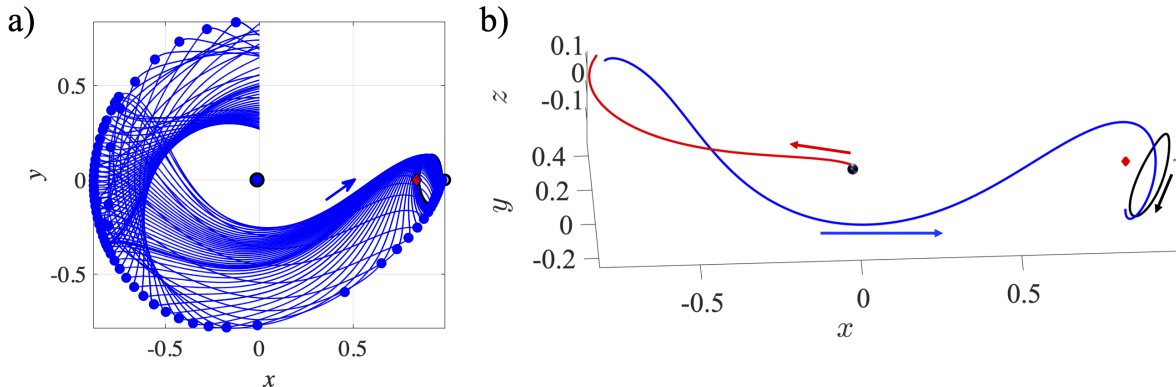


**Fig. 51** a) Stable half-manifold arcs of the selected EM  $L_1$  southern halo orbit projected onto the Earth-Moon plane and b) selected stable manifold and departure arcs used to guide initial guess construction.

in the top left of Fig. 51a) along the stable half-manifold of the halo orbit in the CR3BP. Then, the argument of periapsis and RAAN are varied with the goal of finding one or more arcs that possess apogees that lie near the apogees along the stable manifold arcs. This orbital element description is specified in the GCRF and then converted to a nondimensional state in the Earth-Moon rotating frame. To perform this transformation, an epoch is required but is not known exactly until after corrections. Thus, an approximation is selected by subtracting the time along a stable manifold arc of interest (between apogee and apolune) as well as half the orbit period predicted from the two-body problem from the fixed initial epoch  $t_{des}$  that occurs at apolune right before  $\Delta v_3$  is applied. In this example, a stable manifold arc of interest is selected and its proximity to departure arcs is examined; the selected arc is plotted in blue in 51b). The flight time along this stable manifold arc is 18.67 days and half the orbit period of a conic with the specified semi-major axis is 4.15 days. Thus, the epoch at which  $\Delta v_1$  occurs is estimated as 22.83 days earlier than January 1st, 2025. Following the transformation from the GCRF to the Earth-Moon rotating frame on this epoch, each of the resulting nondimensional state vectors is integrated in the CR3BP forward in time for half a period of the conic from the two-body problem to produce an array of departure arcs.

This analysis reveals that there are departure arcs that end relatively close to the beginning of the stable manifold arc. In fact, an example of a departure arc and stable manifold trajectory segment are plotted in Fig. 51b) in red and blue, respectively, with a position discontinuity of approximately 25,000 km. Such a position discontinuity is expected, but not guaranteed, to be small enough to indicate the potential for successful recovery of a continuous trajectory with suitable guesses for the targeting problem variables. In addition, there is a discontinuity between the end of the stable manifold arc and the fixed initial state that lies close to the periodic orbit (plotted in black) from the CR3BP. Along this initial guess, the spacecraft initially travels towards  $L_3$  before passing close to a stable manifold arc in the configuration space. The stable manifold arc then naturally approaches the EM  $L_1$  southern halo orbit, and the arc is terminated near apolune of the orbit, i.e., the southernmost point along the orbit. This process does not guarantee the recovery of a transfer that minimizes the total maneuver magnitude or another metric. However, this approach guides constructing an initial guess for a transfer that exists within a large solution space; albeit with the use of custom codes to perform this analysis. An alternative approach is to use a guess-and-check process within GMAT.

The constructed initial guess for a transfer enables definition of initial guesses for the individual parameters that are varied by the corrector in GMAT. First, recall that the target state along the mission orbit lies at apolune. The selected arc along the stable manifold of the EM  $L_1$  southern halo orbit in the CR3BP also begins near apolune in the backward time problem; thus, the target state  $x_{M,des}^{MI}$  at  $t_{des}$  is propagated backward in time along the mission orbit for a small integration time with an initial guess of  $\Delta t_{int} = -2$  hours. The initial guess for the maneuver to depart the mission orbit in backward time or insert into it in forward time is equal to  $\Delta v_3 = [5, 0, 0]$  m/s in a VNC frame defined relative to the Moon; this initial guess possesses a small nonzero magnitude to reflect that a state along the periodic orbit does not exactly coincide with a nearby state on the stable manifold and a maneuver is required to step off the natural path that

resembles a periodic orbit. Next, the state is integrated backward in time to depart the vicinity of  $L_1$  until reaching apogee. Then, an initial guess for the path adjustment maneuver that occurs at apogee is selected as  $\Delta v_2 = [-250, 0, 0]$  m/s in a VNC frame defined relative to the Earth. The magnitude of the velocity difference between the two arcs that form the initial guess is over 500 m/s. However, the initial guess is constructed with a smaller magnitude of 250 m/s in the velocity component of this adjustment maneuver in case the corrector can approach a transfer with a lower maneuver magnitude. Next, the spacecraft state is integrated backward in time until perigee and  $\Delta v_1$ , the maneuver that is typically supplied by a stage of the launch vehicle to depart LEO, is defined using VNC axes calculated relative to the Earth. The initial guess provided to GMAT is  $\Delta v_1 = [-3.13, 0, 0]^T$  km/s. This initial guess is simply selected using the approximation from the direct transfer design subsection because the apoapsis distance along the departure arc between  $\Delta v_1$  and  $\Delta v_2$  is approximately  $0.87l^*$ ; this value is slightly below the apoapsis radius of the initial guess for the direct transfer but is expected to change during each iteration of the corrector. Recall that the elements of these maneuvers differ from their associated values in a forward time problem by a negative sign.

The constraints and their thresholds for satisfaction must also be specified. Because the problem is solved using single-shooting, only constraints on the initial LEO, or the target orbit at the end of the time interval in backward time, must be specified. Consider a requirement that the initial LEO possess an inclination of 28.5 degrees in the GCRF. The target perigee and apogee radii are both equal to 6578.14 km, corresponding to a circular orbit with a 200 km altitude. The right ascension of the ascending node and location of perigee are allowed to vary in this example (although that may not always be the case). The threshold for meeting these three constraints is equal to 0.1 km for the perigee and apogee radii and 0.01 degrees for the inclination. These values are selected to be small; however, in practice, these thresholds may be derived from mission or launch vehicle provider requirements.

This two-point boundary value problem is solved in GMAT using a two-step corrections approach. In the first corrections step, the integration time along the mission orbit (that defines the location of  $\Delta v_3$ ) and the two maneuvers,  $\Delta v_2$  and  $\Delta v_3$ , are all varied to achieve the desired periapsis radius and inclination at perigee before the LEO departure maneuver is applied. Thus, seven variables are updated to achieve two independent constraints. In the second corrections step, the integration time along the mission orbit  $\Delta t_{int}$  and all three maneuvers are varied to achieve the desired periapsis and apoapsis radii and inclination at perigee after the LEO departure maneuver is applied. The initial guesses for  $\Delta t_{int}$ ,  $\Delta v_2$ , and  $\Delta v_3$  in the second step are set equal to the values calculated by the first corrections step. One reason to separate out this corrections process into two steps is to reduce the sensitivity of solving a problem where the variables take on values on different orders of magnitude and correspond to motion near two different bodies. The differential corrector in each step is configured to use a Newton-Raphson method for up to 50 iterations; this maximum number of iterations can be adjusted as needed to limit computational time or accommodate a poor initial guess. Maximum changes in the value of each variable are also specified as 0.1 km/s for each maneuver component and 1 hr for  $\Delta t_{int}$ ; these values can be updated if a problem is too sensitive or the initial guess is being updated too many times before reaching a solution.

Finally, a forward differencing method is used to numerically approximate the derivatives of the constraints with respect to each variable. The perturbations used to calculate the finite difference is left at the default value in GMAT of 0.0001. This value influences the error in the approximation of the derivative and may be updated as needed. During both corrections steps, this transfer is modeled using a point mass ephemeris model of the Earth, Moon, and Sun, with SRP and a  $36 \times 36$  higher-order gravity field of the Earth. Recall that when implementing a multi-step corrections process in GMAT, it is important to remember to re-initialize the spacecraft to ensure that the spacecraft possesses the same initial state and epoch during each corrections step.

After implementing this procedure in GMAT, the initial guess and final values at each corrections step are listed in Table 12. The first corrections step requires 16 iterations to meet the required constraints whereas the second corrections step requires 2 iterations. The resulting direct transfer, computed in GMAT appears in Fig. 52 in royal blue. 16 revolutions around the mission orbit, as calculated in Sec. 8.2.4 using multiple-shooting, are also added to this figure in dark blue; recall that this mission orbit requires a total maneuver magnitude of approximately 0.33 m/s over 176 days. The magnitude of  $\Delta v_1$  to depart the initial circular orbit is 3.125 km/s. The magnitude of the second maneuver at the first apogee along the transfer is 457.57 m/s and the magnitude of the third maneuver to insert into the mission orbit at apolune is 55.47 m/s. The total transfer time is 23.15 days. Finally, the corrected transfer approximately resembles the two arcs in the initial guess plotted in Fig. 51b). Using a multiple-shooting approach may produce a closer resemblance between an initial guess constructed using those two arcs and the corrected transfer. A multiple-shooting approach may also help to reduce the sensitivity of solving an alternative formulation of this problem in forward time.

Variable	Initial Guess	Value After 1st Corrections Step	Value After 2nd Corrections Step
$\Delta v_1$ (VNC, km/s)	$\begin{bmatrix} -3.13 \\ 0 \\ 0 \end{bmatrix}$	N/A	$\begin{bmatrix} -3.124835 \\ 1.936560 \times 10^{-6} \\ -7.125414 \times 10^{-6} \end{bmatrix}$
$\Delta v_2$ (VNC, km/s)	$\begin{bmatrix} -0.250 \\ 0 \\ 0 \end{bmatrix}$	$\begin{bmatrix} -0.457445 \\ -0.009962 \\ 0.000322 \end{bmatrix}$	$\begin{bmatrix} -0.457456 \\ -0.010035 \\ -0.000322 \end{bmatrix}$
$\Delta v_3$ (VNC, km/s)	$\begin{bmatrix} 0.05 \\ 0 \\ 0 \end{bmatrix}$	$\begin{bmatrix} -0.026031 \\ 0.023660 \\ -0.042933 \end{bmatrix}$	$\begin{bmatrix} -0.025851 \\ 0.023681 \\ -0.042982 \end{bmatrix}$
$\Delta t_{int,3}$ (hours)	-2	-2	-2
Target Parameter	Target Value	Value After 1st Corrections Step	Value After 2nd Corrections Step
Periapsis radius (km)	6578.14	6578.140937	6578.122910
Apoapsis radius (km)	6578.14	N/A	6578.166759
Inclination (deg)	28.499999	28.5	28.500004

**Table 12 Values of variables and target parameters after each corrections step when constructing an indirect transfer by solving the targeting problem in backward time.**

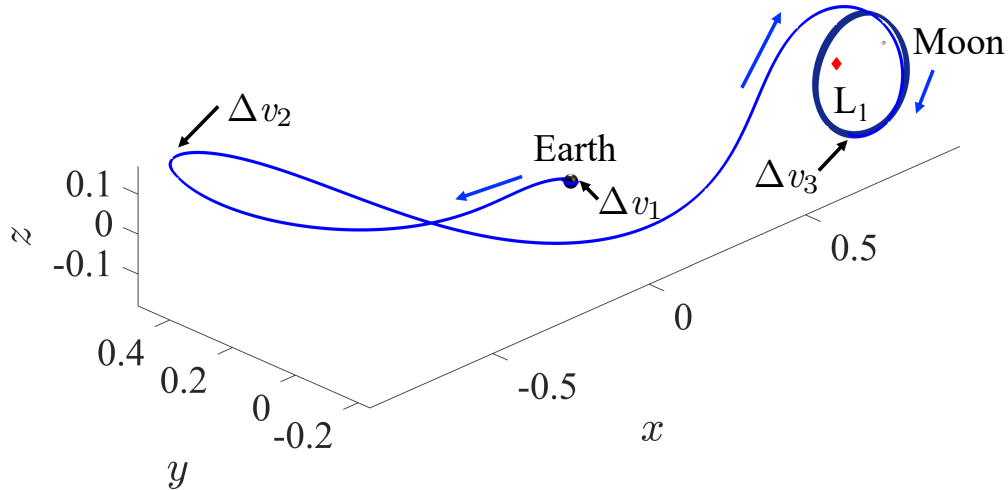


**Fig. 52** Corrected indirect transfer from LEO to selected EM  $L_1$  southern halo orbit, calculated by solving the targeting problem in backward time.

#### Notes: Maneuver Magnitudes for this Indirect Transfer

For this indirect transfer, a slightly larger total maneuver magnitude is required in comparison to the direct transfer. However, the total maneuver magnitude of the indirect transfer is within the anticipated range of impulsive maneuver requirements to an Earth-Moon halo orbit [100, 102]. Furthermore, optimization techniques can be used to further reduce the total maneuver cost of the transfer. Astrodynamics software packages such as GMAT often possess optimizer plugins. An alternative approach to reduce the maneuver magnitude is to construct the transfer in a custom code that implements a multiple shooting strategy using the initial guess constructed in the CR3BP. Optimization or a gradual reduction in the maneuver magnitude can then be applied.

#### 8.4 Station-Keeping Near the Mission Orbit

The final analysis in this use case focuses on designing impulsive station-keeping maneuvers that produce a spacecraft path that remains bounded in the vicinity of a desired motion. These maneuvers are necessary as, for example, state uncertainties, model uncertainties or errors, and maneuver execution errors produce a spacecraft path that deviates from the designed or expected path. There are a variety of useful station-keeping maneuver design strategies, problem formulations, and solution approaches that have been developed within the astrodynamics community. This subsection will present one foundational approach that involves designing maneuvers that occur at each  $xz$ -plane crossing in the Earth-Moon rotating frame to target a desired combination of  $x$  and  $z$  coordinates at the second subsequent  $xz$ -plane crossing. The presented approach uses a single shooting scheme within a local constrained optimization problem to design maneuvers with the minimum magnitude that target components of the state at each  $xz$ -plane crossing to lie within a specified threshold of those associated with the desired path computed in Sec. 8.2.4.

### Problem Formulation Example: Designing Station-Keeping Maneuvers via Single Shooting in GMAT

**Problem:** Calculate a sequence of impulsive maneuvers at each  $xz$ -plane crossing in the Earth-Moon rotating frame to produce a bounded trajectory that remains close to a desired path in an ephemeris model.

**Known information and constraints:**

- Desired trajectory in a selected dynamical model for specified initial epoch  $t_{des}$  and desired number of revolutions around the orbit  $N_r$
- Maneuvers occur at each  $xz$ -plane crossing to target  $x$  and  $z$  coordinates of second subsequent  $xz$ -plane crossing, each within a tolerance of  $\Delta r$
- State uncertainty error with maximum magnitude of  $e_{pos}$  and  $e_{vel}$  in the position and velocity components
- Maneuver execution errors of  $e_{dv}\%$  are applied

**Variables to calculate:**

- Impulsive maneuvers  $\Delta v_i$  for  $i = [1, 2N_r]$  with the locally minimum magnitude that satisfies the station-keeping problem

**Maneuver design approach:**

- 1) Define initial state  $\mathbf{x}_{M,1,0}^{MI}$  at  $t_1$  in Moon inertial frame
- 2) Use local constrained optimization to calculate the  $i$ -th impulsive station-keeping maneuver  $\Delta v_i$  to apply at  $\mathbf{x}_{M,i,0}^{MI}$  and  $t_i$  for  $i = [1, 2N_r]$ . This maneuver is calculated to possess the locally minimum magnitude to produce  $x$  and  $z$  coordinates at the second subsequent crossing of the  $xz$ -plane that each lie within  $\Delta r$  of the associated  $xz$ -plane crossing of the desired trajectory in the Earth-Moon rotating frame
- 3) Apply a state uncertainty
- 4) Apply the calculated maneuver  $\Delta v_i$  with a maneuver magnitude execution error
- 5) Integrate the perturbed path forward in time until the next  $xz$ -plane crossing
- 6) Repeat Steps 2-5 until completing  $N_r$  revolutions around the orbit

**Benefits of this example?** This single-shooting strategy can be straightforwardly implemented in custom codes or GMAT. Targeting the station-keeping maneuvers to achieve a desired state after one revolution produces a straightforward targeting condition.

**Limitations of this specific example?** Targeting the station-keeping maneuvers to achieve a desired state after one revolution encourages, but doesn't necessarily guarantee, the recovery of motion that remains near a desired path between each  $xz$ -plane crossing. If the computed maneuver is too small to implement, the designer may wish to target an  $xz$ -plane crossing that is further downstream.

Station-keeping maneuvers are calculated to produce a controlled path that remains near the desired trajectory calculated in Sec. 8.2.4 despite state uncertainty and maneuver execution errors. First, a small perturbation is applied to

the initial condition that is calculated in Sec. 8.2.4; the resulting state is the initial condition for the controlled path. In addition, state uncertainties are added to the state at each  $xz$ -plane crossing after each maneuver has been calculated. The position and velocity components of these uncertainties are randomly selected from a uniform distribution to possess a maximum magnitude of 1 km and 1 cm/s, respectively [108]. Maneuver magnitude execution errors are also applied and randomly selected from a uniform distribution to possess a maximum magnitude of 2%. With state uncertainty and maneuver execution errors applied after each station-keeping maneuver has been computed, the spacecraft will not follow its predicted path. Finally, the dynamical environment is modeled using a point mass ephemeris model of the Earth, Moon, and Sun, with SRP, consistent with the mission orbit computation example.

In this example, impulsive station-keeping maneuvers are calculated at each  $xz$ -plane crossing to target the  $x$  and  $z$  coordinates of the second subsequent  $xz$ -plane crossing to within 100 km of the associated crossing of the desired trajectory that is calculated in Sec. 8.2.4 in the ephemeris model. In this particular formulation, the three components of an impulsive maneuver, located at an  $xz$ -plane crossing, may vary without any magnitude or direction constraints. Then, the trajectory associated with a state and the current guess for the impulsive maneuver at the  $xz$ -plane crossing is numerically integrated in the same dynamical model as the desired trajectory in Sec. 8.2.4 until it completes two crossings of the  $xz$ -plane, i.e., when  $y = 0$ . The resulting state is then described by 5 state components that may vary as the impulsive maneuver is also varied. To avoid overconstraining the problem, only 2 of these state components are used to define target variables: in this example, the goal is to adjust the impulsive maneuver until the  $x$  and  $z$  components of the state vector at the  $xz$ -plane crossing equal their desired values in the Earth-Moon rotating frame to within 100 km. The desired values for these state components is selected using the associated  $xz$ -plane crossing of the desired trajectory at a similar epoch. Although this formulation means that the desired values will vary at each maneuver computation, this approach is designed to produce a trajectory that closely resembles a desired trajectory that exists in the same dynamical model in both space and time. Alternative, simpler formulations may constrain the state components to equal the associated values along a periodic orbit from the CR3BP. In that case, the goal may be to simply recover nearby bounded motion, rather than a trajectory that lies close to a specific reference path that exists in the higher-fidelity model.

Based on the target and free variable definitions, more than one maneuver may satisfy the station-keeping maneuver design problem. Thus, local constrained optimization is also employed to calculate the maneuver with the locally minimum magnitude that solves the station-keeping problem. This constrained optimization problem involves defining the free variable vector:

$$\mathbf{V} = [\Delta v_X, \Delta v_Y, \Delta v_Z]^T$$

to contain the three components of the nondimensional impulsive maneuver  $\Delta\mathbf{v}$  in the Moon inertial frame applied to a nondimensional state  $\mathbf{x}_{M,0}^{MI}$  that is also expressed in the Moon inertial frame but located along the  $xz$ -plane of the Earth-Moon rotating frame. These maneuver components are expressed in the inertial frame to limit the computational

time associated with additional frame transformation steps during optimization; however, this problem could be straightforwardly modified to use maneuver components expressed in the rotating frame. The goal is to compute a free variable vector that minimizes the following scalar objective function:

$$J(\mathbf{V}) = ||\Delta\mathbf{v}||^2$$

while satisfying the following constraints:

$$(x_f - x_{des})^2 \leq (100/l^*)^2, (z_f - z_{des})^2 \leq (100/l^*)^2$$

This constraint includes the desired values,  $x_{des}$  and  $z_{des}$ , of the  $x$  and  $z$  components of the state in the Earth-Moon rotating frame at the second subsequent  $xz$ -plane crossing, derived from the reference trajectory. In addition,  $x_f$  and  $z_f$  are their actual values along the perturbed path of the spacecraft. Once a free variable vector and, therefore, an impulsive maneuver is calculated to solve this local constrained optimization problem, the nondimensional state  $\mathbf{x}_{M,0}^{MI}$  is perturbed by the state uncertainties and the maneuver is applied along with an error in its magnitude. The resulting trajectory is generated for half a revolution until the next  $xz$ -plane crossing in the Earth-Moon rotating frame. The state at this  $xz$ -plane crossing then supplies the nondimensional state  $\mathbf{x}_{M,0}^{MI}$  for the next station-keeping maneuver computation.

Of course, there are other station-keeping strategies that may be useful. Alternative formulations may involve other maneuver locations and cadences, targeting other state components (e.g., a velocity component at a subsequent  $xz$ -plane crossing), reaching these targets over different time horizons (e.g., after more revolutions near the halo orbit or a specified time interval), calculating multiple maneuvers simultaneously, and using initial guesses derived from dynamical systems theory (e.g., using stable mode information), etc [108–112]. The development, implementation and comparison of these formulations has been a significant avenue of research in the astrodynamics community. Some of these alternative formulations may produce a lower cumulative station-keeping maneuver magnitude than the values in this particular example.

Following the procedure used in this example, a sequence of 30 station-keeping maneuvers over 15 revolutions of the  $L_1$  northern halo orbit are computed in custom codes implemented in MATLAB with the same ephemeris model as Sec. 8.2.4. The resulting path is displayed in Fig. 53a) in the pulsating Earth-Moon rotating frame in blue. The maneuver locations are plotted using black circles with scaled red arrows reflecting the maneuver directions and relative magnitudes. The magnitudes of these maneuvers, applied every half a revolution, are plotted in Fig. 53b). Over the span of approximately 166 days, the station-keeping maneuvers possess a total cumulative magnitude of 11.17 m/s; this value is below the 100 m/s available for station-keeping maneuvers. Note, however, that the expected total magnitude of these maneuvers typically depends on the goals, variables, and thresholds specified in the station-keeping maneuver design

problem. Finally, the position difference between the controlled path and the desired trajectory at each  $xz$ -plane crossing is plotted in Fig. 53c). The red line indicates the threshold on the desired deviation between the  $xz$ -plane crossings before any state uncertainty or maneuver execution errors are applied. The blue points indicate their actual values at each  $xz$ -plane crossing when state uncertainty and maneuver execution errors perturb the path of the spacecraft; if these errors and uncertainties were not incorporated, the maneuvers would produce  $xz$ -plane crossings that remain below the red line. Although some of these blue points exceed the threshold of 141 km, each of the 30  $xz$ -plane crossings still remains relatively close to those of the desired trajectory in the configuration space.

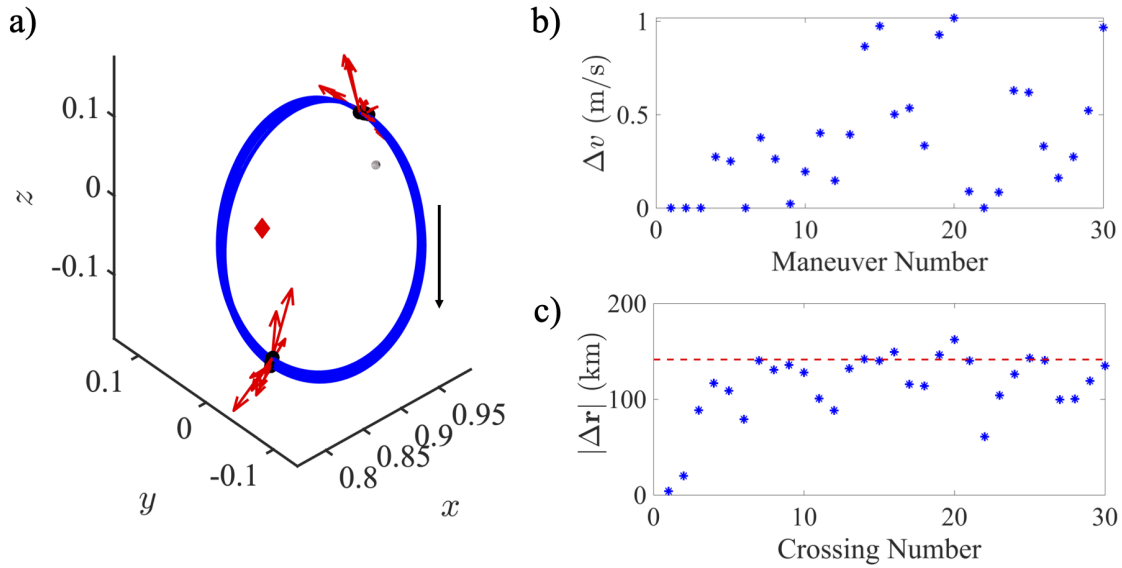


**Fig. 53** a) Trajectory generated for 15 revolutions in the ephemeris model, b) magnitudes of the impulsive station-keeping maneuvers, and c) position deviation in the  $xz$ -plane crossings between the controlled path and the desired path calculated in Sec. 8.2.4.

## 9 Summary

As stated in the executive summary, the purpose and direction of this document is to provide U.S. government agencies, specifically National Aeronautics and Space Administration (NASA) and Department of Defense (DoD) space related centers, with a foundational summary of astrodynamics concepts for trajectory design, navigation, and operations in the cislunar, lunar, and libration point regions. The information and examples included in this document are critical to mission design and navigation where lunar perturbations are required to be modeled accurately and consistently. The authors hope that each section supplies the reader with the necessary mathematical background, coordinate system definitions and transformations, dynamical systems descriptions, and methods and guidance to design trajectories within these Earth and lunar regions. The Goddard Space Flight Center (GSFC) open source General Mission Analysis Tool (GMAT) is used as the reference software for demonstration but the information applies to any astrodynamics tool or application. A wide variety of resources constructed by NASA and other government agencies, academia, and industry, for mathematical specifications and practical considerations are listed in the numerous references.

In closing, the authors wish to thank the National Geospatial-Intelligence Agency (NGA) for their support and collaboration in the design and development of this valuable reference. Future versions of this document are expected to address in-depth integration techniques, dynamics of stable lunar orbits, applications to other mission types such as distant retrograde orbits and Near Rectilinear Halo Orbits, and consideration of relative and co-orbiting spacecraft.

## References

- [1] Drewes, H., 2009, "Reference Systems, Reference Frames, and the Geodetic Datum," In: Sideris M.G. (eds) *Observing our Changing Earth* International Association of Geodesy Symposia, Vol 133. Springer, Berlin, Heidelberg.
- [2] Greenwood, D.T., 1988, *Principles of Dynamics, Second Edition*, Pearson Education Company, Upper Saddle River, NJ.
- [3] Seidelmann, P.K., 1992, *Explanatory Supplement to the Astronomical Almanac*, University Science Books, Mill Valley, CA.
- [4] XXVIth International Astronomical Union General Assembly, 2006, *IAU 2006 Resolution B1: Adoption of the P03 Precession Theory and Definition of the Ecliptic*.
- [5] Gurfil, P.; Seidelmann, P.K., 2016, *Celestial Mechanics and Astrodynamics: Theory and Practice*, Springer-Verlag Berlin Heidelberg.
- [6] Vallado, D.A., 2013, *Fundamentals of Astrodynamics and Applications: Fourth Edition*, Microcosm Press, Hawthorne, CA.
- [7] Petit, G.; Luzum, B. (eds), 2010, "IERS Conventions (2010)", International Earth Rotation and Reference Systems Service, Technical Note 36.
- [8] Charlot, P.; Jacobs, C.S.; Gordon, D.; Lambert, S.; de Witt, A.; Bohm, J.; Fey, A.L.; Heinkelmann, R.; Skurikhina, E.; Titov, O.; Arias, E.F.; Bolotin, S.; Bourda, G.; Ma, C.; Malkin, Z.; Nothnagel, A.; Mayer, D.; MacMillan, D.S.; Nilsson, T.; Gaume, R., 2020, "The Third Realization of the International Celestial Reference Frame by Very Long Baseline Interferometry", *Astronomy and Astrophysics*, Vol. 644, doi: 10.1051/0004-6361/202038368.
- [9] Park, R.S; Folkner, W.M.; Williams, J.G.; Boggs, D.H., 2021, "The JPL Planetary and Lunar Ephemerides DE440 and DE441," *The Astronomical Journal*, Vol. 161, No. 105, doi: 10.3847/1538-3881/abd414.
- [10] Office of Geoinformatics, National Geospatial-Intelligence Agency (NGA), 2014, "Department of Defense World Geodetic System 1984: Its Definition and Relationships with Local Geodetic Systems"
- [11] Chairman of the Joint Chiefs of Staff Instruction 6130.01G, "2019 Chairman of the Joint Chiefs of Staff Master Positioning, Navigation, and Timing Plan", dated 3 June 2019
- [12] (U) Intelligence Community (IC), "(U//FOUO) Time, Frequency, Ephemeris, Geodesy and Weather Reference and Guidance Handbook (TFEGW-RGH)", Version 16, dated February 24 2021
- [13] General Mission Analysis Tool Version R2020a: Mathematical Specifications.
- [14] Lunar Reconnaissance Orbiter Project and Lunar Geodesy and Cartography Working Group, 2008, "A Standardized Lunar Coordinate System for the Lunar Reconnaissance Orbiter and Lunar Datasets," White paper, Version 5.
- [15] Archinal, B.A.; A'Hearn, M.F.; Bowell, E.; Conrad, A.; Consolmagno, G.J.; Courtin, R.; Fukushima, T.; Hestroffer, D.; Hilton, J.L.; Krasinsky, G.A.; Neumann, G.; Oberst, J.; Seidelmann, P.K.; Stooke, P.; Tholen, D.J.; Thomas, P.C.; Williams, I.P., 2011, "Report of the IAU Working Group on Cartographic Coordinates and Rotational Elements: 2009," *Celestial Mechanics and Dynamical Astronomy*, Vol. 109, pp. 101-135, doi: 10.1007/s10569-010-9320-4

- [16] International Laser Ranging Service, "Lunar Laser Ranging", Online: <https://ilrs.gsfc.nasa.gov/science/scienceContributions/lunar.html>, Last accessed: 9/13/21
- [17] Williams, J.G.; Boggs, D.H.; Folkner, W.M., 2013, "Interoffice Memorandum", IOM 335-JW,DB,WF-20130722-016, July 22.
- [18] Map Projections Used by the U.S. Geological Survey Bulletin 1532. <https://pubs.er.usgs.gov/publication/b1532>
- [19] Smith, D.E.; Zuber, M.T.; Neumann, G.A.; Mazarico, E.M.; Lemoine, F.G.; Head III, J.W.; Lucey, P.G.; Aharonson, O.; Robinson, M.S.; Sun, X.; Torrence, M.H.; Barker, M.K.; Oberst, J.; Duxbury, T.C.; Mao, D.; Barnouin, O.S.; Jha, K.; Rowlands, D.D.; Goossens, S.; Baker, D.; Bauer, S.; Gläser, P.; Lemelin, M.; Rosenburg, M.; Sori, M.M.; Whitten, J.; Mcclanahan, T., 2017, "Summary of the Results from the Lunar Orbiter Laser Altimeter after Seven Years in Lunar Orbit," *Icarus*, Vol. 283, pp. 70-91, doi: 10.1016/j.icarus.2016.06.006
- [20] Archinal, B.A.; Acton, C.H.; A'Hearn, M.F.; Conrad, A.; Consolmagno, G.J.; Duxbury, T.; Hestroffer, D.; Hilton, J.L.; Kirk, R.L.; Klioner, S.A.; McCarthy, D.; Meech, K.; Oberst, J.; Ping, J.; Seidelmann, P.K.; Tholen, D.J.; Thomas, P.C.; Williams, I.P., 2018, "Report of the IAU Working Group on Cartographic Coordinates and Rotational Elements: 2015," *Celestial Mechanics and Dynamical Astronomy*, Vol. 130, No. 22, doi: 10.1007/s10569-017-9805-5.
- [21] Vallado, D., Cefola, P., 2012, "Two-Line Element Sets - Practice and Use," *63rd International Astronautical Congress*, Naples, Italy.
- [22] Hoots, F.; Roehrich, R.; 1988, "Spacetrack Report No. 3: Models for Propagation of NORAD Element Sets"
- [23] Früh, C.; Schildknecht, T., 2012, "Accuracy of Two-Line-Element Data for Geostationary and High-Eccentricity Orbits," *Journal of Guidance, Control, and Dynamics*, Vol. 35, No. 5, doi: 10.2514/1.55843.
- [24] Hoots, F., 2021, "SGP4-XP Informational Briefing", TOR-2021-00780
- [25] Aida, S.; Kirschner, M., 2013, "Accuracy Assessment of SGP4 Orbit Information Conversion into Osculating Elements," *6th European Conference on Space Debris*, Darmstadt, Germany.
- [26] Kopeikin, S.; Efroimsky, M.; Kaplan, G., 2011, *Relativistic Celestial Mechanics of the Solar System* Wiley-VCH Verlag GmbH & Co. KGaA, Weinheim, Germany. doi: 10.1002/9783527634569.
- [27] The Consultative Committee for Space Data Systems, 2019, "Report Concerning Space Data System Standards: Navigation Data - Definitions and Conventions," Informational Report CCSDS 500.0-G-4.
- [28] Bureau International des Poids et Mesures, Online: <https://www.bipm.org/en/si-base-units/second> Last Accessed: June 8, 2021.
- [29] Jekeli C.; Montenbruck O, 2017, "Time and Reference Systems," In: Teunissen P.J., Montenbruck O. (eds) *Springer Handbook of Global Navigation Satellite Systems*. Springer Handbooks, Springer, Cham.

- [30] Kaplan, G.H., 2005, "The IAU Resolutions on Astronomical Reference Systems, Time Scales, and Earth Rotation Models," United States Naval Observatory, Circular No. 179.
- [31] Harada, W.; Fukushima, T., 2003, "Harmonic Decomposition of Time Ephemeris DE405," *Astronomical Journal*, Vol. 126, pp. 2557-2561, doi: 10.1086/378909.
- [32] International Earth Rotation and Reference Systems Service, Online: [https://www.iers.org/IERS/EN/Home/home\\_node.html](https://www.iers.org/IERS/EN/Home/home_node.html), Last Accessed: October 4, 2021.
- [33] NASA Goddard Space Flight Center, 2018, *Goddard Enhanced Onboard Navigation System (GEONS), Mathematical Specifications*, Release 3.0
- [34] Ashby, N., 2003, "Relativity in the Global Positioning System," *Living Reviews in Relativity*, Vol. 6, No. 1. doi: 10.12942/lrr-2003-1
- [35] Nelson, R.A.; Ely, T., 2006, "Relativistic Transformations for Time Synchronization and Dissemination in the Solar System." *38th Annual Precise Time and Time Interval (PTTI) Meeting*, Reston, VA.
- [36] Soffel, M.; Langhans, R., 2013, *Space-Time Reference Systems*, Springer-Verlag.
- [37] Beard, R.; Senior, K., 2017, "Clocks," In: Teunissen P.J., Montenbruck O. (eds) *Springer Handbook of Global Navigation Satellite Systems* Springer Handbooks. Springer, Cham.
- [38] Nelson, R.A., 2011, "Relativistic Time Transfer in the Vicinity of the Earth and in the Solar System." *Metrologia*, Vol. 48.
- [39] Acton, C.H., 1996, "Ancillary Data Services of NASA's Navigation and Ancillary Information Facility," *Planetary and Space Science*, Vol. 44, No. 1, pp. 65-70, doi: 10.1016/0032-0633(95)00107-7.
- [40] NASA Navigation and Ancillary Information Facility, "Ephemeris Subsystem SPK," SPICE Tutorial Documentation, January 2020.
- [41] "JPL Planetary and Lunar Ephemerides," [https://ssd.jpl.nasa.gov/?planet\\_eph\\_export](https://ssd.jpl.nasa.gov/?planet_eph_export), Last accessed: 9/13/21.
- [42] Ephemerides of Planets and the Moon, Online: <http://iaaras.ru/en/about/issues/emp/> Last accessed: 9/13/21
- [43] Fienga, A.; Deram, P.; Viswanathan, V.; Di Ruscio, A.; Bernus, L.; Durante, D.; Gastineau, M.; Laskar, J., 2019, "INPOP19a Planetary Ephemerides," *Notes Scientifiques et Techniques de l'Institut de mécanique céleste* No. 109.
- [44] Seago, J.H.; Vallado, D.A., 2000, "Coordinate Frames of the US Space Object Catalogs," *AAS/AIAA Astrodynamics Specialist Conference*, Denver, CO.
- [45] International Astronomical Union, 2021, "Standards of Fundamental Astronomy: SOFA Tools for Earth Attitude," Software Documentation.

- [46] Capitaine, N.; Guinot, B.; and Souchay, J., 1986, "A Non-Rotating Origin on the Instantaneous Equator: Definition, Properties and Use," *Celestial Mechanics and Dynamical Astronomy*, Vol. 36, pp. 283-307, doi: 10.1007/BF01234311.
- [47] Capitaine, N.; Wallace, P.T., 2006, "High Precision Methods for Locating the Celestial Intermediate Pole and Origin," *Astronomy and Astrophysics*, Vol. 450, pp. 855-872, doi: 10.1051/0004-6361:20054550.
- [48] Coppola, V.; Seago, J.H.; Vallado, D.A., 2009, "The IAU 2000A and IAU 2006 Precession-Nutation Theories and Their Implementation," *19th AAS/AIAA Space Flight Mechanics Meeting*, Savannah, Georgia.
- [49] Bradley, B.K.; Sibois, A.; Axelrad, P., 2016, "Influence of ITRS/GCRS Implementation for Astrodynamics: Coordinate Transformations," *Advances in Space Research*, Vol. 57, Issue 3, pp. 850-866, doi: 10.1016/j.asr.2015.11.006.
- [50] Lambert, S.; Bizouard, C., 2002, "Positioning the Terrestrial Ephemeris Origin in the International Terrestrial Reference Frame," *Astronomy and Astrophysics*, Vol. 394, pp. 317-321, doi: 10.1051/0004-6361:20021139.
- [51] McCarthy, D.D.; Petit, G. (eds), 2003, "IERS Conventions (2003)", International Earth Rotation and Reference Systems Service, Technical Note 32.
- [52] Long, A.C.; Cappellari Jr., J.O.; Velez, C.E.; Fuchs, A.J., (eds), 1989, *Goddard Trajectory Determination System (GTDS): Mathematical Theory, Revision 1*
- [53] AGI Documentation Team and Subject Matter Experts, "Rotating Libration Point Coordinate System Technical Note," July 2020. Online: <https://help.agi.com/stk/index.htm#gator/eq-rlp.htm>, Last Accessed: 27 May 2021.
- [54] Stoer, J.; Bulirsch, R., 2002, *Introduction to Numerical Analysis*, Texts in Applied Mathematics, Springer.
- [55] Butcher, J.C., 1963, "Coefficients for the study of Runge-Kutta integration processes," *Journal of the Australian Mathematical Society* Vol. 3, No. 2.
- [56] Butcher, J.C., 1964, "On Runge-Kutta Processes of High Order," *Journal of the Australian Mathematical Society* Vol. 4, No. 2, doi: 10.1017/S1446788700023387
- [57] Butcher, J.C., 2016, *Numerical Methods for Ordinary Differential Equations*, John Wiley and Sons, Ltd.
- [58] Rosales, J.J.; Colomina, I., 2005, "A Flexible Approach for the Numerical Solution of the INS Mechanization Equations", *Proceedings of the 6th Geometric Week*, Barcelona, Spain.
- [59] Jorba, À; Zou, M., 2005, "A Software Package for the Numerical Integration of ODE by Means of High-Order Taylor Methods", *Experimental Mathematics* 14, pp. 99-117.
- [60] Meyer, K.; Offin, D., 2017, *Introduction to Hamiltonian Dynamical Systems and the N-Body Problem*, Springer International Publishing, 3rd edition.
- [61] Channell, P. J.; Scovel, C., 1990, "Symplectic Integration of Hamiltonian Systems", *Nonlinearity* Vol. 3, No. 231, doi: 10.1088/0951-7715/3/2/001.

- [62] Gladman, B.; Duncan, M.; Candy, J., 1991, "Symplectic Integrators for Long-Term Integrations in Celestial Mechanics", *Celestial Mechanics and Dynamical Astronomy* Vol. 52, pp. 221-240, doi: 10.1007/BF00048485.
- [63] Keller, H.B., 2018, *Numerical Methods for Two-Point Boundary-Value Problems*, Dover Publications.
- [64] Betts, J.T., 2010, *Practical Methods for Optimal Control and Estimation Using Nonlinear Programming* Society for Industrial and Applied Mathematics.
- [65] Kelley, C.T., 2003, *Solving Nonlinear Equations with Newton's Method*, Society for Industrial and Applied Mathematics.
- [66] Beyn, W.-J., Champneys, A.; Doedel, E.; Govaerts, W.; Kuznetsov, Y. A.; Sandstede, B., 2001, "Numerical continuation, and computation of normal forms," in *In Handbook of dynamical systems III: Towards applications*, Citeseer.
- [67] Keller, H.B., 1977, "Numerical solution of bifurcation and nonlinear eigenvalue problems," in *Applications of Bifurcation Theory*, pp. 359–384.
- [68] Rao, A., 2010, "A Survey of Numerical Methods for Optimal Control," *Advances in the Astronautical Sciences*, Vol. 135.
- [69] Betts, J. T., 1998, "Survey of Numerical Methods for Trajectory Optimization," *Journal of Guidance, Control, and Dynamics* Vol. 21, No. 2, doi: 10.2514/2.4231.
- [70] Conway, B. A., 2012, "A Survey of Methods Available for the Numerical Optimization of Continuous Dynamic Systems," *Journal of Optimization Theory and Applications*, Vol. 152, pp. 271–306, doi: 10.1007/s10957-011-9918-z.
- [71] Conway, B. A. (Ed.), 2014, "Spacecraft Trajectory Optimization" *Cambridge Aerospace Series, Series Number 29*.
- [72] Szebehely, V., 1967, *Theory of Orbits: The Restricted Problem of Three Bodies*, Academic Press, London, UK.
- [73] Folkner, W.M.; Williams, J.G.; Boggs, D.H., 2009, "The Planetary and Lunar Ephemeris DE 421," IPN Progress Report 42-178.
- [74] Koon, W.S.; Lo, M.W.; Marsden, J.E.; Ross, S.D., 2006, *Dynamical Systems, the Three Body Problem and Space Mission Design*, Springer-Verlag New York Incorporated.
- [75] Bosanac, N., 2016, "Leveraging Natural Dynamical Structures to Explore Multi-Body Systems," Ph.D. Dissertation, Purdue University, West Lafayette, IN.
- [76] K. C. Howell, 1984, "Three-Dimensional, Periodic, 'Halo' Orbits," *Celestial Mechanics*, Vol. 32, No. 1, pp. 53–71, doi: 10.1007/BF01358403.
- [77] Wiesel, W. E.; Pohlen, D. J., 1994, "Canonical Floquet Theory," *Celestial Mechanics and Dynamical Astronomy*, vol. 58, no. 1, pp. 81–96, doi: 10.1007/BF00692119.
- [78] T.A. Pavlak, 2010, "Mission Design Applications in the Earth-Moon System: Transfer Trajectories and Station-Keeping," Masters Thesis, Purdue University, West Lafayette, IN.

- [79] Folta, D.C.; Bosanac, N.; Guzzetti, D.; Howell, K.C., 2015, "An Earth-Moon System Trajectory Design Reference Catalog," *Acta Astronautica*, Volume 110, pp. 341-353, doi: 10.1016/j.actaastro.2014.07.037
- [80] Doedel, E.J.; Romanov, V.A.; Paffenroth, R.C.; Keller, H.B.; Dichmann, D.J.; Galán-Vioque, J.; Vanderbauwhede, A., 2007, "Elemental Periodic Orbits Associated with the Libration Points in the Circular Restricted 3-Body Problem," *International Journal of Bifurcation and Chaos*, Vol. 17, No. 8, pp. 2625-2677, doi: 10.1142/S0218127407018671.
- [81] Broucke, R.A., 1968, "Periodic Orbits in the Restricted Three-Body Problem With Earth-Moon Masses," NASA Technical Report 32-1168.
- [82] Vaquero, M, 2013, "Spacecraft Transfer Trajectory Design Exploiting Resonant Orbits in Multi-Body Environments," PhD Dissertation, Purdue University, West Lafayette, IN.
- [83] Dichmann, D.J.; Parker, J.K.; Williams, T.W.; Mendelsohn, C.R., 2014, "Trajectory Design for the Transiting Exoplanet Survey Satellite," *24th International Symposium on Space Flight Dynamics*, Laurel, MD.
- [84] Dichmann, D.J.; Lebois, R.; Carrico, J.P., 2013, "Dynamics of Orbits Near 3:1 Resonance in the Earth-Moon System," *Journal of Astronautical Sciences*, Vol. 60, No. 1, pp. 51-86, doi: 10.1007/s40295-014-0009-x.
- [85] McComas, D.J.; Carrico, J.P.; Hautamaki, B.; Intelisano, M.; Lebois, R.; Loucks, M.; Policastri, L.; Reno, M.; Scherrer, J.; Schwadron, N.A.; Tapley, M.; Tyler, R., 2011, "A New Class of Long-Term Stable Lunar Resonance Orbits: Space Weather Applications and the Interstellar Boundary Explorer," *Space Weather*, Vol. 9, S11002, doi: 10.1029/2011SW000704.
- [86] Contopoulos, G., 2002, *Order and Chaos in Dynamical Astronomy*, Springer-Verlag, Berlin, Heidelberg.
- [87] Perko, L., 2000, *Differential Equations and Dynamical Systems: Third Edition*, New York, Springer.
- [88] Pavlak, T.A., 2013, "Trajectory Design and Orbit Maintenance Strategies in Multi-Body Regimes," PhD Dissertation, Purdue University, West Lafayette, IN.
- [89] Olikara, Z.P.; Scheeres, D.J., 2012, "Numerical Method for Computing Quasi-Periodic Orbits and their Stability in the Restricted Three-Body Problem," *IAA Conference on Dynamics and Control of Space Systems*, Porto, Portugal.
- [90] Schilder, F.; Osinga, H.M.; Vogt, W., 2005, "Continuation of Quasi-Periodic Invariant Tori," *SIAM Journal on Applied Dynamical Systems*, Vol. 4, No. 3, pp. 459-488, doi: 10.1137/040611240.
- [91] Gómez, G.; Mondelo, J.M., 2001, "The Dynamics Around the Collinear Equilibrium Points of the RTBP," *Physica D*, Vol. 157, No. 4, pp. 283-321, doi: 10.1016/S0167-2789(01)00312-8.
- [92] Jorba, Á., 2001, "Numerical Computation of the Normal Behavior of Invariant Curves of n-Dimensional Maps," *Nonlinearity*, Vol. 14, No. 5, pp. 943-976, doi: 10.1088/0951-7715/14/5/303.
- [93] Jorba, Á., 1999, "A Methodology for the Numerical Computation of Normal Forms, Centre Manifolds and First Integrals of Hamiltonian Systems," *Experimental Mathematics*, Vol. 8, No. 2, pp. 155-195.

- [94] Bosanac, N., 2020, "ASEN 6060 Lecture Notes," University of Colorado Boulder.
- [95] Zardań, L.; Farrés, A.; Puig, A., 2020, "High-Fidelity Modeling and Visualizing of Solar Radiation Pressure: A Framework for High-Fidelity Analysis," *AAS/AIAA Astrodynamics Specialist Conference*.
- [96] Gibbs, B.P., 2011, *Advanced Kalman Filtering, Least-Squares and Modeling*, Wiley, Hoboken, NJ.
- [97] NASA Goddard Space Flight Center, 2020, *General Mission Analysis Tool (GMAT) User Guide: Propagator*, <http://gmat.sourceforge.net/doc/R2020a/html/Propagator.html>.
- [98] Haapala, A.F.; Vaquero, M; Pavlak, T.A.; Howell, K.C.; Folta, D.C., 2013, "Trajectory Selection Strategy for Tours in the Earth-Moon System," *AAS/AIAA Astrodynamics Specialist Conference*, Hilton Head, SC.
- [99] Restrepo, R.L.; Russell, R.P., 2018, "A Database of Planar Axi-Symmetric Periodic Orbits for the Solar System," *Celestial Mechanics and Dynamical Astronomy* Vo. 130, No. 49, doi:10.1007/s10569-018-9844-6.
- [100] Parker, J.S.; Born, G.H., 2008, "Direct Lunar Halo Orbit Transfers," *The Journal of the Astronautical Sciences*, Vol. 56, No. 4, pp. 441-476, doi: 10.1007/BF03256561.
- [101] Parker, J.S.; Anderson, R.L., 2014, *Low-Energy Lunar Trajectory Design*. Vol. 12. John Wiley & Sons.
- [102] Folta, D.C., Dichmann, D.J., Clark, P., Haapala, A.F., Howell, K.C., 2015, "Lunar Cube Transfer Trajectory Options," *AAS/AIAA Space Flight Mechanics Meeting*, Williamsburg, VA.
- [103] Ozimek, M.T.; Howell, K.C., 2010, "Low-Thrust Transfers in the Earth-Moon System, Including Applications to Libration Point Orbits," *Journal of Guidance, Control, and Dynamics* Vol. 33, No. 2, pp. 533-549, doi: 10.2514/1.43179.
- [104] McGuire, M.L., Burke, L.M., McCarty, S.L., Hack, K.J., Whitley, R.J., Davis, D.C., Ocampo, C., 2017, "Low Thrust Cis-Lunar Transfers Using a 40 kw-class Solar Electric Propulsion Spacecraft," *AAS/AIAA Astrodynamics Specialist Conference*, Stevenson, WA.
- [105] Bosanac, N.; Cox, A.D.; Howell, K.C.; Folta, D.C., 2018, "Trajectory Design for a Cislunar CubeSat Leveraging Dynamical Systems Techniques: The Lunar IceCube Mission," *Acta Astronautica*, Vol. 144, pp. 283-296, doi: 10.1016/j.actaastro.2017.12.025.
- [106] Parker, J.S.; Anderson, R.L.; Peterson, A., 2013, "A Survey of Ballistic Transfers to Low Lunar Orbit," *Journal of Guidance Control and Dynamics*, Vol. 36, No. 5, pp. 1501-1511, doi: 10.2514/1.55661.
- [107] Bosanac, N; Webster, C.M.; Howell, K.C.; Folta, D.C., 2019, "Trajectory Design for the Wide Field Infrared Survey Telescope Mission," *Journal of Guidance, Control, and Dynamics* Vol. 42, No. 9, pp. 1899-1911, doi: 10.2514/1.G004179.
- [108] Davis, D.C.; Phillips, S.M.; Howell, K.C.; Vutukuri, S.; McCarthy, B.P., 2017, "Stationkeeping and Transfer Trajectory Design for Spacecraft in Cislunar Space," *AAS/AIAA Astrodynamics Specialist Conference*, Stevenson, WA.
- [109] Guzzetti, D.; Zimovan, E.M.; Howell, K.C.; Davis, D.C., 2017, "Stationkeeping Analysis for Spacecraft in Lunar Near Rectilinear Halo Orbits," *27th AAS/AIAA Space Flight Mechanics Meeting*, San Antonio, Texas.

- [110] Dunham, D.W.; Roberts, C.E., 2001, "Stationkeeping Techniques for Libration-Point Satellites," *Journal of Astronautical Sciences*, Vol. 49, pp. 127–144, doi: 10.1007/BF03546340.
- [111] Farrés, A.; Gao, C.; Masdemont, J. J.; Gómez, G.; Folta, D. C.; Webster, C., 2022, "Geometrical Analysis of Station-Keeping Strategies About Libration Point Orbits," *Journal of Guidance, Control, and Dynamics*, Vol. 45, No. 6, pp. 1108-1125, doi: 10.2514/1.G006014.
- [112] Folta, D.C.; Pavlak, T.; Haapala, A.F.; Howell, K.C.; Woodard, M.A., 2014, "Earth–Moon Libration Point Orbit Stationkeeping: Theory, Modeling, and Operations," *Acta Astronautica*, Vol. 94, No. 1, pp. 421-433, doi: 10.1016/j.actaastro.2013.01.022.